Gdańsk University of Technology
Faculty of Civil and Environmental Engineering

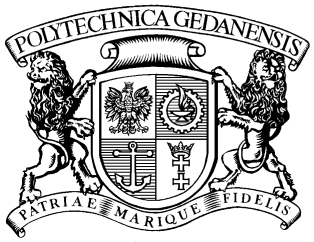

mgr inż. Krzysztof Arendt

Influence of external walls' thermal capacitance on indoor thermal comfort

Doctoral thesis

Supervisor: dr hab. inż. Marek Krzaczek

Gdańsk, 2012

Summary

The doctoral thesis presents the results of numerical investigations on the influence of walls' thermal capacitance on indoor thermal comfort. A proper set of thermal parameters of a building structure can considerably limit the heating / cooling demand, and passively increase the indoor thermal comfort. However the effect of building thermal capacitance on indoor conditions is complex and not always beneficial. Among a great number of interfering factors are e.g. climatic conditions, building shape, ventilation system type, operational schedule and many others. The aim of the present study is to investigate the potential of high thermal capacitance walls under the climatic conditions typical for Poland.

The investigations are based on a number of simulations performed using a numerical model of a part of buildings. The model consists of two main separate components: the indoor air submodel and the external wall submodel. The submodels work together in a co-simulation, exchanging the solution at the common boundaries. A considerable part of the model has been developed by the author.

The model treats indoor space as a nonuniform environment, and provides the basic indoor environment parameters affecting the human thermal comfort, i.e. the air temperature and velocity. The output parameters are analyzed separately but they are also used to calculate the expected thermal sensation in the considered space.

The evaluation of the walls' thermal capacitance potential to increase the level of the indoor thermal comfort is based on the results produced by a significant number of various simulations. The analysis covers different wall structures, two different ventilation air exchange rates and two types of the outdoor temperature profiles: (1) one-week sol-air temperature profile and (2) simple step change temperature profile.

The results indicate that indoor thermal comfort can be increased by a proper thermal capacitance of building walls. However, it is also shown that the ventilation air exchange rate can have a prevailing influence on indoor conditions, limiting stabilizing effects of the walls' thermal capacitance.

Contents

List of Figures

List of Tables

List of important symbols

Latin symbols

ACH – air exchange rate [h^{-1}]
c – specific heat [J/(kg K)]
C – heat capacity [J/(m^3 K)]
C_{wall} – wall planar thermal capacitance [J/(m^2 K)]
C_{th} – thermal capacitance [J/K]
DR – percentage of people dissatisfied from draft [%]
h – convective heat transfer coefficient (HTC) [W/(m^2 K)]
k – turbulent kinetic energy [m^2/s^2]
p – air pressure [Pa]
PMV – predicted mean vote [–]
PDD – percentage of people dissatisfied from thermal environment [%]
q – heat flux per area [W/m^2]
$\dot{Q}$ – heat flux [W]
t – time [s]
T – temperature [°C]
T_{DB} – dry-bulb temperature [°C]
T_{MR} – mean radiant temperature (MRT) [K]
T_{sol} – sol-air temperature [°C]
$\mathbf{u}$ – air velocity vector [m/s]
U – overall heat transfer coefficient (U-value) [W/(m^2 K)]

Greek symbols

α – thermal diffusivity [m^2/s]
α_T – turbulent thermal diffusivity [m^2/s]
ϵ – turbulent kinetic energy dissipation rate [m^2/s^3]
λ – thermal conductivity [W/(m K)]
μ – viscosity [Pa·s]
μ_T – turbulent viscosity [Pa·s]
ρ – density [kg/m^3]

Chapter 1

Introduction

1.1 Phenomenon and problem

The human body can maintain a thermal balance with the environment under a wide range of conditions thanks to the great capabilities of a body thermoregulatory system. However, human beings inhabit different climate zones, hence, there is a need of the additional heating or cooling of the indoor space in most world regions.

One of the main building functions is to maintain thermally comfortable indoor conditions and protect occupants from undesirable or unpredictable heating or cooling loads. Thus, buildings should be designed having not only architectural and structural aspects in mind, but also indoor environment quality aspects. Comfortable indoor conditions are crucial for occupants to work or rest efficiently, and since most of the human lifetime is spent in indoors, the impact of the buildings quality on the entire human activity is invaluable.

Heating and cooling technologies used to maintain indoor thermal comfort can be divided into two groups:

- active technologies,
- passive technologies.

The active technologies are based on mechanical systems which are usually powered by the electric energy, e.g. the HVAC systems. These technologies are responsible for a significant share of the building energy demand. The passive technologies on the other hand rely on special architectural and structural design solutions which allow for controlling indoor conditions using the renewable energy, particularly the solar energy, e.g. the Trombe wall . The utilization of passive technologies can decrease the building energy demand significantly.

According to the recent data from the European Union [14] and United States of America [1] buildings are responsible for approximately 40% of the total energy demand. It is estimated that the space heating and cooling consume about 57% of the energy used by European residential buildings [14]. At present, most of this energy comes from the non-renewable energy sources. Thus, the maintenance of the comfortable indoor environment generates a great environmental and financial cost.

To reduce the building energy consumption there are ongoing efforts to increase the efficiency of active heating and cooling systems. On the other hand, there are initiatives to improve the building thermal parameters. Building thermal standards become more and more restrictive on the thermal resistance of the building envelope. A high thermal resistance minimizes the building heat loss and attenuates the influence of outdoor temperature variations to some extent. However, the thermal resistance is a static thermal parameter, describing the steady state characteristics, while buildings are mainly exposed to transient conditions. To describe the dynamic thermal characteristics of building components, their thermal capacitance has to be taken into account. Walls with the equal thermal resistance can still have significantly different thermal capacitances, that results in a different thermal performance and impact on the indoor environment.

It is well known that buildings with massive and heavyweight walls can provide more comfortable indoor conditions than buildings with lightweight walls, especially during the summer season [13]. Massive and heavyweight walls due to their high thermal capacitance and thermal inertia limit indoor temperature variations and delay peak temperatures. By keeping the indoor temperature closer to the mean outdoor temperature they decrease the temporal overheating risk. Thus, the use of the high thermal capacitance of walls can be regarded as a passive heating / cooling technology, decreasing the energy demand of buildings.

However, the influence of the thermal envelope thermal capacitance on the indoor environment is complex and still not thoroughly understood. The performance of passive heating and cooling technologies highly depends on climatic conditions. The actual potential of high thermal capacitance walls under Polish climatic conditions is not well documented.

The influence of the envelope thermal capacitance was mostly studied treating the indoor space as a uniform and instantly air-mixing zone, using lumped capacitance models [146, 130, 112, 149]. Up to the now a little attention was devoted to check the validity of this assumption. Moreover, such approach does not allow for calculating the indoor air velocity, an important factor affecting the thermal comfort level.

Indoor air temperature and velocity can be nonuniform due to both the forced and natural convection. The forced convection can dominate, e.g. due to the ventilation, while the natural convection occurs due to nonuniform temperatures of the indoor air and adjacent surfaces. A simple lumped capacitance model cannot take any of these nonuniformities into account. On the other hand, complex CFD models are often too computationally demanding to perform transient simulations, or are just not capable to include the effects of the heat transfer in adjacent solids.

By these reasons, the stabilizing influence of high thermal capacitance walls on indoor conditions has not been extensively studied so far, especially in terms of both spatial and temporal effects and with respect to Polish climatic conditions.

1.2 Aims

The main aim of the thesis is to analyze the influence of the external walls' thermal capacitance on the indoor thermal comfort for Polish climate conditions. Two kinds of heat loads are assumed: due to the heat transmission and due to the ventilation. In contrast to many other studies (as e.g. Rodrigues [112] or Zhang et al. [146]), the indoor space is treated as a nonuniform medium in this work. The local values of indoor environment parameters, like the air temperature and velocity, are available for any point in space and time. Subsequently from these basic parameters, local and space-averaged thermal comfort indices are evaluated using the well known approaches of PMV and PPD and draft prediction models.

The influence of thermal capacitance is evaluated for two different wall insulation levels: one closely meeting the Polish standards and the second meeting the passive house standard. The analysis covers single-layer walls and multilayer wall assemblies. By comparing the results for single- and multilayer walls, the consequences of the nonuniform heat capacity distribution are discussed.

The present study was performed using a numerical model of a single-room space representing a part of buildings. The model is able to simulate three-dimensional transient indoor airflow in fluid domains and one-dimensional transient heat conduction in solid layers of thermal envelope components. A co-simulation method is implemented to solve the multi-domain problem.

1.3 Outline

The thesis consists of 6 chapters. Chapter 2 presents a review of the scientific literature in the field of the human thermal comfort, building thermal modeling and

influence of the building thermal capacitance on indoor conditions. The information included in this chapter is crucial to justify the assumed methodology of investigations.

Chapter 3 presents a thermal model of a building utilized in investigations. The model consists of two submodels running together in the co-simulation. The first submodel simulates the air flow in the indoor zone, while the second the heat transfer in the building thermal envelope. The model is capable to provide basic indoor environment parameters affecting the human thermal comfort, i.e. air temperature and air velocity distribution. These parameters are used to estimate the expected thermal sensation, based on the PMV / PPD thermal comfort indices.

Chapter 4 presents the model validation results. Each component of the model is verified against experimental data or results provided by a reliable commercial code.

Chapter 5 presents the numerical investigations of the influence of the thermal capacitance of external walls on the indoor thermal comfort. The investigations are divided into two main stages: (1) a comparison of the performance during a summer one-week time period, (2) and an indoor environment stability test, aiming at showing inertial characteristics of different walls exposed to a simple step change of the outdoor temperature.

Chapter 6 includes the final conclusions and future work plan.

1.4 Novelties

The novel research points of the thesis are as follows:

1. numerical analysis of the influence of the external walls' thermal capacitance on the indoor thermal comfort, accounting for nonuniformities of the indoor environment,

2. the wall function and finite volume mesh refinement procedure implementation to fit the convective heat transfer coefficients to the empirical data for both natural and forced convection conditions,

3. self-developed procedure for a co-simulation of a three-dimensional fluid domain and adjacent one-dimensional solid domains, based on the mutual exchange of spatially-averaged temperatures and heat fluxes.

Chapter 2

Literature review

2.1 Thermal comfort

The thermal comfort is often defined as the condition of the mind expressing satisfaction with the surrounding thermal environment [4]. Under close-to-steady conditions, the thermal comfort is reached when a human body is in a thermal balance with the surrounding environment, and this balance is maintained without experiencing sweating or shivering. The thermal sensation under transient conditions is far more complex to evaluate. Any change in the thermal environment enforces a reaction of the human thermoregulatory system to maintain the thermal balance. The more intensive the reaction is, the higher is the thermal strain of the body.

The research on the human thermal comfort in various environmental conditions started in the first half of the 20th century and was intensified during the World War II. It is estimated that till now over a half of a million people totally took part in various investigations concerning the indoor microclimate and thermal comfort [124]. The acquired data cover both sexes, almost all geographical regions, cultural groups and age ranges. It is now clear, that thermal comfort depends on a great number of factors including physical, physiological, psychological and other [36].

As a result of the ongoing research, a significant number of standards and mathematical models evaluating thermal comfort have been developed. However, due to the huge number of factors contributing to the thermal comfort, mathematical models are usually valid only for a limited range of conditions. Some models give the most accurate predictions in hot and humid climates, while the other are more suitable for mild climates. In addition, mathematical models for the thermal comfort assessment give the best results depending upon the accuracy of input data, while many parameters are difficult to measure or evaluate. It is especially the case of psychological factors.

In the first half of the 20th century, only simple thermal comfort indices existed. They usually described how warm or cold a human body would feel in a given environment. All of these indices were purely empirical. Usually, the input variables were the temperature and humidity.

In 1970s three the most significant thermal comfort models were developed: the Gagge's two-node model, the Fanger's PMV-PPD model and the Stolwijk's multi-node model. These models predict the human thermal comfort by assessing the net heat load on the human body.

The two most known and cited standards regarding indoor thermal comfort are:

- ISO Standard 7730 [74],
- ASHRAE Standard 55 [4].

Both standards are in a close agreement by specifying the conditions acceptable for the majority of occupants. They are mostly based on the PMV-PPD thermal comfort model (described in Section 2.1.4.2). The specified conditions cannot represent a comfortable range for all occupants because it is not possible to determine the exact values of occupants' personal factors, like metabolic rates or clothing levels. Therefore, operating set points for buildings cannot be practically mandated by these standards [4].

The thermal comfort assessment methods presented in the standards are suitable for close-to-steady-state indoor conditions. The thermal comfort evaluation is divided into two parts: an entire-body thermal comfort evaluation and an evaluation of the local thermal discomfort (caused by unwanted local cooling or heating of the body). Four possible causes of the local thermal discomfort are specified: radiant temperature asymmetry (cold or warm surfaces), draft (local cooling of the body caused by air movement), vertical air temperature difference and cold or warm floors.

2.1.1 Human thermoregulatory system

Human is a warm-blooded animal, what means that the human body keeps almost a constant internal temperature regardless of the external temperature variations. The core body temperature is one of the most tightly regulated parameters of the human physiology [84]. It is possible thanks to the human thermoregulatory system which uses a negative feedback mechanism to regulate the heat exchange between the body and its surroundings. The core body temperature is kept at the level of about 37 °C (±1°). The thermoregulation is so effective that in most conditions the

body temperature deviates no more than a few tenths of the degree from its normal value [84].

The human body constantly generates heat. The heat must be dissipated to surroundings through the skin and by the respiration. In thermally neutral conditions the average share of the heat transfer for the skin and respiration is approximately 88% and 12%, respectively. The heat transfer through the skin is a result of conduction in the tissue and convection in the blood.

In mammals the dominant thermoregulatory controller is the hypothalamus. The stimuli from the body skin surface, deep tissues, spinal cord and the brain are the inputs for the thermoregulatory system. The possible outputs, i.e. the phenomena occurring to diminish the excessive body heat load, are: sweating, vasolidation, vasoconstriction, non-shivering thermogenesis and shivering. Sweating and vasolidation occur under hot conditions, when the heat flux from the body to the surroundings has to be intensified. On the other hand, vasoconstriction, non-shivering thermogenesis and shivering occur under cold conditions. These three phenomena increase the heat generation in the body, helping to maintain a constant temperature. The approximate body core temperature thresholds for all the thermoregulatory responses are presented in Fig. 2.1.

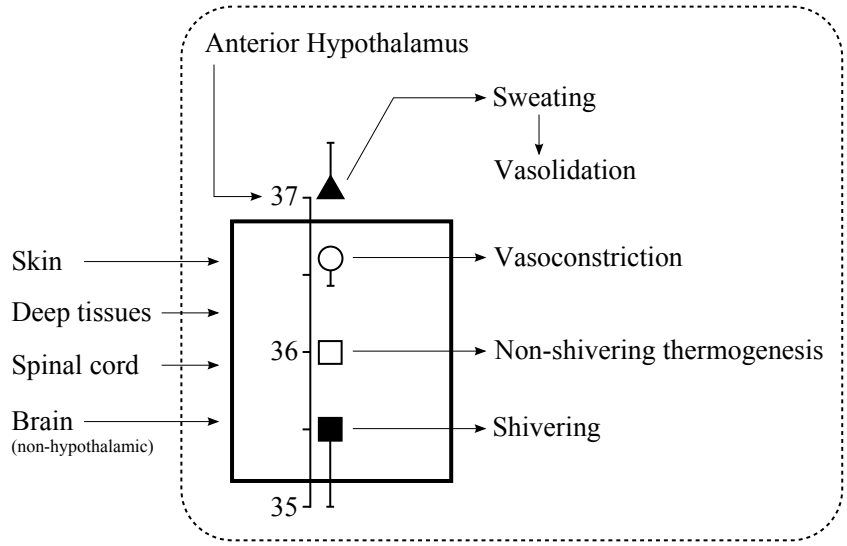

Figure 2.1: Human thermoregulatory system scheme [84]

Sweating (perspiration) allows the body to decrease its temperature, due to the sweat evaporation from the skin surface. The cooling effect is caused by the latent heat of evaporation.

Vasolidation is the act of blood vessels widening, which occurs in hot conditions. The increased blood flow to the skin increases its temperature. A higher skin

temperature result in a higher heat flux from the body to surroundings.

Vasoconstriction is the narrowing of blood vessels. It is the opposite action to vasolidation. It decreases the blood flow to the skin, simultaneously decreasing its temperature and therefore the heat loss to the surrounding environment. The skin temperature decreases the most on the peripheral areas of the body, like feet and hands, where the temperature can drop down to 10 °C. The forehead is the least affected region, with the possible temperature drop of about 1 °C [124].

Additionally, in order to preserve the heat balance, an increased heat generation in the body can occur. The heat can be generated either by non-shivering thermogenesis or by shivering. At first, the body tries to obtain the heat balance by non-shivering thermogenesis, during which brown adipose tissue (brown fat) is metabolized to generate heat. If the generated heat production rate is insufficient, shivering occurs. Basically, the shivering is the heat production by the conversion of the chemical energy into the kinetic energy, which partially shows up as heat.

Although the body core temperature keeps tightly within a certain range (usually not wider than 0.2 °C), the skin temperature varies considerably in time as well as between different parts of the body. The average skin temperature of a human being in a thermal comfort is approximately 33.5 °C, with a standard deviation of 0.5 °C [124]. Usually, the highest temperature occurs on the neck — about 35 °C, while the lowest on the feet surface — about 32 °C.

2.1.2 Thermal comfort — contributing factors

Human's sensation of the thermal comfort depends on the balance between the body heat gains and losses. The heat gains and losses are affected by many factors, which can be grouped into personal and environmental ones. There are four environmental factors: air temperature, mean radiant temperature, air velocity and humidity [41]. The personal factors are the activity and clothing. These six factors are considered as basic ones, having the most significant influence on the thermal sensation. Among many minor factors are: acclimation, body shape, age, gender, state of health and many others including psychological factors. The influence of minor factors is usually not considered in the engineering practice.

The total impact of each factor (environmental or personal) is usually represented as a heat flux acting on a human body. In most cases to evaluate this heat flux, the human body surface area has to be known. The most common approach to evaluate the body surface area is by the means of the DuBois formula [37]:

$$A_D = 0.202\mathrm{m}^{0.425}\mathrm{h}^{0.725}\,, \tag{2.1.1}$$

where A_D is the body surface, m is the body mass [kg] and h is the body height [m]. Typically, the body surface area is in the range of $1.4 \div 2.3\,\mathrm{m}^2$.

Environmental factors

The air temperature is the most obvious and usually regarded as the most important environmental factor affecting the thermal comfort. Its influence is taken into account in all thermal comfort models. The term "air temperature" usually refers to the dry bulb temperature (DBT), which is measured by a thermometer exposed to the air, but shielded from radiation and moisture.

The higher the air temperature, the more difficult is the dissipation of the body generated heat. On the other hand, if the temperature is too low, the body thermoregulatory responses, like shivering or non-shivering thermogenesis, can be insufficient to maintain the thermal balance. The comfortable temperature range depends on many factors, like the human activity, air humidity or local air movement.

In most cases, the air flow around body has a cooling effect, because the body is usually hotter than the surrounding air. The air flow increases the convective heat exchange between a person and the environment [74]. The higher the air velocity, the more significant the cooling effect.

The high air velocity decreases the neutral temperature, i.e. the temperature perceived by an occupant feeling neutrally from a thermal point of view in a given space. Therefore, increased air velocities are often used to offset the sensation of warmth due to the high air temperature.

Generally, the air velocities up to 0.5 m/s are considered as pleasant. However, in hot conditions the sensation due to the air flow may be different and even velocities of up to 1 m/s may be considered as pleasant. The average sensations of people subjected to different air velocities in everyday conditions in moderate climates are presented in Tab. 2.1 [11].

Table 2.1: Average human sensations due to different air speeds [11]

Air velocity (m/s)	Average human sensation
< 0.25	unnoticed
0.25–0.50	pleasant
0.50–1.00	awareness of air movement
1.00–1.50	drafty
> 1.50	annoyingly drafty

The next environmental factor, humidity, affects the evaporation rate at the skin surface. The humidity can be expressed in various ways, including a relative humidity, absolute humidity or vapor pressure. In moderate conditions, the air humidity has a limited impact on the thermal sensation [74]. In typical conditions, a 10% raise of the relative humidity is felt as the 0.3 °C temperature raise. The humidity has a more significant influence in high temperatures (>26 °C) and for humans engaged in some intensive activities (> 2 met). A significant influence is observed also under transient conditions.

The human heat balance is also affected by the thermal radiation. The exact evaluation of the radiative heat exchange is extremely complex, since each part of the body has a different temperature and is faced toward a different direction.

In most thermal comfort models, the radiative heat exchange between a body and its surroundings is simplified by using a single value describing the temperature of surrounding surfaces: the *mean radiant temperature* (MRT). The MRT is defined as a uniform temperature of hypothetical surroundings comprised of black surfaces, which would cause a radiative heat exchange with the considered object equal to the actual heat exchange in given conditions. The MRT depends on the object type, shape and position in space. The use of the MRT is convenient, but it also imposes some limitations. The main is that MRT neglects the radiation asymmetry, which also affects the thermal comfort sensation (as discussed in Section 2.1.2).

The radiative heat exchange between a clothed person and surrounding environment is governed by the Stefan-Boltzmann law for gray bodies. Utilizing the MRT it can be written as follows [40]:

$$Q_R = A_{ef}\epsilon\sigma\left(t_{cl}^4 - {T_{MR}}^4\right) ,$$

where $Q_R$is the radiative heat flux between the body and surroundings [W], A_{ef} is the clothed body surface effective area [m^2], ϵ is the clothing surface emissivity [–], σ is the Stefan-Boltzmann constant, $\sigma = 5.6704 \cdot 10^{-8}$ [W/m^{2}K], T_{MR} is the mean radiant temperature [K] and t_{cl} is the clothing surface temperature [K].

One of the main difficulties related to the radiative heat flux Q_R comes with the evaluation of the clothed body surface effective area. Since the clothed human body has a very irregular shape with many convexities and folds, some radiated heat is absorbed directly by other body parts. Hence, the effective area of the body is lower than the actual area and is usually calculated as:

$$A_{ef} = f_{ef} f_{cl} A_D ,$$

where f_{ef} is the effective area factor defined as the ratio of the effective area of a clothed body to the actual area of the clothed body [–], f_{cl} is the ratio of the clothed body area to naked body area [–], A_D is the naked body area (Eq. 2.1.1).

Both factors, f_{ef} and f_{cl}, can be obtained using the experimental data [40]. The effective area factor f_{ef} has different values for a standing and a seating position. The average value of f_{ef} is approximately 0.725 and 0.696 for a standing person and a seating person, respectively.

Personal factors

The most important personal factors affecting the human thermal comfort are the activity level and clothing.

The activity level affects a human metabolic rate. The human body constantly produces heat due to the non-conscious basal metabolism and conscious controllable muscular metabolism [11]. The metabolic rate is proportional to the rate of the O_2 consumption [52]. The metabolic rate is usually expressed as the power density per the unit body surface area [W/m^2]. In thermal comfort studies the common unit of the metabolic rate is *met*: $1\,\text{met} = 58.2\,\text{W/m}^2$. The typical values of human metabolic rates at some chosen activities are presented in Table 2.2 [4]. The total heat rate generated by a given person can be calculated by multiplying its metabolic rate with the body surface area.

Table 2.2: Metabolic rates for typical tasks (ASHRAE Standard 55 [4])

Activity	Met units	Metabolic rate [W/m^2]
Sleeping	0.7	40
Seated, reading, writing	1.0	60
Typing	1.1	65
Standing, relaxed	1.2	70
Walking on level surface (3.2 km/h)	2.0	115
Driving automobile	1.0-2.0	60-115
House cleaning	2.0-3.4	115-200
Handling 50 kg bags	4.0	235
Dancing, social	2.4-4.4	140-225

The heat produced by a body must dissipate to the environment. Otherwise, a change in the body temperature will occur. The main factor affecting the heat dissipation is the clothing insulation. In thermal comfort studies the unit which reflects

insulating capabilities of clothing is *clo* (1 clo is equivalent to the 6.45 W/(m^{2}K) U-value or the 0.155 (m^{2}K)/W thermal resistance). Some typical levels of the clothing insulation for various garment sets are presented in Table 2.3.

Table 2.3: Clothing insulation values (ASHRAE Standard 55 [4])

Clothing Description	Garments Included	I_{cl} [clo]
Trousers	1) Trousers, short-sleeve shirt	0.57
	2) Trousers, long-sleeve shirt	0.61
	3) #2 plus suit jacket, vest, T-shirt	1.14
	4) #2 plus long-sleeve sweater, T-shirt	1.01
	5) #4 plus suit jacket, long underwear bottoms	1.30
Skirts/Dresses	6) Knee-length skirt, short-sleeve shirt (sandals)	0.54
	7) Knee-length skirt, long-sleeve shirt, half slip, long-sleeve sweater	1.10
	8) Knee-length skirt, long-sleeve shirt, half slip, suit jacket	1.04
Shorts	9) Walking shorts, short-sleeve shirt	0.36
Overalls/Coveralls	10) Long-sleeve coveralls, T-shirt	0.72
	11) Overalls, long-sleeve shirt, T-shirt	0.89
	12) Insulated coveralls, long-sleeve thermal underwear tops and bottoms	1.37

Nonuniform environment

The combined environmental factors create a uniform or a nonuniform environment. In a nonuniform environment there exists a risk of the so-called local thermal discomfort independently of the total thermal balance. The local thermal discomfort can be particularly experienced by people at light activity (< 1.2 met). Higher levels of activity cause the lower thermal sensitivity. The common environmental nonuniformities are drafts, vertical air temperature differences, warm and cool floors, or radiant asymmetries.

A draft is the unwanted local cooling of the human body due to the air flow [4]. Factors contributing to the draft sensation are: air velocity, air temperature, turbulence intensity, activity and clothing. The parts of the body most sensitive to drafts are the head, neck, shoulders, ankles, feet and the legs. The drafts increase

the convective heat loss of the body, hence the skin areas not covered by clothing are the most influenced.

Vertical air temperature differences are typical for naturally ventilated buildings, where air is removed from the building due to temperature differences – a so-called stack effect. People are more sensitive when the temperature increases upwards than downwards. According to ISO 7730 [74], a vertical temperature difference of 7 °C contributes to approximately 55 % of dissatisfied people.

The heat transfer between the human feet and a floor is caused by the conduction. The local thermal sensation of a human standing on a floor depends not only on the floor temperature, but also on the floor material and the footwear material. Hot and cold floors can cause a local thermal discomfort even though a human is in a thermal balance in total. If a space is occupied by people with bare feet, the thermal sensation depends on the thermal activity b [$\mathrm{W\,s^{0.5}/(m^2\,K)}$] of a floor:

$$b = \sqrt{\lambda \rho c}\,,$$

where λ is the thermal conductivity [$\mathrm{W/(m\,K)}$], ρ is the density [$\mathrm{kg/m^3}$] and c is the specific heat [$\mathrm{J/(kg\,K)}$]. The higher the thermal activity of the floor material, the higher is the sensitivity to the floor temperature. Thus, a concrete floor is perceived as much cooler than e.g. a wooden floor.

The next nonuniformity, the radiant asymmetry, is caused by the temperature differences of internal surfaces in a given space. The influence of the radiant asymmetry on the human thermal comfort becomes important when the temperature differences are relatively large, i.e. tenths of Celsius degrees. Such temperature differences can be caused e.g. by high intensity infrared heaters. Small surface temperature differences cause a nonuniform heat exchange between the body and environment to a smaller extent than the clothing [40]. Therefore, a small radiant asymmetry is not relevant for the thermal comfort.

The assessment of the thermal discomfort caused by the radiant asymmetry is complex. Some general guidelines concerning the maximum radiant asymmetry can be found in the ISO 7730 [74] and ASHRAE–55 [4] standards (Tab. 2.4). These guidelines are based on experimental studies. However, they are valid only for temperature differences up to 15–35 °C. When considering high intensity radiant heaters, more sophisticated methods have to be applied. A common approach is to divide the human model into several segments and analyze the radiative heat exchange between the environment and each body segment [55].

Table 2.4: Allowable Radiant Temperature Asymmetry (data from ASHRAE Standard 55 [4])

Radiant Temperature Asymmetry [°C]			
Warm Ceiling	Cool Wall	Cool Ceiling	Warm Wall
<5	<10	<14	<23

Transient conditions

The thermal conditions in a given space can be steady or transient. When the environmental parameters variations in time are small, the human heat balance can be considered as steady [40]. In steady and close to steady environments, a simple steady heat balance equation can be applied to assess the thermal load and thermal comfort level. However, if a given environment undergoes dynamic changes in time, the steady state heat balance is no longer valid. A transient heat transfer is significantly more complex to analyze, since such factors like the human body thermal capacitance and thermal history have to be taken into account. In addition, the thermal comfort in transient conditions is considerably less investigated. Thus, it is desirable to use steady state equations.

The ISO 7730 [74] and ASHRAE–55 [4] standards distinguish three types of non-steady state conditions: temperature cycles, temperature drifts or ramps, and transients. Although the thermal sensation assessment under non-steady state conditions is complex, some general guidelines can be drawn. In particular, the standards specify the range of conditions under which steady state equations and a PMV-PPD thermal comfort model (described in Section 2.1.4.2) can be used with a reasonable accuracy.

Temperature cycles occur in conditioned spaces, where the control system tries to maintain a constant indoor temperature. It is assumed, that if the amplitude of oscillations is less than 1 °C, it does not affect the thermal comfort. Steady state requirements can be applied in such conditions.

The temperature drifts or ramps are monotonic and noncyclic changes in indoor temperature. Drifts refer to passive temperature changes, while ramps refer to actively controlled temperature changes [4]. The maximum allowable temperature change rate in which steady state recommendations still apply is 2.0 K/h.

In the general case of transient thermal conditions, the ISO 7730 standard [74] allows to meet the following assumptions:

- an rapid step-change of operative temperature is felt instantaneously,

- when the temperature raises, the PMV-PPD model can be used to predict the thermal comfort directly,
- when the temperature drops, at first the thermal sensation is lower than the one predicted by the PMV-PPD model, then it increases and after approximately 30 minutes it reaches a steady state in which model predictions apply again; the actual time to reach steady state conditions depends on initial conditions.

The indoor conditions usually can be treated as a steady state since the temperature change rate is mostly less than 2.0 K/h. A typical example of highly transient conditions, significantly more dynamic than the indoor climate, is the one met in vehicles. It characterizes strongly transient conditions, high localized air velocities or highly asymmetric radiation conditions (due to the solar radiation) [3].

2.1.3 Thermal comfort scales

In order to express the level of the thermal comfort in specific conditions, a scale has to be adopted. Up to now, a considerable number of thermal comfort scales were developed and used in experimental investigations. Due to an incompatibility of distinct scales, the results of various studies often cannot be compared directly. The three most commonly used scales are: the overall thermal sensation scale, the overall thermal comfort scale and the DISC scale. The thermal sensation scale was adopted in ISO 7730 [74] and ASHRAE–55 [4] standards. The thermal sensation scale and thermal comfort scale are quite similar (Table 2.5).

Table 2.5: Thermal comfort scale vs. thermal sensation scale

Scale value	Thermal comfort descriptor	Thermal sensation descriptor
+3	Much too warm	Hot
+2	Too warm	Warm
+1	Comfortably warm	Slightly warm
0	Comfortable	Neutral
-1	Comfortably cool	Slightly cool
-2	Too cool	Cool
-3	Much too cool	Cold

The DISC scale is often used together with the standard comfort temperature (SET*) described on page 35. The DISC represents possible votes on a scale of the thermal discomfort. The possible votes are:

- intolerable,
- very uncomfortable,
- uncomfortable,
- slightly uncomfortable,
- comfortable.

Considerable efforts were performed by many researchers to understand relationships between different thermal comfort scales under steady conditions (uniform and nonuniform), but relationships under dynamic or transient conditions need further studies [147]. Under steady conditions, the thermal comfort scale and thermal sensation scale are in a good agreement with each other.

2.1.4 Thermal comfort models

Due to a considerable number of variables influencing the thermal comfort, its evaluation is always difficult. Thermal comfort models have been available for more than 30 years due to efforts started in the mid-20$^{\text{th}}$ century to develop such models for military and aerospace applications [28].

The thermal comfort models developed so far can be roughly divided into empirical models, analytical models and adaptive models. The analytical models can be furthermore divided into two subcategories: relatively simple heat balance based models and considerably more complex multi-node models. This classification is only conventional, since some analytical models are partially based on empirical relations, some of them also partially take into account the adaptation phenomenon, and the nature of many of adaptive models is purely empirical. Nonetheless, the presented classification reflects the main differences between the main approaches in the thermal comfort modeling.

2.1.4.1 Empirical models

The empirical models do not take into account any physiological aspects of the human body. They are developed using empirical fits to experimental data. These models usually indicate the range of comfortable temperatures, air speeds or humidity levels under given conditions, rather than directly predict the thermal sensation. Despite their simplicity, they are still intensively used in the thermal comfort prediction [49]. Due to their simplicity they are often referred in literature as thermal comfort “indices” instead of “models”. The following empirical models are described

in this work: effective temperature (ET), wet bulb globe temperature (WBGT), operative temperature (OT) and draft prediction model (DR).

a) Effective temperature (ET)

The effective temperature (ET) is one of the first thermal comfort models. It was developed by Houghten and Yagloglou in 1923 [66, 67]. The model is purely empirical. The effective temperature ET [°C] combines the effects of the dry bulb air temperature T_{DB} [°C] and relative humidity RH [%]:

$$ET = T_{DB} - 0.4(T_{DB} - 10) \cdot (1 - \frac{RH}{100}) .$$

After its development, the model was the most widely used as the thermal comfort index for the next 50 years [11]. However, during 1940s and 1950s it was found that the index overestimates the humidity effect under cool and comfortable conditions.

The ET index underwent a number of modifications from the time of its development. One of the major modifications was the inclusion of air velocity effects. The modified index was called the corrected effective temperature (CET) [10]. Two kinds of air velocity effects were taken into account: the cooling effect when the air temperature is below 37.8 °C and relative humidity is below 100%, and the heating effect in temperatures higher than 37.8 °C together with a 100% relative humidity. Further modifications of ET included the effects of the radiation and clothing level.

b) Wet bulb globe temperature (WBGT)

The wet bulb globe temperature (WBGT) model was developed in 1957 by Yaglou and Minard [141]. The WBGT is an index of the thermal stress in hot environments. The index was developed for the purpose of the control of heat casualties at military training centers in USA [105]. The index combines the effect of air temperature, low temperature radiation, solar radiation and air movement. The index has two versions: for indoors and for outdoors. For indoors, the formula is as follows:

$$WBGT = 0.7 \cdot T_{WB} + 0.3 \cdot T_{MR} ,$$

while for outdoors:

$$WBGT = 0.7 \cdot T_{WB} + 0.2 \cdot T_{MR} + 0.1 \cdot T_{DB} ,$$

where T_{WB} is the wet bulb temperature (measured using a naturally ventilated wet bulb thermometer) [°C], T_{MR} is the mean radiant temperature (sometimes referred

as *globe temperature*, because it is measured using a black-globe thermometer) [°C] and T_{DB} is the dry bulb temperature [°C]. The mean radiant and natural wet bulb temperatures can be estimated only empirically, because they are not thermodynamic properties [23]. The WBGT index is still in use across the globe to control heat stresses in many contexts including military, industrial, domestic, sporting and commercial applications [105]. It can be evaluated using ISO 7243 standard [72].

c) Operative temperature (OT)

The operative temperature is an index developed by Winslow, Herrington and Gagge [137]. It is defined as a uniform temperature of a radiantly black enclosure in which an occupant would exchange the heat by radiation and convection at the same rate as in the actual nonuniform environment [11]. In other words, it is the average of the MRT and the DBT weighted by the radiative and the convective heat transfer coefficient, respectively:

$$OT = \frac{h_r T_{MR} + h_c T_{DB}}{h_r + h_c} ,$$

where h_r is the radiative heat transfer coefficient [W/(m^2 K)] and h_c is the convective heat transfer coefficient [W/(m^2 K)]. As shown, the index neglects the effects of the humidity and air velocity. According to ASHRAE suggestions, the following simplified formula gives results of with the acceptable accuracy [11]:

$$OT = \frac{T_{MR} + T_{DB}}{2} .$$

The index is still in use, often as a part of some more complex models.

d) Draft prediction model (DR)

The draft is the undesired cooling of the human body due to the air flow. The most common model for the draft effect evaluation is the one introduced by Fanger et al. [42]. The model is derived based on experiments in which 50 people were exposed to various temperatures, mean air velocities and turbulence intensities. The DR model is incorporated in the ISO 7730 [74] and ASHRAE 55 [4] standards. The model predicts a percentage of people dissatisfied by drafts using the following formula [74]:

$$DR = (34 - t_{a,I})(\bar{v}_{a,I} - 0.05)^{0.62}(0.37 \cdot \bar{v}_{a,I} \cdot Tu + 3.14) , \qquad (2.1.2)$$

where:

$t_{a,I}$ is the local air temperature, (°C),

$\bar{v}_{a,I}$ is the local mean air velocity, (m/s),

Tu is the local turbulence intensity, (%).

According to ISO 7730 the given formula is valid for $t_{a,I}$ within the range of 20–26 °C and Tu within the range of 10–60 %. The turbulence intensity is defined as the ratio of the standard deviation of the air velocity to the mean air velocity. In a typical office environment, the turbulence intensity is at the level of 40 % [49]. Since the thermal discomfort due to draft is considered as the local discomfort, it mainly affects people at lower activities, i.e. < 1.2 met.

2.1.4.2 Heat balance based models

a) Two-node model (ET* and SET*)

The two-node model was proposed by Gagge et al. [52] in 1971, specifically to formulate a new effective temperature scale [49]. It is often referred as *the Pierce two-node model*, because the model was developed at the John B. Pierce Foundation at Yale University [80]. From the time of its development, the model underwent many modifications. At present, usually the term "two-node model" is used to name the model modification presented by Gagge et al. [53] in 1986. The purpose of the model development was to determine particular combinations of physical conditions producing the equal physiological strain [49]. On the basis of the extensive data obtained from the climate chamber experiments, Gagge stated that the skin temperature indicates well the thermal sensation in cold conditions, while in warm conditions the skin wettedness (Eq. (2.1.3)) should be used instead. In warm conditions the skin temperature remains relatively constant due to a sweating phenomenon occurring at the skin surface. The concept of the model is to represent the human body by two thermally lumped nodes, the first representing the human body core, and the second representing the skin and clothing. The nodes can be visualized as two concentric cylinders (Fig. 2.2). The internal heat is generated in the body core node. This heat is partially lost due to the respiration and partially transported to the skin. The skin exchanges the heat with the environment by convection, radiation, water vapor diffusion and evaporation of sweat from the skin surface. Clothing and sweat are assumed to be uniformly distributed on the skin surface.

The evolution of the two-node model is thoroughly explained in Takada et al. [126]. In this work only the basic equations of the most known edition (1986) of the model are presented to explain the model structure. The model equations are valid for moderate activity levels and uniform environmental conditions [28, 52]. The heat

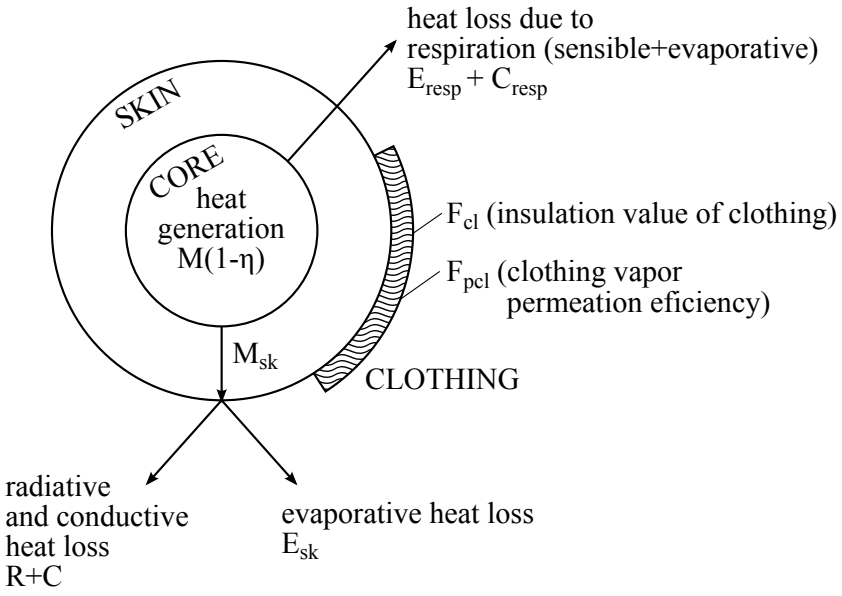

Figure 2.2: Summary of 2-node thermal model of human body (based on Auliciems and Szokolay [11])

balance equations are written separately for the core node and the skin node. Both equations are written for transient conditions, taking the body heat capacity into account. The heat balance for the core node is:

$$cm_{cr}\frac{\mathrm{d}T_{cr}}{\mathrm{d}t} = A(-q_{cr:sk} - q_{cr:am} + M - W)\,,$$

while for the skin node:

$$cm_{sk}\frac{\mathrm{d}T_{sk}}{\mathrm{d}t} = A(q_{cr:sk} - q_{sk:am})\,,$$

where c is the body specific heat [J/(kg K)], m_{cr} and m_{sk} are the body core and skin masses [kg], T_{cr} and T_{sk} are the body core and skin temperatures [°C], A is the body surface area [m^2], $q_{cr:sk}$ is the heat flux from core to skin [W/m^2], $q_{cr:am}$ is the heat flux from core to ambient [W/m^2], $q_{sk:am}$ is the heat flux from skin to ambient [W/m^2], M is the metabolic rate [W/m^2] and W is the external work [W/m^2]. As shown, three possible body heat flow paths are assumed: (1) from the core to the skin, (2) from the core to the ambient, (3) and from the skin to the ambient. The heat flow from the core to the skin is due to the blood flow and heat conduction:

$$q_{cr:sk} = \left(c_{bl}\rho_{bl}\dot{V}_{bl}\frac{1}{3600}\cdot\frac{1}{1000} + K_{min}\right)(T_{cr} - T_{sk})\,,$$

where c_{bl} is the specific heat of blood [J/(kg K)], ρ_{bl} is the blood density [kg/m^3],

$\dot{V}_{bl}$ is the skin blood flow rate [l/(m^2 h)] and K_{min} is the minimum heat conductance by skin tissue, $K_{min} = 5.28$ [W/(m^2 K)]. The direct heat flow from the core to the ambient is due to the respiration:

$$q_{cr:am} = 1.4 \cdot 10^{-3} \cdot M(34 - T_{am}) + 0.0023 \cdot M(44 - P_{am}) \,,$$

where T_{am} is the ambient temperature [°C] and P_{am} is the ambient vapor pressure [mmHg]. The heat flow from the skin to the ambient is due to the convection, radiation, vapor diffusion through the skin and sweat evaporation:

$$\begin{aligned} q_{sk:am} &= [\alpha_c(T_{sk} - T_{am}) + \alpha_r(T_{sk} - T_{MR})]\, F_{cl} \\ &\quad +0.06 \cdot r \cdot \alpha' \cdot F_{pcl} \cdot (P_{sk,sat} - P_{am}) + 0.94 \cdot r \cdot \dot{m}_{rsw} \cdot \frac{1}{3600} \cdot \frac{1}{1000} \,, \end{aligned}$$

where α_c is the convective heat transfer coefficient [W/(m^2 K)], α_r is the radiative heat transfer coefficient [W/(m^2 K)], α' is the moisture transfer coefficient [kg/(m^2 · s · mmHg)], T_{MR} is the mean radiant temperature [°C], F_{cl} is the heat transfer efficiency of clothing [–], F_{pcl} is the vapor transfer efficiency of clothing [–], $P_{sk,sat}$ is the saturated vapor pressure for the skin temperature [mmHg], r is the evaporative heat of water [J/kg] and $\dot{m}_{rsw}$ is the regulatory sweating rate [g/m^2 h].

The masses of the core and skin are not constant. They are calculated using the variable skin mass ratio to the total body α [–]:

$$\begin{aligned} m_{cr} &= m_{bm}(1 - \alpha) \,, \\ m_{sk} &= m_{bm}\alpha \,, \end{aligned}$$

where m_{bm} is the body total mass [kg] and the skin to total body mass ratio α is a function of the blood flow rate:

$$\alpha = 0.042 + \frac{0.745}{\dot{V}_{bl} + 0.585} \,.$$

The skin blood flow rate $\dot{V}_{bl}$, sweating rate $\dot{m}_{rsw}$ and increase in the metabolic rate due to shivering M_{shiv} are functions of the so-called warm and cold signals for the body temperature: $wsig_{cr}$, $wsig_{sk}$, $wsig_{bm}$, $csig_{cr}$ and $csig_{sk}$ [°C]. The warm and cold signals are evaluated as follows:

$$wsig_{cr} = \begin{cases} T_{cr} - T_{cr,set} & (T_{cr} > T_{cr,set}) \\ 0 & (T_{cr} \leq T_{cr,set}) \end{cases} \,,$$

$$wsig_{sk} = \begin{cases} T_{sk} - T_{sk,set} & (T_{sk} > T_{sk,set}) \\ 0 & (T_{sk} \leq T_{sk,set}) \end{cases},$$

$$wsig_{bm} = \begin{cases} T_{bm} - T_{bm,set} & (T_{bm} > T_{bm,set}) \\ 0 & (T_{bm} \leq T_{bm,set}) \end{cases},$$

$$csig_{cr} = \begin{cases} 0 & (T_{cr} \geq T_{cr,set}) \\ T_{cr,set} - T_{cr} & (T_{cr} < T_{cr,set}) \end{cases},$$

$$csig_{sk} = \begin{cases} 0 & (T_{sk} \geq T_{sk,set}) \\ T_{sk,set} - T_{sk} & (T_{sk} < T_{sk,set}) \end{cases},$$

where the set point temperatures $T_{cr,set} = 36.8°\text{C}$ and $T_{sk,set} = 33.7°\text{C}$. T_{bm} and $T_{mb,set}$ are the actual temperature and the temperature set point for the whole body, respectively. They are calculated as:

$$\begin{aligned} T_{bm} &= \alpha \cdot T_{sk} + (1 - \alpha) \cdot T_{cr}\,, \\ T_{bm,set} &= \alpha \cdot T_{sk,set} + (1 - \alpha) \cdot T_{cr,set}\,. \end{aligned}$$

Finally, the skin blood flow rate can be expressed as:

$$\dot{V}_{bl} = \frac{6.3 + 200 \cdot wsig_{cr}}{1 + 0.1 \cdot csig_{sk}}\,.$$

The sweating rate is as follows:

$$\dot{m}_{rsw} = 170 \cdot wsig_{bm} \cdot \exp\left(\frac{wsig_{sk}}{10.7}\right)\,.$$

The increase of a metabolic rate due to shivering is as follows:

$$M_{shiv} = 19.4 \cdot csig_{cr} \cdot csig_{sk}\,.$$

The steady state solution is obtained by performing a long enough transient simulation. At the initial time step the body core and skin temperatures are set to their set points values T_{cr} and T_{sk}, respectively [126]. Afterward, the transient simulation of the human thermoregulatory system proceeds. The simulation continues until the simulation time specified by the user is reached. The steady state is usually reached after about 60 minutes of the run-time.

There is a number of ways to use the results from the two-node model to evaluate the thermal strain of a person in the given conditions. The two most known thermal

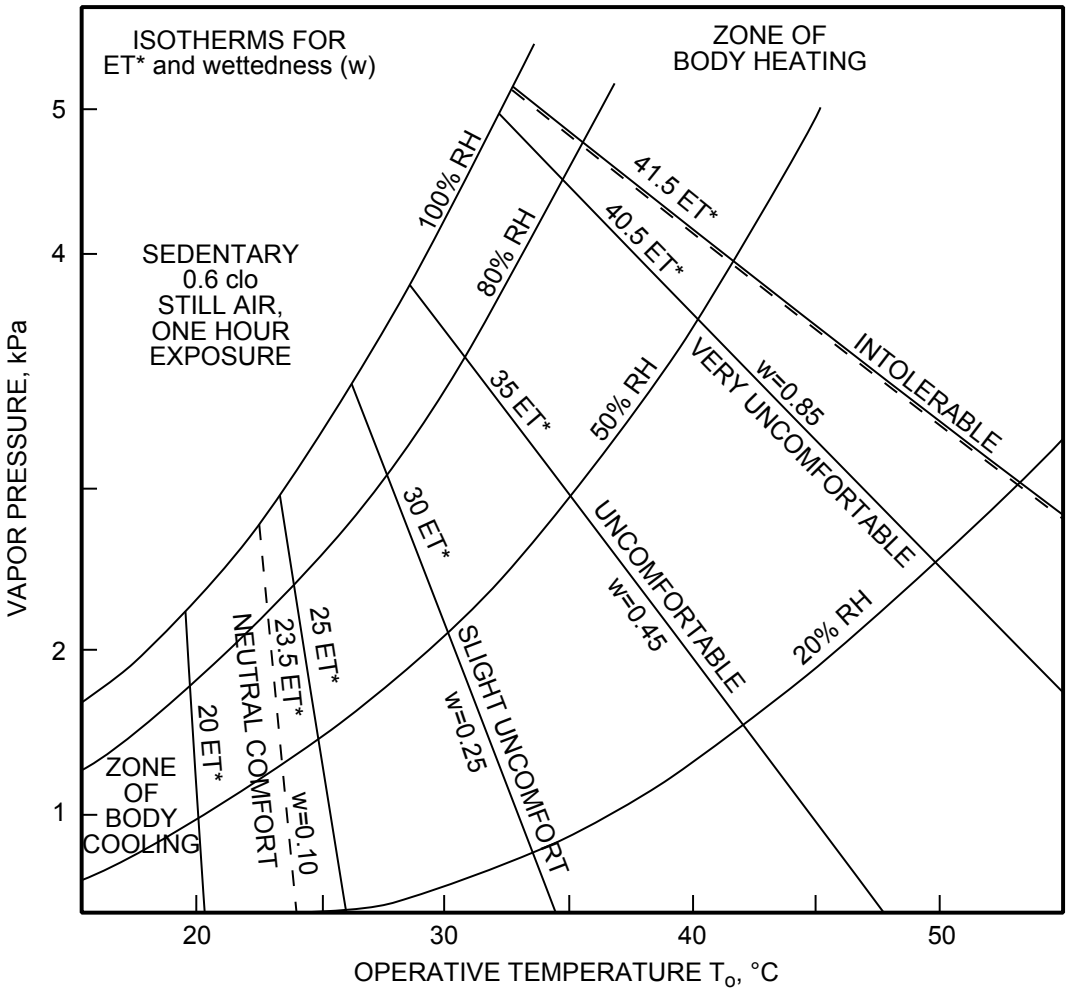

Figure 2.3: Psychrometric chart showing constant ET* lines and corresponding discomfort levels (DISC scale) (based on Auliciems and Szokolay [11])

indices proposed by Gagge et al. [52, 53] are: the new effective temperature (ET*) index (developed in 1971) and the standard effective temperature (SET*) index (developed in 1986). Gagge assumed that the thermal strain is proportional to the so-called skin wettedness w, which is defined as follows:

$$w = \frac{E_{sk}}{E_{max}} = \frac{E_{diff} + E_{rsw}}{E_{max}}\,, \tag{2.1.3}$$

where E_{sk} is the evaporative heat loss from the skin surface [W/m^2], E_{diff} is the heat of vaporized water diffusing through the skin layer [W/m^2], E_{rsw} is the heat of vaporized sweat necessary for the regulation of body temperature [W/m^2] and E_{max} is the maximum possible evaporative heat loss from the body surface in the given conditions [W/m^2]. Both ET* and SET* can be calculated using the final skin surface temperature and wettedness obtained from the two-node model simulation.

The ET* temperature is defined as the temperature of a uniform environment at the 50% relative humidity, which would produce the same net heat exchange with a given person as actual conditions [11]. The definition of SET* is similar to ET*, with the difference that SET* refers to subjects wearing "standard" clothing for the given activity and conditions. The ET* and SET* lines are represented on the psychrometric chart as straight lines, each referring to a constant skin wettedness.

According to the study of Takada et al. [126], the 1986 edition of the two-node model shows a good agreement with the experimental data in both low-temperature and high-temperature steady state conditions. The relatively good accuracy is obtained mainly thanks to the inclusion of the shivering effect, which was not present in the original model (1971).

Although the model is based on non-steady state equations, it should be used with care when assessing the thermal comfort in transient conditions. The available information concerning the validity of the two-node model in transient situations is limited [126]. However, the another study of Takada et al. [125] showed, that the two-node model could accurately predict the transient skin temperature of individual people, if the constants used in the model were properly tuned. Each constant used in the model relates to a different physiological response and responses are different for each person. The two-node model is one of the most widely used human thermal models at present. The ET* and SET* thermal indices are commonly used especially in hot and humid regions, where it is important to evaluate quantitatively the degree of effects of the temperature and humidity [92].

b) PMV-PPD

The PMV-PPD model was developed by Fanger around 1970 [40]. From that time it became arguably the most known thermal comfort index used in the practice. The model remained essentially unchanged since its first publication [81]. The model is included in the two most often cited thermal comfort standards: ASHRAE 55-2004 [4] and ISO 7730 [74]. The model is derived from the physics of the heat transfer using an empirical fit to the sensation[49]. The model does not attempt to simulate transient conditions or thermal regulatory system [81]. Instead, the model evaluates a thermal strain under steady state conditions. The strain amount correlates with the total heat flux between the body and environment. Despite its steady state basis, the model is often used to evaluate transient but still close-to-steady conditions, like those met in most buildings.

The PMV index represents the "predicted mean vote" (on the thermal sensation scale) of a large population of people exposed to a certain environment. The PMV is

the expected comfort vote on the ASHRAE scale of the subjective thermal sensation (cold (-3), cool (-2), slightly cool (-1), neutral (0), slightly warm (1), warm (2), hot (3); see Table 2.5) [70]. When the thermal comfort is achieved for the majority of the population, the PMV equals 0. Even under these "ideal" conditions, there are still 5% of dissatisfied people. Any oscillation from the thermal balance results in a PMV change. When the thermal sensation is "too warm", PMV experiences a positive change. If the thermal sensation is "too cold", the PMV change is negative. The greater the load, the more comfort votes deviate from zero.

The PMV is correlated with the predicted percent of people dissatisfied at given conditions (PPD). The PPD has a minimum value for PMV = 0. When the PMV changes away from zero, PPD increases (Fig. 2.4).

The derivation of the PMV model starts from the human heat balance equation written for a steady state [40]:

$$M - Ed - Esw - Ere - Lr = R + C\,, \tag{2.1.4}$$

where M is the metabolic rate (internal heat production), Ed is the heat loss due to water vapor diffusion through the skin, Esw is the heat loss due to sweating, Ere is the latent heat loss due to respiration, Lr is the dry respiration heat loss, R is the heat loss by radiation from the surface of the clothed body and C is the heat loss by convection from the surface of the clothed body. Usually, all of the quantities are calculated in watts per square meter [W/m^2].

Generally, Eq. (2.1.4) is valid only for steady-state conditions. It can be applied to humans exposed for a long time period to constant conditions at a constant metabolic rate. Each component from the equation can be substituted with a function derived from basic physics. All of the functions have measurable values with the exception of the clothing surface temperature and the heat transfer coefficient, because these two quantities depends on each other [49]. Thus, in order to solve the equation, the clothing temperature and the convective heat transfer coefficient must be calculated iteratively. At first, an initial clothing temperature must be estimated. Subsequently the convective heat transfer coefficient is computed which, in turn, is a basis for a new clothing temperature. The procedure continues until a satisfactory degree of accuracy is met.

Based on the experiments using climate chamber, Fanger concluded that the satisfaction of the heat balance equation is required for the optimum human comfort [49]. The heat balance equation (Eq. 2.1.4) can be reorganized in a way to represent

a possible thermal load on the body which is not in a thermal balance:

$$L = M - Ed - Esw - Ere - Lr - R - C\,, \tag{2.1.5}$$

where L is the thermal load on the body. Then a thermal strain (mean vote) Y is a function of L [W/m^2] and the metabolic rate M [W/m^2]. Fanger correlated the thermal load L with the mean vote Y from a large number of laboratory studies carried out using a climate chamber. The following empirical correlation was obtained (constants valid for SI units):

$$\frac{\delta Y}{\delta L} = 0.303 \exp\left(-0.036M\right) + 0.028\,,$$

thus the expression for the mean vote is:

$$Y = \left\{0.303 \exp\left(-0.036M\right) + 0.028\right\} L\,.$$

After expanding all of the terms and naming Y as PMV, the full predicted mean vote equation is as follows [74]:

$$\begin{aligned} PMV \;=\; & \left[0.303 \exp\left(-0.036M\right) + 0.028\right] \cdot \\ & \cdot \Bigg\{ (M-W) - 3.05 \cdot 10^{-3} \left[5733 - 6.99(M-W) - p_a\right] - \\ & -0.42\left[(M-W) - 58.15\right] - 1.7 \cdot 10^{-5} M (5867 - p_a) - \\ & -0.0014M(34 - t_a) - 3.96 \cdot 10^{-8} f_{cl} \left[(t_{cl}+273)^4 - (t_{MR}+273)^4\right] - \\ & -f_{cl} h_c (t_{cl} - t_a) \Bigg\}\,, \end{aligned} \tag{2.1.6}$$

where W is the effective mechanical power [W/m^2] (usually around 0), I_{cl} is the clothing insulation [m^{2}K/W], p_a is the water vapor partial pressure [Pa], t_a is the air temperature [°C], t_{MR} is the mean radiant temperature (MRT) [°C], f_{cl} is the fraction of body clothed [–], t_{cl} is the temperature of clothing surface [°C] and h_c is the convective heat transfer coefficient [W/(m^{2}K)]. The clothing temperature t_{cl} must be found by iteration from:

$$\begin{aligned} t_{cl} \;=\; & 35.7 - 0.028(M-W) - I_{cl} \cdot \\ & \cdot \left\{ 3.96 \cdot 10^{-8} f_{cl} \left[(t_{cl}+273)^4 - (t_{MR}+273)^4\right] + f_{cl} h_c (t_{cl} - t_a) \right\}\,, \end{aligned} \tag{2.1.7}$$

where h_c is found by:

$$h_c = \begin{cases} 2.38 \cdot |t_{cl} - t_a|^{0.25} & \text{for } 2.38 \cdot |t_{cl} - t_a|^{0.25} > 12.1\sqrt{v_{ar}} \\ 12.1\sqrt{v_{ar}} & \text{for } 2.38 \cdot |t_{cl} - t_a|^{0.25} < 12.1\sqrt{v_{ar}} \end{cases}, \quad (2.1.8)$$

where v_{ar} stands for the relative air velocity [m/s]. The fraction of the body clothed f_{cl} can be approximated using the following formula:

$$f_{cl} = \begin{cases} 1.00 + 1.290 I_{cl} & \text{for } I_{cl} \leq 0.078 \\ 1.05 + 0.645 I_{cl} & \text{for } I_{cl} > 0.078 \end{cases}. \quad (2.1.9)$$

The PPD index, which establishes a quantitative prediction of the percentage of thermally dissatisfied people, can be calculated using the following formula [74]:

$$PPD = 100 - 95 \exp(-0.03353 \cdot PMV^4 - 0.2179 \cdot PMV^2). \quad (2.1.10)$$

The main drawbacks of the PMV-PPD model are related with the difficulties in the accurate measurement of the clothing thermal insulation and activity level in field studies [25]. These two factors can "dominate" the resulting PMV.

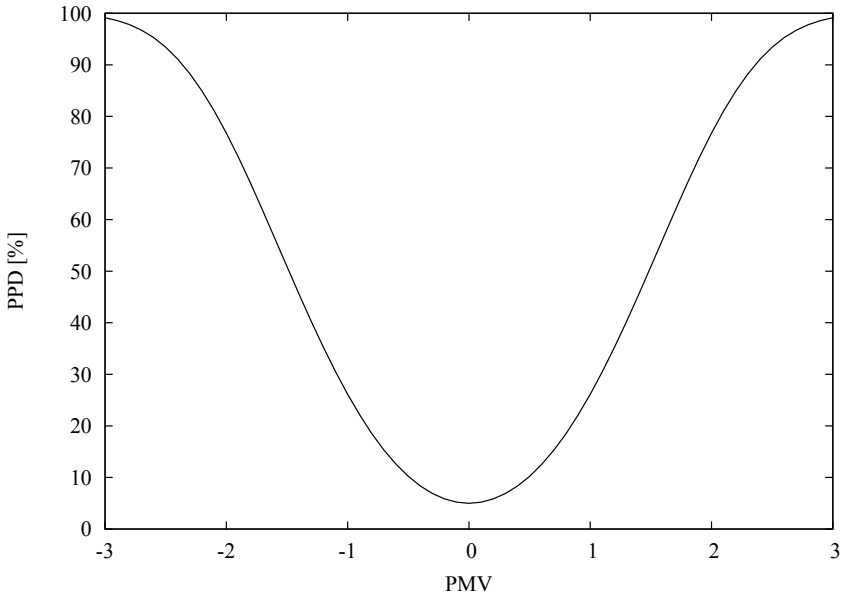

Figure 2.4: PMV-PPD correlation

According to de Dear and Brager [34] the PMV is more accurate for air-conditioned spaces than naturally ventilated ones. In warm naturally ventilated buildings the PMV overestimates the human subjective warmth sensations.

A concise summary of the range of applicability of the PMV model is presented

in Humphreys and Nicol [70]. The authors investigated the applicability of the PMV model using the ASHRAE database [33] of field studies. They found that taking these world-wide data as a single distribution, the PMV is free from any serious bias. However, some underlying biases in relation to each contributing variable still exist. Additionally, a further bias related to the outdoor temperature was found. The authors concluded that the PMV predicts the actual thermal sensation most accurately for the following ranges of input variables:

- clothing insulation in the range of 0.3–1.2 clo (light clothing),
- activity levels below 1.4 met (mainly sedentary activities),
- room temperatures below 27 °C,
- air speed below 0.2 m/s,
- humidity below 60%,

The authors compared the obtained limits with the the ranges for the valid use of the PMV given in ISO 7730 [74], i.e.:

- clothing insulation — 0–2.0 clo,
- metabolic rate — 0.8–4.0 met,
- room temperature — 10–30°C,
- air speed — 0–1 m/s,
- humidity — maximum vapor pressure of 2.7 kPa.

It was found, that ISO 7730 limits are not restrictive enough in order to ensure the validity of the PMV.

Despite its limitations, the PMV-PPD model is probably the most widely used thermal comfort model to evaluate indoor conditions. It presents a good balance between the ease of use and the prediction accuracy. Although the model is based on steady state equations, it can be used to evaluate slightly time-varying conditions, like those met in most buildings.

2.1.4.3 Complex multi-node models

The complex multi-node models are aimed at modeling the human thermoregulatory system. In fact, they are often named as “human thermal models” instead of “thermal comfort models”. These models do not give the thermal sensation directly.

The provided outputs cover the thermal parameters of each body segment, i.e. the temperature, the heat exchange due to the conduction, convection or radiation between individual body segments or with the environment. The models can be used in thermal comfort analyses, because the thermal sensation highly depends on the body heat load, which can be assessed using these models.

The common feature of the multi-node models is that they take into account the effects of environment nonuniformities. Some of these models are also suitable for highly non-steady conditions. These characteristics make them a suitable tool to evaluate vehicular environments, which are usually far more dynamic than building indoor environments.

One of the most influential multi-node model is the 25-node model proposed by Stolwijk [123] for the aerospace applications. The model is comprised of two separate systems of the thermoregulation: the control system and the controlled system. The controlled system is the body described by the thermal characteristics of its different parts. The control system is responsible for recognizing the thermal state of the controlled system, integrating it and forcing appropriate actions to minimize the thermal strain of the organism. The possible actions to be taken are the sweating, vasolidation, vasoconstriction and shivering.

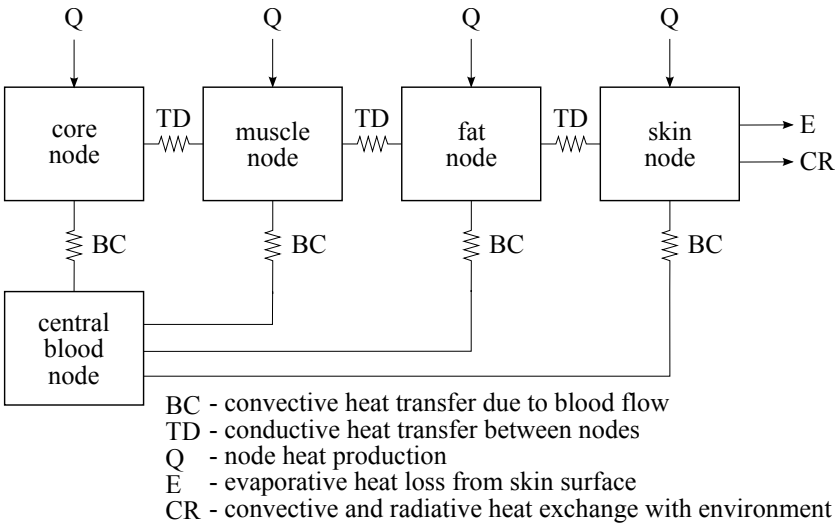

Figure 2.5: Schematic diagram of the body segment in the Stolwijk's model (based on Stolwijk [123])

The controlled system is comprised of six segments: head, trunk, arms, hands, legs and feet. Each segment consists of four concentric layers representing the core, muscle, fat and skin. Each layer is represented by a one node. The body model has also an additional central blood node, which is connected with all the other nodes. The total number of nodes in a model is 25: 4 nodes in an each of the 6 segments,

plus the 25$^{\text{th}}$ central blood node. A schematic diagram of the body segment is presented in Fig. 2.5.

The Stolwijk's model is a transient model. At each time step a transient heat balance equation is solved for each node. The heat balance equations for a node (i, j) are as follows [97]:

$$\begin{aligned}
C(i,1)\frac{\mathrm{d}T(i,1)}{dt} &= Q(i,1) - BC(i,1) - TD(i,1) - E(i,1)\,,\\
C(i,2)\frac{\mathrm{d}T(i,2)}{\mathrm{d}t} &= Q(i,2) - BC(i,2) + TD(i,1) - TD(i,2)\,,\\
C(i,3)\frac{\mathrm{d}T(i,3)}{\mathrm{d}t} &= Q(i,3) - BC(i,3) + TD(i,2) - TD(i,3)\,,\\
C(i,4)\frac{\mathrm{d}T(i,4)}{\mathrm{d}t} &= Q(i,4) - BC(i,4) + TD(i,3) - E(i,4) - CR(i,4)\,,
\end{aligned}$$

where:

i	– segment number: 1) heat, 2) trunk, 3) arms, 4) hands, 5) legs, 6) feet,
j	– layer number: 1) core, 2) muscle, 3) fat, 4) skin,
$C(i,j)$	– thermal capacitance of the node (i,j) [J/K],
$T(i,j)$	– temperature of the node (i,j) [°C],
$Q(i,j)$	– rate of heat production in the node (i,j) [W],
$BC(i,j)$	– convective heat transfer from the node (i,j) to the central blood [W],
$TD(i,j)$	– conductive heat transfer from the layer j to the layer $j+1$ [W],
$E(i,j)$	– evaporative heat loss from the skin surface [W],
$CR(i,j)$	– convect. and radiat. heat exch. rate between skin and environment [W],
t	– time [s].

The heat balance equation for the central blood node is as follows:

$$C_{CB}\frac{\mathrm{d}T_{CB}}{\mathrm{d}t} = \sum_{i=1}^{6}\sum_{j=1}^{4} BC(i,j)\,,$$

where C_{CB} and T_{CB} are the thermal capacitance [J/K] and the temperature [°C] of the central blood compartment, respectively. The physiological and thermal parameters, like the blood flow rate, metabolic heat production and conductivity of the tissues are obtained from empirical studies. The heat balance equations are solved using the finite difference method.

It is proven that the original Stolwijk's model predicts transient mean skin temperature with a reasonable accuracy, although some deviations may exist in local skin temperatures [97]. However, the model can be properly tuned to improve its performance. According to Munir et al. [97], a modification of the distribution of the basal skin blood flow and the distributions of the vasoconstriction and workload

significantly improves the performance.

A significant number of researchers used the Stolwijk's concept as the framework for further development [97]. The derived models usually consist of more body segments and have modified parameters or thermal control equations. Some of the most validated models based on the Stolwijk's model are: the UCB (the University of California, Berkeley) comfort model [68], the 65-node Tanabe model [127], or the Fiala model [44, 45].

Of course, not all of the recently used human thermal models are based on the Stolwijk's model. For example, some of them are detailed three-dimensional finite element human body models, like the Wissler's model (225 nodes) [138], the Smith's model (3000 nodes) [117], or the Fu's model (an extended Smith's model, 3000 nodes) [51].

A comprehensive review of the complex multi-node models is presented by Alahmer et al. [3], Foda et al. [47] and Cheng et al. [28].

Up to the present, none of the complex multi-node human thermal models has been adopted by any international standard regarding the prediction of human thermal sensations [47].

2.1.4.4 Adaptive models

The previously described heat balance based models in an elegant and consistent way connect the analytically derived body heat load with a predicted thermal sensation. These models are proven to be valid when factors like clothing or activity level are known. However, they are based on the assumption that a building occupant is a passive recipient of the thermal environment and does not take any action when the body is not in a thermal balance. This is one of the limitations of the heat balance based models. This limitation can be resolved in the so-called adaptive approach of the thermal comfort modeling. The adaptive approach is based on the concept that building occupants are not just passive recipients of thermal stimuli, but rather they interact with the surrounding environment.

The adaptation can be defined as a gradual diminution of the organism's response to the repetitive or long-term environmental stimuli. It can be achieved by [22, 50]:

1. behavioral adjustments,
2. physiological adaptation,
3. psychological habituation or expectation.

The behavioral adjustments include all actions a person take to modify heat and mass fluxes acting on a body in order to preserve the heat balance. There is a

great number of actions occupants can take to modify the thermal conditions, e.g.: putting on additional clothes, opening a window, turning on fans, turning on or adjusting the heating / cooling system, drink / eat hot / cold food or beverages. The behavioral adjustment of the heat balance is often considered as an opportunity to maintain thermal comfort [22].

The physiological adaptation connects with a gradual diminution in the strain induced by an exposure to thermal environmental factors [22]. It refers to both genetic adaptation and acclimation. Both these terms cover the changes in person's physiological thermoregulation setpoints (e.g. the onset of sweating) that come from prolonged exposure to certain climatic conditions [50]. These are long-term processes. The time scale of the genetic adaptation is beyond a human lifetime, while the time needed for the acclimation spans from several days up to few months. In a cold climate the human body acclimates by increasing the metabolic rate and, hence, the heat generation rate. In a hot and dry climate the acclimation tends to increase the sweating capacity. In a hot and humid climate the main reaction is to increase the peripheral blood flow and elevate the skin temperature.

Finally, the psychological aspect is related with the so-called perceptual adaptation, which is a diminution of the sensation intensity in the case of a repeating or constant exposure to environmental stressors [22]. In contrast to the behavioral and physiological factors, the psychological factors are non-thermal, i.e. they cannot alter the body heat load. Rather, they reflect the occupant's expectation what the indoor conditions should be like. The expectation is affected by the past exposure, demographic factors, cultural factors or outdoor climate conditions. The research on the influence of the psychological adaptation is still ongoing. However, it is argued that psychological adaptation is responsible for the discrepancies between the thermal comfort ranges in naturally ventilated and air-conditioned buildings [35]. It was found that the occupants of naturally ventilated buildings are more tolerant for the variations of the indoor conditions, while the users of air-conditioned buildings have a very narrow range of acceptance. It is due to different expectations put on these different control strategies.

The present adaptive models of thermal comfort tend to be based purely on empirical relations rather than on analytical formulae. It is due to the fact that most of the above-mentioned factors affecting the perception of the environmental conditions are difficult to be taken into account directly (they are difficult to be measured or predicted). In addition, the recent research results showed that simple thermal comfort indices have better correlation with the actual comfort votes of respondents than the complex ones [71]. The increased complexity of a model may

actually introduce more error than it removes.

Most of the adaptive models predicts a comfortable temperature depending on the outdoor climate conditions (mainly on the mean outdoor temperature). It is believed that weather and seasons have a crucial influence on human ability to adapt to the thermal environment [35]. People take into account the weather forecasts when making a decision what clothes to put on. Thus, the expected outdoor temperature impacts the clothing level and, therefore, also the neutral temperature.

The idea that the comfortable temperature may depend on the outdoor conditions was proposed as first by Humphreys [69]. Humphreys analyzed field data and found that the neutral temperature and the mean outdoor temperature in free-running naturally ventilated buildings are correlated in the following way:

$$T_{comf} = 0.534 T_{om} + 11.9\,,$$

where T_{comf} is the comfortable (neutral) temperature (°C) and T_{om} is the monthly mean outdoor temperature (°C). Since that time a considerable number of adaptive thermal comfort models were developed. The most known and recent adaptive models are those defined in the ASHRAE Standard 55 [4] and in the European Standard EN 15251 [38]. In the both standards the adaptive models are optional (the basic approach is to use the PMV-PPD model). They can be used to evaluate the environment in naturally ventilated and free-running buildings, where indoor conditions are regulated by occupants primarily by opening and closing windows. The adaptive models can be applied for spaces where the occupants are engaged in near sedentary activities and they are free to adapt their clothing level.

The ASHRAE Standard model and the EN 15251 model are similar, but not the same. It is because of the following differences [99]:

- different databases used to derive the models,
- slightly different building classifications,
- different derivation procedure for the neutral temperature,
- different type of outdoor temperature taken into account.

a) Adaptive model in ASHRAE Standard 55

The model incorporated in the ASHRAE Standard 55 [4] was proposed by de Dear and Brager [35]. It is based on the analysis of field studies conducted in 160 buildings located on four continents in varied climate zones. The model applies only for naturally conditioned spaces [35], i.e. the spaces which:

- are regulated primarily by the occupants through opening and closing of windows,
- can be equipped with a mechanical heating, but the model does not apply for the periods when it is in operation,
- are not equipped with any mechanical cooling system,
- can be equipped with a mechanical ventilation with unconditioned air.

The model predicts a comfortable indoor temperature T_{comf} with the following equation [35]:

$$T_{comf} = 0.31 T_{om} + 17.8\,,$$

where T_{om} is the monthly mean outdoor temperature.

b) Adaptive model in EN 15251

The EN 15251 adaptive model is based on the data collected in the EU project Smart Controls and Thermal Comfort (SCATs) [99]. In opposition to the ASHRAE adaptive model, the EN 15251 model applies to all buildings in the so-called free-running mode. These include buildings with no mechanical cooling or heating in operation, regardless of the presence of those systems. Buildings in a free-running mode do not use energy to increase indoor thermal comfort. They are equipped with operable windows, which are the main means to adjust indoor conditions. Buildings equipped with mechanical fans or a mechanical ventilation are also considered as free-running if the air is not conditioned.

The comfortable temperature T_{comf} is defined by the following formula:

$$T_{comf} = 0.33 T_{rm} + 18.8\,,$$

where T_{rm} is the running mean temperature for the considered day. This temperature is defined as follows:

$$T_{rm} = (1-\alpha)(T_{ed-1} + \alpha T_{ed-2} + \alpha^2 T_{ed-3} + \ldots)\,, \tag{2.1.11}$$

where T_{rm-1} is the running mean temperature for the previous day, α is a constant between 0 and 1 (the recommended value is 0.8), T_{ed-1} is the daily mean external temperature for the previous day, T_{ed-2} is the daily mean external temperature for the day before, and so on. Since α is less than 1, the presented series put greater weights on the temperature for days closer to the present [99]. It means, that the

impact of recent experiences is higher than the older ones. In practice, Eq. (2.1.11) is often simplified to:

$$T_{rm} = (1 - \alpha)T_{ed-1} + \alpha T_{rm-1}\,.$$

Because the model was derived using data collected in European countries, it is more applicable to European climate conditions than the ASHRAE adaptive model, which is based on worldwide data. [99].

2.1.5 Summary

The human thermal comfort is a highly multidisciplinary problem. The human's thermal perception of the surrounding environment is affected by a number of environmental and personal factors. The environmental factors describe the thermal properties of the environment, i.e. air temperature, air velocity, humidity, mean radiant temperature, nonuniformity, etc. The personal factors divide to physiological, psychological and behavioral factors. These factors include the thermal properties of the human organism as well as the attitude and expectations of a person. Most of the above-mentioned factors are difficult to predict or calculate.

As shown in the preceding sections, a significant number of approaches to evaluate indoor conditions, in terms of the thermal comfort, were developed. It is clear that there is no any fit-to-all solution. Each model has its strengths and weaknesses, and a corresponding range of applicability.

The purely empirical models are the oldest ones. They are easy to use and, if used in the dedicated range of conditions, they produce reasonable results. Some of them are still in use, like the WBGT which is a good indicator of the heat stress in hot environments. Their main disadvantage is that the applicability range is often very narrow.

The heat balance based models, like the Gagge's two-node model or the Fanger's PMV-PPD model, have a much higher level of applicability. However, the heat balance based models are considerably more complex than the empirical models. The calculations evaluating the surrounding environment in these models are usually made using computer programs due to the presence of iteration loops (as in PMV-PPD model) or non-steady state equations (as in two-node model). One of the most significant disadvantages of these models is the difficulty of a correct prediction of input parameters, particularly of the personal factors (level of clothing and activity). The two-node model also needs, as an additional input, the convective heat transfer coefficient, which is not easily measured in the case of a human body. Nevertheless, in the present time the heat balance based models are the most widely used ones.

The evidence of this fact is that the two most known thermal comfort standards, ISO 7730 [74] and ASHRAE Standard 55 [4], are based on the PMV-PPD model.

The adaptive models were developed to overcome the obvious limitations of the heat balance based models. According to the adaptive approach to the thermal comfort modeling, building occupants interact with the indoor environment. People can adapt to new conditions physiologically as well as behaviorally. They can take a number of actions in order to maintain the thermal comfort, i.e. change the clothing, open or close windows, etc. Moreover, the perception of the indoor conditions depends also on psychological factors, like expectations or the attitude. Most of these models are based on empirical fits of the indoor neutral (comfortable) temperature to the mean (daily or monthly) outdoor temperature. It is based on the assumption, that outdoor climate is the main factor influencing the behavior and expectations. The adaptive models are suitable to evaluate the indoor conditions in free-running buildings during the summertime.

The complex multi-node models are, on the other hand, the only tools which can be used to evaluate highly transient and nonuniform conditions. Such conditions are particularly characteristic for vehicles. Those models are used in the automobile, aerospace and military industry. They simulate the human thermoregulatory system, giving an extensive, quantitative data about the heat transfer in a human body. However, they are significantly more complex and difficult to use. Some of them, especially those based on the finite element method, require a high computing power. The complex models are preferred in studies concerning vehicular environments, which are much more dynamic than building environments.

As shown, in order to choose an appropriate thermal comfort model for a given study, a compromise between the capabilities and the complexity of a model must be found.

2.2 Thermal modeling of buildings

The aim of the present section is to present some background information concerning the building thermal modeling. The main issues of the buildings thermal modeling and main modeling approaches are discussed. In order to choose a right approach, the pros and cons of each method need to be evaluated.

The energy exchange process between the building and its outdoor environment is very complex. The phenomena governing this process are conduction, convection, radiation, and, in some cases, phase changes. Buildings lose heat mainly through the envelope and by ventilation. The major heat gains are solar heat gains and internal

heat gains due to the human metabolism and equipment being in use. With so many diverse factors affecting the thermal performance of buildings the use of an accurate assessment method is crucial. The available methods can be grouped into three categories: experimental, analytical and numerical.

The experimental studies are based on investigations of real systems. These studies are usually the most expensive, although the cost highly depends on the problem type. Experiments give an opportunity to investigate even the most complex problems, when many phenomena influence the results. Such problems are often difficult to be analyzed analytically. On the other hand, it can be hard to create ideal, fully controllable conditions when a particular phenomenon has to be isolated. Also, there can be significant difficulties with the collection and interpretation of the measurement results due to a limited number of measuring instruments. Moreover, each instrument has a limited precision, what introduces additional errors. The experimental results are often used to validate numerical results.

In contrast, analytical and numerical methods study simplified systems. The simplified system is represented by its mathematical model. Depending on the aim, a real system can be simplified in terms of the geometry and underlying physics. Hence, the results of analytical and numerical investigations depend mainly on a mathematical model precision.

The analytical methods give a precise solution of the mathematical problem. The solution is obtained for the entire computational domain. However, analytical solutions exist only for relatively simple problems, with regular geometries and simple boundary conditions. When the problem is too complex to be solved analytically, a numerical method has to be applied.

The numerical methods are capable to find an approximate solution to complex mathematical problems. Such problems are often described using one or more differential equations, e.g. the heat equation or transient heat balance. In the numerical methods, the governing differential equations are not solved directly. The computational domain is first spatially discretized, and then a set of algebraic equations approximating the differential equations is constructed. The solution provides the output values for all the relevant variables, but is obtained only in a finite number of points called *mesh nodes*. The numerical methods enable to simulate ideal conditions, where only one certain phenomenon can be studied without the influence of other factors [106].

In general, numerical studies are usually less expensive than experiments, both at small-scale and full-scale. In addition, in many cases, computers enable to investigate a problem many times faster than real-time experiments. For example, a

simulation of the building's thermal behavior over a one-year time period can be completed in just several seconds to several days, depending on the model complexity. It is possible thanks to a rapid increase in the computing power in the last three decades, making numerical investigations incomparably cheaper and faster. However, the computing time needed to solve the most complex problems can be still significantly greater than the real time. It often happens in the case of the computational fluid dynamics (CFD) studies.

There is a number of types of numerical thermal models of buildings. They differ in the number of considered phenomena, spatial discretization methods and applied numerical schemes. The most simple models can be only used to estimate an approximate building energy demand. The most complex ones can provide comprehensive data regarding building indoor environment. In addition, the models can be mixed: elements of the most interest can be modeled using a more sophisticated method giving more detailed results, while the rest of a building can be significantly simplified.

Sometimes, a model may consist of a set of submodels which exchange data between each other during the simulation, that is called the *co-simulation*. There is a number of algorithms to exchange solution results between the submodels working in a co-simulation.

The numerical thermal models of buildings can be divided into the following two groups:

- static models,
- dynamic models.

The static models are based on a steady state form of equations, and therefore they cannot account for thermal capacity effects. The dynamic models are based on a time-dependent form of equations, making it possible to consider time-dependent effects, like the thermal inertia due to thermal capacitance of building structures. In some cases however, static and dynamic models can work in a co-simulation, as discussed in Wang and Wong [134, 135] or Zhai et al. [144]. It is especially typical to run a co-simulation between a static CFD solver and a dynamic building energy simulation solver (e.g. based on a multizone model).

A building thermal model usually consists of minimum two components: the model of the building envelope and the model of the indoor air. They are usually considered as separate domains. The conduction prevails in the building envelope, while the convection prevails in the indoor air (although many of the models do not take it into account). The most common approaches to model the building envelope

and the indoor air are shortly described in two separate subsections (Sections 2.2.1 and 2.2.2).

2.2.1 Building envelope modeling

Usually, the heat transfer through a building envelope is described using the heat conduction equation. The building envelope models differ in the numerical schemes applied to solve the equation and in the simplifying assumptions set on the geometry. The heat is transferred through the building envelope particularly by the conduction. The heat conduction can be treated as the steady or transient heat transfer. The transient heat conduction in building components can be computed using either numerical methods (e.g. the finite difference method) or a superposition principle with so-called response factors [122]. The most popular approaches to model the building envelope are presented below.

a) Steady state approach

The steady state approach in modeling of the building envelope is based on a steady state form of the heat transfer equation (Laplace's equation):

$$\nabla^2 T = 0\,,$$

where $\nabla^2 T$ is the divergence of the temperature gradient. In general, the temperature T is a function of three space coordinates x, y, z:

$$T = f(x, y, z)\,.$$

In a steady state, the temperature does not depend on time. In building thermal models, the heat transfer is usually assumed to be one-dimensional:

$$\frac{\mathrm{d}^2 T}{\mathrm{d}x^2} = 0\,.$$

When the temperature distribution in building structure elements is known, it is possible to calculate the related heat fluxes using the Fourier's law. For a one-dimensional case the Fourier's law is:

$$\overrightarrow{q} = -\lambda \frac{\mathrm{d}T}{\mathrm{d}x}\,,$$

where $\overrightarrow{q}$ is the local heat flux [W/m^2], λ is the material's conductivity [W/m^2 K] and $\mathrm{d}T/\mathrm{d}x$ is the temperature gradient [°C/m]. In the practice, the transmission

heat loss Q_{tr} [W] through the thermal envelope during the considered time period Δt [s] is calculated as follows:

$$Q_{tr} = \left(\sum_i U_i A_i \right) \cdot \Delta T \cdot \Delta t \,, \tag{2.2.1}$$

where ΔT is the difference between indoor and outdoor temperatures [°C], and U_i and A_i are the heat transmission coefficient [W/(m^2 K)] and the area [m^2] of the partition i, respectively. Eq. (2.2.1) is valid only for the one-dimensional heat transfer. The influence of the two- and three-dimensional effects is often included by the so-called linear- and point-type thermal bridges. The thermal bridges are characterized by linear and point heat transmission coefficients, ψ [W/m K] and χ [W/K], respectively. The coefficients can be obtained experimentally or numerically. The default values of ψ for some typical linear thermal bridge types can be found in the EN ISO 14683 [39]. The transmission heat loss, including the thermal bridges effects, is given by:

$$Q_{tr} = \left(\sum_i U_i A_i + \sum_j \psi_j L_j + \sum_k \chi_k \right) \cdot \Delta T \cdot \Delta t \,,$$

where j is the number of linear thermal bridges, k is the number of punctual thermal bridges and L_j is the length of the linear thermal bridge j [m]. The steady state approach (often referred as the U-value approach) in the building envelope modeling exists in many national building codes, including the Polish one [113].

b) Response factor method

The response factor method is based on a superposition principle which is valid for linear and invariable systems [122]. Using this method, it is possible to find transient heat fluxes in one-dimensional building components. The method is applicable to single-layer as well as to multilayer components. The method utilizes analytical solutions to unit excitations, and therefore it is generally not considered as a numerical method. However, due to the total number of calculations (summation of the analytically derived responses) needed to reach the final result, the method has to be implemented as a computer program.

In the method, the building excitations are resolved into a series of simple components. The possible excitations acting on a building are e.g.: solar radiation absorbed at any surface, air dry-bulb temperature, sol-air temperature, etc. The continuous excitation functions are represented as time-series. Subsequently, a re-

sponse to each excitation component is calculated. Finally, the responses are added. The sum of the responses represents the total response of the system to the given total excitation. If the method is applied to calculate the heat flow through external walls, there are four types of response factors which has to be calculated [88]:

1. response on the outside surface due to an outside excitation,
2. response on the inside surface due to an outside excitation,
3. response on the outside surface due to an inside excitation (equal to the previous one),
4. response on the inside surface due to an inside excitation.

The analytical formulae to calculate the response factors exist for slabs composed of homogeneous layers. The response factors for components of highly inhomogeneous materials (e.g. hollow bricks) can be evaluated numerically or experimentally [88]. Using this method it is also possible to construct a set of equations to describe the dynamic thermal characteristics of an entire room [91]. The equations describe the heat balances for the indoor air and at each of the surfaces enclosing the room. The equations can be used directly to calculate surface temperatures or indoor air temperature.

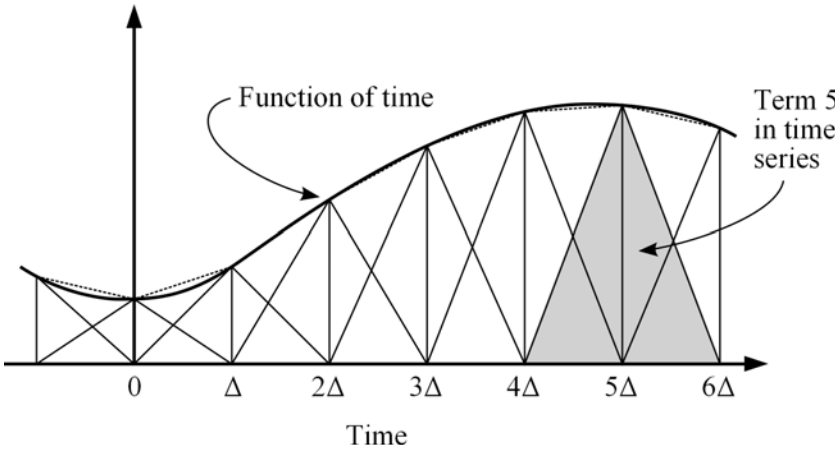

Figure 2.6: Time-series representation of continuous function in response factor method [122]

The time-series of the excitation function is a series of numbers or quantities representing its values at successive equal intervals of time [122]. The function can be represented as a series of step functions or triangular pulses. The triangular pulse approach gives a better approximation to the original function, since the sum

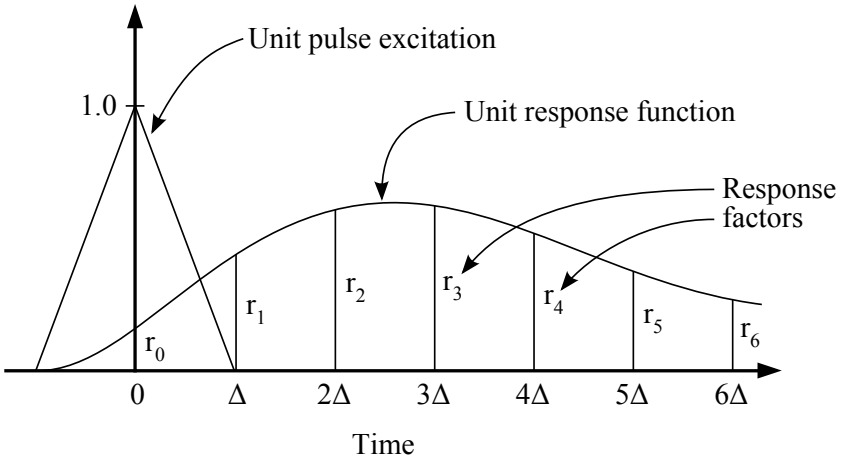

Figure 2.7: Unit triangular excitation and unit response function [122]

of overlapping triangles is a continuous function made up of straight line segments (Fig. 2.6) [122].

The response factor method is less computationally demanding than numerical methods, since calculations of response factors are done only once at the simulation beginning. In the subsequent steps, elementary response factors can be combined with any set of excitation data [91]. The difference in a computing power demand between this method and numerical methods was especially noticeable in the 1970's and 80's, when computers where significantly slower than present ones. Nowadays, the available computing power makes this advantage less significant.

c) Numerical methods

Numerical methods approximate a solution of the heat transfer equation, which governs the heat transfer in the building envelope. The solution is provided only at a finite number of points and not for the entire (continuous) computational domain. The most widely used numerical methods applied in the heat transfer problems are the Finite Difference Method (FDM), Finite Volume Method (FVM) and Finite Element Method (FEM) [86].

From the three above-mentioned methods, FDM is the easiest to be implemented. FDM replaces all partial derivatives in the differential equation by approximations, using the truncated Taylor series [106]. The approximated equations are called the difference equations. The difference equations are written for an array of grid points, called nodes. The system of nodes represents a discretized domain of the problem. The solution accuracy can be increased by increasing the number of nodes. However, the method becomes difficult when the problem has an irregular geometry or a complex definition of boundary conditions [86]. FDM is probably the most

often used numerical method when a one-dimensional heat conduction is assumed. A considerable number of the finite difference schemes exist. The most widely used schemes to solve the heat transfer equation are: the Forward Time Centered Space (FTCS) scheme, the Backward Time Centered Space (BTCS) scheme and the Crank-Nicolson scheme.

In FVM, the computational domain is divided into a number of finite volumes. In the method the equations are presented in the integral form. The divergence terms in the equations are expressed as surface integrals, based on a divergence theorem. Surface integrals represent fluxes at finite volume surfaces. Each finite volume can have an arbitrary defined shape, making the method convenient when a domain geometry is complex. In a uniform Cartesian mesh, the FVM method can be regarded as a FDM [24]. On the other hand, the vertex-centered FVM is very similar to the linear FEM [86].

In FEM, the solution domain is divided into small, interconnected regions, called elements. In the method, a piecewise (element-based) continuous function (based on linear, quadratic or higher-order polynomial subfunctions) for a solution is assumed. Subsequently, the parameters of functions are found in a manner to reduce the error in the solution. The concept of the FEM is very broad, i.e. the method can be used in a variety of different ways to solve a given problem [16]. The method was originally developed to be applied in the structural analysis of solids [17]. During the last decades, however, the method applicability was extended also to other fields, like fluid flow and heat transfer. The method is robust for solving problems with complex geometries. As in the FVM, it is possible to use irregular meshes, finer in regions of a special interest and coarser elsewhere. The exemplary works in which the concept of FEM is thoroughly explained are those of Bathe [16, 17] or Zienkiewicz and Morgan [150]. The adaptation of FEM to problems of heat transfer and fluid flow is discussed by Lewis et al. [86].

FEM is probably the most versatile method, but also the most difficult to implement. FVM method is considerably easier to implement than FEM and in many cases it has a comparable accuracy. FDM is easy to implement, but when a geometry is complex it is difficult to generate a suitable mesh.

2.2.2 Indoor air modeling

The indoor air models are more diverse than the building envelope models. The building envelope models are based on the same mathematical basis: the heat transfer equation. The indoor air models, on the other hand, differ not only in applied solution methods, but also in underlying equations. The numerical air models can

be divided into: lumped models, multizone models (airflow network), zonal models and CFD models. The lumped models are the simplest ones with a low computing demand, while the CFD models are the most complex and computing demanding. The most influential indoor air models are shortly described below.

a) Steady-state heat balance

This is the simplest approach to model the indoor air. It is based on the first law of thermodynamics with the assumptions that the internal energy of the analyzed system is constant and there is no work done by the system. Since it is based on a steady-state heat balance, it is a static model. It should be regarded as an analytical model rather a than the numerical model. The steady-state heat balance for an arbitrary number of heat fluxes entering a thermal zone i is:

$$\sum_{j=1}^{n} \Phi_{j \to i} + \Phi_{source} = 0\,,$$

where i is the thermal zone number, j is the number of a surface adjacent to the zone i, $\Phi_{j \to i}$ is the heat flux between the surface j and zone i [W] and Φ_{source} is the total heat flux generated by internal heat sources (or sinks) [W]. Each component in the equation can be negative. The indoor air temperature must be known in order to evaluate the heat amount to be supplied or extracted from the zone in order to keep the temperature at a given level. The model cannot evaluate the ventilation performance. The air exchange rate has to be defined explicitly. With a known air exchange rate, it is possible to calculate the ventilation heat loss (or heat gain). The steady-state heat balance is implemented in many national building codes dealing with the building energy demand. The calculations are simple enough to make them without any help of computers. However, the model cannot provide any information for the thermal comfort analysis, because no information regarding the indoor temperature variations and airflow is included.

b) Transient heat balance (lumped model)

The transient heat balance model is the simplest dynamic model. The transient heat balance can be presented in the following differential form:

$$\sum_{j=1}^{n} \Phi_{j \to i} + \Phi_{source} = \rho_i V_i c_p \frac{\mathrm{d}T_i}{dt}\,,$$

where i is the thermal zone number, j is the number of a surface adjacent to the zone i, $\Phi_{j \to i}$ is the heat flux between the surface j and zone i [W] and Φ_{source} is the

heat flux generated by the internal heat source [W], ρ_i is the air density [kg/m^3], V_i is the air volume [m^3], c_p is the air specific heat [J/(kg^3 K)], T_i is the air temperature [K] and t is time [s]. The model takes into account the heat capacity of a considered air volume and it can be used to calculate the time-varying internal temperature. Usually, the indoor air is treated as a single volume, i.e. as a single thermal zone. Thus, the model is often referred as the *lumped model*. The model cannot provide any results concerning indoor airflow. The transient heat balance can be solved numerically, e.g. using the finite difference method.

c) Multizone model (airflow network)

The indoor air is treated as a set of nodes representing air zones, e.g. rooms [15]. Each zone is assumed to be instantaneously well-mixed. In other words, homogeneous conditions are assumed within zones. The connections between the nodes can be defined to represent components like cracks, doors, windows, fans, etc. Each component has a different flow characteristics (Table 2.6). The flows in nodes are calculated from nodal pressures and inter-nodal component characteristics [63].

Table 2.6: Typical inter-nodal component equations [65]
($\dot{m}$ - mass flow rate, ΔP - pressure difference, $\dot{q}$ - volumetric flow rate, a, b - constants)

Type	General Equations
Power law flow resistance element	$\dot{m} = \rho a \Delta P^b$
Quadratic law flow resistance element	$\Delta P = a\dot{m} + b\dot{m}^2$
Constant flow rate element	$\dot{m} = \rho a$
General flow inducer (fan or pump)	$\Delta P = \sum_{i=0}^{3} a_i (\frac{\dot{m}}{\rho})^i$ $\dot{q}_{min} \leq \frac{\dot{m}}{\rho} \leq \dot{q}_{max}$

In all indoor nodes, the mass conservation law has to be satisfied. The mass balance leads to a system of non-linear equations describing the airflow in the computational domain. It can be solved numerically, e.g. using the Newton-Raphson method. The "external" nodes in the system represent ambient conditions, e.g. ambient temperature, pressure or wind velocity. The model offers a considerable flexibility in describing a range of designs [63]. It can be used to simulate not only the indoor airflow, but also the fluid flow in a plant system, e.g. heating system, mechanical ventilation system (ducts, fans, etc.) or solar collector system. It is possible to combine the building airflow and plant fluid flow networks [64].

Up to now, the multizone model is the only model capable to perform annual simulations of the building airflow within a reasonable computing time. Thus, it is

the best choice for design optimization purposes [27]. It is because the number of nodes needed to build a numerical model, and therefore the number of equations to be solved at each time step, is relatively small (comparing for example to CFD models). However, as reported by Chen [26], a multizone model can be incapable to deal with a natural ventilation system. Especially, buoyancy-driven natural ventilation systems are difficult to model using only one node per room, since this system strongly depends on the air stratification. Also, the model application in indoor comfort analyses is limited, because the local air flow inside rooms cannot be studied [15].

The multizone model is implemented in all major building energy simulation programs, e.g. in ESP-r [63] or EnergyPlus [60]. The model is often named also as: airflow network, mass balance network, or nodal network [65].

d) Zonal models

The zonal models are an intermediate approach between the lumped models, which are extremely fast but cannot provide any information about local airflow, and CFD models, which can provide the full information about the airflow but in most cases are too computationally intensive [140]. Several zonal models have been developed so far [62, 140].

The room in the zonal model is divided into several zones, in which the temperature and density are assumed to be homogeneous. The pressure distribution within a zone is assumed to be hydrostatic [94]. The air is treated as an incompressible fluid. The general equations governing the mass and energy conservation in each zone can be written as follows [62]:

$$\begin{aligned} \frac{\mathrm{d}m_i}{\mathrm{d}t} &= \sum_{j=1}^{n} \dot{m}_{ij} + \dot{m}_{source} + \dot{m}_{sink} = 0\,, \\ \frac{\mathrm{d}Q_i}{\mathrm{d}t} &= \sum_{j=1}^{n} q_{ij} + q_{source} + q_{sink} = 0\,, \end{aligned}$$

where t is time [s], n is the number of the zones adjacent to the zone i, m_i is the air mass [kg] of the zone i, $\dot{m}_{ij}$ is the air mass flow rate [kg/s] from the zone i to the zone j, $\dot{m}_{source}$ is the the rate of mass supplied by the "internal" source in the zone [kg/s] and $\dot{m}_{sink}$ is the rate of mass removed from the zone [kg/s], Q_i is the internal energy [J] of the zone i, q_{ij} is the heat flux [W] entering the zone i from the zone j, and q_{source} and q_{sink} are the heat supplied and removed from the zone [W], respectively. The mass supply $\dot{m}_{source}$ and removal $\dot{m}_{sink}$ can be in example due to a mechanical ventilation system.

A common approach to calculate the mass flow rate across vertical faces is to assume a nonlinear dependency of the pressure difference [140]:

$$\dot{m}_{ij} = \rho_{ij} \cdot A_{ij} \cdot C_d (P_i - P_j)^n \,, \tag{2.2.2}$$

where ρ_{ij} is the air density [kg/m^3] in the zone i or j depending on the sign of $\dot{m}_{ij}$, A_{ij} is the area [m^2] of the surface between zones i and j, P_i and P_j are the pressures [Pa] in the zones, and C_d and n are some empirical coefficients for the given flow regime. The mass flow rate across horizontal faces depends also on the hydrostatic pressure [140]:

$$\dot{m}_{ij} = \rho_{ij} \cdot A_{ij} \cdot C_d (P_i - P_j - \frac{1}{2}(\rho_i h_i + \rho_j h_j))^n \,,$$

where ρ_i and ρ_j are the densities of air [kg/m^3] in the zones i and j, and the h_i and h_j are the faces height from cell j center [m].

The presented equations cannot take into account the momentum effects. That is why the zonal models have difficulties in predicting momentum-driven flows. To increase the model accuracy, two cell (zone) types can be used: standard cells and specialized cells. The standard cells are used for zones where the air velocity is low. The mass flow rate in these cells can be calculated using the standard power-law pressure distribution, like in Eq. (2.2.2). The specialized cells are used in zones where the airflow is momentum-driven [140], e.g. by fans. Since, the zonal model does not include momentum conservation equations, some empirical relations have to be used instead to predict a momentum-driven flow. Unfortunately, the use of two different cell types limits the model applicability to a few simple configurations [98]. The model is valid as long as the airflow pattern is similar to the one predicted by the designer of the model for a given room geometry [27]. In addition, such a modified zonal model may require a similar computing effort as CFD with the same cell number [26]. These limitations can be overcome by models that can correctly predict the airflow in both standard and momentum-driven zones using only a one cell type, like the POMA model [62] (which is however applicable only to steady-state two-dimensional flows). Due to a semi-empirical nature of the equations governing the airflow, increasing the number of cells (zones) does not guarantee more accurate results. Many zonal models are limited to a specific number of zones.

Although initially developed for two-dimensional airflows, some zonal models can also predict three-dimensional airflows and temperatures with a reasonable accuracy [139].

e) Computational Fluid Dynamics

The Computational Fluid Dynamics (CFD) can give an insight in the airflow pattern in the building. It is the most complex and computationally intensive approach to model indoor airflow. Each CFD model is based on a different set of partial differential equations. If the airflow pattern is needed only, the Navier-Stokes equations (momentum conservation equations) and the mass conservation equation are solved. The Navier-Stokes equations are derived from the Newton's second law applied to a continuum, and in a general form can be written as follows [19]:

$$\rho\left(\frac{\partial \mathbf{u}}{\partial t} + \mathbf{u}\cdot\nabla\mathbf{u}\right) = -\nabla p + \nabla\cdot\bar{\bar{\tau}} + \mathbf{f}\,, \tag{2.2.3}$$

where ρ is the fluid density, $\boldsymbol{u}$ is the flow velocity vector, t is time, p is the pressure, $\bar{\bar{\tau}}$ is the deviatoric stress tensor and $\mathbf{f}$ stands for volumetric body forces. The mass conservation equation is as follows [106]:

$$\frac{\partial \rho}{\partial t} + \nabla\cdot(\rho\mathbf{u}) = 0\,. \tag{2.2.4}$$

Such approach can give an accurate airflow solution in domains without significant temperature gradients, such as some HVAC-equipped spaces.

If temperature gradients cannot be ignored, additionally the energy conservation equation has to be solved [128]:

$$c_v\rho\frac{\partial T}{\partial t} = \Phi_\mu + \nabla\cdot(\lambda\nabla T)\,,$$

where c_v denotes the specific heat, ρ is the density, T is the temperature, t is the time, Φ_μ is the viscous dissipation of energy and λ is the thermal conductivity. The temperature gradients can considerably affect indoor airflow. The effect is especially important in buildings equipped with buoyancy-driven ventilation systems. In such cases the indoor air velocity field cannot be accurately predicted if the energy equation is not taken into account.

It is possible to treat the indoor air as a mixture of gases (multiphase flow) if another equation is included in the model — species transport equation. Such model enables to track a contaminant concentration (e.g. CO_2) in the considered space. Depending on the problem formulation, the total number of equations to be solved varies from few to several. The solution algorithm is highly complex. The major difficulties are related to the Navier–Stokes equations, which are non-linear, and the pressure and velocity are interdependent variables.

A number of methods exists to solve the Navier–Stokes equations. The most

often used numerical methods applied to solve the governing equations are the Finite Difference Method, Finite Volume Method and Finite Element Method. In addition, the equations can be solved using a coupled solver or a sequential solver. Coupled solvers are especially suitable to solve high-speed compressible flows, where a strong interdependence between variables exists, while segregated solvers are usually used for incompressible flows or low-speed compressible flows [46]. The coupled solvers solve all the equations simultaneously (a single matrix is constructed), while the sequential solvers solve one equation after another, using the so-called inter-equation coupling. There is a number of inter-equation coupling methods. In all of them the solution of pressure and velocity is obtained iteratively. Commonly used algorithms for the pressure-velocity coupling are the Semi-Implicit Method for Pressure-Linked Equations (SIMPLE) algorithm [106] and its derivatives, and the Pressure Implicit with Splitting of Operators (PISO) algorithm [76]. There are also some mixed algorithms, like e.g. the PIMPLE algorithm (PISO + SIMPLE) [102].

Depending on the fluid viscosity and velocity, the flow is laminar or turbulent. Typical air velocities in buildings are in the range of 0.05–0.5 m/s [32]. Velocities are usually slightly higher in naturally ventilated buildings than in HVAC-equipped buildings, especially during the summer season. The indoor air speed rarely exceeds 1 m/s. Indoor airflows are usually near a transitional range between the laminar and turbulent flow. Although it is assumed that Navier-Stokes equations properly describe the turbulence [128], a direct simulation of turbulence by the time-dependent Navier-Stokes equations is very computationally expensive [19]. Such a direct modeling is known as the *Direct Numerical Simulation* (DNS). Up to now, DNS is too computationally demanding to be applied in most cases. It is often used to validate other turbulence modeling approaches. There are two main approaches to simplify the Navier-Stokes equations and enable faster calculations: the *Reynolds-Averaged Navier Stokes* (RANS) approach and the *Large-Eddy Simulation* (LES) approach.

The RANS models are based on a decomposition of flow variables into a mean and a fluctuating part [19]. The averaging simplifies a solution, but there is an additional need to model a fluctuating part via a turbulence model. Some of the most widely used RANS turbulence models are e.g. the $k-\epsilon$ and the $k-\omega$ models. In the LES, on the other hand, the time-varying fluctuation is calculated directly, but the turbulence in the sub-grid scale still has to be modeled. LES generally gives more accurate results, but is considerably more computationally expensive than RANS simulations. Each turbulence model is valid only in some certain range of conditions. There is no any fit-to-all approach.

The CFD solution is strongly dependent on a mesh geometry. In most cases

the geometry of indoors is complex, especially when furniture is taken into account. The problem is not only to generate a reasonable quality mesh, but also to validate it. The validation requires to conduct some preliminary but still computationally expensive simulations. From the designer point of view, the effort-to-result ratio is usually too high.

In CFD a special care must be taken to obtain an accurate result in the near-wall regions. While these regions are often not so important in many non-thermal cases, in thermal analyses an accurate heat exchange between solid and fluid is crucial. There are two approaches to solve the boundary layer properly: by using a very fine mesh near the wall, or by using the so-called wall functions based on empirical studies. The first approach is too computationally demanding for long-term simulations. The second one needs to be used with care. The log-law of the wall, on which wall functions rely, is valid only for particular range of conditions.

In the last years many researchers successfully coupled CFD with some building energy simulation (BES) models. A CFD program and a BES program can be linked externally or internally. An example of the internal linking is the ESP-r software, which has an implemented CFD module [15]. However, this module is limited only to cuboidal spaces. In addition, a special care must be taken to obtain a converged solution. On the other hand, there are many successful attempts to link CFD and BES externally [134, 135, 144]. Such an approach enables to take the advantage of mature and reliable CFD codes. Although, a special care must be taken to exchange the data between two separate computer programs what introduces some inflexibility.

As shown by Mora et al. [94], coarse-grid conventional $k-\epsilon$ CFD models can be a satisfactory alternative to zonal modeling from the point of view of both computing effort and accuracy. The coarse-grid CFD models are in better agreement with experimental results than zonal models [94]. The latest trends in the literature showed, that studies on zonal models were aimed at the model development rather than at practical applications [26].

Concluding, CFD has a great potential in the field of building thermal analyses, but there are still significant difficulties making its use possible only by engineers and scientists with a strong theoretical background. In addition, although the available computing power increases year by year, it is still far from enough from the point of view of long-term CFD simulations. Despite these difficulties, in the last few years CFD was used in the majority of studies concerning the ventilation performance, thermal comfort or indoor air quality [26].

2.2.3 Summary

The thermal modeling of buildings enables to evaluate and compare various building design concepts in terms of the energy consumption and indoor thermal comfort. The use of numerical models in building thermal analyses has the following advantages:

- a relatively low cost as compared to experimental studies,
- a full control over input parameters of experiments,
- complete results in the entire domain of interest,
- a possibility to isolate a specific problem.

Building thermal models consist of two main parts. The first part is a model of the thermal envelope. The second is the model of the indoor air. Due to different natures of these two environments, different equations are used to describe the heat and mass transfer and different methods are used to solve them.

Among thermal envelope models, the most simple is the steady-state lumped model. Its simplicity lets to conduct calculations manually, however the method cannot take into account thermal capacitance effects. If a transient solution is required, a dynamic model has to be applied. One of the simplest methods for transient problems is the response factor method. However, if the considered geometry cannot be simplified to one dimension, a numerical model (e.g. based on FDM, FVM, or FEM) has to be developed.

Similarly, the indoor air can be modeled using diverse methods. The most commonly used are the simple steady state heat balance approach, the transient heat balance approach, the multizone modeling, the zonal modeling and the CFD modeling. The heat balance based models are the easiest to implement, but they cannot provide any information concerning indoor airflow. The air mass flow rates between rooms can be studied using multizone models. If the local (within a room) air velocities have to be known, the zonal modeling or CFD modeling has to be applied.

The decision which thermal model to choose to study a given problem is not trivial. The simplest models enable to perform simulations in very short time, but they can provide relatively little reliable information. The most complex models provide realistic information, but the cost related with the development and computational time is often too high. Therefore, a reasonable balance is needed between the model complexity and its capabilities.

2.3 Building thermal capacitance

2.3.1 Basic definitions

The heat capacity is the property of a material describing how much heat is needed to increase or decrease the material temperature by 1 K. A thermodynamic system heat capacity is not constant, but varies with state variables: temperature, pressure and volume. The heat capacity can be defined as a value per unit mass, per unit volume or as a value related to the entire considered thermodynamic system. To avoid ambiguity, terms related to the heat capacity which are used in this work are defined below.

The heat capacity per unit mass of a material is referred as *specific heat* or *specific heat capacity* and is denoted with c [J/(kg K)]. The specific heat is usually measured at constant pressure (denoted as c_p) or constant volume (denoted as c_V). In general, c_p and c_V are different functions of the temperature. From the building material point of view, more relevant is the the specific heat at constant pressure c_p, since the volume of building materials is generally not constant (e.g. due to the thermal expansion).

The product of the material density ρ [kg/m^3] and specific heat c [J/(kg K)] is referred as the *heat capacity* or *volumetric heat capacity*, denoted with the capital letter C [J/(m^3 K)]:

$$C = \rho \cdot c \,.$$

The heat capacity is a dynamic thermal parameter. In other words, to study heat capacity effects, a transient heat transfer must be considered. From a mathematical point of view the influence of the heat capacity on the heat transfer is easy to explain using the heat equation:

$$C\frac{\partial T}{\partial t} = \lambda \nabla^2 T \,,$$

or the transient heat balance equation:

$$VC\frac{\partial T}{\partial t} = \sum \dot{q} \,,$$

where ρ is the density [kg/m^3], C is the heat capacity [J/(m^3 K)], T is the temperature [K], t is time [s], λ is the conductivity [W/(m K)], V is the material's volume [m^3] and $\sum \dot{q}$ is the sum heat fluxes entering the considered space [W]. It can be noticed that the lower heat capacity C materials, the faster is the temperature change due to any heat load. When a material is not exposed to heat loads, its temperature eventually evens out. The higher material heat capacity, the longer it takes.

As shown, there is a positive correlation between the material density and heat capacity, i.e. heavier materials have higher heat capacity. The examples of common building materials with a relatively high heat capacity are concrete and masonry. Such materials are capable to absorb and store high amount of energy without a significant change in the material temperature.

The total heat capacity of a specific material volume is referred as the *thermal capacitance* C_{th} [J/K] and is calculated as follows:

$$C_{th} = C \cdot V = \rho \cdot c \cdot V \,.$$

The thermal capacitance is a property often used to describe the total potential of an entire building structure or its separate components to store the thermal energy.

In building engineering, the thermal capacitance of building structure components is often referred as the *thermal mass* to emphasize inertial effects [143, 142, 147, 148, 149, 58, 112]. These effects affect the indoor environment and building energy demand. The thermal mass and thermal capacitance are equivalent, fully interchangeable terms. In this work, however, the *thermal capacitance* is the preferred term.

When one compares certain wall structures it is useful to define the *wall planar thermal capacitance* or simply the *wall thermal capacitance* C_{wall} [kJ/(m^{2}K)], i.e. the thermal capacitance per unit area of a wall. In this work, the wall thermal capacitance is defined as follows:

$$C_{wall} = \sum_{i}^{n} c_i \rho_i d_i \,,$$

where n is the total number of layers in a wall, and c_i, ρ_i, d_i are the specific heat [J/(kg K)], the density [kg/m^3] and the width [m] of the i-layer, respectively. It should be noticed, that the wall thermal capacitance C_{wall} does not take into account the spatial distribution of the thermal capacitance, that also influences the wall thermal inertia to some extent.

2.3.2 Influence on indoor environment

The thermal capacitance of buildings can be divided into the external and internal thermal capacitance. The external thermal capacitance is the thermal envelope. The internal thermal capacitance consists of internal walls, floors and furniture [149]. The external thermal capacitance is exposed both to the ambient and to indoor air, while the internal thermal capacitance is exposed only to the indoor air. Due to its

location, the external thermal capacitance is highly efficient in the attenuation of outdoor temperature swings. However, the internal thermal capacitance also considerably contributes to the temperature stabilization, especially because it has higher surface area exposed to the indoor space than the external thermal capacitance.

The thermal capacitance, both external and internal, can be used as a sink to absorb excessive energy during the day. The stored energy is released when the building cools down. It makes indoor temperature more stable throughout a day. A more stable indoor temperature reduces the reliance on mechanical services to heat or cool buildings [58]. If the building is equipped with a heating and / or cooling system, in high thermal capacitance buildings, there are lower heating / cooling peak loads. The thermal capacitance has a potential for passive cooling in summer [58, 143], which can reduce or eliminate the need for mechanical cooling. Also, winter heating loads can potentially be decreased [59].

The high thermal capacitance is especially desirable in buildings where a night ventilation technique is used [148]. In hot climates such buildings are cooled during the night. It gives few extra hours during the day when the cooling system can be turned off. In some cases if the building thermal capacitance is high, the cooling system may even not be required at all.

The positive effects of the thermal capacitance can be demonstrated using examples of a traditional architecture in different parts of the world. Massive buildings with the high thermal capacitance are favorable in relatively dry climates, where high diurnal temperature swings are present, e.g. in Southwest Asia or Central Asia. On the other hand, light buildings with large openings are common in hot and humid climates, where the average diurnal temperature is high, like in some tropical climates of South America or Southeast Asia. These natural examples show that the thermal capacitance may not be beneficial in some climates. But even if the climate is suitable, the impact of the thermal capacitance on the indoor environment is complex and still not necessarily favorable [59]. The effect of the thermal capacitance of building elements on the overall performance depends on the climatic conditions (solar radiation, outdoor temperatures), building geometry, thermal envelope resistance (U-value / R-value), heat transfer coefficients, location and area of glazed surfaces or the of a mechanical heating (and cooling) system. There is no one optimum amount of the thermal capacitance applicable to all conditions and all kind of buildings [143].

In addition, to answer the question to the optimum amount of the thermal capacitance in a given building, the building's occupancy schedule must be also considered. The high thermal capacitance may not be desirable in buildings which are

intermittently occupied, like e.g. office buildings. In such buildings it is economically justified to set the heating or cooling system to work also intermittently. If the building is occupied, the system is turned on. If not, the system is turned off. In such case the high thermal capacitance is not beneficial. Light and well insulated buildings with the low thermal capacitance have the advantage that they can be warmed up or cooled down quickly, without significant energy losses.

However, the low thermal inertia of light buildings can contribute to the overheating [18]. In well-insulated buildings with the low thermal capacitance even small energy gains can result in a significant increase of the indoor temperature, because most of the excessive energy cannot be stored in the building structure or transmitted through walls to the outdoor. On the other hand, recent studies show that even though peak loads in light buildings are higher, overheating can be prevented using good ventilation, that is more effective in light buildings than in massive ones [83].

The efficiency of external thermal capacitance in the summer overheating prevention was extensively studied by Rodrigues [112]. The author performed numerous numerical simulations using a simple numerical model of a small one-room building with one external window using different types of external walls. All of the analyzed walls had the same U-value but different dynamic characteristics. The entire building was well insulated — the U-value of the walls was equal to 0.12 W/m^2K (passive building standard). The simulation results showed that using the thermal capacitance is beneficial to a limited extent. The performance difference between walls with different thermal capacitances is noticeable — indoor air temperature peaks can be decreased up to few degrees using massive external walls. However, it was found that other design factors, like the size and position of glazing and openings, and the control of internal heat gains are far more important in the overheating prevention than the external thermal capacitance. It is because highly insulated walls minimize heat gains through the transmission. In highly insulated buildings the overheating is mainly due to the solar radiation entering through the glazing.

According to Yam et al. [142] there is an optimum amount of the thermal capacitance which should be used in buildings relying on a passive design. The authors studied a nonlinear coupling between ventilation and internal thermal capacitance. No heat transfer through the thermal envelope was assumed. The outdoor temperature was assumed to be periodic, based on a sinus function with a 24 h frequency. The study showed that the maximum indoor temperature phase shift induced by the direct outdoor air supply without control is 6 h. It was concluded that if the thermal capacitance is already high, its further increase brought a little effect.

To allow designers to make easier decisions concerning material selection for

passive heated or cooled buildings, a number of dynamic thermal parameters were developed, e.g. admittance, decrement factor, time lag or time constant. The parameters are intended to help to evaluate the thermal capacitance impact on indoor thermal conditions. These factors are analyzed often by focusing on the characteristics of a given wall [6, 7, 8, 9, 131, 129, 104], rather than on a performance of the entire building. Although the thermal capacitance directly affects dynamic parameters of building elements, some works showed that dynamic parameters did not necessarily correspond with the performance of the entire whole building [112]. The factors influencing the building thermal behavior are strongly coupled making it difficult to extrapolate conclusions from simple simulations to real buildings.

2.3.3 Summary

The influence analysis of the buildings structural components thermal capacitance on the heat exchange between the building and outdoor environment requires to consider a number of factors impacting the thermal behavior of a building. Since each case study is different, it is difficult to give some fit-to-all guidelines. The numerical model and solution method should be carefully chosen.

The studies mentioned in the section provide a great contribution in the field of building thermal capacitance and indoor thermal comfort. However, none of these studies analyzes building thermal capacitance as a factor simultaneously affecting both the temperature and air velocity, while both these factors contribute to the thermal sensation. According to the author's knowledge such a study has not been conducted yet.

In most of the studies, the thermal comfort is investigated based on the temperature distribution results only. If influence of the air velocity is taken into account, usually it is assumed to be constant and uniform. It is reasonable since investigations require long-term simulations, while indoor airflow solutions can be obtained only using computationally intensive numerical methods, which make such long-term simulations difficult to perform. The building thermal capacitance studies require to consider long periods of time, because the effects of the thermal capacitance can span over days, weeks or even months.

However, since the thermal capacitance contributes to the indoor temperature stabilization, it also affects indoor airflow by limiting the impact of the natural convection. The question is: how much the indoor thermal comfort can benefit from the thermal capacitance when both factors are taken into account: indoor air temperature and indoor airflow. It is also interesting to what extent the high thermal capacitance of external walls make indoor environment more spatially uniform. The

aim of the present work is to answer these questions. The analysis of both spatial and time environment stabilization capabilities of the thermal capacitance are presented, by taking not only the temperature into account but also the air velocity and airflow pattern.

Chapter 3

Model formulation

3.1 Introduction

The numerical model developed in this work is capable to be used in transient simulations. Both transient indoor airflow and transient heat conduction in the building envelope are taken into account. This allows to analyze the effect of the thermal capacitance of external walls on indoor conditions. The model consists of two submodels: the external wall submodel and indoor air submodel. The term "submodel" is used in both cases to underline that these models are independent domains, but both are the parts of the numerical model. The external wall submodel is based on the one-dimensional transient heat transfer equation. The indoor air submodel is based on the conservation equations of momentum, mass and energy. The both submodels run together in a co-simulation. The results obtained by a single submodel are exchanged between each other in predefined time intervals. The model is able to predict a number of parameters describing the thermal comfort:

- the distribution of the indoor air temperature,
- the indoor air velocity and airflow patterns,
- the turbulence intensity,
- the temperatures of wall surfaces.

3.1.1 Geometry

The building geometry has a significant influence on the thermal capacitance performance. Therefore, to limit influencing variables, the geometry of the model is kept rather simple. The model geometry is similar to the one used by Rodrigues [112],

i.e. it consists of a one-room cuboidal space. However, to make the results interpretation easier, only one external wall is defined while all other surfaces are adiabatic (apart the inlet and outlet surfaces). The external wall has a single built-in window. The wall is faced toward the south. Its width depends on wall structures analyzed (see Section 5.1).

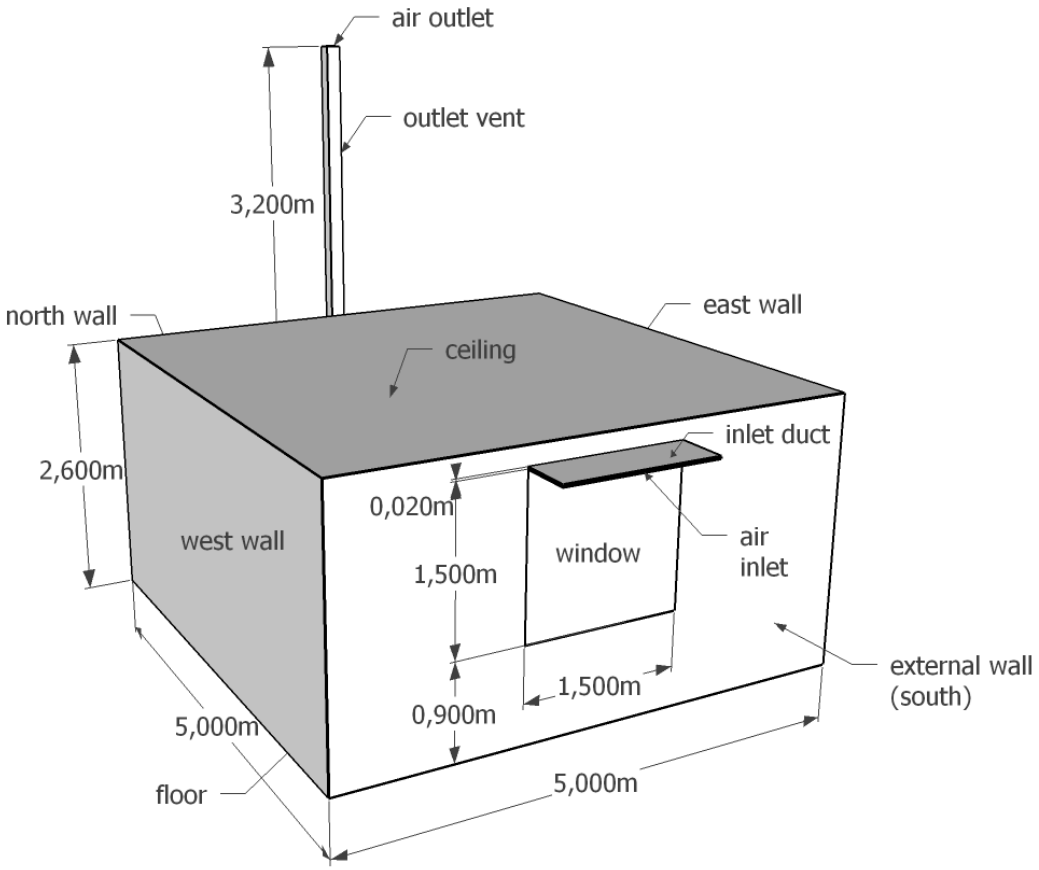

Figure 3.1: Model geometry

The space represents a room surrounded by similar rooms in all directions but the south. The room internal dimensions are $5 \times 5 \times 2.6\,\mathrm{m}^3$ (length x width x height), as shown in Fig. 3.1. The room is not equipped with furniture. Also, no occupants are modeled within the space.

The window dimensions are $1.5 \times 1.5\,\mathrm{m}^2$. The window is located in the center of the south wall, 0.9 m above the floor. The window is equipped with a trickle vent located at the top of the window. It would be infeasible to simulate the trickle vent geometry realistically due to its complex shape and relatively small dimensions. To make the geometry simpler, the vent is assumed to be a rectangular duct attached to the window. The height of the duct is 0.02 m. The inlet surface is located at the beginning of the duct. It is a good practice to place the inlet surface at some

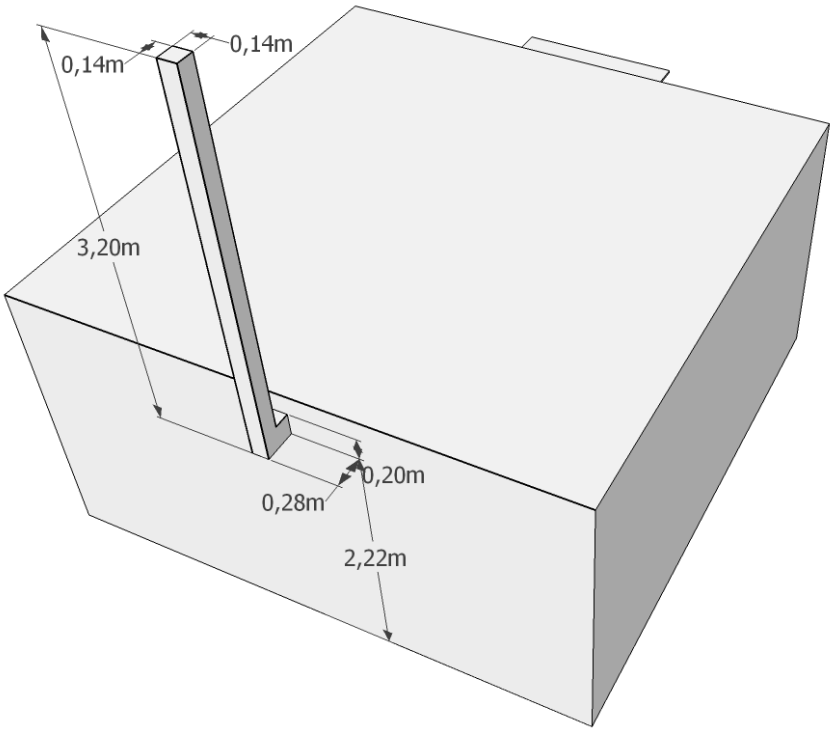

Figure 3.2: Geometry of outlet vent

distance to the indoor space to let the airflow stabilize and isolate the boundary from any irregularities. After some preliminary tests the duct's length was set to be 0.5 m long. The shorter ducts caused convergence problems, especially when a constant pressure and zero-gradient velocity boundary conditions were prescribed at the inlet. The inlet / outlet boundary conditions are discussed in Section 3.2.2.

The exhaust air duct is located on the opposite side of the room (Fig. 3.2). The exhaust duct is vertical and rectangular in shape with the dimensions of $0.14 \times 0.14\,\mathrm{m}^2$. Its length is equal to 3.2 m. The exhaust duct is connected with the room by a short horizontal duct connector. It is 0.14 m wide, 0.2 m high and 0.14 m long. The horizontal duct connector is located in the center of the north wall, 0.2 m under the ceiling.

3.1.2 Physical assumptions

In order to limit the computational demand and also to isolate the problem, i.e. to capture the influence of the external thermal capacitance on indoor conditions, a number of simplifying assumptions are prescribed. Some phenomena present in real buildings are consciously excluded from the analysis.

The short-wave radiation (solar radiation) is taken into account by the so-called

sol-air temperature. The sol-air temperature is based on the assumption that heat is exchanged on the external surfaces by convection only and the equivalent convective heat flux is equal to the radiative and convective heat flux. In consequence, the solar radiation reflecting the transparent component does not directly reach internal surfaces of the room, but rather is absorbed by the window material and then is conducted towards the internal surface. This assumption is obviously not realistic. If a window is modeled as a solid partition subjected to the sol-air temperature, non-physical window surface temperatures are obtained. In reality, the part of the solar radiation passes through the window and is mostly absorbed by the room internal surfaces. The non-physical temperatures have no influence on results in lumped-models which do not take into account nonuniformities of the indoor environment. However, when the indoor environment is modeled as a nonuniform space, the non-realistic window surface temperatures are a source of some errors, affecting indoor airflow pattern to some extent.

A realistic model of the solar radiation distribution would greatly complicate the model and increase the computing demand. Since the indoor environment has a three-dimensional geometry there would be a need to calculate which parts of the indoor surfaces are exposed to the sun radiation. Also, the procedure controlling the reflected surfaces topology should be developed. Moreover, the adiabatic boundary condition being assumed on the internal surfaces would be no longer valid. A realistic approach would make present investigations impossible to accomplish due to a rapid increase of the run-time demand. Thus, a simpler approach based on the sol-air temperature is adopted. This approach is reasonable, because the indoor environment parameters are mainly analyzed as spatially-averaged values and the nonuniformity impact on results is discussed for each simulation. Hence, although the "local" accuracy of the present numerical model may be questioned, it is still able to provide realistic average results with some auxiliary "spatial" information. Moreover, since the window is modeled identically in all cases, it does not contribute much to differences between results. Therefore the presented results can be used to evaluate the properties of various wall constructions.

The second major assumption is that the long-wave radiation inside the building is not taken into account. The long-wave radiation occurs between surfaces located in a building. It is assumed, that in well insulated buildings, the differences in internal surface temperatures are not significant. In the presented model, the indoor surfaces cannot also be heated up due to the solar radiation. Thus, the influence of the long-wave radiation is negligible.

The building is assumed to be naturally ventilated, i.e. no fans or air diffusers are

present. However, the natural ventilation highly depends on outdoor climate conditions [140] which are not precisely modeled in this work. The natural ventilation is driven by pressure differences caused by wind and by buoyant forces due to temperature differences. The factors influencing the efficiency of the natural ventilation are: ambient temperature, solar radiation, wind, humidity, building shape, topology of the surrounding terrain, location and types of openings in buildings. The model considering all these factors would be too complex. Also, since the present work aims to evaluate the impact of the thermal capacitance on indoor thermal conditions, realistic variations of outdoor climate parameters would make the interpretation of the results more difficult. Thus, a constant inlet air velocity is assumed. Two different velocities are analyzed: the first providing the air exchange rate (ACH) equal to 0.01 h^{-1}, the second reflecting the air exchange rate of 0.3 h^{-1}(a minimum ACH for residential buildings from the hygienic point of view according to ISO 13790 [73]). It is obvious that the thermal capacitance contributes to the stabilization of the indoor environment. However, the analysis of these two air supply levels enables to evaluate the ventilation attenuation of the thermal capacitance impact. This impact decreases with increasing ventilation rate.

It would be reasonable to analyze even more air supply levels, e.g. up to ACH = 2 h^{-1}. Unfortunately, the computational demand significantly increases with an increase of the indoor air velocity. The simulation time of the case with ACH = 0.01 h^{-1} is around 24–48h, while for the case with ACH = 0.3 h^{-1} it is around 7–13 days using a modern desktop computer. All simulations performed for the purpose of this work (including all preliminary simulations) took about 6 months using a quad-core processor. Therefore, only two ACH levels are analyzed.

The next important assumptions are that the heating and / or cooling system is turned off during the analysis and there are no internal heat gains in the building. Hence, the indoor temperature is intentionally allowed to exceed the thermal comfort range. This approach makes the assessment of the thermal capacitance influence easier. In example, it is possible to measure the time after which the indoor temperature drops below a comfortable level when a building is exposed to low outdoor temperatures. These results give quantitative relations between the thermal capacitance and some indoor environment parameters. Of course, the results of such tests should be carefully justified before making a decision concerning the economical amount of the thermal capacitance in a particular building. The final decision should reflect also the building heating and cooling system, building type and other factors which are discussed in Section 2.3.2.

Some assumptions concerning the factors affecting the thermal comfort are made.

As described in Section 2.1.2, the human thermal comfort depends on the environmental factors like the air temperature, air movement, humidity, mean radiant temperature and personal factors like metabolic rate or clothing level. The present model can provide air temperature and airflow results, but other factors must be assumed.

The mean radiant temperature (MRT) is assumed to be equal to the average indoor air temperature. In many cases this assumption is close to the reality. If building glazing is not exposed to the intensive solar radiation, indoor surface temperatures are relatively close to indoor air temperatures [118], especially in well-insulated buildings. The same assumption for the MRT was adopted in a number of indoor thermal comfort studies [56, 118]. The other factors, i.e. the relative humidity of the indoor air, metabolic rate and clothing level are assumed to be constant and equal to 50%, 1.2 met and 1 clo, respectively. The 50% relative humidity is a typical value for many indoor spaces in residential buildings. The assumed metabolic rate is typical for a standing and relaxed person. The chosen clothing level corresponds with a standard business suit.

The presented assumptions are aimed at shorten simulation times and to make the easier understanding of results. The goal is not to simulate fully realistic conditions, but rather to investigate the influence of the thermal capacitance on the indoor thermal comfort. The model is simple enough to perform transient simulations in a reasonable time, while on the other hand the model is complex enough to provide realistic results from the thermal comfort point of view. Contrary to models used in other studies [112], the model provides not only the indoor temperature, but also the air velocity and airflow pattern.

3.2 Indoor air submodel

The airflow in the building is modeled using Computational Fluid Dynamics (CFD). The air model takes into account turbulence and buoyancy effects. The air is treated as a compressible, viscous and Newtonian fluid. The air state variables obey the perfect gas law.

3.2.1 Mathematical formulation

The first part of the mathematical formulation (Section 3.2.1.1) consists of the formulation of three basic principles governing the airflow: momentum conservation (Navier-Stokes equations), mass conservation and energy conservation. The

description of basic airflow equations is followed with a list of assumed air thermophysical properties needed to be defined to solve the governing equations (Section 3.2.1.2). The last part (Section 3.2.1.3) describes the RANS decomposition (Reynolds-Averaged Navier-Stokes) and the so-called turbulence model needed to complete the RANS equations, implemented into the numerical model. The approach is adopted to allow the use of coarser computational grids and larger time steps.

3.2.1.1 Momentum, mass and energy conservation equations

The airflow in the model is governed by the Navier-Stokes equations together with the equations of mass and energy conservation.

The Navier-Stokes equations describe the fluid motion. They are derived from the Newton's second law of motion applied to a fluid particle. According to the Newton's second law, the rate of the change of momentum of a fluid particle equals the sum of forces acting on a particle. Two types of forces acting on fluid particles are considered: surface forces and body forces. The surface forces consist of pressure forces and viscous forces. The body forces may exist e.g. due to the presence of a force field (e.g. gravitational, electromagnetic). The momentum conservation equation for a fluid particle is as follows [132]:

$$\begin{aligned}
\rho\frac{Du}{Dt} &= \frac{\partial(-p+\tau_{xx})}{\partial x}+\frac{\partial\tau_{yx}}{\partial y}+\frac{\partial\tau_{zx}}{\partial z}+S_{M_x}\,,\\
\rho\frac{Dv}{Dt} &= \frac{\partial\tau_{xy}}{\partial x}+\frac{\partial(-p+\tau_{yy})}{\partial y}+\frac{\partial\tau_{zy}}{\partial z}+S_{M_y}\,,\\
\rho\frac{Dw}{Dt} &= \frac{\partial\tau_{xz}}{\partial x}+\frac{\partial\tau_{yz}}{\partial y}+\frac{\partial(-p+\tau_{zz})}{\partial z}+S_{M_z}\,,
\end{aligned}$$

where ρ is the density, p is the pressure, τ_{xx}, τ_{yy}, τ_{zz}, τ_{xy}, τ_{yx}, τ_{xz}, τ_{zx}, τ_{yz}, τ_{zy} are the viscous stress components, $S_{M_x}, S_{M_y}, S_{M_z}$ are the body forces, u, v and w are the x, y and z components of the velocity vector $\mathbf{u}$:

$$\mathbf{u}=\begin{bmatrix} u(x,y,z,t)\\ v(x,y,z,t)\\ w(x,y,z,t)\end{bmatrix}.$$

The viscous stress components form a viscous stress tensor $\boldsymbol{\tau}^V$:

$$\boldsymbol{\tau}^V = \begin{bmatrix} \tau_{xx} & \tau_{xy} & \tau_{xz} \\ \tau_{yx} & \tau_{yy} & \tau_{yz} \\ \tau_{zx} & \tau_{zy} & \tau_{zz} \end{bmatrix} . \tag{3.2.1}$$

All the variables are the functions of time and space. The substantive derivative $\frac{Df}{Dt}$ of a function $f(x, y, z, t)$ is defined as:

$$\frac{Df}{Dt} = \frac{\partial f}{\partial t} + \mathbf{u} \cdot \nabla f \,,$$

where ∇ is the gradient operator:

$$\nabla = \frac{\partial}{\partial x}\mathbf{i} + \frac{\partial}{\partial y}\mathbf{j} + \frac{\partial}{\partial z}\mathbf{k} \,,$$

where $\mathbf{i}$, $\mathbf{j}$, $\mathbf{k}$ denote the unit vectors in the the x, y, z directions, respectively.

In the present model the fluid obeys the Newton's law of viscosity according to which the viscous stresses are proportional to the rates of deformation [132]:

$$\begin{aligned} \tau_{xx} &= 2\mu\frac{\partial u}{\partial x} + \mu'\nabla \cdot \mathbf{u} \,, \\ \tau_{yy} &= 2\mu\frac{\partial v}{\partial y} + \mu'\nabla \cdot \mathbf{u} \,, \\ \tau_{zz} &= 2\mu\frac{\partial w}{\partial z} + \mu'\nabla \cdot \mathbf{u} \,, \end{aligned}$$

$$\begin{aligned} \tau_{xy} &= \tau_{yx} = \mu\left(\frac{\partial u}{\partial y} + \frac{\partial v}{\partial x}\right) , \\ \tau_{yz} &= \tau_{zy} = \mu\left(\frac{\partial v}{\partial z} + \frac{\partial w}{\partial y}\right) , \\ \tau_{zx} &= \tau_{xz} = \mu\left(\frac{\partial u}{\partial z} + \frac{\partial w}{\partial x}\right) , \end{aligned}$$

where μ stands for the shear (dynamic) viscosity, μ' is the second viscosity (also called *bulk viscosity* or *volumetric viscosity*) and $\nabla\cdot$ is the divergence operator:

$$\nabla\cdot = \frac{\partial}{\partial x} + \frac{\partial}{\partial y} + \frac{\partial}{\partial z} \,.$$

The viscosity is a measure of the fluid resistance to flow. As shown, the shear viscosity relates viscous stresses to linear deformations, while the bulk viscosity

relates viscous stresses to volumetric deformations. The bulk viscosity for a perfect gas is equal to [119]:

$$\mu' = -\frac{2}{3}\mu\,.$$

It is a common practice to use this relationship also for real fluids [119]. This approach is adopted also in the present model. The only body force in the model is the gravitational force acting in the z-direction:

$$\begin{aligned} S_{M_x} &= 0\,, \\ S_{M_y} &= 0\,, \\ S_{M_z} &= -\rho g\,. \end{aligned}$$

Taking all the above-mentioned assumptions, the momentum conservation equations can be recast as follows:

$$\begin{aligned} \rho\frac{Du}{Dt} &= -\frac{\partial p}{\partial x} + \frac{\partial}{\partial x}\left\{\mu\left[2\frac{\partial u}{\partial x} - \frac{2}{3}\nabla\cdot\mathbf{u}\right]\right\} + \frac{\partial}{\partial y}\left[\mu\left(\frac{\partial v}{\partial x} + \frac{\partial u}{\partial y}\right)\right] + \\ &\quad + \frac{\partial}{\partial z}\left[\mu\left(\frac{\partial w}{\partial x} + \frac{\partial u}{\partial z}\right)\right], \end{aligned} \tag{3.2.2}$$

$$\begin{aligned} \rho\frac{Dv}{Dt} &= -\frac{\partial p}{\partial y} + \frac{\partial}{\partial x}\left[\mu\left(\frac{\partial v}{\partial x} + \frac{\partial u}{\partial y}\right)\right] + \frac{\partial}{\partial y}\left\{\mu\left[2\frac{\partial v}{\partial y} - \frac{2}{3}\nabla\cdot\mathbf{u}\right]\right\} + \\ &\quad + \frac{\partial}{\partial z}\left[\mu\left(\frac{\partial w}{\partial y} + \frac{\partial v}{\partial z}\right)\right], \end{aligned} \tag{3.2.3}$$

$$\begin{aligned} \rho\frac{Dw}{Dt} &= -\frac{\partial p}{\partial z} + \frac{\partial}{\partial x}\left[\mu\left(\frac{\partial w}{\partial x} + \frac{\partial u}{\partial z}\right)\right] + \frac{\partial}{\partial y}\left[\mu\left(\frac{\partial w}{\partial y} + \frac{\partial v}{\partial z}\right)\right] + \\ &\quad + \frac{\partial}{\partial z}\left\{\mu\left[2\frac{\partial w}{\partial z} - \frac{2}{3}\nabla\cdot\mathbf{u}\right]\right\} - \rho g\,. \end{aligned} \tag{3.2.4}$$

The airflow obeys also the mass conservation [119]:

$$\frac{\partial \rho}{\partial t} + \nabla\cdot(\rho\mathbf{u}) = 0\,, \tag{3.2.5}$$

and the energy conservation [132]:

$$\frac{\partial(\rho i)}{\partial t} + \nabla\cdot(\rho i\mathbf{u}) = -p\nabla\cdot\mathbf{u} + \nabla\cdot(k\nabla T) + \phi\,, \tag{3.2.6}$$

where i is the internal (thermal) energy, T denotes the temperature and ϕ is the

viscous dissipation, i.e. the transformation of the kinetic energy to the internal energy, which in general is given by:

$$\begin{aligned}\phi &= \mu\left\{2\left[\left(\frac{\partial u}{\partial x}\right)^2+\left(\frac{\partial v}{\partial y}\right)^2+\left(\frac{\partial w}{\partial z}\right)^2\right]+\left(\frac{\partial u}{\partial y}+\frac{\partial v}{\partial x}\right)^2\right.\\ &\left.+\left(\frac{\partial u}{\partial z}+\frac{\partial w}{\partial x}\right)^2+\left(\frac{\partial v}{\partial z}+\frac{\partial w}{\partial y}\right)^2\right\}-\frac{2}{3}\mu(\nabla\cdot\mathbf{u})^2\,.\end{aligned}$$

The energy equation (Eq. 3.2.6) is derived from the first law of thermodynamics. The left hand side term stands for the rate of an increase of the energy of fluid particles. The right hand side term is the sum of the net rate of heat added to fluid particles and net rate of work done on fluid particles. However, in the case of gases, the viscous dissipation has an insignificant effect, so it is assumed that $\phi = 0$.

In the present model, the energy conservation is ensured by the implementation of the conservation of enthalpy (h) equation, which is equivalent to Eq. (3.2.6). Based on the relation $h = i - p\rho^{-1}$ [132], which is valid for the ideal gas, the enthalpy equation is formulated as follows:

$$\frac{\partial(\rho h)}{\partial t}+\nabla\cdot(\phi h)-\nabla\cdot\alpha\nabla h=\frac{\partial p}{\partial t}-\frac{\partial\rho K}{\partial t}-\nabla\cdot(\phi K)\,, \tag{3.2.7}$$

where ϕ is the mass flux, α is the thermal diffusivity and K is the kinetic energy of the fluid calculated as:

$$K=\frac{1}{2}\left(u^2+w^2+v^2\right)\,.$$

The air is assumed to behave like the ideal gas. Therefore, the following equations of state are used [132]:

$$p=\rho RT\,,$$

$$i=c_V T\,,$$

where R denotes the ideal gas constant, T describes the temperature and c_V is the constant volume specific heat.

3.2.1.2 Air thermophysical properties

A constant specific heat of air (at constant pressure) $c_p = 1005\,\mathrm{J/(kg\ K)}$ is assumed. The molecular weight of air is $n = 29.97$ g/mol. Since the ideal gas law is adopted, the specific heat at constant volume c_V is calculated as $c_V = c_p - nR$, where R is the universal gas constant ($R = 8.314462(75)\,\mathrm{J(mol\ K)^{-1}}$).

The transport properties are also taken to be constant: the dynamic viscosity

$\mu = 1.8208 \cdot 10^{-5}\,\mathrm{kg/(m\ s)}$ and the Prandtl number $Pr = 0.7$. The Prandtl number Pr is a dimensionless number which gives the ratio of the momentum diffusivity (kinematic viscosity) to the thermal diffusivity:

$$Pr = \frac{\nu}{\alpha} = \frac{c_p \mu}{\lambda}\,,$$

where ν is the kinematic viscosity given by:

$$\nu = \frac{\mu}{\rho}\,.$$

Other thermophysical properties are derived from the specific heat c_p, dynamic viscosity μ, Prandtl number Pr and enthalpy h. The enthalpy is calculated at each time step from the energy conservation equation, i.e. Eq. (3.2.7).

3.2.1.3 RANS equations and $k - \epsilon$ model

Indoor airflow is usually near a transitional range between the laminar and turbulent flow.

Laminar flows are characterized by a steady fluid motion. Streamlines are nearly parallel to each other and there are no mixing tendencies, eddies or swirls.

Turbulent flows characterize chaotic motions of molecules along complex irregular paths [19], even if boundary conditions are constant (Fig. 3.3). Turbulence fluctuations have always a three-dimensional character [132]. In turbulent flows there is always a great amount of rotational flows, called eddies. The eddies' dimensions are highly diverse. In other words, a wide range of length scales can be observed. In a typical engineering flow the smallest observed turbulence length scales can be as small as hundredths of a millimeter. In the smallest length scales, viscous forces are of the same order of magnitude as inertial forces (the Reynolds number equals 1). In these scales the flow kinetic energy is dissipated into the internal energy.

In addition to the wide length scale range, turbulent fluctuations appear also in a very wide range of frequencies, up to several kHz and higher (in high Reynolds numbers flow). In general, length scales and frequencies depend on the flow type and problem dimensions.

The Navier-Stokes equations model both laminar and turbulent flow properly [128]. However, modeling turbulence using the complete time-dependent Navier-Stokes equations requires a huge computational power. Both space and time discretizations are to be fine enough to resolve all rapid oscillations and chaotic motions at all scales. This approach to solve the Navier-Stokes equations is called *Direct Numerical Simulation* (DNS). DNS is at the present time too computationally de-

manding for routine engineering applications, although there are first attempts to use it in some real applications [111]. DNS is however an important tool helping to understand turbulent structures and the transition between turbulent and laminar flows [19].

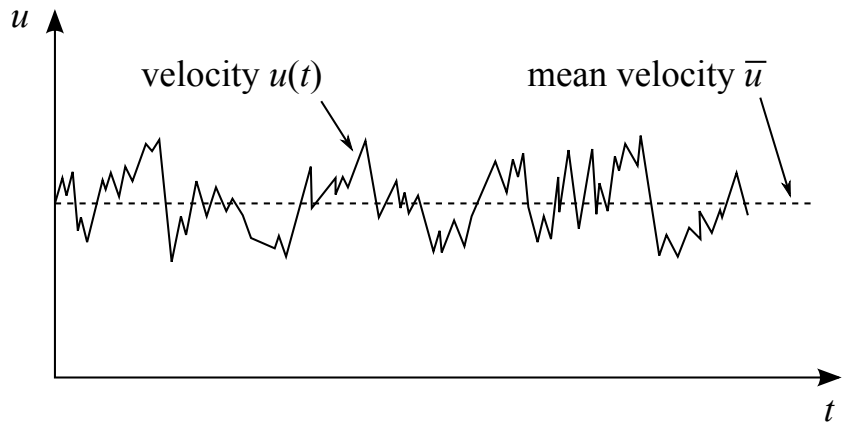

Figure 3.3: Typical velocity fluctuations in steady turbulent flow (based on Versteeg and Malalasekera [132])

To enable analyses of engineering flows, some less demanding calculation procedures are needed. Usually, an averaged solution of a flow is satisfactory. The two major modeling frameworks aimed at different levels of approximation are the LES approach (*Large Eddy Simulation*) and RANS approach (*Reynolds-averaged Navier-Stokes*).

The LES approach is the first level of approximation, where the turbulent large eddies are resolved accurately, but the small-scale eddies are modeled [19] (by a turbulence model). Thanks to the subgrid-scale turbulence modeling, LES requires significantly less mesh points than in the case of DNS. The computational power requirements of LES are somewhere between DNS and RANS. LES is usually applied when a detailed solution of an engineering flow is needed, i.e. when the solution provided by the RANS modeling is too general. In recent years, LES has been successfully used in some building airflow simulations [79].

The RANS approach, which introduces the next level of approximation, is probably the most widely used CFD modeling approach. This approach is adopted in the present work. It is based on the concept of a flow variables decomposition. The velocity $\mathbf{u}(x, y, z, t)$ and pressure $p(x, y, z, t)$ are decomposed into the mean and fluctuating parts:

$$\begin{aligned} \mathbf{u}(x, y, z, t) &= \overline{\mathbf{u}}(x, y, z, t) + \mathbf{u}'(x, y, z, t)\,, \\ p(x, y, z, t) &= \overline{p}(x, y, z, t) + p'(x, y, z, t)\,, \end{aligned}$$

where $\overline{\mathbf{u}}$, $\overline{p}$ are the mean velocity and pressure, and $\mathbf{u}'$, p' are the fluctuating velocity and pressure, respectively. Both the mean and fluctuating components are functions of time and space. Since the problem is time-dependent, the mean values are defined using the so-called ensemble averages [132, 19], i.e.:

$$\overline{\mathbf{u}}(x,y,z,t) = \lim_{N\to\infty} \frac{1}{N} \sum_{m=1}^{N} \mathbf{u}(x,y,z,t)\,,$$

$$\overline{p}(x,y,z,t) = \lim_{N\to\infty} \frac{1}{N} \sum_{m=1}^{N} p(x,y,z,t)\,,$$

where N is the number of identical experiments with the same initial and boundary conditions [30]. Due to the ensemble averaging, the average properties are still functions of time. They can be regarded as mean functions obtained from a large number (N) of identical experiments. It is assumed that at each point in space the time average of each fluctuation remains zero for an arbitrary time period large enough comparing to the time-scale of the turbulent fluctuations [132]:

$$\overline{\mathbf{u}'}(x,y,z,t) = \frac{1}{\Delta t}\int_0^{\Delta t} \mathbf{u}'(x,y,z,t)dt \equiv 0\,,$$

$$\overline{p'}(x,y,z,t) = \frac{1}{\Delta t}\int_0^{\Delta t} p'(x,y,z,t)dt \equiv 0\,.$$

By expressing the variables into the sum of the mean and fluctuating parts, the standard Navier-Stokes equations are transformed into the so-called Reynolds-averaged Navier-Stokes (RANS) equations. These equations have the same form as the standard time-dependent Navier-Stokes equations (Eqs. (3.2.2-4)) with the only difference of the existence of new additional stresses, called *Reynolds stresse*s. The Reynolds stress tensor τ^R for a three-dimensional flow is as follows [19]:

$$\boldsymbol{\tau}^R = \begin{bmatrix} \rho\overline{(u')^2} & \rho\overline{u'v'} & \rho\overline{u'w'} \\ \rho\overline{v'u'} & \rho\overline{(v')^2} & \rho\overline{v'w'} \\ \rho\overline{w'u'} & \rho\overline{w'v'} & \rho\overline{(w')^2} \end{bmatrix}.$$

The Reynolds stress tensor contains six independent unknown variables: $\overline{(u')^2}$, $\overline{(v')^2}$, $\overline{(w')^2}$, $\overline{u'v'}$, $\overline{u'w'}$, $\overline{v'w'}$. In the RANS equations, the Reynolds stress components are subtracted from their counterparts from the viscous stress tensor $\boldsymbol{\tau}^V$ (Eq. 3.2.1). The resulting complete stress tensor $\boldsymbol{\tau} = \boldsymbol{\tau}^V - \boldsymbol{\tau}^R$ is not resolved directly [89]. Instead, this is the aim of a turbulence model to close the RANS equations by introducing the influence of these unknowns on the flow. Thus, in the RANS modeling,

the detailed information on turbulent structures is not available. The resulting flow is the mean flow and only the effect of the turbulence on the mean flow is known, but not the turbulence itself.

The turbulence influence on a flow can be evaluated using the Boussinesq hypothesis (from 1877) [20, 115] according to which the turbulent shear stress is related linearly to the mean rate of strain. The proportionality factor is the so-called the *turbulent viscosity* μ_T (or *eddy viscosity*). Using a suffix notation, the extended Boussinesq's relationship for the Reynolds-stress components $\boldsymbol{\tau}_{ij}^R$ can be written as:

$$\boldsymbol{\tau}_{ij}^R = 2\mu_T \overline{\boldsymbol{S}}_{ij} - \frac{2}{3}\rho k \delta_{ij} \,, \tag{3.2.8}$$

where k is the turbulent kinetic energy per unit mass, δ_{ij} is the Kronecker symbol and $\overline{\boldsymbol{S}}_{ij}$ are the components of the Reynolds-averaged strain rate tensor $\overline{\boldsymbol{S}}$:

$$\overline{\boldsymbol{S}} = \begin{bmatrix} \frac{\partial \overline{u}}{\partial x} & \frac{1}{2}\left(\frac{\partial \overline{v}}{\partial x} + \frac{\partial \overline{u}}{\partial y}\right) & \frac{1}{2}\left(\frac{\partial \overline{w}}{\partial x} + \frac{\partial \overline{u}}{\partial z}\right) \\ \frac{1}{2}\left(\frac{\partial \overline{u}}{\partial y} + \frac{\partial \overline{v}}{\partial x}\right) & \frac{\partial \overline{v}}{\partial y} & \frac{1}{2}\left(\frac{\partial \overline{w}}{\partial y} + \frac{\partial \overline{v}}{\partial z}\right) \\ \frac{1}{2}\left(\frac{\partial \overline{u}}{\partial z} + \frac{\partial \overline{w}}{\partial x}\right) & \frac{1}{2}\left(\frac{\partial \overline{v}}{\partial z} + \frac{\partial \overline{w}}{\partial y}\right) & \frac{\partial \overline{w}}{\partial z} \end{bmatrix} .$$

The turbulent kinetic energy per unit mass is represented by:

$$k = \frac{1}{2}(\overline{u'^2} + \overline{v'^2} + \overline{w'^2}) \,.$$

The relationship given in Eq. (3.2.8) is written for incompressible flows, i.e. flows with a constant density of a fluid. However, according to the Morkovin's hypothesis [95, 19], if density fluctuations in turbulent flow are not significant, their influence on turbulent structures is negligible. This is usually true for flows characterized by Mach numbers below 5. Similarly, Bradshaw et al. [21] state that density fluctuations are insignificant to Mach numbers up to 3–5 if root mean square velocity fluctuations are not higher than about 5% of the mean velocity. If velocity fluctuations will reach about 20% of the mean value, density fluctuations are unimportant up to Mach numbers around 1 [132]. Hence, Eq. (3.2.8) is certainly valid within the range of conditions expected in the simulations to be performed (maximum expected air velocity is about 1–2 m/s only). The discussion concerning the validity of the Boussinesq hypothesis is presented by Schmitt [115]. Although the hypothesis is not valid in most of the complex flows, it is still widely used. The hypothesis is the core of many turbulent viscosity models.

The eddy-viscosity turbulence models intend to calculate μ_T. In the present work the well-known $k - \epsilon$ model is applied. The chosen model is based on the standard $k - \epsilon$ model [85], which is one of the most widely used turbulence models.

It is accurate in a relatively broad range of conditions. The model is used by many researchers studying indoor airflow [136, 110]. The $k-\epsilon$ model takes advantage of two equations for the turbulent kinetic energy k and its dissipation rate ϵ [89]:

$$\frac{\partial(\rho k)}{\partial t}+\frac{\partial(\rho \mathbf{u}_j k)}{\partial \mathbf{x}_j} = \frac{\partial}{\partial \mathbf{x}_j}\left[\left(\mu+\frac{\mu_T}{\sigma_k}\right)\frac{\partial k}{\partial \mathbf{x}_j}\right]+P-\rho\epsilon\,, \tag{3.2.9}$$

$$\begin{aligned}\frac{\partial(\rho \epsilon)}{\partial t}+\frac{\partial(\rho \mathbf{u}_j \epsilon)}{\partial \mathbf{x}_j} &= \frac{\partial}{\partial \mathbf{x}_j}\left[\left(\mu+\frac{\mu_T}{\sigma_\epsilon}\right)\frac{\partial \epsilon}{\partial \mathbf{x}_j}\right]+\frac{\epsilon}{k}(C_{\epsilon 1}G-C_{\epsilon 2}\rho\epsilon)- \\ &\quad -\left(\frac{2}{3}C_{\epsilon 1}+C_{\epsilon 3}\right)\rho\epsilon\frac{\partial \mathbf{u}_j}{\partial \mathbf{x}_j}\,,\end{aligned} \tag{3.2.10}$$

where P is the production rate of the kinetic energy per unit volume due to velocity field gradients:

$$P=\tau_{ij}\frac{\partial \mathbf{u}_i}{\partial \mathbf{x}_j}\,.$$

Since the components τ_{ij} of the stress tensor τ are not known, P is evaluated using the following formula:

$$P=G-\frac{2}{3}\rho k\frac{\partial \mathbf{u}_k}{\partial \mathbf{x}_k}\,, \tag{3.2.11}$$

where G is

$$G=2\mu_T\left[S_{ij}S_{ij}-\frac{1}{3}\left(\frac{\partial \mathbf{u}_k}{\partial \mathbf{x}_k}\right)^2\right]\,, \tag{3.2.12}$$

The model constants are tuned using experimental data concerning free turbulent flows [85]. The constants are:

$$\begin{aligned}C_\mu &= 0.09,\ C_{\epsilon 1}=1.44,\ C_{\epsilon 2}=1.92,\ C_{\epsilon 3}=-0.33,\\ \sigma_k &= 1.00,\ \sigma_\epsilon=1.30.\end{aligned}$$

The constant $C_{\epsilon 3}$ is not present in the standard model. It is used to make the prediction more accurate for compressible turbulent flows [89]. Despite this minor addition to the model, it will be still referred in the text as the "standard" $k-\epsilon$ model. Using the solution of k and ϵ equations the turbulence viscosity μ_T is calculated by means of:

$$\mu_T=C_\mu\rho\frac{k^2}{\epsilon}\,.$$

Finally, to take turbulent effects into account in the momentum transport, the dynamic viscosity μ in Eq. (3.2.2-4) is substituted with the so-called *effective viscosity* μ_{eff}:

$$\mu_{eff}=\mu+\mu_T\,.$$

In the present model the turbulent heat transport is modeled analogically to the

turbulent momentum transport, since it is affected by the same mechanism of eddy mixing. In order to account to the turbulent effect in heat transport a turbulent diffusivity α_T is added to the molecular (laminar) thermal diffusivity α giving the so-called *effective thermal diffusivity*:

$$\alpha_{eff} = \alpha + \alpha_T \,. \tag{3.2.13}$$

The turbulent diffusivity is calculated from the turbulent Prandtl number Pr_T and turbulent viscosity μ_T:

$$\alpha_T = \frac{\mu_T}{Pr_T} \,.$$

The turbulent Prandtl number Pr_T for air is 0.9 [19]. It is assumed that Pr_T is constant in the entire flow field. Similarly, the fluid effective thermal conductivity is denoted as λ_{eff}:

$$\lambda_{eff} = c_p \left(\frac{\mu}{Pr} + \frac{\mu_T}{Pr_T} \right) ,$$

where Pr is the Prandtl number. The $k-\epsilon$ model, as most of turbulent viscosity models, enables to use relatively coarse grids and large time steps in numerical simulations (compared to LES and DNS).

3.2.2 Initial and boundary conditions

The boundary and initial conditions are prescribed for the following variables: temperature $T(\mathbf{x},t)$, pressure $p(\mathbf{x},t)$, velocity $\mathbf{u}(\mathbf{x},t)$, turbulent viscosity $\mu_T(\mathbf{x},t)$, turbulent diffusivity $\alpha_T(\mathbf{x},t)$, turbulent kinetic energy $k(\mathbf{x},t)$, dissipation rate $\epsilon(\mathbf{x},t)$. Each variable is a function of the position $\mathbf{x} = [x,y,z]^T$ and time t.

The initial conditions ($t = 0$) are identical in all simulations:

- $T(\mathbf{x},0) = 293.15$ [K],
- $p(\mathbf{x},0) = 10^5$ [Pa],
- $\mathbf{u}(\mathbf{x},0) = 0$ [m/s],
- $\mu_T(\mathbf{x},0) = 0$ [Pa·s],
- $\alpha_T(\mathbf{x},0) = 0$ [m^2/s],
- $k(\mathbf{x},0) = 0.1$ [m^2/s^2],
- $\epsilon(\mathbf{x},0) = 0.1$ [m^2/s^3].

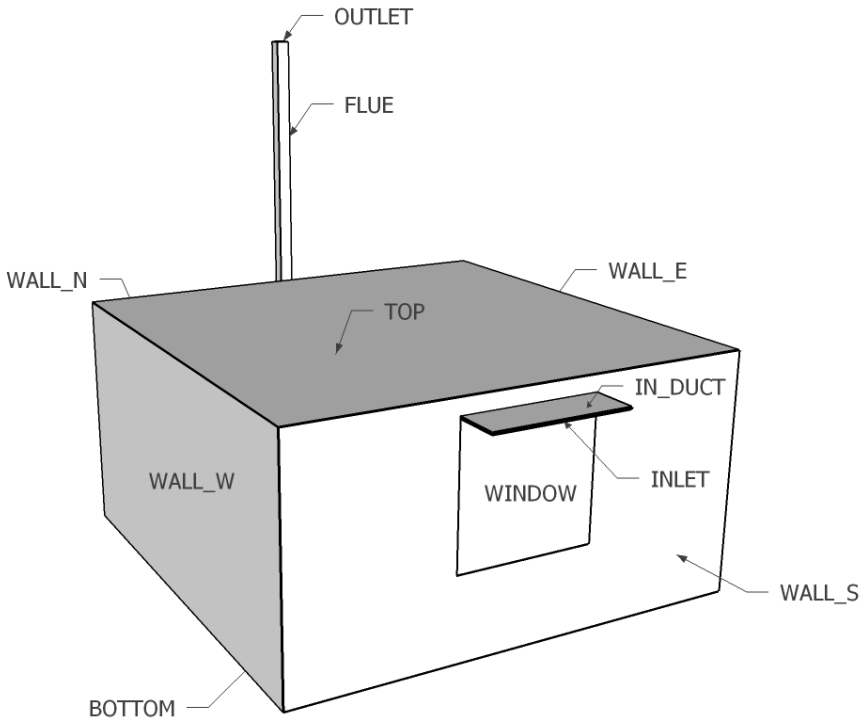

Figure 3.4: Air model boundary surfaces

It is assumed, that at the beginning of each simulation the air temperature is uniform and equal to $20\,°C$, the air is stagnant and the pressure is of the order of the atmospheric pressure. Since at the beginning nothing is known about the turbulence, the initial values of μ_T, α_T, k and ϵ are chosen arbitrary, based on the values used in the OpenFOAM's standard tutorial cases [102]. It was checked however, that these values have no visible influence on the later results under the given conditions.

During simulations, the solution at each time step is calculated using the results from the previous step and boundary conditions. The boundary values for the temperature $T(\mathbf{x}, t)$, pressure $p(\mathbf{x}, t)$ and velocity $\mathbf{u}(\mathbf{x}, t)$ are given in Table 3.1. The boundary conditions are prescribed for all boundary surfaces. The boundary surfaces are grouped into 10 categories: INLET, OUTLET, IN_DUCT, WALL_S, WINDOW, WALL_N, WALL_E, WALL_W, TOP, BOTTOM. The surfaces are shown in Fig. 3.4.

The air flows in to the room across the INLET surface and flows out at the OUTLET surface. At the inlet the velocity is constant and the pressure gradient is zero (the derivative along the vector normal to the surface equals zero). At the outlet the pressure is constant and the velocity gradient is zero. At the remaining surfaces, a "no-slip impermeable wall" condition [100] is assumed: the velocity and the pressure gradient along normal to the surface are zero.

Table 3.1: Boundary conditions

3.1-1	Boundary surface S		
Variable	INLET	OUTLET	IN_DUCT
$T(\mathbf{x},t)$	$\frac{\partial T(\mathbf{x},t)}{\partial \mathbf{n}}\Big\vert_S = 0$	$\frac{\partial T(\mathbf{x},t)}{\partial \mathbf{n}}\Big\vert_S = 0$	$T(\mathbf{x},t)\vert_S = T_{inlet}(t)$
$p(\mathbf{x},t)$	$\frac{\partial p(\mathbf{x},t)}{\partial \mathbf{n}}\Big\vert_S = 0$	$p(\mathbf{x},t)\vert_S = p_{outlet}$	$\frac{\partial p(\mathbf{x},t)}{\partial \mathbf{n}}\Big\vert_S = 0$
$\mathbf{u}(\mathbf{x},t)$	$\mathbf{n}\cdot\mathbf{u}(\mathbf{x},t)\vert_S = u_{inlet}$	$\frac{\partial \mathbf{u}(\mathbf{x},t)}{\partial \mathbf{n}}\Big\vert_S = 0$	$\mathbf{u}(\mathbf{x},t) = 0$

3.1-2	Boundary surface S		
Variable	WALL_S	WINDOW	other
$T(\mathbf{x},t)$	$T(\mathbf{x},t)\vert_S = T_{w1}(t)$	$T(\mathbf{x},t)\vert_S = T_{w2}(t)$	$\frac{\partial T(\mathbf{x},t)}{\partial \mathbf{n}}\Big\vert_S = 0$
$p(\mathbf{x},t)$	$\frac{\partial p(\mathbf{x},t)}{\partial \mathbf{n}}\Big\vert_S = 0$	$\frac{\partial p(\mathbf{x},t)}{\partial \mathbf{n}}\Big\vert_S = 0$	$\frac{\partial p(\mathbf{x},t)}{\partial \mathbf{n}}\Big\vert_S = 0$
$\mathbf{u}(\mathbf{x},t)$	$\mathbf{u}(\mathbf{x},t) = 0$	$\mathbf{u}(\mathbf{x},t) = 0$	$\mathbf{u}(\mathbf{x},t) = 0$

$\mathbf{n}$ – vector normal to surface S
$T_{sol}(t)$ – sol-air temperature
$T_{w1}(t)$ – temperature of wall's internal surface (from the wall model)
$T_{w2}(t)$ – temperature of window's internal surface (from the wall model)

It is assumed that the room has only one external wall — the south wall. Hence, WALL_S and WINDOW are the only external partitions in the model, i.e. they separate the indoor environment from the outdoor environment. These partitions are modeled using the external wall submodel, described in Section 3.3. The temperatures $T_{w1}(t)$ and $T_{w2}(t)$ of the internal surfaces of the partitions (WALL_S and WINDOW), obtained from the heat transfer simulation at the external wall, are the boundary conditions to the indoor air submodel (Dirichlet boundary condition). The temperatures $T_{w1}(t)$ and $T_{w2}(t)$ are uniform over the related surface. The uniform surface temperatures is an approximation which significantly simplifies and speeds up the air-wall co-simulation, as discussed in Section 3.4. The co-simulation procedure (data exchange) is also discussed in Section 3.4.

At the INLET and OUTLET surfaces, the temperature gradients are set to zero. The INLET's temperature is not explicitly assigned due to convergence problems encountered in the preliminary tests. However, the inlet air temperature is still kept at a desired level thanks to the controlled temperature of the IN_DUCT surface (Dirichlet boundary condition). The outdoor air flowing through the duct above the window quickly heats up or cools down according to the temperature of the IN_DUCT surface, denoted as $T_{inlet}(t)$. The temperature $T_{inlet}(t)$ of the surface depends on the simulation type. In some simulations it is equal to the ambient dry

bulb temperature obtained from the climatic database for the city of Elbląg [29]. On the other hand, in some tests $T_{inlet}(t)$ is kept constant. The all considered cases are presented in Section 5.2.

The adiabatic conditions are prescribed on other boundary surfaces. In other words, no heat transfer across these surfaces is allowed. These surfaces represent internal partitions (walls and floors). The flow and turbulence-related variables (μ_T, α_T, k and ϵ) in the near-wall regions are resolved using the wall function approach. The adopted approach is discussed separately in the next section (Section 3.2.2.1).

At the inlet boundaries, the turbulent kinetic energy k and the dissipation rate ϵ should be provided. However, such data are not available. One of the approaches is to estimate these values based on the expected turbulence intensity [132]. In the present model, however, a zero-gradient condition is applied for both k and ϵ:

$$\left.\frac{\partial k}{\partial \mathbf{n}}\right|_{S_{INLET}} = 0\,,$$
$$\left.\frac{\partial \epsilon}{\partial \mathbf{n}}\right|_{S_{INLET}} = 0\,.$$

In addition, test simulations were conducted in which some exemplary magnitudes of k and ϵ were set. The simulations showed no significant influence of these boundary conditions on the airflow pattern. On the one hand it is due to the presence of the 0.5 m long inlet duct which stabilizes the flow, and on the other hand due to the calm flow conditions (low velocities), in which turbulence does not play a major role.

3.2.2.1 Near-wall treatment: wall function

Turbulent flows are significantly influenced by the presence of walls [2]. The wall presence enforces the vortices to roll in a certain direction. Additionally, in the closest vicinity of the wall, large pressure and velocity gradients occur. Experimental data show that the near-wall flow region consists of three layers: viscous sublayer, buffer layer and fully-turbulent layer.

The first layer to the wall is the viscous sublayer. In this layer, flow is dominated by viscous forces and the mean velocity depends linearly on a distance from the wall. The viscous sublayer ends at the distance of about $y^+ \approx 5$, where y^+ is a non-dimensional distance from the wall given by:

$$y^+ = \frac{y u_\tau}{\nu}\,,$$

where u_τ is the shear (or friction) velocity [m/s] and ν is the kinematic viscosity

[m^2/s]. At $y^+ \approx 30$ the fully-turbulent layer begins. The layer is often called as the log-law layer, because the mean velocity within the layer can be well approximated by a logarithmic profile [2]. This is called the *log law of the wall*. The viscous sublayer and the log-law layer are separated by the buffer layer ($5 < y^+ < 30$). In the buffer layer the velocity can be approximated neither by a linear relation nor a logarithmic profile.

The phenomena in the near-wall region are not well modeled by the approach used to model bulk flow, i.e. flow "far" from a wall. There are two main approaches to simulate near-wall flow: the integration approach and the wall functions.

In the integration method, a large number of computational cells are used to resolve boundary layers. The method requires the grid cell nearest to the wall to to be located within the viscous sublayer, at about $y^+ = 1$ [82]. A fine grid is needed because strong gradients of flow and turbulence variables are present in the near-wall region, especially in the viscous layer.

On the other hand, the wall functions remove from the computational domain the regions where the sharpest gradients are present. Instead, empirical formulae are used to model the flow in the vicinity of the wall. The formula is based on the log law of the wall. The method enables to use relatively coarse meshes and large time steps [93]. The wall function approach is adopted in the present model.

Due to the presence of the wall function the turbulent variables k, ϵ and μ_T are calculated differently in cells adjacent to the walls. To distinguish the calculation procedure for cells adjacent to the wall, all values calculated for those cells are denoted in the following with a subscript C.

The turbulent viscosity at the cell centroid C is calculated as follows [89]:

$$(\mu_T)_C = \mu_C \begin{cases} 0 & , y_C^+ \leq y_{lam}^+ \\ \frac{y_C^+ \kappa}{\ln(E y_C^+)} - 1 & , y_C^+ > y_{lam}^+ \end{cases},$$

where κ is the Von Kármán constant ($\kappa = 0.41$), E is a non-dimensional constant ($E = 9.8$) and y_{lam}^+ is the non-dimensional thickness of the viscous sublayer, calculated using an iterative formula:

$$y_{lam}^+ = \frac{\ln(E y_{lam}^+)}{\kappa},$$

resulting approximately in $y_{lam}^+ \approx 11.53$. The non-dimensional wall distance y_C^+ for

the cell centroid C is calculated as follows:

$$y_C^+ = \frac{C_\mu^{1/4} \rho_C y_C \sqrt{k_C}}{\mu_C} , \tag{3.2.14}$$

where C_μ is the empirical constant in $k - \epsilon$ model ($C_\mu = 0.09$).

As shown, the buffer layer is not modeled. The viscous sublayer is assumed up to $y^+ = 11.53$. From this point, the turbulent layer is assumed. It is due to the fact, that neither law holds in the buffer layer (neither linear nor logarithmic).

The turbulent energy dissipation rate ϵ_C in the wall-adjacent cells is solved from the following algebraic expression:

$$\epsilon_C = \frac{u_\tau^3}{\kappa y_C} .$$

The shear velocity $u_\tau$which is defined as a square root of the wall shear stress τ_w divided by the fluid density ρ:

$$u_\tau = \sqrt{\frac{\tau_w}{\rho}} ,$$

but due to the assumption of a local turbulence equilibrium (which is a main assumption of the $k - \epsilon$ model) can be calculated as [89]:

$$u_\tau = C_\mu^{1/4} \sqrt{k_C} .$$

Hence, the dissipation rate is finally calculated from:

$$\epsilon_P = \frac{C_\mu^{3/4} k_C^{3/2}}{\kappa y_C} .$$

The turbulent kinetic energy k_C in the wall-adjacent cells is calculated using the standard equation (Eq. (3.2.9)), but using different G and P components. The new G component is:

$$G = G_C = \begin{cases} 0 & , y_C^+ \leq y_{lam}^+ \\ \frac{C_\mu^{1/4} \sqrt{k_C}}{\kappa y_C} \left[(\mu_T)_C + \mu_C \right] \frac{|U_C|}{y_C} & , y_C^+ > y_{lam}^+ \end{cases} ,$$

where U_C is the velocity component tangent to the wall surface. Bearing in mind that the P component is the production rate of kinetic energy, and there is an assumption of a local turbulence equilibrium in the $k - \epsilon$ model, the production rate

of kinetic energy must equal to its dissipation rate:

$$P = P_C = \epsilon \,.$$

Since the k-equation is solved, an appropriate boundary condition must be prescribed. A typical boundary condition for k is assumed [46], i.e. a zero-gradient condition:

$$\frac{\partial k}{\partial \mathbf{n}} = 0 \,,$$

where $\mathbf{n}$ is the vector normal to the wall surface.

The interesting characteristics of models which use wall functions is that near-wall grids have to be coarse enough to give accurate results. Fine grids are usually not suitable. Typically, a desired grid resolution when the wall function is applied is $y^+ \approx 30$ [114]. The grid cannot be also too coarse. Improper near-wall grid results in an inaccurate estimation of near-wall effects, such as convective heat transfer coefficients [12].

The wall functions are especially accurate in the case of high Reynolds (high-Re) numbers flows. The function adopted in the present model was validated against some range of "classic" high-Re flows [85]. In the present work both the model geometry and air velocities are non-standard for the $k - \epsilon$ model. Hence, a special care was taken to make sure, that the function provides reasonable results.

The convective heat transfer coefficient is the only near-wall effect important from the point of view of the present work. In CFD the convective heat transfer coefficient h_c is calculated using the formula [145]:

$$h_c = \frac{c_p}{D} \left(\frac{\mu}{Pr} + \frac{\mu_T}{Pr_T} \right) , \tag{3.2.15}$$

where c_p is the specific heat of air, D is the distance of the cell centroid to the wall, μ and μ_T are the dynamic and turbulent viscosities, Pr and Pr_T are the Prandtl number and turbulent Prandtl number, respectively. In CFD, the convective heat transfer coefficient calculated using Eq. (3.2.15) varies both in time and space. The variations are due to oscillations in the turbulent viscosity.

However, in the developed model, the one-dimensional heat transfer between the air and south wall (and window) is assumed. Thus, the convective heat transfer coefficient values provided by the CFD calculations are averaged over the considered surface. The averaging is performed separately for the wall and window surfaces.

The preliminary tests carried out by the author confirmed that the near-wall mesh resolution has a strong influence on the convective heat transfer coefficient.

Thus a near-wall mesh validation was performed. The validation was conducted from natural and forced convection points of view. A mesh resolution guaranteeing the convective heat transfer coefficient close to experimental data in both convective heat transfer regimes (natural and forced) was adopted. The experimental data were provided by Fohanno and Polidori [48] and Jayamaha et al. [78]. The near-wall mesh validation procedure is presented in Section 4.2.

3.2.3 Numerical approach

The governing equations (Eqs. (3.2.2-4), (3.2.5), (3.2.7), (3.2.9), (3.2.10)) are solved using the Finite Volume Method (FVM). The method is thoroughly explained in Patankar [106], Versteeg and Malalasekera [132] and Blazek [19].

In FVM, the continuous computational space is discretized into a set of finite (or control) volumes. Arbitrary polyhedral shapes of finite volumes are allowed.

The method directly uses the conservation laws. All equations are integrated over all finite volumes. The volume integrals containing a divergence term are converted to surface integrals, based on the *divergence theorem* (Gauss–Ostrogradsky theorem) according to which:

$$\iiint_V (\nabla \cdot \mathbf{F}) dV = \oiint_S (\mathbf{F} \cdot \mathbf{n}) dS \,,$$

where $\mathbf{F}$ is the continuously differentiable vector field, V is the considered volume, S is the volume boundary surface and $\mathbf{n}$ is the unit vector field pointing outward the surface S.

Subsequently, the integrated equations are substituted with finite difference approximations representing changes of properties due to diffusion, convection and internal sources. The convection terms are linearized. Each surface integral is approximated by summing the fluxes crossing boundary surfaces (faces) of each volume. All the discretized equations together create a system of algebraic equations. A detailed discussion about the discretization of equations is presented by Jasak [77].

The main issue in the the obtained system of equations is a linear dependence of the velocity on pressure and vice-versa [77]. Although there exist algorithms for solving the fully-coupled set of equations, their computational demand is high. The alternative approach is to use a less computationally expensive segregated algorithm to deal with the inter-equation coupling, as it is done in this work.

The airflow model is based on the *buoyantPimpleFoam* solver from the OpenFOAM toolkit [116], which is discussed in Section 3.6. The solver uses the PIMPLE algorithm for the pressure-velocity coupling [102], which is a mix of the SIMPLE al-

gorithm (Semi-Implicit Method for Pressure-Linked Equations [106]) and the PISO algorithm (Pressure-Implicit Split-Operator [76]).

The PIMPLE algorithm is aimed at solving the transient Navier-Stokes equations. The algorithm implementation in the current model consists of the following steps [77, 101, 102]:

1. Prescribe the boundary conditions.
2. Solve the continuity equation using mass fluxes from the last time step (density predictor).
3. Solve the momentum equation to estimate the velocity field (momentum predictor).
4. Solve the enthalpy equation and update the thermophysical properties.
5. Compute the mass fluxes at the cell faces.
6. Solve the pressure equation.
7. Correct the mass fluxes at the cell faces.
8. Correct the velocity field based on the new pressure field.
9. Update the boundary conditions.
10. Solve the continuity equation again using the new mass fluxes.
11. Repeat steps 5–10 for a prescribed number of times (PISO corrector loop).
12. Repeat from step 3 for a prescribed number of times and apply the under-relaxation (pressure–velocity PIMPLE corrector loop).
13. Solve the transport equations for k and ϵ.
14. If the end time is not reached, go to the next time step. Repeat the steps from the step 1.

In this work, all calculations are conducted using 2 PISO corrector loops (inner loops) and 1 PIMPLE corrector loop (outer loop). Since no additional PIMPLE loops are used, the implemented procedure is actually identical with the PISO algorithm. The potential additional PIMPLE loops allow for larger time steps and improving the solution stability. The under-relaxation is applied between the subsequent PIMPLE corrector loops. Due to the fact that only one PIMPLE corrector

loop is used, the under-relaxation is not applied. In the present work, the solution stability is ensured by using sufficiently small time steps. A limit for the maximum Courant number is applied. The Courant number cannot exceed the value of 1 in any of cells:

$$Co = \frac{u\Delta t}{\Delta x} < 1\,, \tag{3.2.16}$$

where u is the fluid velocity [m/s] at the given cell, Δt is the time step [s] and Δx is the cell dimension [m].

Due to the non-orthogonality, the algorithm allows a correction by repeating the steps 6 and 7. However, the developed mesh is close-to-orthogonal, so the correction is not needed in this case.

3.3 External wall submodel

The external wall model is responsible for the simulation of the heat transfer through the building envelope. The entire wall model was developed and implemented by the author. The term "wall" is used here, although any kind of solid partitions can be modeled, not only wall partitions. Moreover, an arbitrary number of the independent solid partitions can be modeled, as well. The partitions are independent from each other, because the one-dimensional heat transfer (in the indoor–outdoor direction) is assumed. The partition can have a multilayer structure.

Technically, each solid partition in the model is implemented as a new *instance* of the wall model C++ *class*. Thus, by the analogy with the C++ nomenclature, each solid partition will be here termed as an instance of the wall model.

In the present study, the heat transfer across the south elevation is solely considered, i.e. only two wall model instances are present: the south external wall and south window. The window is treated as a solid single-layer partition of which thermal properties are approximated based on the real properties of an exemplary double-glazed window.

The heat transfer across all the other partitions is not considered. Instead, the respective internal surfaces of these partitions are assumed to be adiabatic, i.e. zero heat flux across those surface is assumed. This adiabatic condition is prescribed within the indoor air model, as described in Section 3.2.2.

The wall model runs in a co-simulation with the indoor air model. The results from internal surfaces of modeled solid partitions are treated as boundary conditions in the indoor air model. Analogically, appropriate results from the indoor air model define boundary conditions in models of solid partitions. The co-simulation procedure is explained in Section 3.4.

3.3.1 Mathematical formulation

The external wall model is based on a one-dimensional heat conduction equation [124]:

$$\frac{\partial T(x,t)}{\partial t} = \alpha \frac{\partial^2 T(x,t)}{\partial x^2}\,, \tag{3.3.1}$$

where $T(x,t)$ is the temperature [°C], t is time [s], x is the linear dimension [m] and α is thermal diffusivity [m^2/s] given by:

$$\alpha = \frac{\lambda}{\rho c_p}\,,$$

where λ is the material thermal conductivity [W/(m K)], ρ is the density [kg/m^3] and c_p is the specific heat [J/(kg K)].

The materials parameters are constant and prescribed by the user. The full list of parameters for all investigated cases is presented in Section 5.1.

3.3.2 Initial and boundary conditions

The initial condition is the steady state temperature profile obtained by solving the one-dimensional steady state heat equation:

$$\frac{d^2 T}{dx^2} = 0\,.$$

At the internal surface S_{int} (indoor-side), the Neumann boundary condition (*BC type II*) is applied:

$$\lambda \frac{dT}{dx}\bigg|_{S_{int}} = q_{int}(t)\,,$$

where $q_{int}(t)$ is the known heat flux function. The subsequent values of q_{int} are supplied by the air model. At the external surface S_{ext}, the Robin boundary condition (*BC type III*) is applied:

$$\lambda \frac{dT}{dx}\bigg|_{S_{ext}} = h_{se}(T_{amb} - T_{se})\,,$$

where h_{se} is the convective heat transfer coefficient at the external wall surface [W/(m^2K)], T_{se} is the temperature of the external surface [°C] and T_{amb} is the ambient temperature [°C].

The convective heat transfer coefficient h_{se} at the external surface is not constant, but calculated using the empirical formula provided by Jayamaha [78]. The formula

is valid for the heat transfer due to the forced convection. Jayamaha [78] found that the convective heat transfer coefficient is linearly dependent on the wind speed v_{wind} [m/s]:

$$h_{se}(t) = h_{Jayamaha} = 4.955 + 1.444 \cdot v_{wind}(t)\,.$$

Jayamaha states that the wind direction is not relevant in the case of large walls.

In some simulation cases, the ambient temperature T_{amb} is kept constant at a desired level, while in other it is equal to the sol-air temperature T_{sol}. The sol-air temperature is a fictitious outdoor temperature which is often used to include the effects of the solar radiation. The calculated temperature gives the same heat flux at the external wall surface as the heat flux caused by both the outdoor temperature and solar heat gains. The sol-air temperature is calculated as follows [133, 54]:

$$T_{sol}(t) = T_{DB}(t) + \frac{I_{sol}(t)\epsilon}{h_{se}(t)}\,, \tag{3.3.2}$$

where $T_{DB}(t)$ is the ambient dry-bulb temperature [°C], $I_{sol}(t)$ is the incident total solar radiation [W/m^2] and ϵ is the external surface solar absorptivity [–]. The radiative heat losses due to the difference between the ambient air temperature and sky temperature are not taken into account.

3.3.3 Numerical approach

The governing heat equation is solved using the Finite Difference Method. The well-known Crank-Nicolson scheme [106] is used. The Crank-Nicolson scheme is a combination of fully-explicit and fully-implicit schemes. The time derivative is approximated with the backward difference, while the space derivative is approximated with the average of the central differences from the previous and current time step. In the case of the diffusion problem the scheme is unconditionally stable. It is also more accurate than fully-explicit and fully-implicit schemes when small time steps are applied.

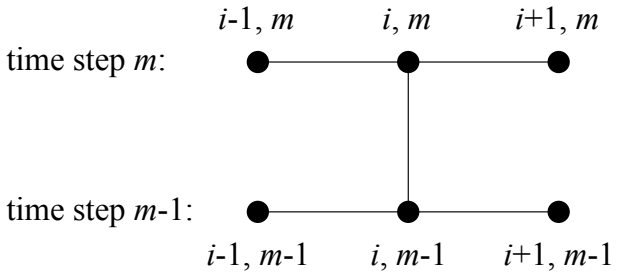

Figure 3.5: Crank-Nicolson computational stencil for one-dimensional problem

The discretized form of the heat equation (Eq. (3.3.1)) using the Crank-Nicolson scheme has the following form:

$$\frac{T_i^m - T_i^{m-1}}{\Delta t} = \frac{\alpha}{2}\left(\frac{T_{i-1}^m - 2T_i^m + T_{i+1}^m}{\Delta x^2} + \frac{T_{i-1}^{m-1} - 2T_i^{m-1} + T_{i+1}^{m-1}}{\Delta x^2}\right), \tag{3.3.3}$$

where T_i^m is the temperature [°C] at node i and time step m, Δt is the time step [s], Δx is the distance between the computational nodes [m] and α is the thermal diffusivity [m^2/s].

In order to obtain a solution for the entire computational domain, a continuous space is discretized into a set of computational nodes. Subsequently, Eq. (3.3.3) is applied to each node, resulting in a system of linear equations:

$$\begin{bmatrix} b_1 & c_1 & & & & & \\ a_2 & b_2 & c_2 & & & & \\ & \cdots & \cdots & \cdots & & & \\ & & a_i & b_i & c_i & & \\ & & & \cdots & \cdots & \cdots & \\ & & & & & a_N & b_N \end{bmatrix} \cdot \begin{bmatrix} T_1^m \\ T_2^m \\ \cdots \\ T_i^m \\ \cdots \\ T_N^m \end{bmatrix} = \begin{bmatrix} d_1^m \\ d_2^m \\ \cdots \\ d_i^m \\ \cdots \\ d_N^m \end{bmatrix}, \tag{3.3.4}$$

where subscripts denote the node numbers, while superscripts denote the time steps. The coefficients a_n, b_n, c_n, d_n^m for any internal node n are derived from Eq. (3.3.3) and are:

$$\begin{aligned} a_n &= -\frac{\alpha}{2\Delta x^2}, \\ b_n &= \frac{1}{\Delta t} + \frac{\alpha}{\Delta x^2}, \\ c_n &= -\frac{\alpha}{2\Delta x^2}, \\ d_n^m &= \frac{1}{\Delta t}T_n^{m-1} + a_n T_{n-1}^{m-1} + (a_n + c_n)T_n^{m-1} + c_n T_{n+1}^{m-1}. \end{aligned}$$

The given coefficients are valid for internal nodes, i.e. for any node not being a boundary node ($n = 1$ and $n = N$) or an interface node ($n = i$). The interface node i is the node placed at the boundary of two adjacent layers having different thermal properties. The implemented mesh generation procedure always generates interface nodes at all layer interfaces. The number of nodes in each layer is arbitrary, but the same or similar distances between nodes are desired.

The coefficients a, b, c and d at boundaries and interfaces are derived from the mathematical formulation of appropriate boundary conditions. All relevant boundary condition types (from the building energy point of view) are implemented

in the model:

- BC type I — *Dirichlet* boundary condition,
- BC type II — *Neumann* boundary condition,
- BC type III — *Robin* boundary condition,
- BC type IV — continuity boundary condition for interface layers.

The derivation of the BC type I and IV is straightforward. However the derivation of the coefficients for the Neumann and Robin boundary conditions is more complex and not easily available in the literature. In this work, the coefficients representing the Neumann and Robin boundary conditions are derived from the fully-implicit Backward-Time Centered-Space (BTCS) scheme instead of the Crank-Nicolson scheme. The BTCS scheme is as follows:

$$\frac{T_n^m - T_n^{m-1}}{\Delta t} = \alpha \frac{T_{n-1}^m - 2T_n^m + T_{n+1}^m}{\Delta x^2} \,. \tag{3.3.5}$$

where subscripts stand for the node number and superscript stand for the time step. The resulting system of equations (Eq. (3.3.4)) is solved using the standard Gauss-Jordan elimination method [109]. The coefficients a, b, c and d for all boundary condition types are derived hereafter. Although the BC type I was not used in the simulations, it is included in the following description because it is a basic and commonly used type of BC.

3.3.3.1 BC type I (Dirichlet)

The first type of the boundary condition occurs when the temperature function at the boundary of the domain is known. Since the assumed geometry is one-dimensional, the temperature $T(x,t)$ must be known at both external surfaces, i.e. at $x = 0$ and $x = L$:

$$\begin{aligned} T(0,t) &= f_1(t)\,, \\ T(L,t) &= f_2(t)\,, \end{aligned}$$

where f_1 and f_2 are the known functions. Hence, the elements of the coefficients matrix for boundary nodes in Eq. (3.3.4) are:

$$\begin{aligned} b_1 &= 1\,, \\ c_1 &= 0\,, \\ d_1 &= T_1^m\,, \end{aligned}$$

$$\begin{aligned} a_N &= 0\,, \\ b_N &= 1\,, \\ d_N &= T_N^m\,, \end{aligned}$$

where T_1^m and T_N^m are the known temperatures.

3.3.3.2 BC type II (Neumann)

The second type of boundary conditions is when the solution derivatives at the boundary of the domain are known. For the one-dimensional heat equation it can be expressed as:

$$\begin{aligned} \lambda\frac{\partial T(0,t)}{\partial x} &= q_{int}(t)\,, \\ \lambda\frac{\partial T(0,L)}{\partial x} &= q_{ext}(t)\,, \end{aligned}$$

where $q_{int}(t)$ and $q_{ext}(t)$ are the known functions. For the internal surface, the above condition may be approximated as follows:

$$-\lambda\frac{T_2^m - T_0^m}{2\Delta x} = q_{int}^m\,,$$

while for the external surface:

$$\lambda\frac{T_{N+1}^m - T_{N-1}^m}{2\Delta x} = q_{ext}^m\,.$$

The nodes 0 and $N+1$ are the auxiliary artificial nodes (lying outside the domain), which must be eliminated from the equations. Temperatures T_0 and T_{N+1} are found by combining external heat fluxes with temperatures at nodes 2 and $N-1$:

$$T_0^m = \frac{2\Delta x}{\lambda}q_{int}^m + T_2^m\,, \tag{3.3.6}$$

$$T_{N+1}^m = \frac{2\Delta x}{\lambda}q_{ext}^m + T_{N-1}^m\,. \tag{3.3.7}$$

The coefficients a, b, c and d are derived by substituting $T_0^m$and T_{N+1}^m from Eqs. (3.3.6) and (3.3.7) into the BTCS scheme, Eq. (3.3.5). For the internal surface the derivation is as follows:

$$\begin{aligned} \frac{T_1^m - T_1^{m-1}}{\Delta t} &= \frac{\alpha}{\Delta x^2}\left(T_0^m - 2T_1^m + T_2^m\right)\,, \\ T_1^m - T_1^{m-1} &= \frac{\alpha\Delta t}{\Delta x^2}\left(\frac{2\Delta x}{\lambda}q_{int}^m + T_2^m - 2T_1^m + T_2^m\right)\,. \end{aligned}$$

Assuming that

$$p_1 = \frac{\alpha_1 \Delta t}{\Delta x_1^2} \quad \text{and} \quad r_1 = \frac{2\Delta x_1}{\lambda_1}\,,$$

the final form of the equation can be written as:

$$T_1^m(1+2p_1) + T_2^m \cdot 2p_1 \;=\; p_1 r_1 \cdot q_{int}^m + T_1^{m-1}\,.$$

If an analogical derivation is performed for the external surface, the following relation is obtained:

$$T_1^m(1+2p_N) + T_2^m \cdot 2p_N \;=\; p_N r_N \cdot q_{int}^m + T_1^{m-1}\,.$$

where $p_N = \alpha_N \Delta t/\Delta x_N^2$ and $r_N = 2\Delta x_N/\lambda_N$.

Hence, the elements of the coefficients matrix for boundary nodes in Eq. (3.3.4) are as follows:

$$\begin{aligned} b_1 &= 1 + 2p_1\,, \\ c_1 &= -2p_1\,, \\ d_1^m &= p_1 r_1 \cdot q_{int}^m + T_1^{m-1}\,, \end{aligned}$$

$$\begin{aligned} a_N &= -2p_N\,, \\ b_N &= 1 + 2p_N\,, \\ d_N^m &= p_N r_N \cdot q_{ext}^m + T_N^{m-1}\,. \end{aligned}$$

3.3.3.3 BC type III (Robin)

The third type of boundary conditions expresses the convective heat transfer at a solid boundary:

$$\lambda \frac{\partial T}{\partial x} = h(T_{amb} - T_{surf})\,. \tag{3.3.8}$$

where T_{amb} is the known ambient temperature and T_{surf} is the surface temperature to be determined. From the mathematical point of view this boundary condition is equivalent to the Robin boundary condition [90], which for the one-dimensional problem can be written as follows:

$$aT(t,x) + b\frac{\partial T(t,x)}{\partial x} = c\,,$$

where a, b and c are some constants or known functions.

For the internal surface, the condition defined using Eq. (3.3.8) can be approximated as follows:

$$-\lambda\frac{T_2^m - T_0^m}{2\Delta x} + h_{si}T_1^m = h_{si}T_{int}^m\,,$$

while for the external surface:

$$\lambda\frac{T_{N+1}^m - T_{N-1}^m}{2\Delta x} + h_{se}T_N^m = h_{se}T_{ext}^m\,,$$

where T_{int}^m and T_{ext}^m are the known ambient temperatures for the indoor and outdoor, respectively, while T_1 and T_N are the surface temperatures. The nodes 0 and $N+1$ are the auxiliary artificial nodes (placed outside the computational domain), which must be eliminated from the equations. The temperatures T_0^m and T_{N+1}^m are determined by combining the ambient temperatures with the temperatures at nodes neighboring the considered surfaces:

$$T_0^m = \frac{2h_{si}\Delta x}{\lambda}T_{int}^m - \frac{2h_{si}\Delta x}{\lambda}T_1^m + T_2^m\,,$$

$$T_{N+1}^m = \frac{2h_{se}\Delta x}{\lambda}T_{ext}^m - \frac{2h_{se}\Delta x}{\lambda}T_N^m + T_{N-1}^m\,.$$

In order to derive the coefficients a, b, c and d, temperatures $T_0^m$and T_{N+1}^m are substituted in the BTCS scheme, Eq. (3.3.5). For the internal surface the derivation is as follows:

$$\begin{aligned}
\frac{T_1^m - T_1^{m-1}}{\Delta t} &= \frac{\alpha_1}{\Delta x_1^2}\left(T_0^m - 2T_1^m + T_2^m\right)\,,\\
T_1^m - T_1^{m-1} &= \frac{\alpha_1\Delta t}{\Delta x_1^2}\left(\frac{2h_{si}\Delta x_1}{\lambda_1}T_{int}^m - \right.\\
&\qquad \left. -\frac{2h_{si}\Delta x_1}{\lambda_1}T_1^m + T_2^m - 2T_1^m + T_2^m\right)\,.
\end{aligned}$$

Assuming that

$$p_1 = \frac{\alpha_1\Delta t}{\Delta x_1^2} \quad \text{and} \quad s_1 = \frac{2h_{si}\Delta x_1}{\lambda_1}\,,$$

the final form of the equation can be written as:

$$\begin{aligned}
T_1^m(1 + p_1s_1 + 2p_1) + T_2^m(-2p_1) &= T_{int}^m(p_1s_1) + T_1^{m-1}\,,\\
T_1^m b_1 + T_2^m c_1 &= d_1\,.
\end{aligned}$$

where h_{si} is the heat transfer coefficient at the internal surface. If an analogical derivation is performed for the external surface, the following relationship is obtained:

$$\begin{aligned} T_{N-1}^m(-2p_N) + T_N^m(1 + 2p_N + p_N s_N) &= T_{ext}^m(p_N s_N) + T_N^{m-1}\,, \\ T_{N-1}^m a_N + T_N^m b_N &= d_N\,, \end{aligned}$$

where $p_N = \alpha_N \Delta t/\Delta x_N^2$, $s_N = 2h_{se}\Delta x_N/\lambda_N$ and h_{se} is the heat transfer coefficient at the external surface.

Hence, the elements of the coefficients matrix for the boundary nodes in Eq. (3.3.4) are as follows:

$$\begin{aligned} b_1 &= 1 + 2p_1 + p_1 s_1\,, \\ c_1 &= -2p_1\,, \\ d_1^m &= p_1 s_1 \cdot T_{int}^m + T_1^{m-1}\,, \end{aligned}$$

$$\begin{aligned} a_N &= -2p_N\,, \\ b_N &= 1 + 2p_N + p_N s_N\,, \\ d_N^m &= p_N s_N \cdot T_{ext}^m + T_N^{m-1}\,. \end{aligned}$$

3.3.3.4 BC type IV (continuity assumption)

The fourth type boundary condition specifies that the functions of the heat flux and temperature are continuous at the interface between two layers (at node i):

$$\begin{aligned} T_{i^-}(t) &= T_{i^+}(t)\,, \\ \lambda_I \frac{\partial T_{i^-}}{\partial x} &= \lambda_{II} \frac{\partial T_{i^+}}{\partial x}\,, \end{aligned}$$

where the subscript i^- denotes the left-side value at the node i and the subscript i^+ denotes the left-side value at the node i. The elements of the coefficients matrix are

derived from the BTCS scheme (Eq. (3.3.5)) and are as follows:

$$\begin{aligned} a_i &= -\frac{\lambda_I}{\Delta x_I}\,, \\ b_i &= \frac{\lambda_I}{\Delta x_I} + \frac{\lambda_{II}}{\Delta x_{II}} + A\,, \\ c_i &= -\frac{\lambda_{II}}{\Delta x_{II}}\,, \\ d_i^m &= A \cdot T_i^{m-1}\,, \end{aligned}$$

where the subscripts I and II stand for values related to materials adjacent to the common surface (interface) represented by the node i, and A:

$$A = \frac{(\rho_I c_I \Delta x_I + \rho_{II} c_{II} \Delta x_{II})}{2\Delta t}\,.$$

3.4 Air-wall co-simulation

The numerical model developed for the purpose of this work consists of two main parts:

1. indoor air submodel,
2. external wall submodel.

The term "submodel" is used to both cases to underline that these models are independent from each other, but both are inevitable parts of the developed numerical model. The term "co-simulation" is used to distinguish the calculation procedure from fully coupled procedures which aim at solving the problem in a coupled manner, what is called the *conjugate heat transfer*. The procedure applied in this work relies on two independent models solving the airflow and heat transfer in solids independently.

In the present model, the air-wall co-simulation procedure depends on the mutual exchange of results at the common boundary between the air and wall models (Fig. 3.6). The procedure is repeated for all the defined external solid partitions (in this case: south wall, south window).

The indoor air model (CFD) sends the heat heat flux per area to the wall model. This heat flux is treated by the wall model as the second-type boundary condition (Neumann BC). Similarly, the wall model sends the temperature of the wall internal surface to the air model. This temperature is the boundary condition for the CFD model (Dirichlet BC). The surface temperature as the boundary condition

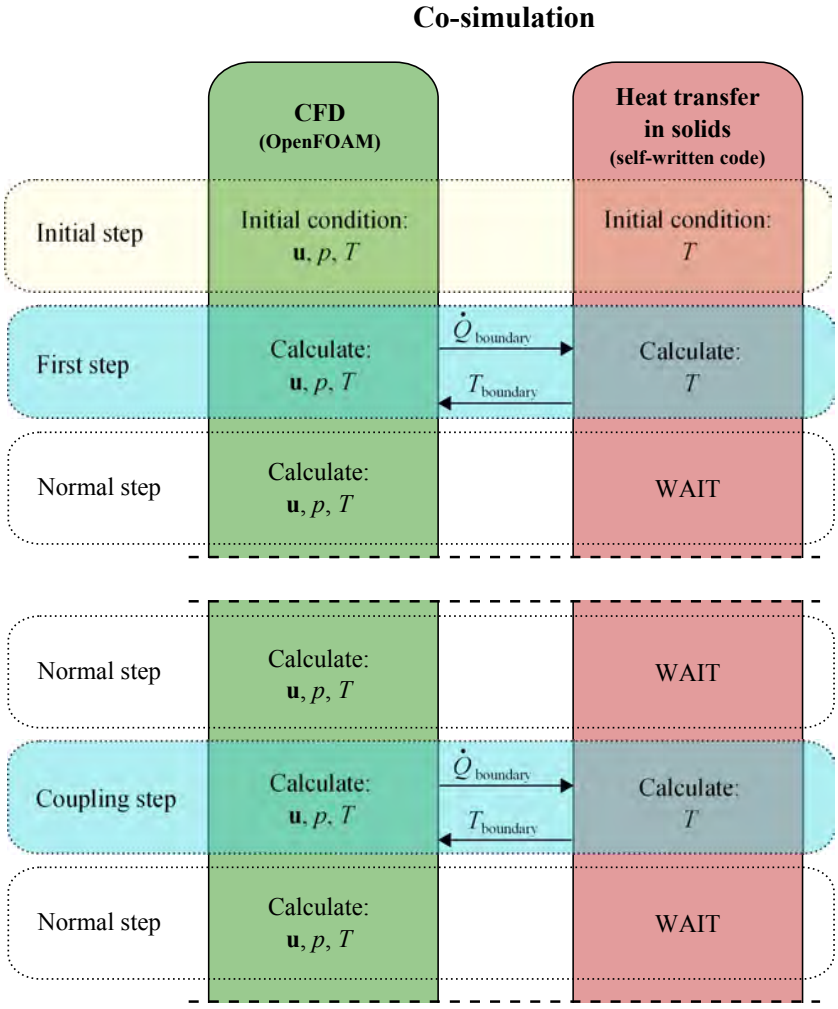

Figure 3.6: Air–wall co-simulation procedure

is assumed to be constant over the respective surface. The heat transfer rate between the wall and air is calculated based on the convective heat transfer coefficient calculated using Eq. 3.2.15.

The both exchanged boundary values, temperature and heat flux, are the average values. The heat flux calculated by CFD is spatially-averaged over the boundary surface before sending it to the wall model. On the other hand, the wall surface temperature is obtained by solving the one-dimensional heat equation. The obtained surface temperature is treated by the CFD model as the average temperature and is applied uniformly over the considered boundary surface. This average-value approach significantly simplifies and speeds up the calculations. Similar approach is used e.g. in the ESP-r [15].

The solution at the common boundary is exchanged in prescribed time intervals. There is no need to exchange the results at the each time step, because CFD time

steps are significantly smaller than time steps required in heat conduction calculations. The time steps during which the solution exchange occurs are referred in this work as *coupling steps*, while the solution exchange intervals as *coupling intervals.*

The coupling interval adopted in this work is 20 s. The influence of the coupling interval on the results is presented in Section 4.4. The validation showed that coupling intervals larger than 20 s could be used. However, due to the simplicity of the adopted co-simulation approach, the coupling step interval has a little influence on the computational time. The computational effort obtained by the 20 s interval is acceptable.

Between the coupling steps, the CFD calculations proceed, while the heat conduction calculations in solid partitions stop and wait for the next coupling step. Thus, the time step size in heat conduction calculations is 20 s. The 20 s time step is sufficient for the wall model to give accurate results in the considered range of conditions.

The air-wall coupling strategy implemented in this work can be referred as *Quasi-Dynamic Coupling* according to the classification of coupling strategies presented by Zhai et al. [144]. The strategy is recognized to be accurate if the solution exchange time interval (coupling time interval) is small, for instance "a few minutes" [144]. The coupling time interval in the present model is even lower (20 s), and thus the quasi-dynamic coupling strategy can be adopted.

3.5 Thermal comfort indices

The present investigation is aimed at the evaluation of the building thermal capacitance influence on the indoor environment, particularly the indoor thermal comfort. The factors taken into account are: indoor temperature, indoor air speed, airflow patterns and nonuniformity of the environment. In addition to the analysis of the raw environment parameters, the results are combined to predict the thermal comfort level. For this purpose some of the thermal comfort indices described in Section 2.1.4 are chosen.

Most of the indoor thermal comfort studies are carried out using the heat balance based thermal comfort models: the PMV-PPD model (Section 2.1.4.2) and the 2-node Gagge's model (Section 2.1.4.2). In this work the PMV-PPD model is chosen because it provides a balance between the accuracy and implementation complexity. The 2-node model is more difficult to implement and does not introduce any significant advantages from the point of view of this study.

To extend the thermal comfort evaluation, the risk of draft is assessed using the

DR model (Section 2.1.4.1). The risk of draft is often calculated in thermal comfort studies as an auxiliary value [87, 120, 121].

In order to calculate the PMV and PPD indices, Eqs. (2.1.6), (2.1.7), (2.1.8), (2.1.9) and (2.1.10) have to be solved. The solution is found iteratively due to the mutual interdependence of the heat transfer coefficient, Eq. (2.1.8), and the clothing temperature, Eq. (2.1.7).

The calculation procedure is based on the algorithm presented in ISO 7730 [74]. The ISO algorithm is written in the BASIC programming language. It was translated to the C++ programming language by the author and implemented into the code. The implemented calculation procedure was validated against the exemplary data included in the aforementioned standard.

Although the PMV-PPD model is based on the steady state heat balance, it is often used to evaluate indoor transient conditions [112, 136]. It is possible because indoors are usually characterized by slow and relatively mild changes of environmental parameters.

The PMV-PPD model is proven to give more accurate results in the case of air-conditioned buildings than naturally ventilated ones. It is found that the thermal comfort scale used with the PMV model is too strict for the natural ventilation. One of the reasons is that expectations upon the free-running buildings are lower than upon the air-conditioned buildings. However, the PMV-PPD model is still often used by researchers to predict the thermal comfort in naturally ventilated buildings [110], despite its potential inaccuracy. Sometimes the standard PMV is simply multiplied by a damping factor n $(0 < n < 1)$ to take into account the lower expectancy upon the natural ventilation [120, 121, 43]. In the present study the type of a ventilation system and its effect on human expectations are not considered and the PMV values are not multiplied by any damping factor.

The PMV is calculated from the following input parameters: clothing level, humidity, activity level, air temperature, air velocity magnitude and mean radiant temperature. In this work, the clothing level, humidity and activity level are assumed to be constant and equal to $1\,\mathrm{m^2K/W}$, $50\,\%$ and $1.2\,\mathrm{met}$, respectively. The air velocity and the temperature are calculated at each time step of the simulation. The mean radiant temperature is assumed to be equal to the spatially averaged indoor air temperature and is updated at every time step. This is a general assumption, valid in most cases.

The DR index is evaluated using Eq. (2.1.2). It depends on the local air temperature, local mean air velocity and local turbulence intensity. The turbulence

intensity Tu (%) is calculated using the following expression [120, 87]:

$$Tu = 100 \cdot \frac{(2k)^{0.5}}{u},$$

where k is the local turbulent kinetic energy and u is the local mean air velocity.

The PMV, PPD and DR indices are used to evaluate the total impact of indoor environment parameters. The indices make the results more meaningful, but should not be treated as a perfectly accurate output. The actual level of the thermal comfort depends on many factors which are difficult to evaluate. These include both personal and environmental factor types. A comprehensive discussion concerning the human thermal comfort and problems with its evaluation is presented in Section 2.1.

All considered thermal comfort indices are presented as spatially averaged quantities. The average value of the given thermal comfort index TCI_{avg} (which can be PMV, PPD, or DR) over a given space is calculated as follows:

$$TCI_{avg} = \frac{\sum_{i=1}^{n} TCI_i \cdot V_i}{\sum_{i=1}^{n} V_i},$$

where TCI_i is the value of the thermal comfort index at the i-th cell of a given space, V_i is the volume of the i-th cell and n is the total number of cells.

The thermal comfort indices are averaged over three different regions of the room: (1) the occupied zone, (2) the near-wall zone adjacent to the external wall (and window) and (3) the entire room (without the ventilation inflow and outflow ducts).

The occupied zone (1) is defined in this work in order to assess the thermal comfort level in the space where people are present for the most of the time. The zone definition is similar to the "breathing zone" from ANSI/ASHRAE Standard 62.1-2004 [5], however its dimensions are slightly different. It is assumed that the occupied zone is the space between the floor and a plane 2 m above it and 1 m away from walls. The near-wall zone (2) is the 1 m wide space adjacent to the external wall and window. Its height is equal to the room height. This zone is taken into account because in many situations this location is highly affected by drafts. The results for the whole room (3) are averaged over the entire indoor space, i.e. 5 x 5 x 2.6 m^3.

The results from different regions of the room space provide more information than only one simple result averaged over the entire space. The analysis enables to verify whether nonuniformities (thermal stratification, drafts) are an issue in the present case.

3.6 Model implementation

The numerical model was implemented by the author through developing an extension code to the OpenFOAM's solver *buoyantPimpleFoam* (version 2.0.1).

OpenFOAM (Open Field Operation and Manipulation) is a free open source CFD software package written in C++ and developed by the OpenFOAM Team at SGI Corp and distributed by the OpenFOAM Foundation [116]. The OpenFOAM toolbox is extensively used by many engineers and researchers as a reasonable alternative to commercial CFD software. The *buoyantPimpleFoam* solver is a transient solver dedicated to buoyant, turbulent flows of compressible fluids for ventilation and heat transfer. The source code of the solver is available at the OpenFOAM C++ documentation website [103]. A validation study of the solver was recently presented by Peltola and Pättikangas [107]. The study showed a good agreement between numerical results and experimental results.

Due to the specific source code structure of the OpenFOAM toolkit, its solvers can be customized or extended. For the purpose of the present work, the *buoyantPimpleFoam* solver served as a template, to which the following capabilities were added by the author:

- one-dimensional heat conduction in solids (thermal envelope),
- solid-fluid heat transfer co-simulation,
- on-the-fly output data processing,
- thermal comfort indices calculation.

At each time step, the program solves equations governing airflow, to subsequently solve the heat conduction equations governing the heat transfer in walls. The results at the solid-fluid interface surfaces are exchanged between submodels in predefined time intervals as shown in Fig. 3.6.

The on-the-fly output data processing feature facilitated the results post-processing. The feature greatly shortened the time needed to compile the outputs to a executable form. The OpenFOAM solvers save the results of each time step in a separate folder. Additionally, in each folder output parameters are saved as separate files. As a result, all analyzed cases produced more than 5 million files (taking over 213 GB of a disk space). Although some tools helping with the data analysis are available in the OpenFOAM toolkit, they are not capable to process all results. It is because some output parameters have to be calculated from basic results provided by the standard solver, e.g. thermal comfort parameters, spatial weighted averages of some

parameters, etc. The developed procedures process the output data and save the results regarding specific parameters in designated files. Afterward, parameters which have to be calculated from basic results (e.g. the iterative calculations of PMV) are calculated and saved. This process is repeated at the end of each time step.

The author developed the Python scripts to automatically generate data plots for considered output variables at the end of the simulation. The plots are generated using a freely redistributable command-line driven graphing utility called "gnuplot" [57] (ver. 4.4.3).

The author's contribution to the code is presented in Fig. 3.7. The developed code consists of approximately 5300 lines.

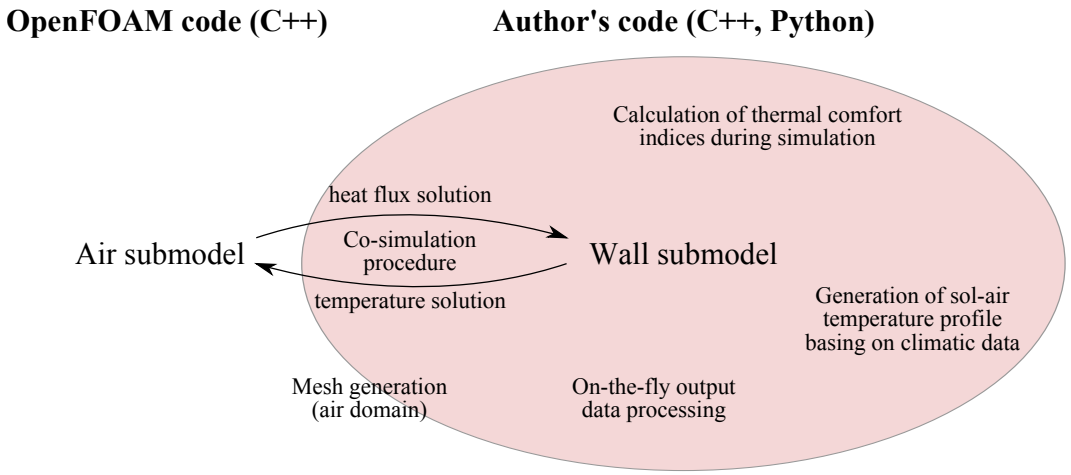

Figure 3.7: Schematic representation of the author's contribution to the source code

3.7 Summary

The developed model consists of two submodels, the indoor air submodel and the external wall submodel, working in a co-simulation. The complete model allows for simulating building transient thermal behavior when exposed to arbitrary variations of the outdoor temperature. It is possible to model an arbitrary number of building envelope components. The components are modeled as one-dimensional multilayer solid partitions. In the present work, the model is used to analyze the influence of different external wall structures (different thermal capacitances) on the indoor thermal comfort.

To make the results easier to interpret and reduce the computational demand only a single air space with one external wall and one window is modeled, while remaining surfaces are assumed to be adiabatic. The adopted outdoor temperature

profiles and the list of wall structures taken into account in the analysis are listed in Section 5.2.

Chapter 4

Model validation

Both the indoor air submodel and external wall submodel are validated. The air submodel is based on the OpenFOAM's solver *buoyantPimpleFoam,* validated by Peltola and Pättikangas [107]. The wall submodel, developed by the author, was also verified. The results provided by the model were compared with the results provided by the commercial software Abaqus, based on the Finite Element Method (Section 4.1).

Despite the fact that the CFD code is capable to provide accurate results, there is still a need to validate the computational mesh. As discussed in Section 3.2.2.1 concerning the near-wall treatment in the airflow model, the air-wall heat transfer rate is highly sensitive to the near-wall mesh resolution due to the presence of the wall function. In the case of the present study the only important quantity affected by the near-wall mesh resolution is the convective heat transfer coefficient. Incorrect rates of the heat transfer between the wall and indoor air can under– or overestimate the influence of wall thermal parameters on indoor conditions. Thus, the main challenge of the mesh validation is to find a near-wall mesh resolution guaranteeing realistic values of the surface heat transfer coefficient. The convective heat transfer coefficients calculated using seven different near-wall mesh resolutions are compared with the data from empirical formula. The conducted procedure is presented in Section 4.2. In addition to the near-wall mesh validation, the standard mesh independence test was performed. Seven different general mesh resolutions and their influence on the results were checked. The mesh independence test is discussed in Section 4.3.

Finally, the independence test of the air-wall coupling interval was carried out. The test aim was to find how often results at common boundaries have to be exchanged between models to keep the convergent solution. Seventeen coupling intervals were checked. The procedure is described in Section 4.4.

To keep the logical sequence of the following sections in this chapter, the near-wall mesh validation is presented first. It is because the results showed that the near-wall mesh resolution has the greatest impact on results. Subsequently, the general mesh (i.e. far from the south wall) independence test is presented. Finally, the coupling interval independence test was performed.

Despite the chosen sequence of the following sections, it should be noted that in reality the validation of the entire model was an iterative process. The author carried out a number of preliminary tests to investigate the model behavior. As a result, the presented near-wall mesh validation was carried out using an optimum general (i.e. far from the south wall) mesh resolution. Similarly, the general mesh resolution was carried out using an optimum near-wall mesh resolution. In addition, all mesh tests were performed using an optimum coupling interval.

4.1 Wall model validation

The wall model was validated against the results of the Abaqus software (FEM, commercial code [31]). In the following section the results obtained by the self-written model are denoted with the subscript "**CWall**" (the name is derived from the name of the respective C++ class in the source code), while the results obtained by Abaqus are denoted with the subscript "**Abaqus**".

The sample case used to validate the wall model code is presented in Fig. 4.1. The sample case has a one-dimensional geometry representing a double-layer wall. Both layers are 0.2 m wide. The assumed material parameters of the Layer 1 are $\lambda_1 = 0.7\,\mathrm{W/(m\,K)}$, $\rho_1 = 1000\,\mathrm{kg/m^3}$, $c_{p1} = 1000\,\mathrm{J/(kg\,K)}$, while the parameters of the Layer 2 are $\lambda_2 = 2.5\,\mathrm{W/(m\,K)}$, $\rho_2 = 1500\,\mathrm{kg/m^3}$, $c_{p2} = 1000\,\mathrm{J/(kg\,K)}$ (Layer 1 is the external layer and Layer 2 is the internal one).

The initial condition is the known temperature distribution: $T(x, 0) = 0°\mathrm{C}$. The boundary condition at the internal surface (Layer 2) is the Robin boundary condition (III type BC) with the indoor temperature $T_i(t) = 0 = \mathrm{const}$, and the surface heat transfer coefficient $h_i = 8,1\,\mathrm{W/(m^2K)}$. The boundary condition at the external surface (Layer 1) is the Neuman boundary condition (II type BC) with the specified heat flux per area $q(t) = 20\,\mathrm{W/m^2} = \mathrm{const}$. The simulation time is 10 h.

The case is modeled using both the self-written code and the commercial Abaqus code. The total number of nodes in the model based on the own code is 10: 2 nodes at the external boundaries, 1 node at the common surface, 3 internal nodes in Layer 1 and 3 internal nodes in Layer 2. The nodes are distributed uniformly and the distance between any two neighboring nodes is 0.05 m. A similar finite element

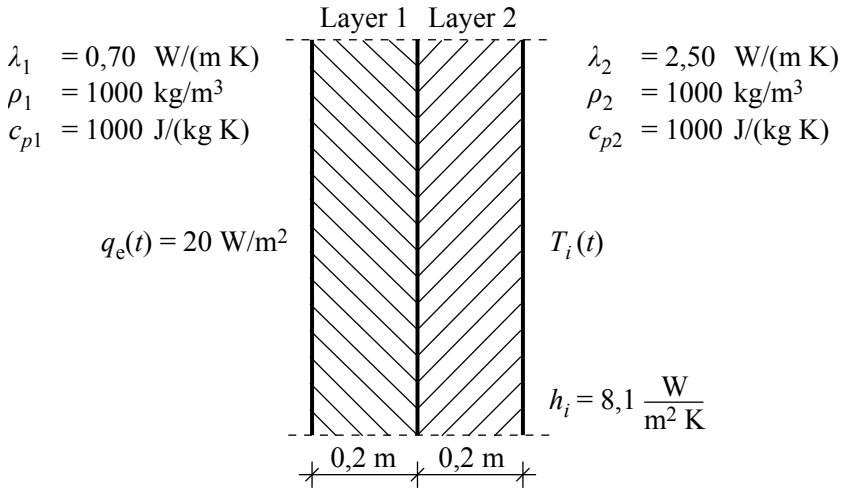

Figure 4.1: Wall model validation case

mesh resolution was implemented in Abaqus.

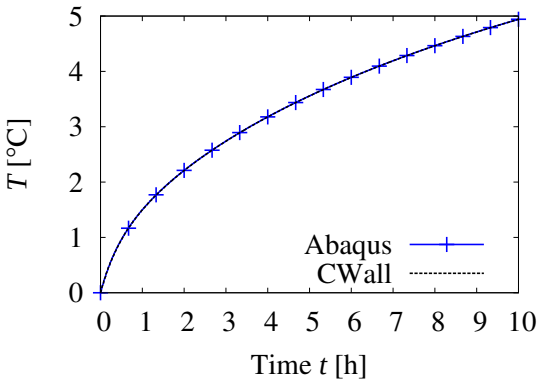

Figure 4.2: External surface temperature: CWall vs. Abaqus

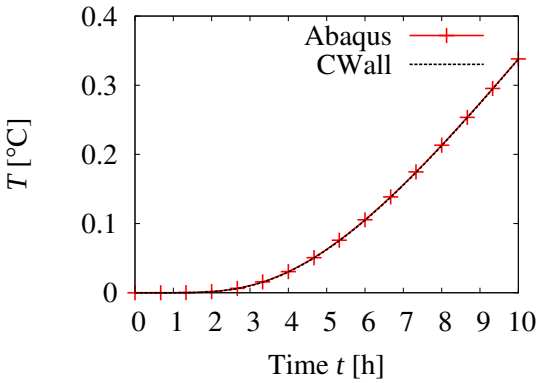

Figure 4.3: Internal surface temperature: CWall vs. Abaqus

As shown in Figs. 4.2 and 4.3, the time-dependent surface temperatures calculated by both codes are identical. Also the cross-section temperature distributions at the final time $t = 10\,\mathrm{h}$ calculated by both codes closely fit to each other, that is presented in Table 4.1. The error is 0.001 °C only.

4.2 Near-wall mesh validation

The aim of the near-wall mesh validation is to ensure that calculated convective heat transfer coefficients (HTC) at the surface of the south wall (and window) have proper values. The south wall mesh region is important only and verified, because all other surfaces are adiabatic (no heat transfer across them is allowed).

In this study the exact value of the HTC is not so important, but still this value

Table 4.1: Wall model validation: cross-section temperatures at time $t = 10$ h

Distance x [m]	$T_{CWall}(x,t)$ [°C]	$T_{Abaqus}(x,t)$ [°C]
0.00	4.94085	4.94143
0.05	3.62149	3.62203
0.10	2.51219	2.51277
0.15	1.58957	1.59022
0.20	0.81868	0.81940
0.25	0.64141	0.64213
0.30	0.50543	0.50612
0.35	0.40574	0.40638
0.40	0.33756	0.33811

should be realistic. The air-wall heat transfer rate depends on flow conditions in the vicinity of the wall surface. Thus, the HTC cannot have a single constant assigned but rather be evaluated as the simulation proceeds.

As described in Section 3.2.2.1 about the near-wall treatment, due to the presence of a wall function, the near-wall mesh resolution has a significant effect on the calculated HTC. For many industrial high-Re (high Reynolds numbers) flows the wall function provides accurate prediction provided that the dimensionless distance y^+ of the cell centroid from the wall is greater than 30 (this is the most often cited threshold value).

However the flow conditions expected in the present investigations are much milder than in the case of industrial flows and therefore the accuracy of the wall function cannot be ensured. Fortunately, from the point of view of the present work, the only important result calculated by the wall function is the HTC. Hence, in this section, the near-wall mesh resolution influence on the HTC calculation is described.

In the reality, the heat transfer rate is much lower when it is caused by the natural convection than by the forced convection. The developed model should take this effect into account. That is why the obtained numerical results are compared with the data provided by two empirical functions: the first for the HTC in natural convection conditions, and the second for the HTC in forced convection conditions. Finally, a next-to-wall cell size giving an acceptable accuracy of HTC under both conditions is adopted.

In the following tests, the next-to-wall cell size is described by the distance D between the wall surface and the cell centroid (Fig. 4.4). Six different cell sizes D are tested: 0.250 m, 0.167 m, 0.125 m, 0.100 m, 0.069 m, 0.055 m.

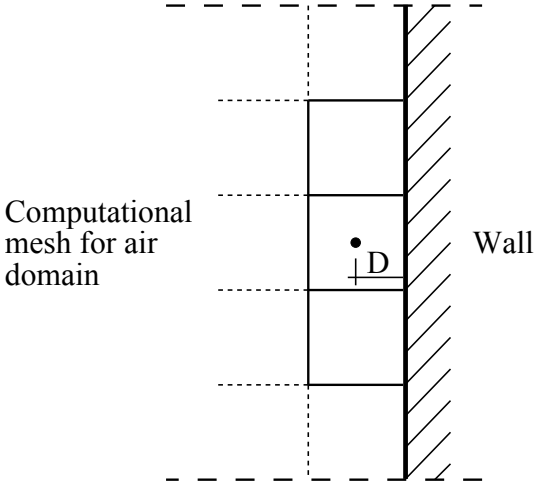

Figure 4.4: Next-to-wall cell size D

4.2.1 Natural convection test

The air-wall heat transfer under the natural convection conditions takes place when the wall internal surface is warmer than the air. Due to the temperature difference, the air is warmed up and it local temperature increases along the wall. In buildings the process is usually quite mild, the air speed is relatively low and the heat transfer rate is lower than for the forced convection.

This section describes the test to compare the convective heat transfer coefficients (HTC) calculated by the CFD code with the convective heat transfer coefficients calculated using the empirical formula provided by Fohanno and Polidori [48].

In order to stimulate the natural convection near the external (south) wall, initial and boundary conditions are defined. The initial temperature in the entire air domain is $T(\mathbf{x}, 0) = 19\,^{\circ}\mathrm{C}$. The initial wall and window temperatures are uniform along the entire cross-section and equal $T_{wall}(x, 0) = 27\,^{\circ}$ and $T_{window}(x, 0) = 27\,^{\circ}\mathrm{C}$. The inlet air temperature $T_{inlet}(t) = 19\,^{\circ}\mathrm{C}$ and ambient temperature $T_{amb}(t) = 27\,^{\circ}\mathrm{C}$ are constant. The inlet air velocity $v_{inlet} = 0.54\,\mathrm{m/s}$, that approximately provides the air exchange rate $ACH = 0.3$. The simulation stops at the time $t = 3\,\mathrm{h}$.

The wall and window are modeled as single-layer partitions. The material parameters of the wall are as follows: width $d_{wall} = 0.5\,\mathrm{m}$, density $\rho_{wall} = 400\,\mathrm{kg/m^3}$, conductivity $\lambda_{wall} = 0.15\,\mathrm{W/(m\,K)}$, specific heat $c_{p,wall} = 1000\,\mathrm{J/(kg\,K)}$. The material parameters of the window are: width $d_{window} = 0.028\,\mathrm{m}$, density $\rho_{window} = 1000\,\mathrm{kg/m^3}$, conductivity $\lambda_{window} = 0.042\,\mathrm{W/(m\,K)}$, specific heat $c_{p,window} = 1000\,\mathrm{J/(kg\,K)}$. The density of the window is evaluated as the approximate weighted average of the densities of the glass and air for a double-glazed (4 / 20 / 4 mm) window. The U-values of the wall and window are $U_{wall} \approx 0.29\,\mathrm{W/(m^2K)}$ and

$U_{window} \approx 1.20\,\mathrm{W/(m^2K)}$. They are calculated using the standard surface heat transfer coefficients: $h_i = 8.1\,\mathrm{W/(m^2K)}$ and $h_e = 23\,\mathrm{W/(m^2K)}$.

The indoor airflow pattern obtained in the test is shown in Figs. 4.5 and 4.6. It can be seen that the air slowly rises along the south wall with the average velocity of about 0.02–0.06 m/s. The highest velocities are noticed just below the ceiling, where the air moves at the speed of 0.15–0.30 m/s, depending on the certain location. The air does not drop just after entering the room because its temperature is close to the indoor temperature.

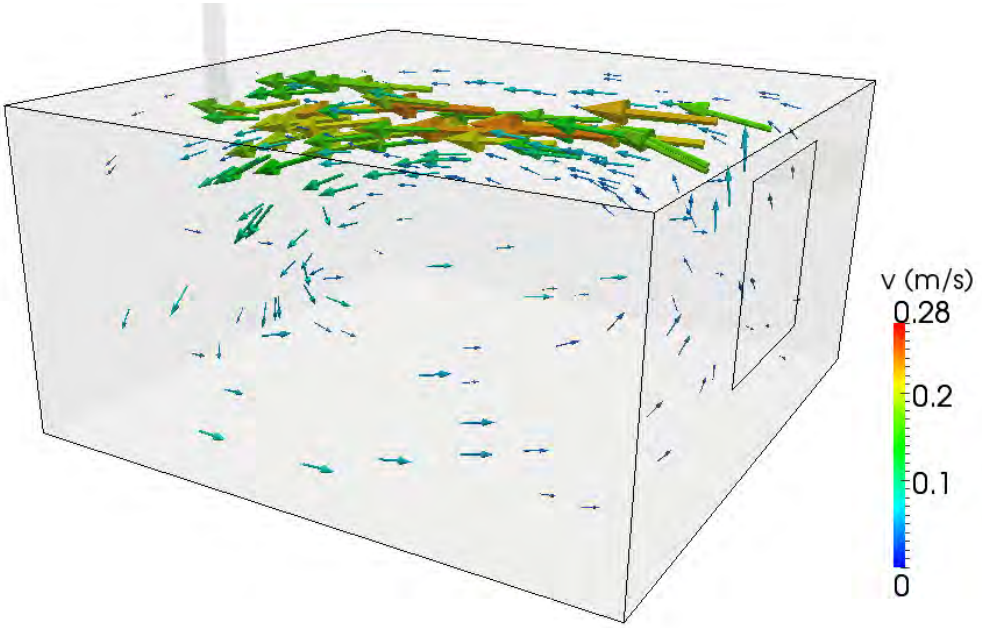

Figure 4.5: Natural convection test: air velocity v at time $t = 1\,\mathrm{h}$

Since the near-wall mesh resolution affects the heat transfer rate between the wall and air, it affects also the indoor temperature. The average indoor temperature T_{int} calculated using different near-wall mesh resolutions is shown in Fig. 4.7. In the analyzed case the maximum observed temperature difference between the results is about 0.5 °C.

The empirical formula for the average HTC for the natural convection $\overline{h}_{cn}$ developed by Fohanno and Polidori [48] has the form:

$$\overline{h}_{cn} = 1.174 \exp(0.0355H)[\overline{q}_c]^{0.24}, \tag{4.2.1}$$

where H is the height of the wall [m] and $\overline{q}_c$ is the average convective heat flux density [W/m^2]. The formula is accurate for both laminar and turbulent regimes, and for wall heights up to 3 m and heat flux intensity up to 200 W/m^2. The conditions in

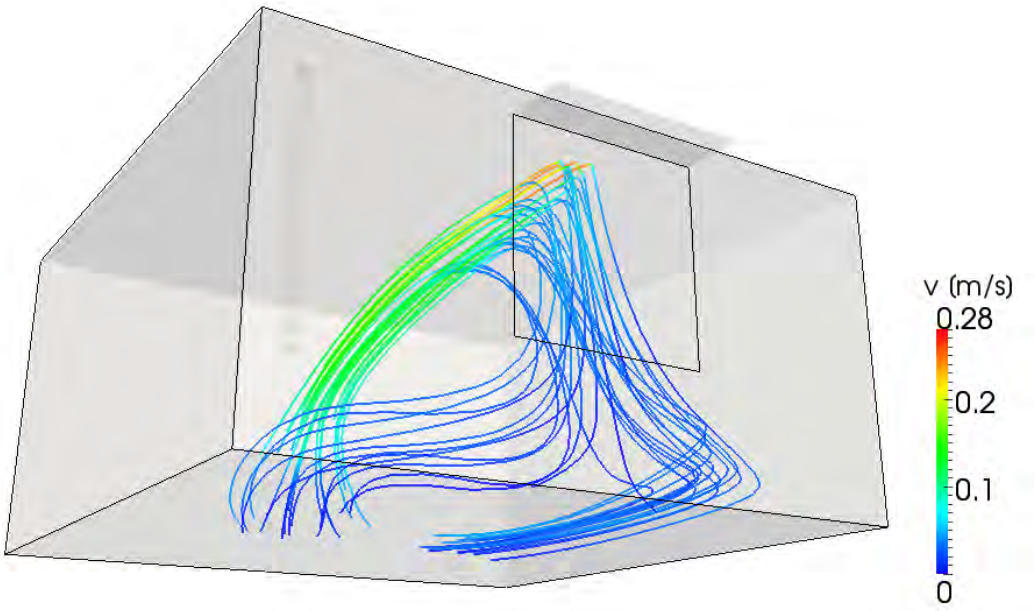

Figure 4.6: Natural convection test: airflow streamlines at time $t = 1\,\mathrm{h}$

the simulations performed in this work are within these ranges.

The empirical HTC calculated separately for each case is presented in Fig. 4.8. As shown, the HTC magnitudes varies between 2 and 3 $\mathrm{W/(m^2K)}$. The values do not differ much between the different near-wall mesh resolutions. Thus, for clarity, in Fig. 4.9 the HTC calculated by the CFD code is compared only with the empirical HTC calculated for $D = 0.167$ m.

As shown in Fig. 4.9, the HTC calculated by the CFD code using Eq. (3.2.15) varies significantly for different near-wall mesh resolutions. The average difference in HTC estimations using the mesh with the smallest next-to-wall cell ($D = 0.055\,\mathrm{m}$) and the ones with the large cells ($D = 0.250\,\mathrm{m}$ and $D = 0.167\,\mathrm{m}$) is about $3\,\mathrm{W/(m^2K)}$. Looking at the absolute magnitudes, the potential error related to the mesh quality can be as high as 100%.

Noticeable oscillations of the HTC values are observed. These oscillations are mainly a result of air velocity solution oscillations. Generally, all auxiliary quantities depending on the air velocity are influenced. The oscillations are obtained during some (random) periods of time. Possibly, the oscillations could be damped down by applying two (or more) PIMPLE loops to the solution algorithm (see Section 3.2.3). However, this would considerably increase the computational time causing the entire investigation infeasible. The oscillations are small enough to not affect the average values of the environmental and thermal comfort parameters, like the temperature.

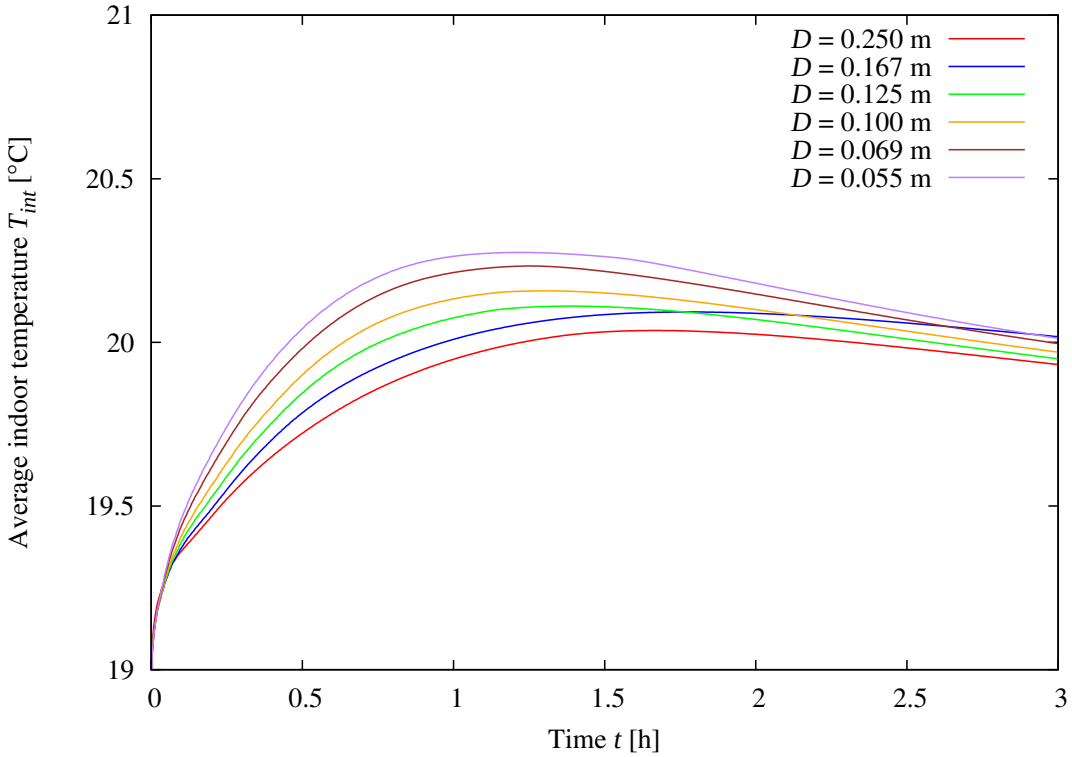

Figure 4.7: Natural convection test: average indoor temperature T_{int} calculated for different near-wall resolutions

The comparison shows that in the case of the natural convection, the larger wall-adjacent cell, the more accurate is the result. However, in the Finite Volume Method the coarser mesh, the more space-averaged is the result. By assumption, meshes with the next-to-wall cells with $D > 0.250\,\mathrm{m}$ are not taken into account because they poorly predict airflow patterns. The accuracy of the meshes with $D = 0.250\,\mathrm{m}$ and $D = 0.167\,\mathrm{m}$ is sufficient from the point of view of the present work.

It can be noticed that the greater size of the next-to-wall cell, the greater is the dimensionless distance y^+(Eq. (3.2.14)). The y^+ value varies in time because it depends on the turbulent kinetic energy, which is not constant. The surface-averaged magnitudes of y^+ for the wall and window surfaces are presented in Figs. 4.10 and 4.11, respectively. The y^+ magnitudes are higher for cells adjacent to the window because air velocities are higher than for wall-adjacent cells. The meshes with large next-to-wall cells provide higher y^+ values. The meshes with $D = 0.250\,\mathrm{m}$ and $D = 0.167\,\mathrm{m}$ produce surface-averaged y^+values close to the recommended minimum value $y^+ = 30$ (but still are lower). The values of y^+ are presented, they are not taken into account, since wall functions were not developed having indoor airflow in mind, i.e. flow with very low air velocity, buoyancy driven and under non-standard

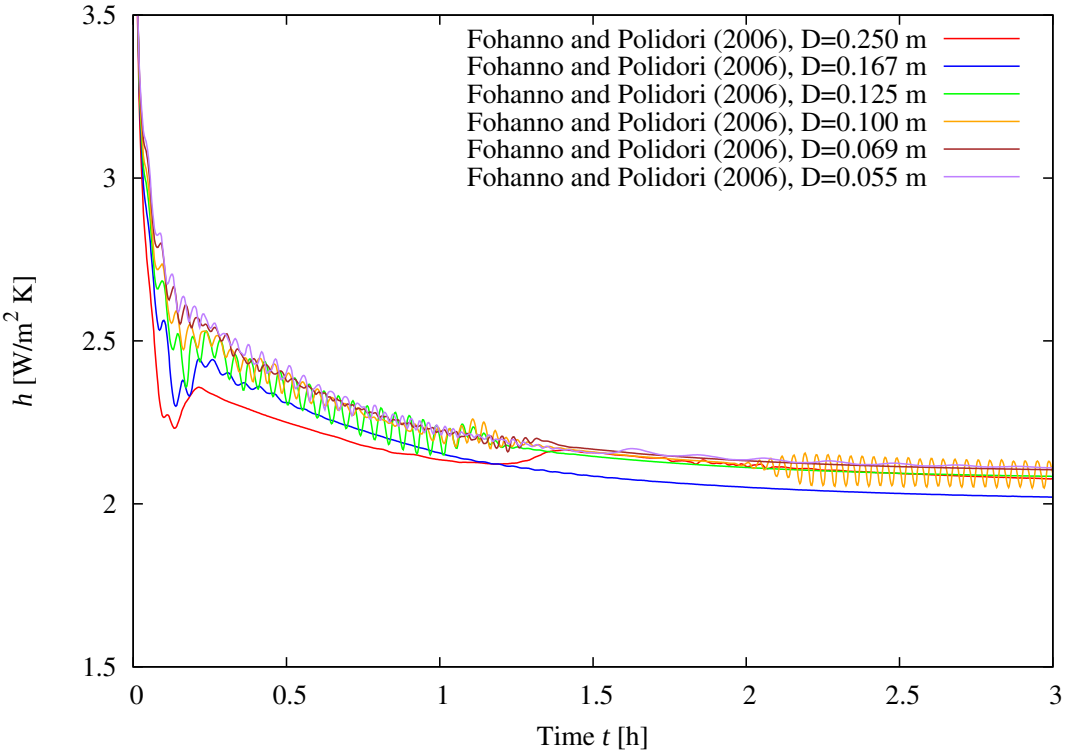

Figure 4.8: Natural convection test: empirical convective heat transfer coefficients for different near-wall resolutions

geometries.

The final decision concerning the adopted near-wall mesh resolution is based on the results of both tests: for natural and forced convection conditions. For the natural convection, the both meshes, $D = 0.250\,\mathrm{m}$ and $D = 0.167\,\mathrm{m}$, are acceptable. However, the mesh with $D = 0.167\,\mathrm{m}$ is more favorable due to a higher resolution of results in the near-wall and inflow regions.

4.2.2 Forced convection test

The forced convection occurs e.g. when the cold air is supplied from the ambient to the indoor. If the inlet is above the window, as in the given model, the cold (and heavy) air suddenly drops along the window and wall, causing a "washing" effect.

In this section the average convective heat transfer coefficients (HTC) calculated by the CFD code are compared with the empirical data obtained using the formula for the average HTC $\overline{h}_{cf}$ developed by Jayamaha [78]:

$$\overline{h}_{cf} = 1.444v + 4.955\,, \tag{4.2.2}$$

where v is the air velocity [m/s]. According to Jayamaha the velocity direction is

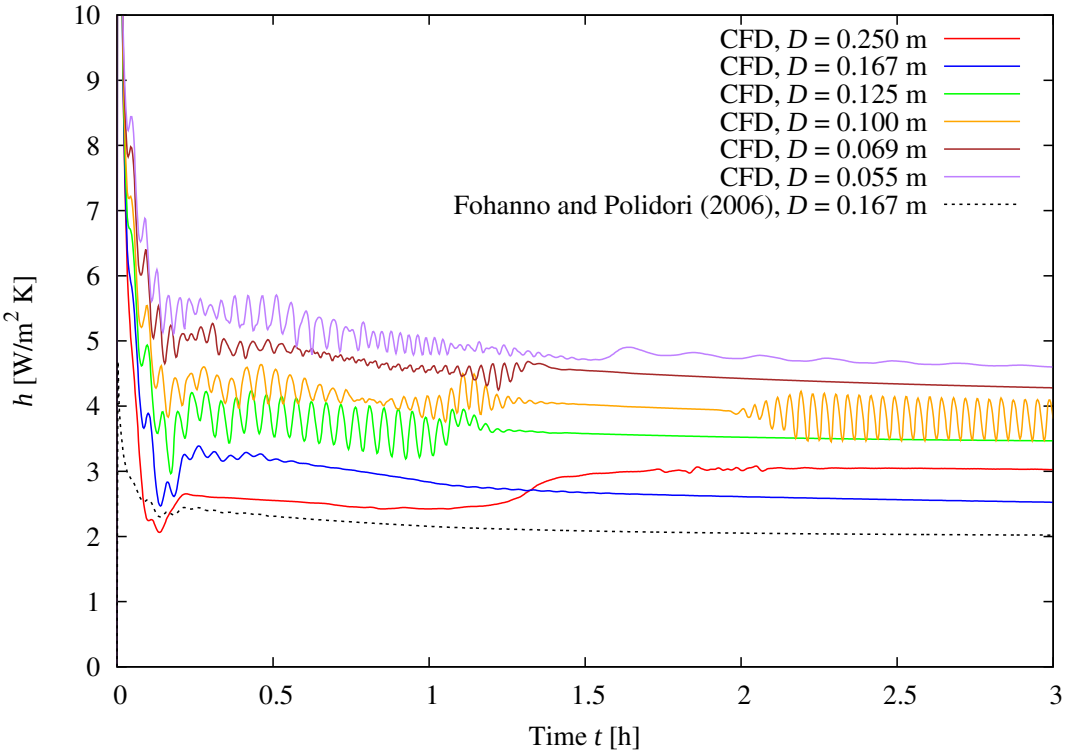

Figure 4.9: Natural convection test: average convective heat transfer coefficients (HTC) calculated by the CFD code vs. empirical HTC

not important.

Although the formula given in Eq. (4.2.2) was developed for the convective heat transfer across external surfaces of buildings, it can be also used in indoor spaces. The nature of the forced convection in these both environments is identical. The difference lies only in the phenomenon intensity. The heat transfer rate under the forced convection is linearly correlated with the local air velocity. The formula gives a reasonable approximation ($\pm 20\%$ error) of the convective heat transfer coefficient for the air velocity in the range of about 0–5 m/s. Data for higher air velocities are not available. However, the expected air velocity in the present simulations are of the order of 0.05–0.5 m/s, due to the fully controlled inlet velocity (constant, relatively low air speed).

In the present test the forced convection along the south wall is induced by a low temperature of the inlet air. When the inlet air is considerably cooler than the indoor air, it drops just after entering the room.

The initial air temperature set in the test is $T(\mathbf{x}, 0) = 19\,^{\circ}\mathrm{C}$, uniform in the entire air domain. The initial wall and window temperatures are uniform along the entire cross-section and equal $T_{wall}(x, 0) = 12\,^{\circ}$ and $T_{window}(x, 0) = 12\,^{\circ}\mathrm{C}$. The inlet air temperature is $T_{inlet}(t) = -10\,^{\circ}\mathrm{C} = \mathrm{const}$, while the ambient temperature

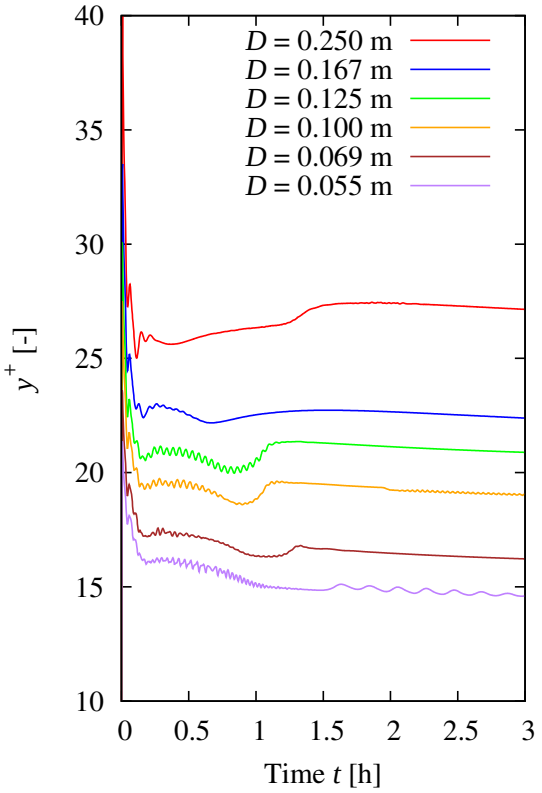

Figure 4.10: Natural convection test: average y^+ at wall's internal surface

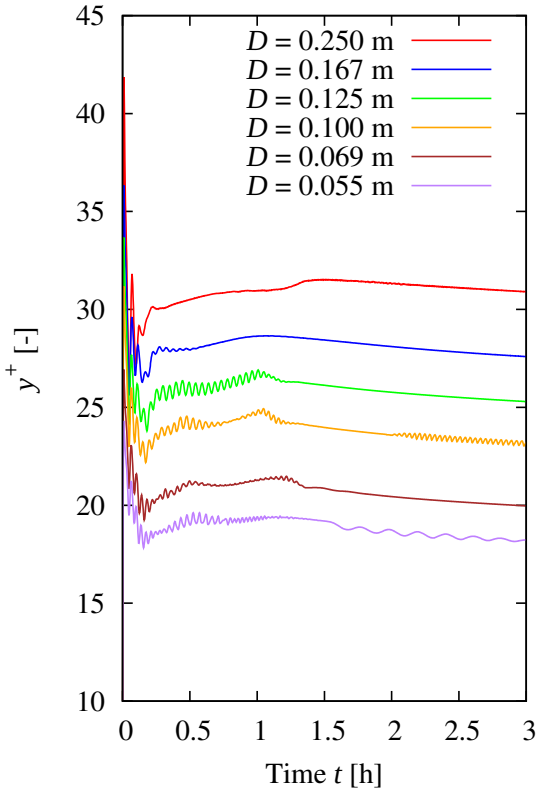

Figure 4.11: Natural convection test: average y^+ at window's internal surface

$T_{amb}(t) = 12\,°\mathrm{C} = \mathrm{const}$. The inlet air velocity $v_{inlet} = 0.54\,\mathrm{m/s}$ corresponds to the air exchange rate $ACH = 0.3$. The simulation stops at the time $t = 3\,\mathrm{h}$.

The wall and window are modeled as single-layer partitions. The material parameters of the wall are as follows: width $d_{wall} = 0.5\,\mathrm{m}$, density $\rho_{wall} = 400\,\mathrm{kg/m^3}$, conductivity $\lambda_{wall} = 0.15\,\mathrm{W/(m\,K)}$ and specific heat $c_{p,wall} = 1000\,\mathrm{J/(kg\,K)}$. In turn, the material parameters of the window are: width $d_{window} = 0.028\,\mathrm{m}$, density $\rho_{window} = 1000\,\mathrm{kg/m^3}$, conductivity $\lambda_{window} = 0.042\,\mathrm{W/(m\,K)}$ and specific heat $c_{p,window} = 1000\,\mathrm{J/(kg\,K)}$. The density of the window is evaluated as the approximate weighted average of densities of the glass and air for a double-glazed (4 / 20 / 4 mm) window. The U-values of the wall and window are $U_{wall} \approx 0.29\,\mathrm{W/(m^2K)}$ and $U_{window} \approx 1.20\,\mathrm{W/(m^2K)}$ (calculated using the standard heat transfer coefficients: $h_i = 8.1\,\mathrm{W/(m^2K)}$ and $h_e = 23\,\mathrm{W/(m^2K)}$).

As shown in Fig. 4.12, the air reaches a considerably higher velocity near the external wall than in the case of the natural convection. At the beginning of the simulation the air velocity in the central region of the wall is almost 0.3 m/s. Then, after reaching the floor, the air velocity rapidly decreases. However, during the

simulation the indoor air temperature rapidly decreases (Fig. 4.13) causing a less intense "wall-washing" effect. At the end of the simulation ($t = 3\,\mathrm{h}$), the average air velocity along the south wall decreases down to $0.06\,\mathrm{m/s}$.

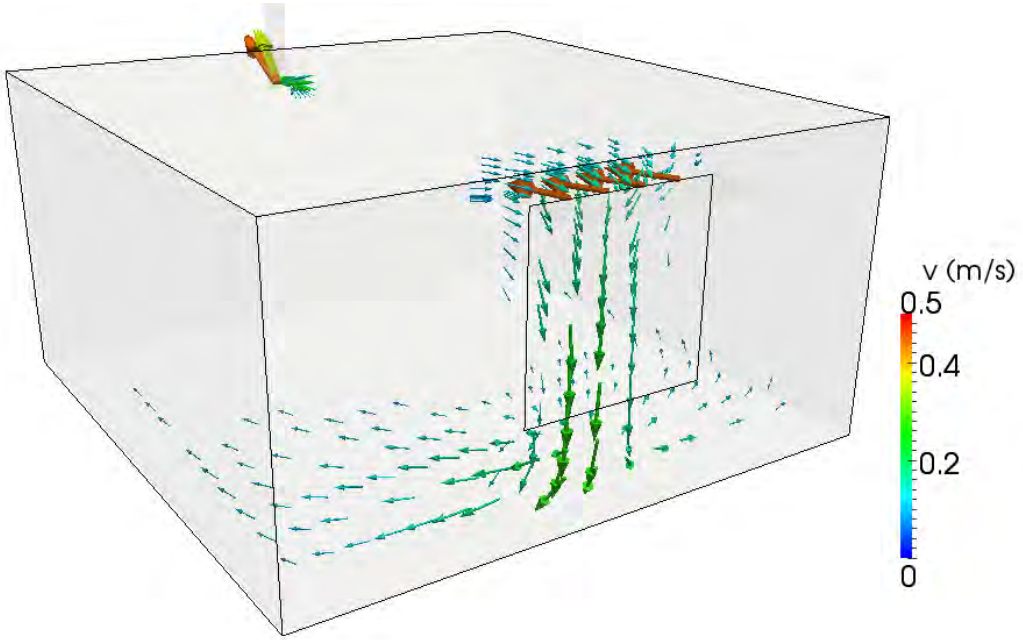

Figure 4.12: Forced convection test: air velocity v at time $t = 0.25$ h

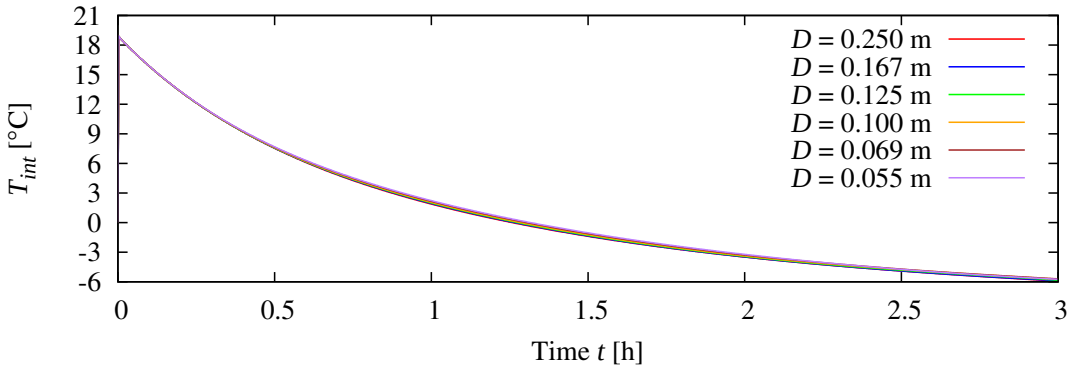

Figure 4.13: Forced convection test: average indoor temperature T_{int} calculated for different near-wall resolutions

The average HTC calculated by the CFD code are presented in Fig. 4.14. The results obtained using the six next-to-wall sizes D are compared with the empirical value of about $5\,\mathrm{W/(m^2K)}$. The empirical HTC calculated according to Eq. (4.2.2) vary between 4.955 and 5.420 $\mathrm{W/(m^2K)}$, depending on the near-wall mesh resolution and time.

As shown in Fig. 4.14, the obtained HTC differ considerably. The finer near-wall mesh, the higher is the overprediction of the heat transfer rate. Similarly to

the natural convection test (presented in the preceding section), the coarse near-wall meshes are the most accurate.

Similar solution oscillations are observed to the ones in the natural convection test. As discussed in the preceding section (page 121), oscillations could be damped down by using more outer loops in the solution algorithm, but this would considerably increase the computational time, while oscillations have a small influence on the average environmental and thermal comfort parameters.

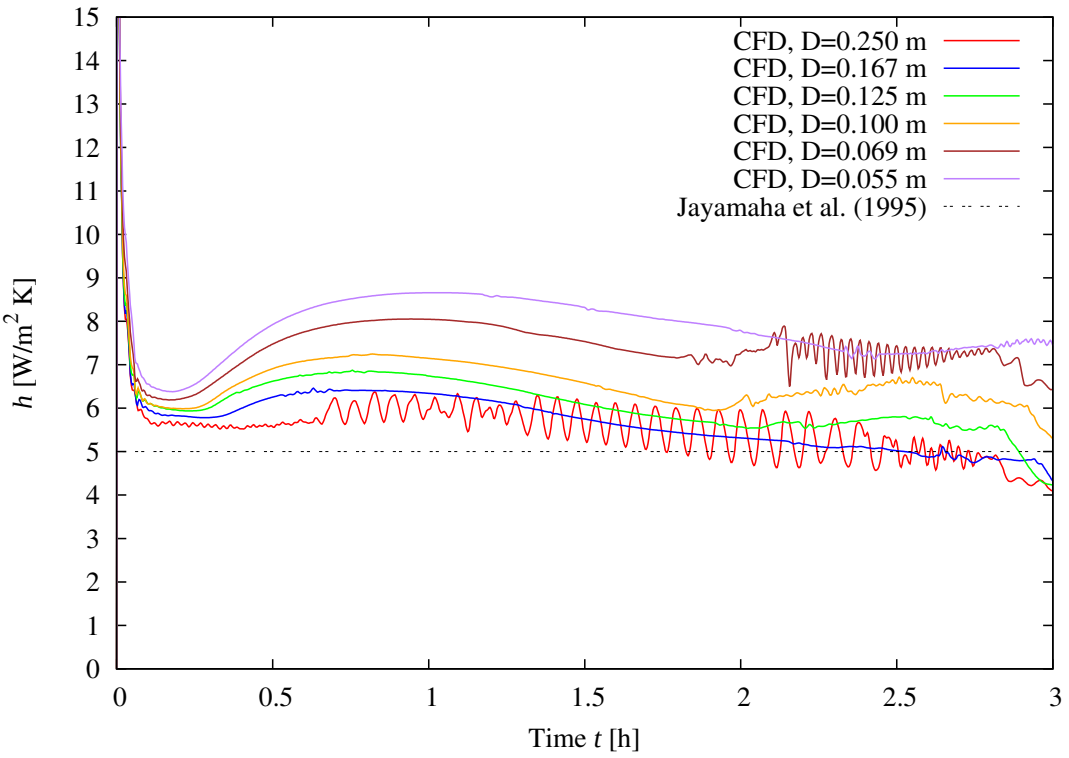

Figure 4.14: Forced convection test: average convective heat transfer coefficients (HTC) calculated by CFD vs. empirical HTC

At the end of the simulation, a noticeable drop of HTC is obtained. It is due to the fact that the indoor airflow pattern changes considerably due to the decreasing indoor temperature. At the time $t = 3\,\mathrm{h}$, the average indoor temperature is approximately -6 °C (Fig. 4.13), while the temperature of the wall is about 0 °C. As a result, a transition between the forced and natural convection along the south wall is observed. Fig. 4.15 shows the air velocity at the final time step $t = 3\,\mathrm{h}$. As shown, the "washing effect" is no present and the main air stream omits the south wall surface.

The average dimensionless wall distance y^+ for the window surface varies between 65 and 20 depending on D and t (Fig. 4.17). For the wall surface, the average y^+varies between 40 and 17 (Fig. 4.16). In the both cases, slightly higher values are

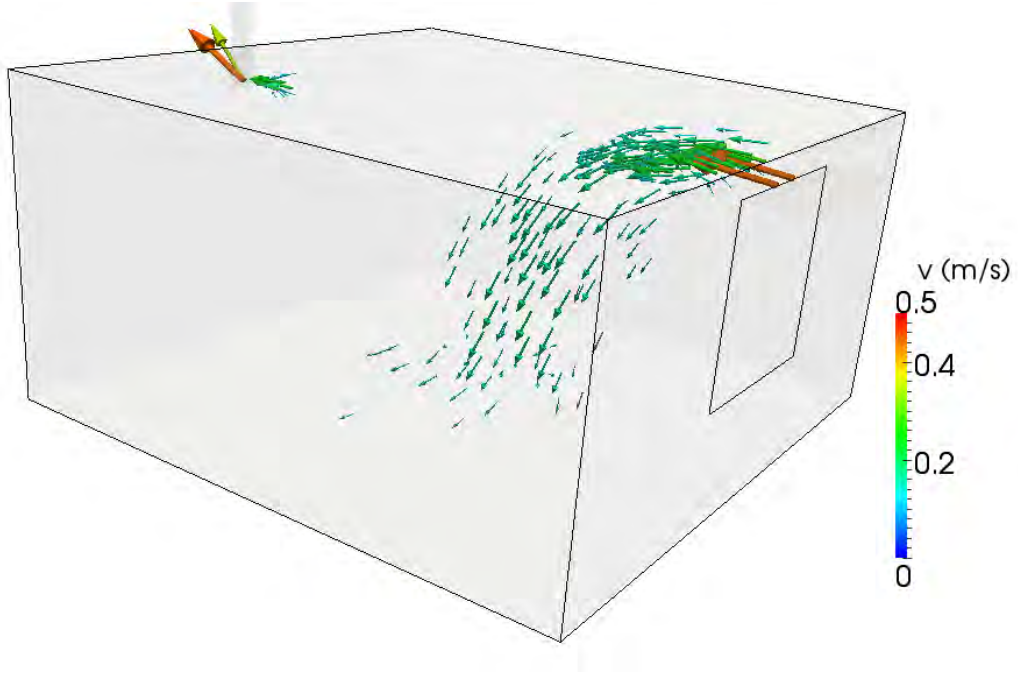

Figure 4.15: Forced convection test: air velocity v at time $t = 3$ h

noted at the beginning of the simulation, during the flow stabilization. Just like in the natural convection test, also in this case the y^+ values are not considered as the decisive factor. The proper next-to-wall cell size is chosen according to the HTC results (Fig. 4.14).

The accuracy of the HTC results obtained by models with the next-to-wall cell sizes $D = 0.250\,\text{m}$, $D = 0.167\,\text{m}$ and $D = 0.125\,\text{m}$ are considered as acceptable. Finally, with respect to the natural convection, the next-to-wall cell size $D = 0.167\,\text{m}$ is chosen, since it provides a good balance between the computational effort, accuracy and resolution.

4.3 Mesh independence test

The mesh independence test was carried out in order to investigate the influence of the mesh resolution (in a whole air domain) on the results. The total amount of cells has a great influence on the computational demand. On the other hand, coarse meshes give solution averaged over bigger control volumes, so the differences between maximum and minimum values are less accurate. However, in this study the main emphasis is put on the analysis of averaged values rather than cell values, so the averaging process is accepted to a certain extent.

Seven different general mesh discretizations are taken into account: 2912, 6840, 10462, 14774, 19776, 24030 and 28110 cells. The finest mesh (28110 cells) is over 15

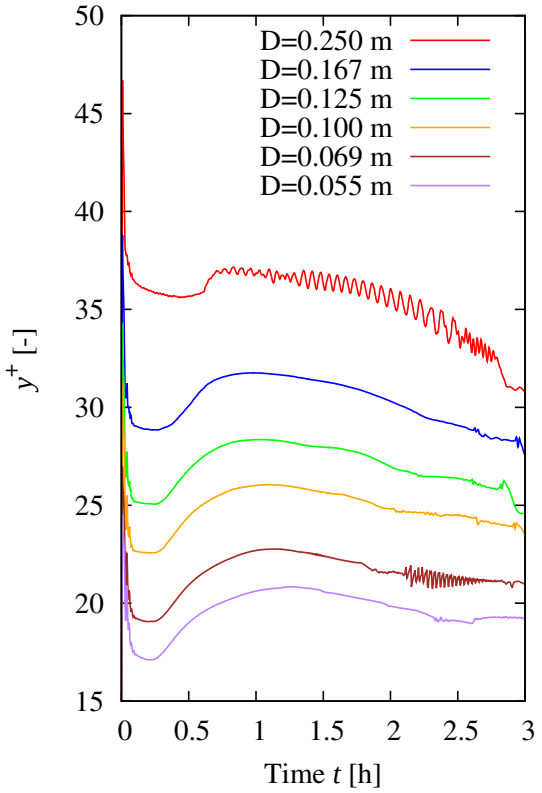

Figure 4.16: Forced convection test: average y^+ at wall's internal surface

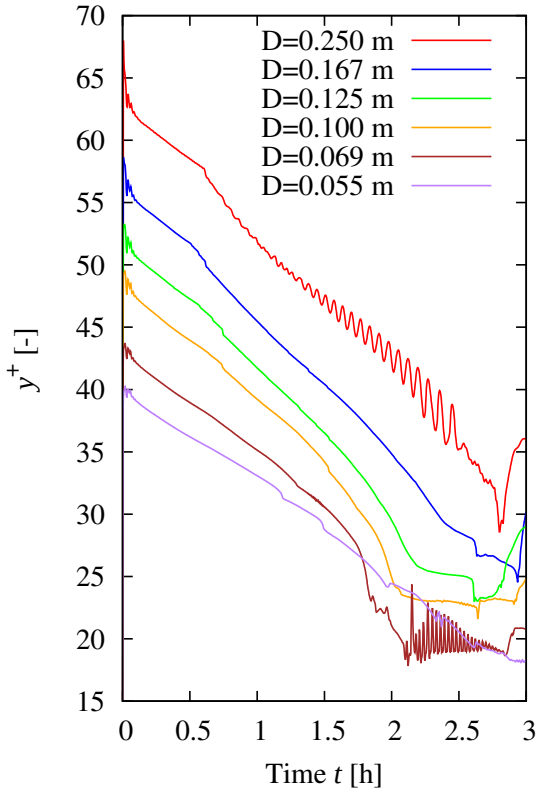

Figure 4.17: Forced convection test: average y^+ at window's internal surface

times more computationally demanding than the coarsest one (2912 cells). Thus, it is desirable to choose one of coarse meshes, because in these investigations one week long time periods are to be simulated.

The initial air temperature in the test is $T(\mathbf{x}, 0) = 20\,^{\circ}\mathrm{C}$, uniform in the entire air domain. The initial wall and window temperatures are uniform along the entire cross-section and equal $T_{wall}(x, 0) = 20\,^{\circ}$ and $T_{window}(x, 0) = 20\,^{\circ}\mathrm{C}$. The inlet air temperature is $T_{inlet}(t) = 10\,^{\circ}\mathrm{C} = \mathrm{const}$, while the ambient temperature $T_{amb}(t) = 12\,^{\circ}\mathrm{C} = \mathrm{const}$. The inlet air velocity $v_{inlet} = 0.54\,\mathrm{m/s}$, that approximately provides the air exchange rate $ACH = 0.3$. The simulation stops at the time step $t = 5\,\mathrm{h}$.

The wall and window are modeled as single-layer partitions. The material parameters of the wall are as follows: width $d_{wall} = 0.5\,\mathrm{m}$, density $\rho_{wall} = 400\,\mathrm{kg/m^3}$, conductivity $\lambda_{wall} = 0.15\,\mathrm{W/(m\,K)}$ and specific heat $c_{p,wall} = 1000\,\mathrm{J/(kg\,K)}$. In turn, the material parameters of the window are as follows: width $d_{window} = 0.028\,\mathrm{m}$, density $\rho_{window} = 1000\,\mathrm{kg/m^3}$, conductivity $\lambda_{window} = 0.042\,\mathrm{W/(m\,K)}$ and specific heat $c_{p,window} = 1000\,\mathrm{J/(kg\,K)}$. The density of the window is evaluated as the approximate weighted average of the densities of the glass and air for a double-glazed (4 / 20 / 4 mm) window. The U-values of the wall and window are $U_{wall} \approx$

0.29 W/(m^{2}K) and $U_{window} \approx 1.20$ W/(m^{2}K) (calculated using the standard heat transfer coefficients: $h_i = 8.1$ W/(m^{2}K) and $h_e = 23$ W/(m^{2}K)).

Fig. 4.18 shows the evolution of the average indoor temperature T_{int}. As shown, the mesh resolution has no significant influence on the average temperature. In all cases during the 5 h time period the temperature drops from the initial 20 °C to approximately 11 °C.

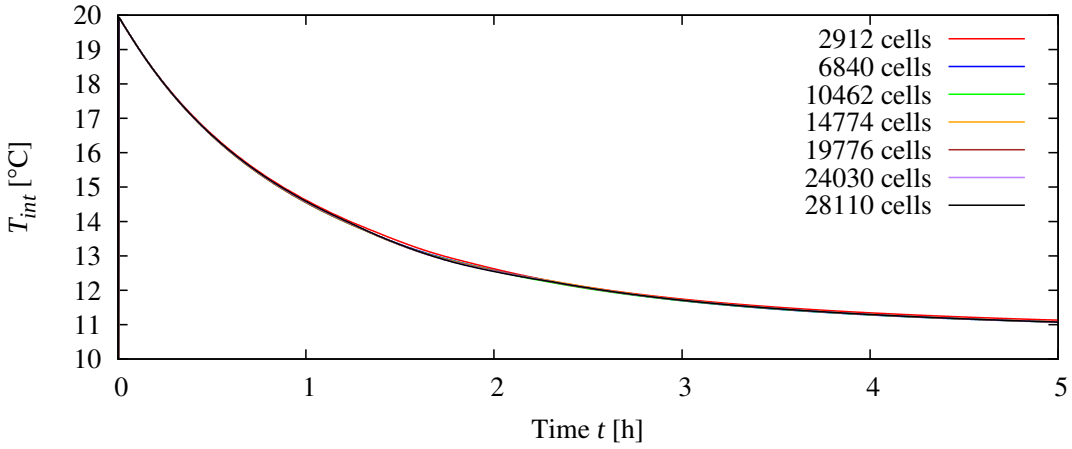

Figure 4.18: Mesh independence test: average indoor temperature T_{int}

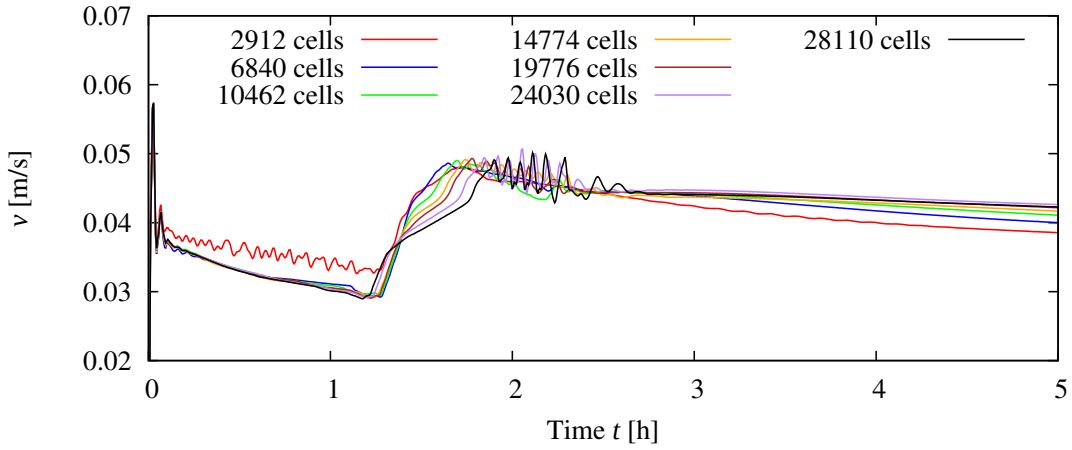

Figure 4.19: Mesh independence test: average air velocity v

More significant differences in the results are in the case of the average indoor air velocity (Fig. 4.19). Average velocities vary during the simulation from about 0.03 m/s to 0.05 m/s. Some solution oscillations ca be observed in all cases. The oscillations could be damped down by employing additional outer loops (PIMPLE loops) in the solution algorithm. However, this would increase the computing time. The oscillations do not significantly influence other environmental parameters, like the temperature (Fig. 4.18). This issue is also discussed in Sections 4.2.1 and 4.2.2.

Initially, the mesh with 6840 cells was applied by the author to perform the

simulations. However, the preliminary tests showed that the mesh is still too computationally demanding. Hence, finally the adopted mesh resolution is 2912 cells (the coarsest one).

This work presents the results of over 100 simulations. Even small increases in computational time of a single simulation significantly extends the total computational time needed to perform all simulations. The results showed that the accuracy of the coarsest mesh is sufficient. Comparing to the results provided by the finest mesh, the error in the average velocity does not exceed 0.005 m/s.

In the adopted mesh (Fig. 4.20) the number of cells in the vertical cross-section of the inlet duct is 12 (3 in the vertical direction and 4 in the horizontal direction). The number of cells in the horizontal cross-section of the outlet duct is also 12 (3 x 4).

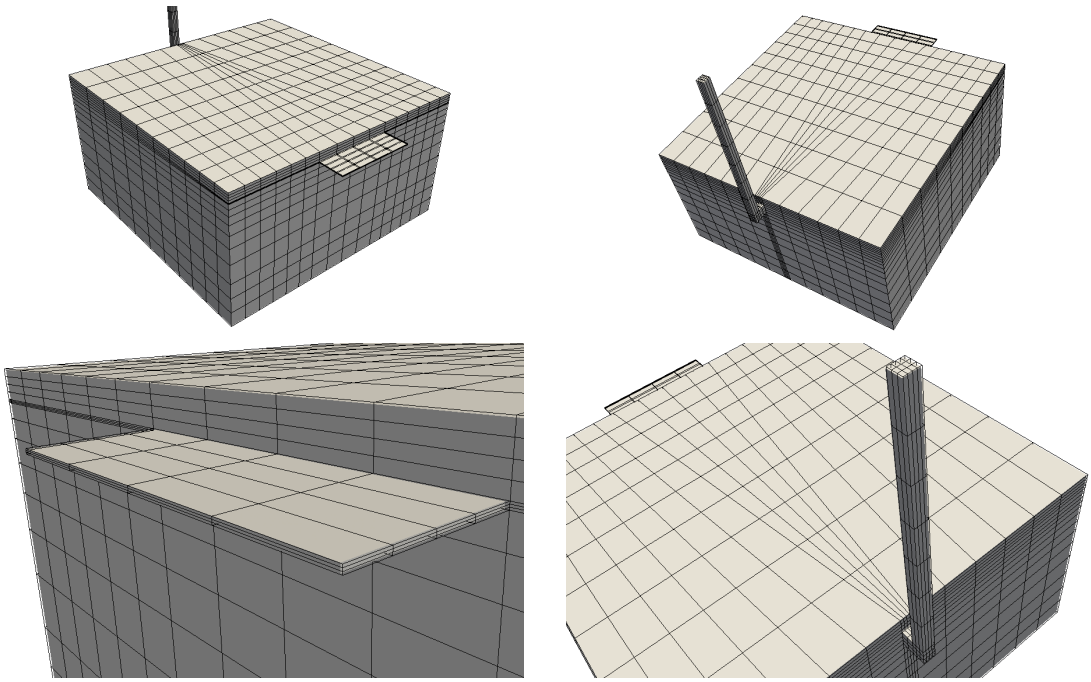

Figure 4.20: Adopted mesh (2912 cells)

4.4 Coupling interval independence test

The aim of the test presented in this section is to find the suitable coupling interval. The coupling interval is the time interval between the coupling steps (Fig. 3.6). The smaller coupling interval, more often the wall and the air submodels exchange data between each other. If the coupling interval is too big, models are poorly linked and solutions are inconsistent or inconvergent. This issue is discussed in Section 3.4.

In the present model, the air submodel is based on CFD, which requires significantly smaller time steps than the wall submodel. Thus, as shown in Fig. 3.6, the

wall model has to wait between the coupling steps. During the coupling step, the calculations are performed in both air and wall submodels, and at the end of the step, the data are exchanged. In the present test 17 different coupling intervals are checked: 1, 5, 10, 15, 20, 25, 30, 35, 40, 45, 50, 55, 60, 100, 150, 200 and 250 seconds.

The initial air temperature prescribed in the test is $T(\mathbf{x}, 0) = 20\,^{\circ}\mathrm{C}$, uniform in the entire air domain. The initial wall and window temperatures are uniform along the entire cross-section and equal $T_{wall}(x, 0) = 12\,^{\circ}$ and $T_{window}(x, 0) = 12\,^{\circ}\mathrm{C}$. The inlet air temperature is $T_{inlet}(t) = -10\,^{\circ}\mathrm{C} = \mathrm{const}$, while the ambient temperature $T_{amb}(t) = 12\,^{\circ}\mathrm{C} = \mathrm{const}$. The inlet air velocity $v_{inlet} = 0.54\,\mathrm{m/s}$ corresponds to the air exchange rate $ACH = 0.3$. The simulation stops at the time step $t = 3\,\mathrm{h}$.

The wall and window are modeled as single-layer partitions. The material parameters of the wall are as follows: width $d_{wall} = 0.5\,\mathrm{m}$, density $\rho_{wall} = 400\,\mathrm{kg/m^3}$, conductivity $\lambda_{wall} = 0.15\,\mathrm{W/(m\,K)}$ and specific heat $c_{p,wall} = 1000\,\mathrm{J/(kg\,K)}$. The material parameters of the window are: width $d_{window} = 0.028\,\mathrm{m}$, density $\rho_{window} = 1000\,\mathrm{kg/m^3}$, conductivity $\lambda_{window} = 0.042\,\mathrm{W/(m\,K)}$, specific heat $c_{p,window} = 1000\,\mathrm{J/(kg\,K)}$. The density of the window is evaluated as the approximate weighted average of the densities of the glass and air for a double-glazed (4 / 20 / 4 mm) window. The U-values of the wall and window are $U_{wall} \approx 0.29\,\mathrm{W/(m^2K)}$ and $U_{window} \approx 1.20\,\mathrm{W/(m^2K)}$ (calculated using the standard heat transfer coefficients: $h_i = 8.1\,\mathrm{W/(m^2K)}$ and $h_e = 23\,\mathrm{W/(m^2K)}$).

The effect of the coupling interval is the most significant at the interface boundaries, i.e. the wall and window internal surfaces. Furthermore, since the window's U-value is higher than the wall's U-value, the coupling intervals affect more the window surface. Therefore, the window internal surface can be considered as the critical one in this test. The comparison of the average window internal surface temperatures T_{si} for different coupling intervals is presented in Fig. 4.21.

It was found that the coupling interval has a small influence on the final result, at least in the considered range of coupling intervals (1–250 s). It can be observed that the large coupling intervals cause the lower heat transfer rate between the air and window surface. The temperature changes are less rapid. In the beginning of the simulation, the temperature differences between cases reach approximately 1 °C. After the 3 hours time period, the temperatures difference decreases significantly.

According to the test results, the coupling interval of 20 s was assumed. The results showed that a larger interval could be even adopted, but the 20 s interval gives more confidence that the solution is convergent for more dynamic conditions and higher U-values.

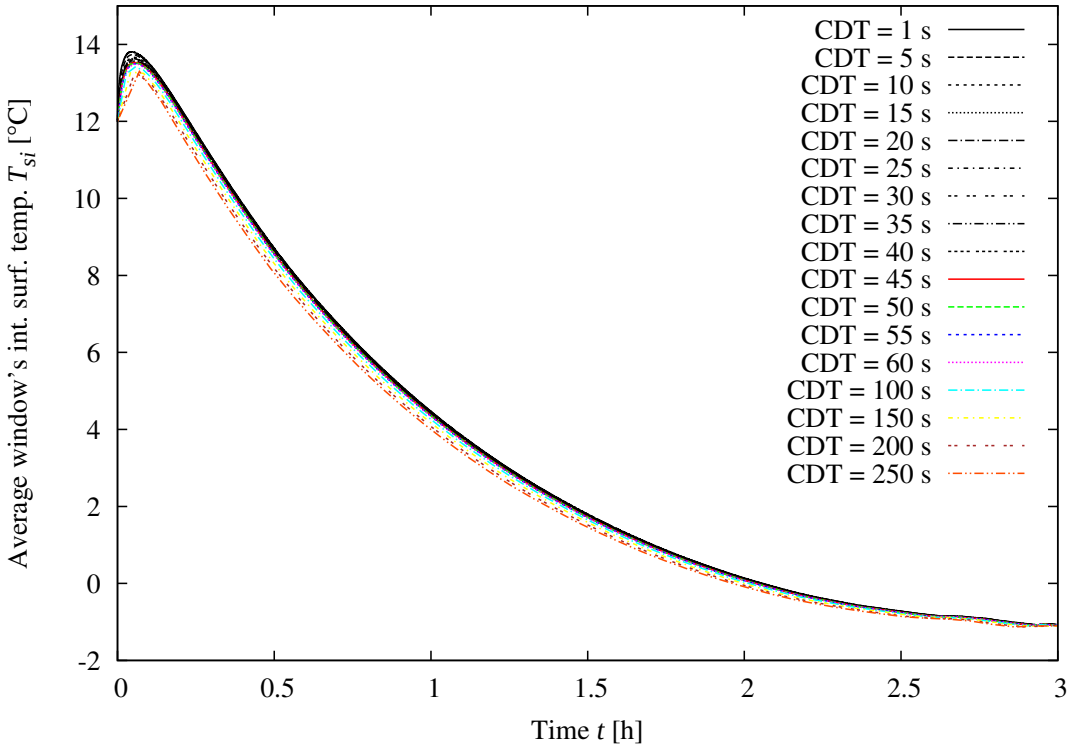

Figure 4.21: Coupling interval independence test: window's internal surface temperature (T_{si}) calculated using different coupling intervals (CDT)

4.5 Summary

The chapter presented validation of the developed model. The performed tests included: wall model validation, near-wall mesh validation, whole-domain mesh independence test and coupling interval independence test.

After the results analysis, the coarse mesh with 2912 cells was assumed. The adopted distance D of the next-to-wall cell centroid to the surface of the south wall was 0.167 m and the coupling interval of 20 s was chosen

Unfortunately, no experimental data were available to the author to fully verify the model. However, the results obtained in the performed tests let to presume that the model is fully correct.

Chapter 5

Simulation results

The aim is to analyze the influence of the thermal capacitance of external walls on the indoor thermal comfort. The numerical model developed for this purpose (Chapter 3) enables to analyze the indoor air as a nonuniform environment. Thanks to the incorporated CFD solver, the model is able to predict the indoor air velocity which significantly contributes to the thermal comfort sensation.

Due to the model complexity, its computational demand is significant. Thus, only a limited number of simulations could be carried out within investigations. One of the challenges was to select a proper set of test cases. To accomplish this task, a number of different wall structures was chosen and tested under various conditions.

Four types of tests were designed and three groups of wall structures were modeled. To limit the computational time, depending on the wall type, the specific wall was designated for all the tests or only for the chosen subset. The wall structures taken into account in the study are presented in Section 5.1. The description of the test cases is presented in Section 5.2.

The total number of the performed simulations (without validation and preliminary tests) is 84, whereof 37 simulations had a long computational time (around 10 days per simulation). The computational time of remaining simulations was around 1 day per simulation. The simulations were performed on a quad-core computer, that enabled to perform simultaneously four simulations. The total run-time of the 84 simulations was around 3.5 months.

5.1 Wall structures

Three groups of wall structures are taken into account. The walls differ in material parameters and number of layers.

The **first group** consists of homogeneous single-layer walls. The walls have the same U-value, $U = 0.3\,\mathrm{W/(m^2K)}$, but the different thermal capacitance. The specific heat c of the materials is constant, but the density ρ varies from 150 up to $3750\,\mathrm{kg/m^3}$. The walls are 0.25 m wide and their conductivity is $\lambda = 0.079\,\mathrm{W/(m\,K)}$. The material parameters of the walls from the first group are listed in Table 5.1.

The **second group** is similar to the first one, with the only difference that the walls have the two times lower U-value, i.e. $U = 0.15\,\mathrm{W/(m^2K)}$ ($\lambda = 0.039$ $\mathrm{W/(m\,K)}$). The material parameters of the walls from the second group are listed in Table 5.2.

The assumed thermal properties of the walls from the first and the second group do not represent any real materials. However, the properties are within the range of typical building materials.

The **third group** of the walls consists of commonly used in the engineering practice, the multilayer wall structures. The goal was to design multilayer walls with the U-value close to $0.3\,\mathrm{W/(m^2K)}$, but the considerably different thermal capacitance. The designed structures have the U-values of about $U = 0.295 \pm 0.002\,\mathrm{W/(m^2K)}$. In the following, the U-value of these walls is approximated to a one decimal place, i.e. $U = 0.3\,\mathrm{W/(m^2K)}$, to underline that their results are to be compared with walls from the first group. All multilayer walls meet Polish building requirements ($U \leq 0.3\,\mathrm{W/(m^2K)}$ [113]). The material parameters and layers composition of multilayer walls are listed in Table 5.3. The first layer (no. 1) in each wall type is placed at the interior side of the wall. Every subsequent layer is closer to the exterior.

The walls in Tables 5.1, 5.2, 5.3 are listed by the increasing wall (planar) thermal capacitance C_{wall} [kJ/(m^{2}K)] which is defined here as follows:

$$C_{wall} = \sum_{i}^{n} c_i \rho_i d_i \,, \tag{5.1.1}$$

where n is the total number of layers in a wall, and c_i, ρ_i, d_i are the specific heat [J/(kg K)], the density [kg/m^3] and the width [m] of the i-layer. It should be noticed, that the wall thermal capacitance C_{wall} does not take into account the spatial distribution of the thermal capacitance, what also influences the wall thermal inertia. The effect of the nonuniform thermal capacitance distribution is investigated in this work by comparing walls with a similar C_{wall} but a different design (e.g. different layer sequence).

The U-values of all walls are calculated using the standard surface heat transfer resistances, $R_{si} = 0.13\,\mathrm{m^2K/W}$ and $R_{se} = 0.04\,\mathrm{m^2K/W}$ (according to ISO 6946 [75]).

Table 5.1: Material parameters of single-layer walls with $U = 0.3\,\mathrm{W/(m^2K)}$

Wall's name	Width d [m]	Density ρ [kg/m^3]	Conductivity λ [W/(m K)]	Specific heat c [J/(kg K)]	Wall heat cap. C_{wall} [kJ/(m^2 K)]
S-1/U-0.3	0.25	150	0.079	1000	37.5
S-2/U-0.3	0.25	550	0.079	1000	137.5
S-3/U-0.3	0.25	950	0.079	1000	237.5
S-4/U-0.3	0.25	1350	0.079	1000	337.5
S-5/U-0.3	0.25	1750	0.079	1000	437.5
S-6/U-0.3	0.25	2150	0.079	1000	537.5
S-7/U-0.3	0.25	2550	0.079	1000	637.5
S-8/U-0.3	0.25	2950	0.079	1000	737.5
S-9/U-0.3	0.25	3350	0.079	1000	837.5
S-10/U-0.3	0.25	3750	0.079	1000	937.5

5.2 Simulation description

The wall structures are subjected to four types of simulations. The analyses are created by combining two driving (i.e. outdoor and inlet) temperature profiles with two air exchange rates. The simulation time in all tests is 7 days (168 h). The assumed initial and the boundary temperatures are described in Sections 3.2.2 and 3.3.2. The initial temperature of the indoor air is uniform and is equal to 20 °C. No internal heat source is taken into account. The study focuses on the influence of the thermal capacitance of the wall on the indoor thermal comfort.

The initial wall temperature distribution in the summer week simulation is a steady state temperature calculated for the indoor initial temperature (20 °C) and the outdoor initial temperature (the first temperature record from the climate database for the considered period: 14.6 °C). The initial temperature distribution in the wall in the stability test is assumed to be uniform in the entire cross-section and equal to 20 °C.

In the first driving temperature profile type, the outdoor temperature is equal to the sol-air temperature T_{sol} (Eq. (3.3.2)) calculated for the southern wall, while the inlet temperature is equal to the ambient dry bulb temperature T_{DBT}. Both temperatures are derived from the climate data for the city of Elbląg (Poland) for the period of August 11–17 [29]. The climate database contains 8760 records representing 8760 hours of the Typical Year. The simulations start at 5328 h (midnight between August 10th and 11th) and stop at 5496 h (midnight between August 17th and 18th). The temperatures between the full hours are linearly interpolated. The functions $T_{sol}(t)$ and $T_{DBT}(t)$ are presented in Fig. 5.1. The tests using the outdoor

Table 5.2: Material parameters of single-layer walls with $U = 0.15\,\mathrm{W/(m^2K)}$

Wall's name	Width d [m]	Density ρ [kg/m^3]	Conductivity λ [W/(m K)]	Specific heat c [J/(kg K)]	Wall heat cap. C_{wall} [kJ/(m^2 K)]
S-1/U-0.15	0.25	150	0.039	1000	37.5
S-2/U-0.15	0.25	550	0.039	1000	137.5
S-3/U-0.15	0.25	950	0.039	1000	237.5
S-4/U-0.15	0.25	1350	0.039	1000	337.5
S-5/U-0.15	0.25	1750	0.039	1000	437.5
S-6/U-0.15	0.25	2150	0.039	1000	537.5
S-7/U-0.15	0.25	2550	0.039	1000	637.5
S-8/U-0.15	0.25	2950	0.039	1000	737.5
S-9/U-0.15	0.25	3350	0.039	1000	837.5
S-10/U-0.15	0.25	3750	0.039	1000	937.5

and inlet temperature profiles are denoted as the *summer week simulations.*

In the second temperature profile type, the outdoor and inlet temperatures are constant and equal to 0 °C. The tests using these constant temperatures are denoted as the *indoor environment stability tests* or just the *stability tests.* Their purpose is to find out how rapid are negative changes in the indoor air temperature due to the outdoor temperature drop in buildings with different external walls.

To quantify stabilizing capabilities of different walls, the time (t_{drop}) needed for the indoor temperature to drop to a certain level (T_{drop}) is measured. In order to take into account a nonlinear character of the indoor temperature function, three different temperature drop levels T_{drop} are taken into account: 15 °C, 10 °C and 5 °C. Due to a nonlinear character of temperature variations, differences in the measured times t_{drop} for different cases are the higher, the lower is the chosen temperature T_{drop} (the temperature for which the time comparison is performed).

Two air exchange rates are taken into account in the tests: $\mathrm{ACH} = 0.01\,\mathrm{h^{-1}}$ and $\mathrm{ACH} = 0.3\,\mathrm{h^{-1}}$. The air exchange rates are obtained by setting the fixed inlet air velocity: $v = 0.018056\,\mathrm{m/s}$ for $\mathrm{ACH} = 0.01\,\mathrm{h^{-1}}$ and $v = 0.541667\,\mathrm{m/s}$ for $\mathrm{ACH} = 0.3\,\mathrm{h^{-1}}$. The tests with ACH close-to-zero show the thermal capacitance performance unaffected by the inlet air. On the other hand, $\mathrm{ACH} = 0.3\,\mathrm{h^{-1}}$ is the minimum air exchange rate from the hygienic point of view, according to the ISO 13790 standard [73].

Although the typical air exchange rates in real buildings reach as much as $1\,\mathrm{h^{-1}}$ (and more), air exchange rates higher than $0.3\,\mathrm{h^{-1}}$ are not taken into account in this study, because of the too long simulation run-time. The air exchange rate is

Table 5.3: Material parameters of multilayer walls with $U = 0.295 \approx 0.3\,\mathrm{W/(m^2K)}$. Walls are arranged by increasing wall thermal capacitance C_{wall}. First layers (no. 1) are placed at the interior side. Acronyms: EPS - expanded polystyrene, AAC - autoclaved aerated concrete, ECAC - expanded clay aggregate concrete.

Wall's name	No.	Layer	Width d [m]	Density ρ [kg/m^3]	Conduct. λ [W/(m K)]	Spec. heat c [J/(kg K)]
M-1	1	Fiber-cem. board	0.013	450	0.14	2090
	2	EPS	0.13	12	0.043	1460
	3	Fiber-cem. board	0.013	450	0.14	2090
		Wall thermal capacitance $C_{wall} = 26.73$ kJ/(m^2 K)				
M-2	1	Lime-cem. plaster	0.015	1620	0.83	1000
	2	AAC	0.22	500	0.22	840
	3	Mineral wool	0.09	140	0.041	750
		Wall thermal capacitance $C_{wall} = 126.15$ kJ/(m^2 K)				
M-3	1	Lime-cem. plaster	0.015	1620	0.83	1000
	2	ECAC	0.15	1200	0.54	840
	3	Mineral wool	0.12	140	0.041	750
		Wall thermal capacitance $C_{wall} = 188.10$ kJ/(m^2 K)				
M-4	1	Gypsum board	0.01	1000	0.23	1000
	2	Mineral wool	0.08	140	0.041	750
	3	Spruce logs	0.20	550	0.16	2510
		Wall thermal capacitance $C_{wall} = 298.31$ kJ/(m^2 K)				
M-5	1	Lime-cem. plaster	0.015	1620	0.83	1000
	2	Ceram. hollow brick	0.25	900	0.33	880
	3	EPS	0.10	12	0.043	1460
	4	Clinker brick	0.12	1900	1.05	880
		Wall thermal capacitance $C_{wall} = 424.69$ kJ/(m^2 K)				
M-6	1	Lime-cem. plaster	0.015	1620	0.83	1000
	2	Ceramic brick	0.25	1800	0.77	880
	3	EPS	0.12	12	0.043	1460
	4	Clinker brick	0.12	1900	1.05	880
		Wall thermal capacitance $C_{wall} = 623.04$ kJ/(m^2 K)				
M-7	1	Lime-cem. plaster	0.015	1620	0.83	1000
	2	Concrete	0.35	2200	1.30	840
	3	Mineral wool	0.12	140	0.041	750
		Wall thermal capacitance $C_{wall} = 683.70$ kJ/(m^2 K)				

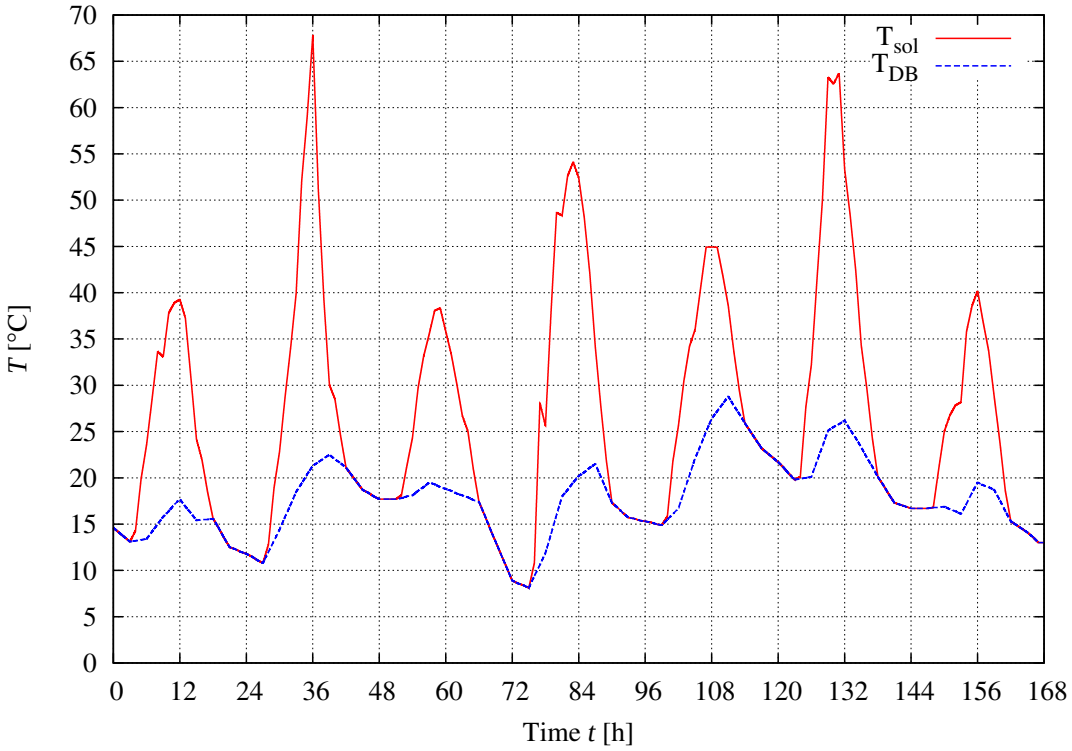

Figure 5.1: Sol-air and dry bulb temperatures in the summer week simulation

set by the fixed inlet air velocity, which in turn, influences indoor air velocities. If the higher velocities are present, the lower time step has to be adopted (due to the maximum Courant number condition, Eq. (3.2.16)), and consequently the run-time increases.

The ACH $= 0.01\,\mathrm{h}^{-1}$ is not replaced with the zero air exchange rate, because the zero inlet air velocity would enforce the change of the inlet / outlet boundary conditions, while the difference in the results would be negligible.

By combining the given driving temperature profiles and air exchange rates, the following four tests are prescribed:

1. summer week simulation, ACH $= 0.01\,\mathrm{h}^{-1}$,
2. summer week simulation, ACH $= 0.3\,\mathrm{h}^{-1}$,
3. indoor environment stability test, ACH $= 0.01\,\mathrm{h}^{-1}$,
4. indoor environment stability test, ACH $= 0.3\,\mathrm{h}^{-1}$.

Fig. 5.2 depicts the wall groups subjected to different tests. The single-layer walls with $U = 0.3\,\mathrm{W/(m^2K)}$ are subjected to all tests. The single-layer walls with $U = 0.15\,\mathrm{W/(m^2K)}$ are subjected to three tests: both stability tests and the summer week

simulation with the close-to-zero ACH. The multilayer walls used in the engineering practice are subjected only to the summer week simulations.

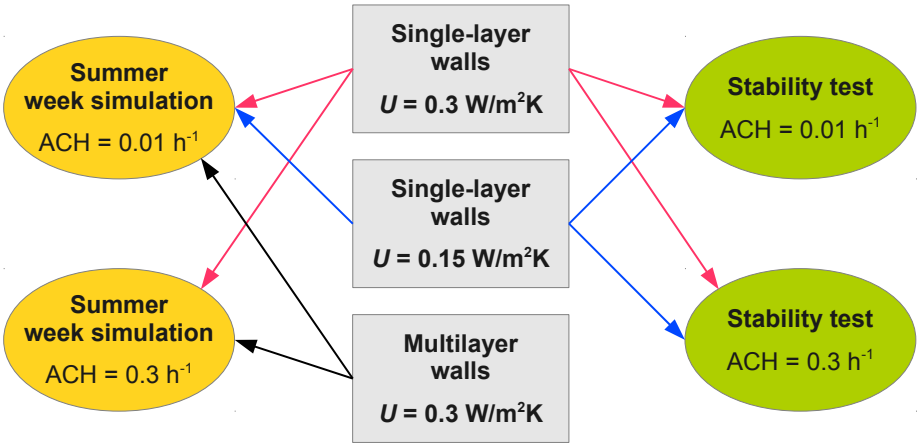

Figure 5.2: Scheme of the conducted tests

The results for ACH $= 0.3\,\mathrm{h}^{-1}$ include the ventilation effect, so they are the most meaningful. The thermal capacitance of the building envelope stabilizes the indoor temperature. However, the indoor temperature is also affected by the heat load due to the ventilation air. The ventilation air affects the indoor temperature directly, unlike the heat loads due to the transmission, which can be attenuated by the building envelope. If the ventilation rate is high, the indoor temperature quickly increases or decreases to the outdoor temperature, even if a building is well insulated. Therefore the results for ACH $= 0.3\,\mathrm{h}^{-1}$ are of a great importance, because they show how the thermal capacitance is effective in the indoor environment stabilization.

It should be noted that all the cases analyzed in this work share the same geometry. Thus, the absolute values of environmental parameters or the relations between different factors should be analyzed with a special care. These results do not provide fit-to-all guidelines. The same walls can perform differently under different conditions. However, the present results still can provide some important information. In order to make the investigation results easier, the case geometry is deliberately kept simple. The obtained results give some quantitative relationships between various factors which can be extrapolated to other similar cases.

Based on the results of the calculations the influence of the thermal capacitance on the indoor thermal comfort can be analyzed from various points of view. The main questions to be answered are:

1. How does the wall thermal capacitance influence the indoor thermal comfort?

2. What is the performance of the thermal capacitance in walls with the different insulation?

3. How does the ventilation rate affect the thermal capacitance performance?

4. How does the thermal capacitance contribute to the uniformity of indoor conditions?

5. How does a nonuniform distribution of the thermal capacitance affect its performance?

The results of simulations are discussed in the following two Sections: 5.3 and 5.4.

5.3 Summer week simulation results

The results of the summer week simulations are listed in the following sequence:

1. single-layer walls with $U = 0.3$ W/(m^{2}K), ACH = 0.01 h^{-1},

2. single-layer walls with $U = 0.15$ W/(m^{2}K), ACH = 0.01 h^{-1},

3. multilayer walls with $U = 0.3$ W/(m^{2}K), ACH = 0.01 h^{-1},

4. single-layer walls with $U = 0.3$ W/(m^{2}K), ACH = 0.3 h^{-1},

5. multilayer walls with $U = 0.3$ W/(m^{2}K), ACH = 0.3 h^{-1}.

The most important results are the average indoor temperatures, average air velocities, t south wall temperatures and average values of thermal comfort indices: PMV, PPD and DR. The spatial distribution of these variables is also discussed.

5.3.1 Simulation case: ACH = 0.01 h^{-1}

5.3.1.1 Single-layer walls with $U = 0.3$ W/(m^{2}K)

The wall thermal capacitance has a significant influence on the time-dependent temperature distribution. The effect is the more pronounced, the higher U-value of the wall is. Fig. 5.3 presents the temperatures on the internal surface of single-layer walls with $U = 0.3\,\mathrm{W/(m^2K)}$ at different thermal capacitances. As shown, the walls with the low thermal capacitance (low thermal inertia) experience large temperature swings. The temperature at the surface of the wall S-1/U-0.3 (with the lowest thermal capacitance) varies dynamically between 17 °C and 31 °C during the analyzed time period. The maximum daily temperature change on its surface

is 8 °C. In turn, the wall S-10/U-0.3 is slightly affected by outdoor temperature changes (sol-air temperature). The changes of its surface temperature are mild and slow. During the entire week the temperature varies between 18.5 °C and 20.4 °C. The temperature range is over 7 times narrower for the wall S-1/U-0.3.

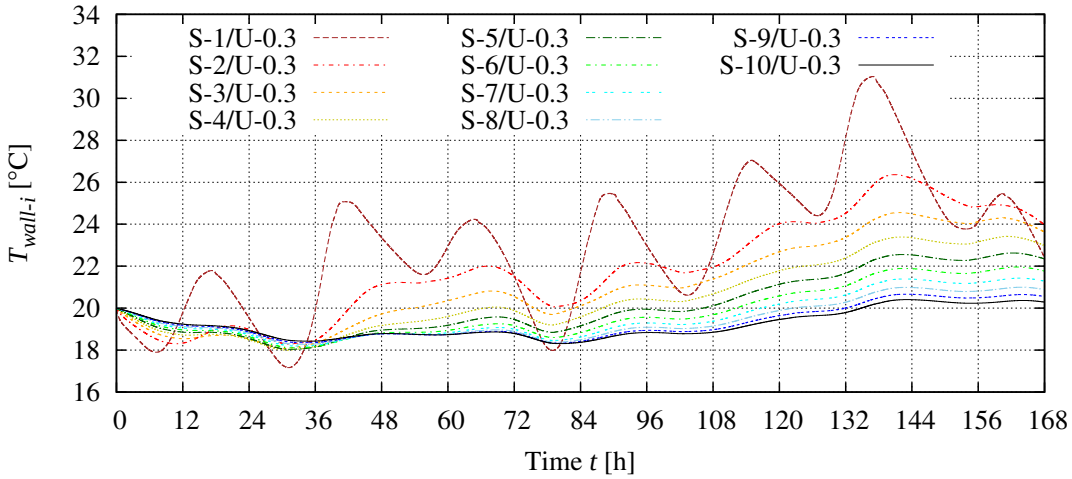

Figure 5.3: Summer week simulation, ACH = 0.01 h^{-1}, single-layer walls with U = 0.3 W/(m^2K): average wall internal surface temperature T_{wall-i}

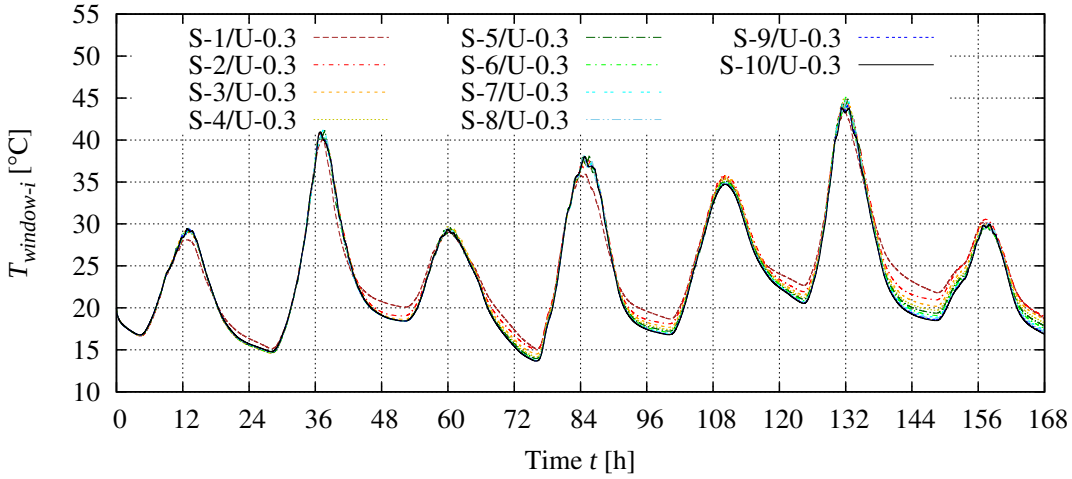

Figure 5.4: Summer week simulation (ACH = 0.01 h^{-1}, single-layer walls with U = 0.3 W/(m^2K)): average window's internal surface temperature $T_{window-i}$

By comparing Figs. 5.3 and 5.1 it can be noticed, that there is a time lag between the extreme surface and outdoor temperatures. The higher the wall thermal capacitance, the higher is the time lag. The maximum difference in the time lags is observed between S-1/U-0.3 and S-10/U-0.3 and is about 4–6 h (it varies in time).

The temperature of indoor surfaces has a direct influence on the thermal comfort because indoor surfaces exchange the heat with a human body by the thermal radiation. In this work, however, it is assumed that the mean radiant tempera-

ture (MRT) is equal to the average indoor temperature. This assumption is often adopted in building thermal simulations. It does not generate any significant errors. Nevertheless, it should be taken into account, that when the surface temperature strongly differs from the indoor temperature, its influence on the thermal comfort is underestimated. Thus, in this work the wall surface temperature is presented in all cases.

The temperature of the window internal surface is presented in Fig. 5.4. The window surface experiences larger temperature swings than the wall surface. It is due to significant differences in U-values and thermal capacitances. The window internal surface temperature do not differ significantly between the cases. The largest differences are observed during nights when the temperature rapidly drops. At the approximately 148 hour of the simulation, the surface temperature for S-1/U-0.3 is by 4 °C higher than for S-10/U-0.3.

As discussed in Section 3.1.2, the way how the heat transfer through the window was modeled can produce some errors in the airflow pattern. However, more realistic model would be significantly more complex and computationally demanding. Such model would be desirable in performing e.g. case-studies.

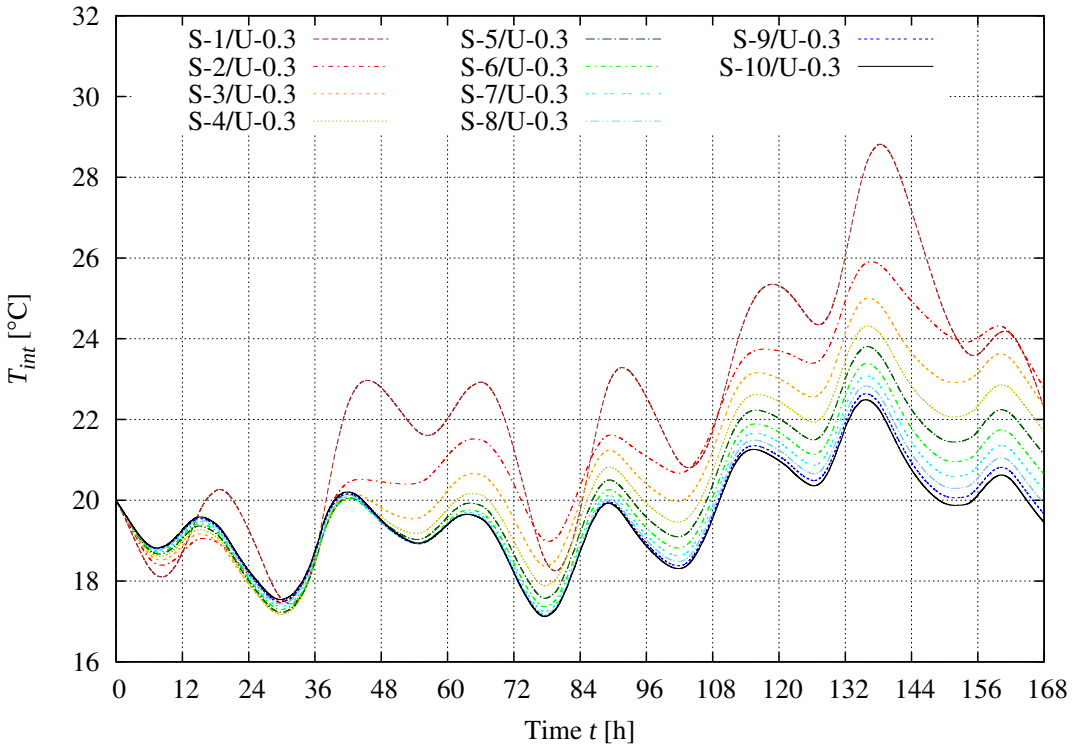

Figure 5.5: Summer week simulation (ACH = 0.01 h^{-1}, single-layer walls with U = 0.3 W/(m^2K)): average indoor air temperature T_{int}

In the case of ACH = 0.01 h^{-1} , the indoor temperature depends only on the

window and wall temperatures. The temperature swings are significant and highly depend on the wall thermal capacitance. During the week period, the indoor temperature in the room with the external wall of the highest thermal capacitance (S-10/U-0.3) varies between 17 °C and 22.5 °C. The temperature variations in time for S-1/U-0.3 are in the range of 17.5–29 °C. In all cases the spatial temperature distribution is close to uniform, similar to the one presented in Fig. 5.7 (S-1/U-0.3). The thermal stratification can be observed, but due to the relatively low height of the room (2.6 m), the temperature differences in a vertical direction are usually within 1 °C.

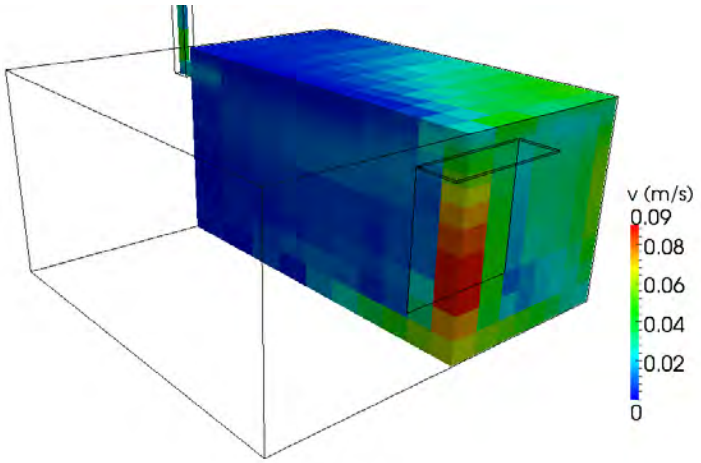

Figure 5.6: Air velocity v [m/s] distribution in room at time $t = 138\,\mathrm{h}$ (case S-1/U-0.3, ACH $= 0.01\,\mathrm{h}^{-1}$)

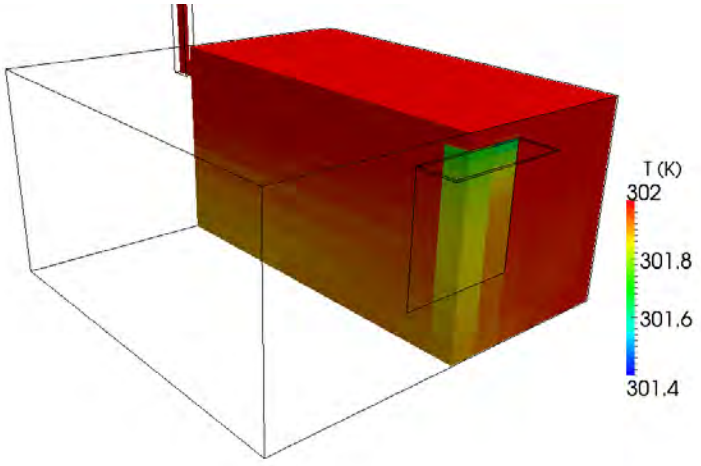

Figure 5.7: Temperature T [K] distribution in room at time $t = 138\,\mathrm{h}$ (case S-1/U-0.3, ACH $= 0.01\,\mathrm{h}^{-1}$)

By comparing Fig. 5.5 and Fig. 5.1 it can be noticed, that there is a time lag between the extremum indoor and outdoor temperatures. The time lags seem to be

higher for lighter walls. It is due to the several times higher temperature amplitudes and relatively low rate of the heat transfer between the wall and indoor air (the average convective heat transfer coefficient varies between 0.5 to 2.5 $\mathrm{W/(m^2K)}$). In addition, the indoor temperature is affected also by the heat gains and losses through the window, which has a very small thermal capacitance. The final result is that the extremum temperatures at the wall internal surface occur later than the extremum indoor temperatures.

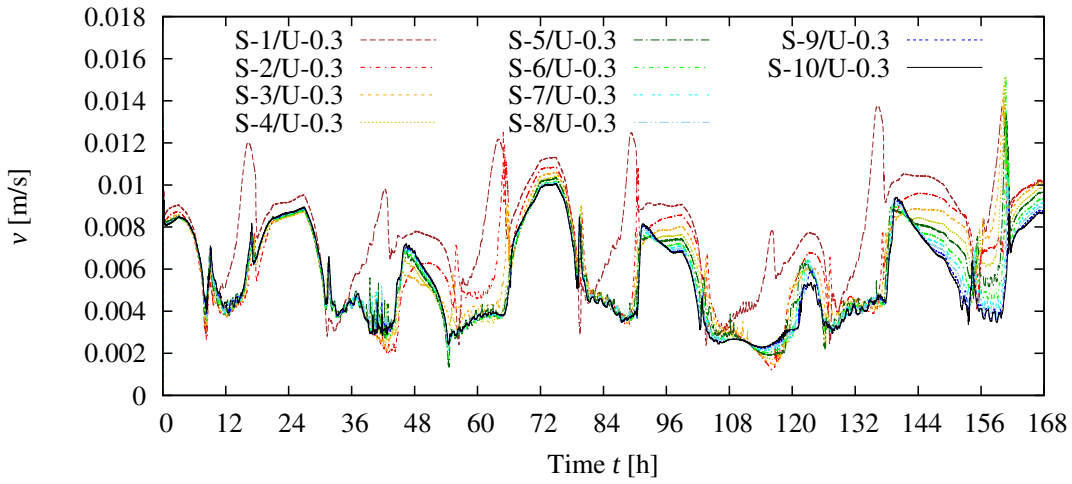

Figure 5.8: Summer week simulation ($\mathrm{ACH} = 0.01\,\mathrm{h^{-1}}$, single-layer walls with $U = 0.3\,\mathrm{W/(m^2K)}$): average indoor air velocity v

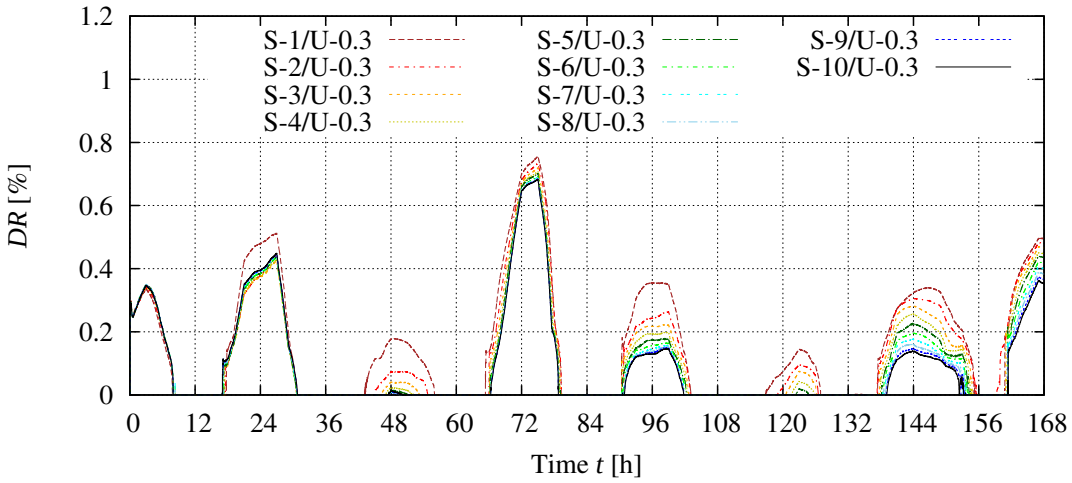

Figure 5.9: Summer week simulation ($\mathrm{ACH} = 0.01\,\mathrm{h^{-1}}$, single-layer walls with $U = 0.3\,\mathrm{W/(m^2K)}$): average DR in the near-wall zone

The average air velocity in the analyzed cases is very low and does not exceed 0.015 m/s (Fig. 5.8). It does not vary significantly between different cases, although the results differ noticeably in the case of S-1/U-0.3.

In contrast to the temperature, the velocity spatial distribution is considerably nonuniform during most of the time (Fig. 5.6). The natural convection can accelerate the near-wall air to about 0.1 m/s. However, it is only a local effect. The results show that the natural convection does not introduce a sufficient force to accelerate the indoor air to the level affecting the thermal comfort in the occupied zone. The natural convection can increase the local discomfort due to the draft in the window vicinity (Fig. 5.10).

The velocity results indicate that during some periods the solution is oscillating. As long as the solution is stable and the oscillations are relatively low, it does not affect other environmental parameters. A smoother solution could be obtained by adopting additional iterations, so-called PIMPLE loops or outer loops (this issue is discussed in Section 3.2.3).

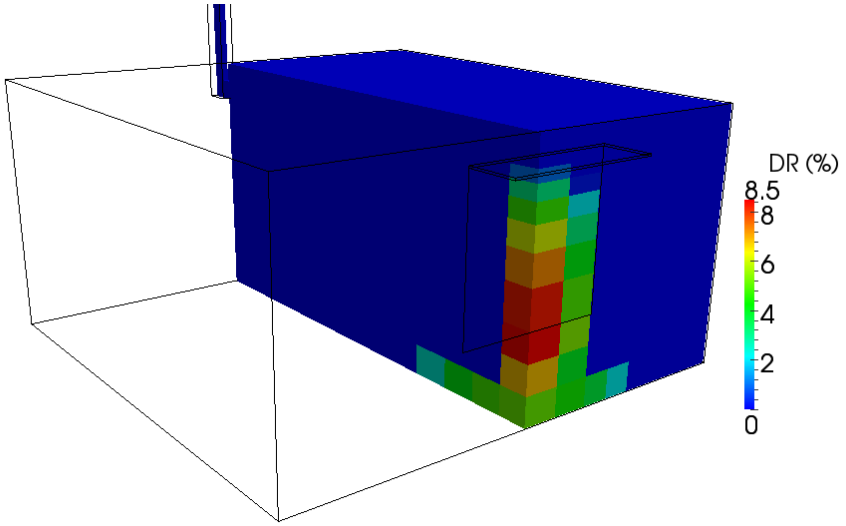

Figure 5.10: DR distribution in the room at time $t = 74\,\mathrm{h}$ (case S-1/U-0.3, $\mathrm{ACH} = 0.01\,\mathrm{h}^{-1}$)

Since the air velocities are rather low, also the draft risk is not significant. Fig. 5.9 shows the resultant percentage of people dissatisfied due to the draft (DR). The results from each cell are averaged over the near-wall zone (1 m wide). As shown, although the relative differences between the cases are considerable, the absolute values of the average DR are small. The highest local values of DR are met in the direct vicinity of the wall region (in the next-to-wall cells), as shown in Fig. 5.10. The maximum local DR generated by the natural convection near the window is about 8.5 %. Nonetheless, the average DR values in the near-wall zone are lower than 0.8 %.

Fig. 5.11 shows the evolution of the thermal comfort level in the occupied zone

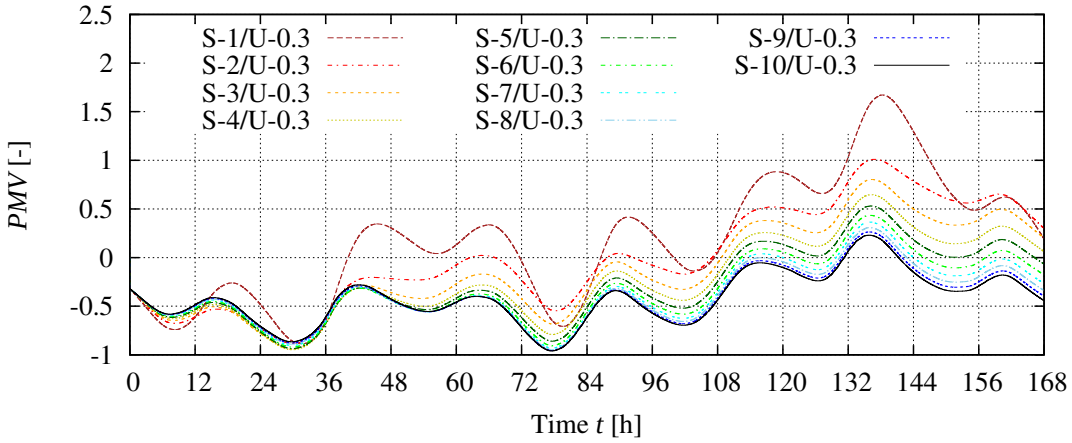

Figure 5.11: Summer week simulation (ACH = 0.01 h^{-1}, single-layer walls with U = 0.3 $W/(m^2K)$): average PMV in the occupied zone

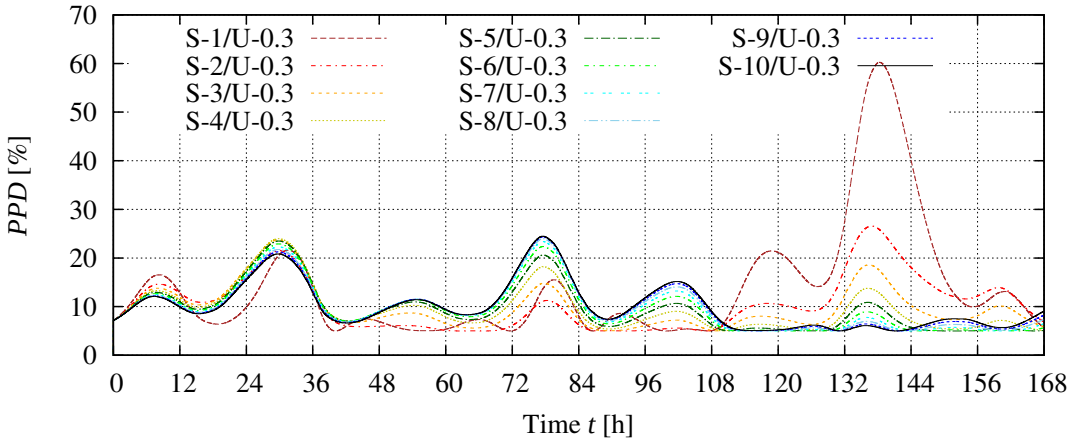

Figure 5.12: Summer week simulation (ACH = 0.01 h^{-1}, single-layer walls with U = 0.3 $W/(m^2K)$): average PPD in the occupied zone

(space between floor and a plane 2 m above it and 1 m from the walls; see Section 3.5) during the one week period. Due to the low air velocities the PMV-time profile is very similar to the temperature-time profile. PMV varies between -1 and 1.75 in the case of the lowest wall thermal capacitance (S-1/U-0.3). The lowest variations (-1–0.25) are for S-10/U-0.3. The analyzed walls are single-layered, so the results of intermediate cases show a gradual influence of the increasing thermal capacitance. The spatial distribution of PMV is close to uniform caused by uniform temperatures and low air velocities.

The PMV-PPD function is not linear (Fig. 2.4), so it is interesting to see also the PPD results (percentage of people dissatisfied with the current thermal conditions). As shown in Fig. 5.12, PPD varies between the minimum possible value of 5 % to approximately 24 % in most cases. However, in S-1/U-0.3 PPD reaches 60 %.

Therefore, even though temperature differences are not so large, the discrepancies

in the percentage of dissatisfied people are significant due to a nonlinear dependency between PMV and PPD.

It can be concluded that in walls with $U = 0.3\,\mathrm{W/(m^2K)}$ and $\mathrm{ACH} = 0.01\,\mathrm{h^{-1}}$, the thermal capacitance has a strong influence on the indoor thermal comfort. Especially, massive walls protect the indoor space from the temporary overheating. However, these results do not take into account the effect of the ventilation air. This is considered with $\mathrm{ACH} = 0.3\,\mathrm{h^{-1}}$.

5.3.1.2 Single-layer walls with $U = 0.15$ W/(m^{2}K)

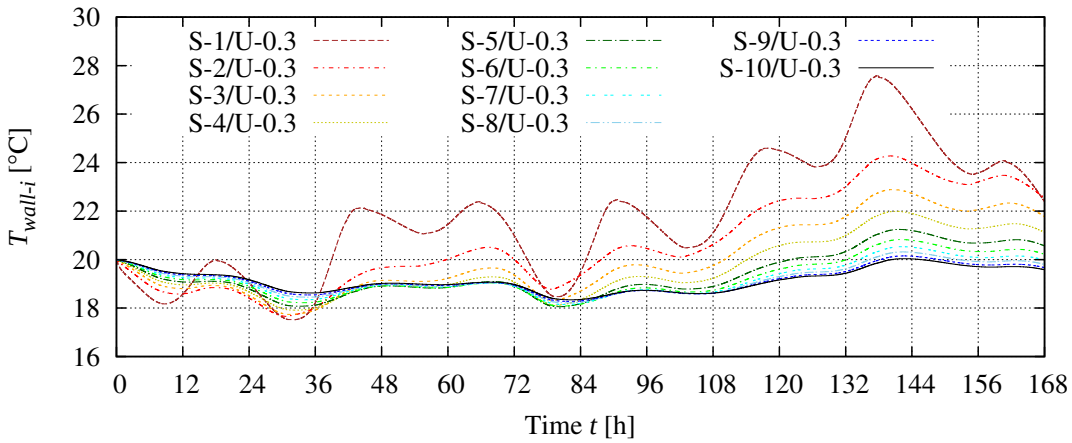

Figure 5.13: Summer week simulation ($\mathrm{ACH} = 0.01\,\mathrm{h^{-1}}$, single-layer walls with $U = 0.15\,\mathrm{W/(m^2K)}$): average wall internal surface temperature T_{wall-i}

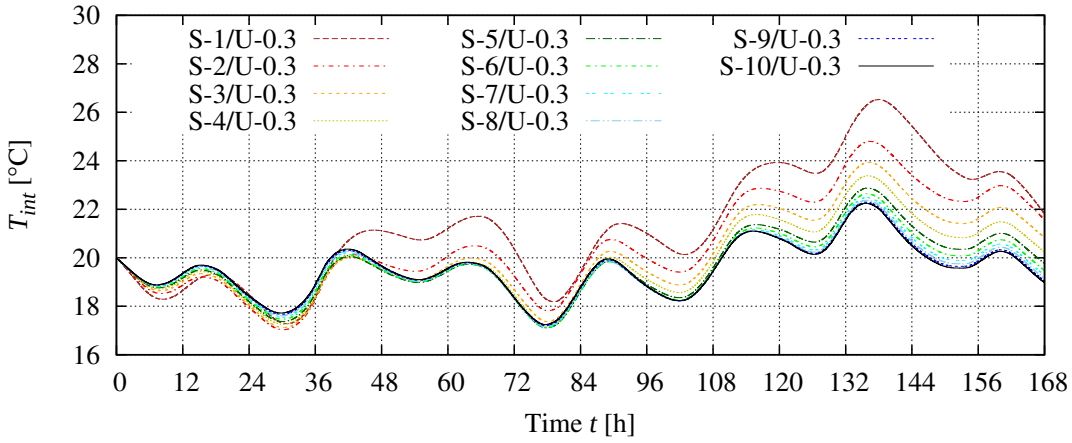

Figure 5.14: Summer week simulation ($\mathrm{ACH} = 0.01\,\mathrm{h^{-1}}$, single-layer walls with $U = 0.15\,\mathrm{W/(m^2K)}$): average indoor air temperature T_{int}

The results for the single-layer walls with $U = 0.15\,\mathrm{W/(m^2K)}$ and $\mathrm{ACH} = 0.01\,\mathrm{h^{-1}}$ explain the effect of the thermal capacitance in well-insulated walls.

Figs. 5.13 and 5.14 depict the average temperature of the wall internal surface

and the indoor space, respectively. Due to the window presence the average indoor air temperature is more unstable than the wall surface temperature. The surface temperature variations in the case of S-10/U-0.15 are in the range of 18–20 °C, while the indoor air temperature variations are in the range of 17–22 °C. This effect is not obtained for the lightest wall, where the surface temperature undergoes slightly larger variations than the indoor air (17.5–27.5 °C and 17–26.5 °C, respectively).

As compared to single-layer walls with $U = 0.3\,\mathrm{W/(m^2K)}$, similar walls with the two times lower U-value guarantee only slightly lower temperature variations. Especially the high thermal capacitance walls provide almost similar conditions regardless of the U-value (0.3 or 0.15 W/(m^{2}K)).

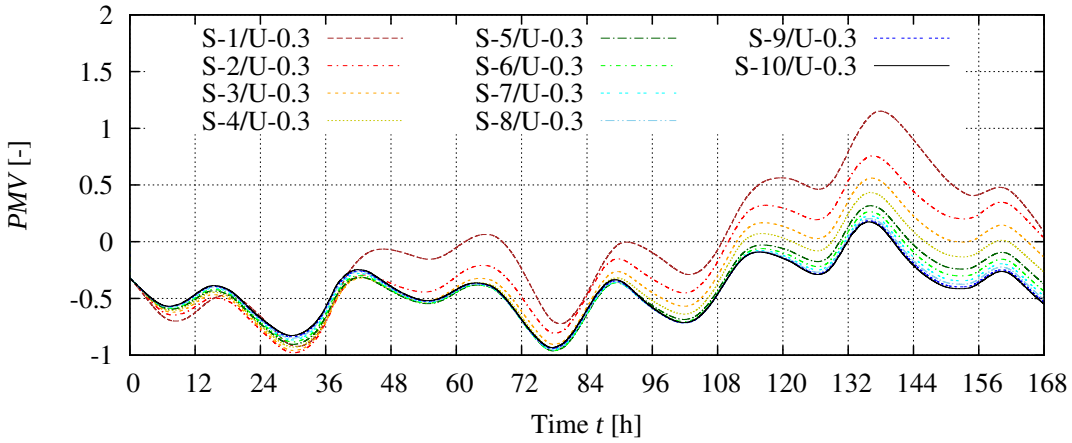

Figure 5.15: Summer week simulation (ACH = 0.01 h^{-1}, single-layer walls with $U = 0.15\,\mathrm{W/(m^2K)}$): average *PMV* in the occupied zone

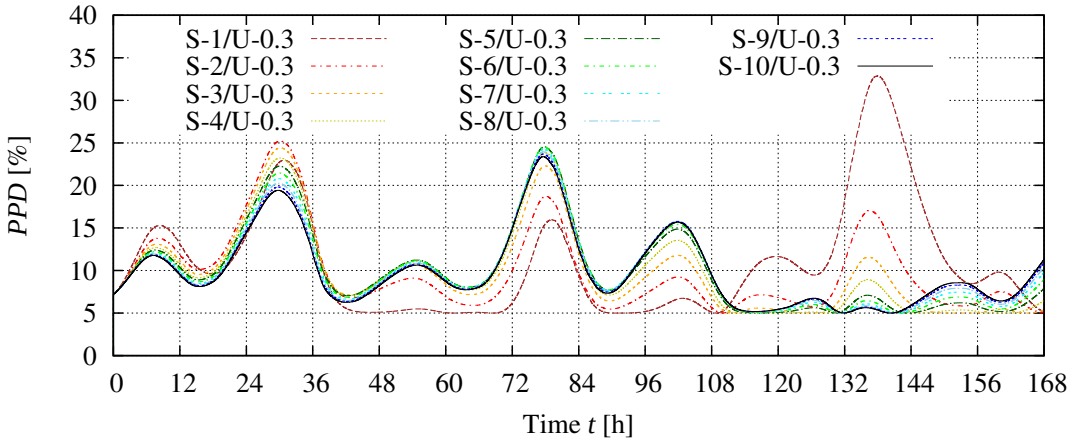

Figure 5.16: Summer week simulation (ACH = 0.01 h^{-1}, single-layer walls with $U = 0.15\,\mathrm{W/(m^2K)}$): average *PPD* in the occupied zone

The indoor air velocities are very similar to the ones obtained with S-1–S-10/U-0.3. Thus, the air velocity does not affect the thermal comfort and the PMV functions (Fig. 5.15) have similar profiles to the indoor temperature functions (Fig.

5.14). The PPD variations (Fig. 5.16) are similar to the ones calculated with walls with the higher U-value. The one significant difference is that the maximum PPD is almost two times lower and equal to 33 % (compared to 60 % in the previous cases). Such low maximum PPD value of S-1/U-0.15 compared to the case S-1/U-0.3 is due to the nonlinearity of the PMV-PPD function. Even small temperature variations in this range result in large PPD changes.

5.3.1.3 Multilayer walls with $U = 0.3$ W/(m^{2}K)

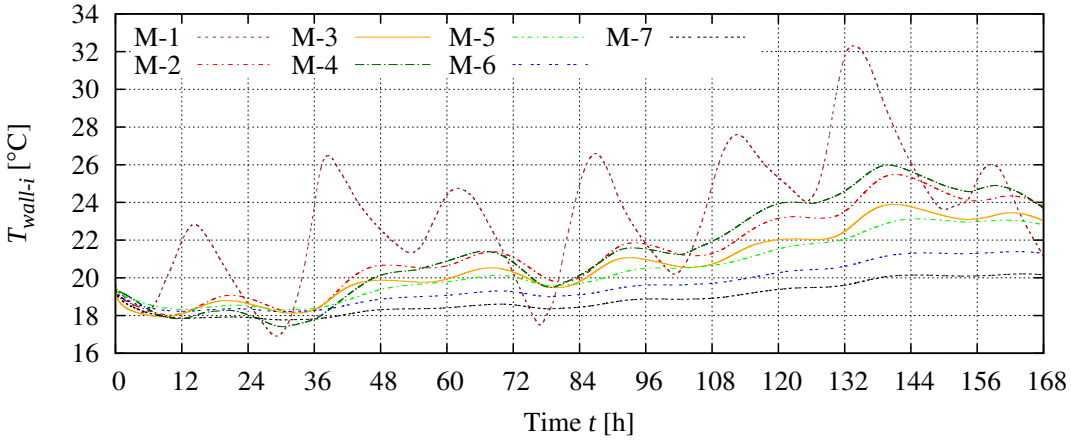

Figure 5.17: Summer week simulation (ACH = 0.01 h^{-1}, multilayer walls with U = 0.3 W/(m^{2}K)): average wall internal surface temperature T_{wall-i}

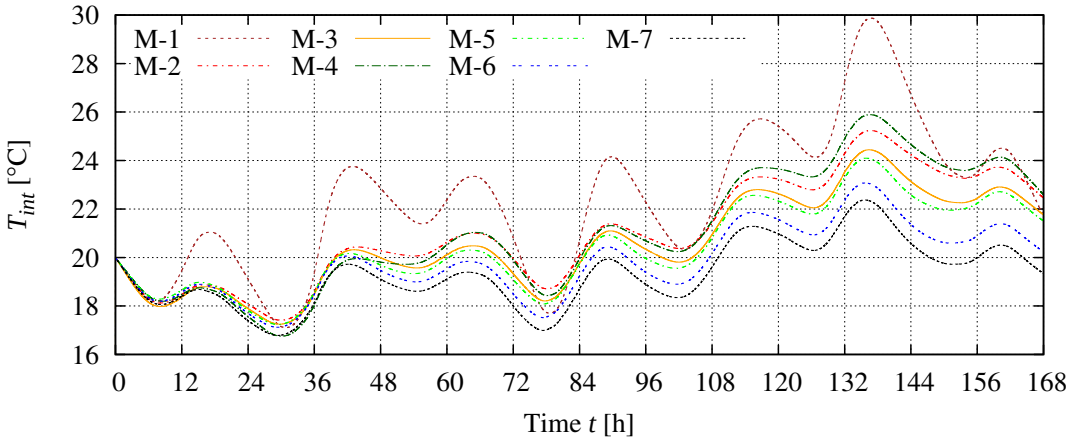

Figure 5.18: Summer week simulation (ACH = 0.01 h^{-1}, multilayer walls with U = 0.3 W/(m^{2}K)): average indoor air temperature T_{int}

The results for the multilayer walls show the inertial effects of the thermal capacitance affected by its nonuniform spatial distribution. As shown in Fig. 5.17, the temperature variations of the wall internal surface are similar to the ones obtained with the single-layer walls (U = 0.3 W/(m^{2}K)). The thermal capacitance influence

on the resultant temperatures is significant. As shown, the wall denoted as M-1 is the most vulnerable to temperature swings. The temperature on its internal surfaces varies in time in the range of 17–32 °C. Any other wall does not encounter such low (17 °C) or such high (32 °C) temperatures during the analyzed time period.

The influence of a nonuniform thermal capacitance distribution is clearly seen in the M-4 results. The wall M-4 has the higher wall thermal capacitance (C_{wall}, Table 5.3) than M-2 and M-3. However, in the case of M-4, the layer with the high thermal capacitance (i.e. spruce logs) is placed at the exterior side of the thermal insulation. The observed temperatures are between the temperatures of the M-1 and M-2 cases. In other words, the effect of the high thermal capacitance can be lost by an improper layer sequence. The location of the thermal insulation at the exterior wall side is the most advantageous for the thermal performance.

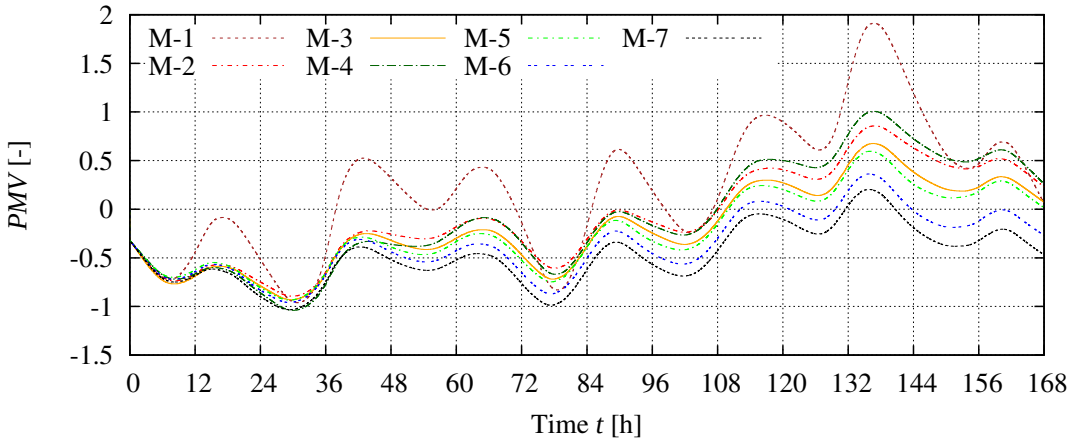

Figure 5.19: Summer week simulation (ACH = 0.01 h^{-1}, multilayer walls with U = 0.3 W/(m^2K)): average PMV in the occupied zone

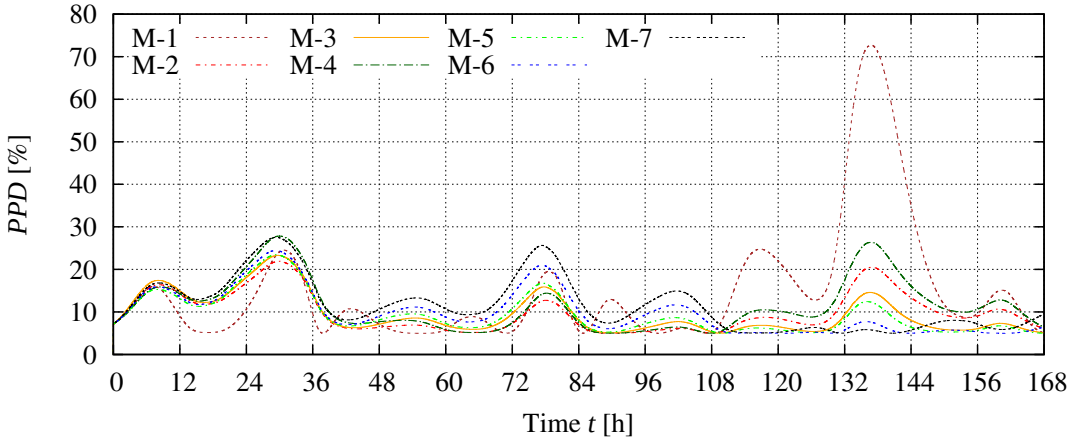

Figure 5.20: Summer week simulation (ACH = 0.01 h^{-1}, multilayer walls with U = 0.3 W/(m^2K)): average PPD in the occupied zone

As shown in Fig. 5.18, the indoor temperature is more unstable than the wall

surface temperature. It is a result of the heat transfer through the window. This is the same effect as for single-layer walls. Due to an unfavorable layer sequence, the wall M-4 stabilizes the indoor temperature worse than M-2 and M-3.

As in the other ACH $= 0.01\,\mathrm{h}^{-1}$ cases, there is no significant draft risk in multi-layer wall cases. The average DR in the near-wall zone is lower than 1 %.

The PMV and PPD results are presented in Figs. 5.19 and 5.20. In the analyzed building there are no additional heat sources or heat sinks, thus the thermal comfort is not maintained by any of the wall.

By comparing the total time of comfortable indoor conditions ($-0.5 < \mathrm{PMV} < 0.5$), it turns out that the best performers are M-3, M-5 and M-6. However, these results are highly dependent on the outdoor conditions. To fully evaluate the thermal comfort in free-running buildings a much longer time period should be analyzed. On the other hand, such short time period (1 week) still provides interesting results. The results show that very light walls (M-1) introduce the high risk of temporary overheating. The maximum PPD for M-1 is over 70 %, while for the remaining cases it is about 29 %.

The M-1 wall represents the group of wall structures called SIPs (structural insulated panels) or CSIPs (composite structural insulated panels). The technology has gained a considerable attention recently due to favorable thermal and mechanical properties of SIP / CSIP panels [96]. SIP / CSIP panels usually have an extremely low thermal capacitance. The results show that buildings based on this technology characterize with the increased risk of overheating.

5.3.2 Simulation case: ACH = 0.3 h^{-1}

5.3.2.1 Single-layer walls with U = 0.3 W/(m^2K)

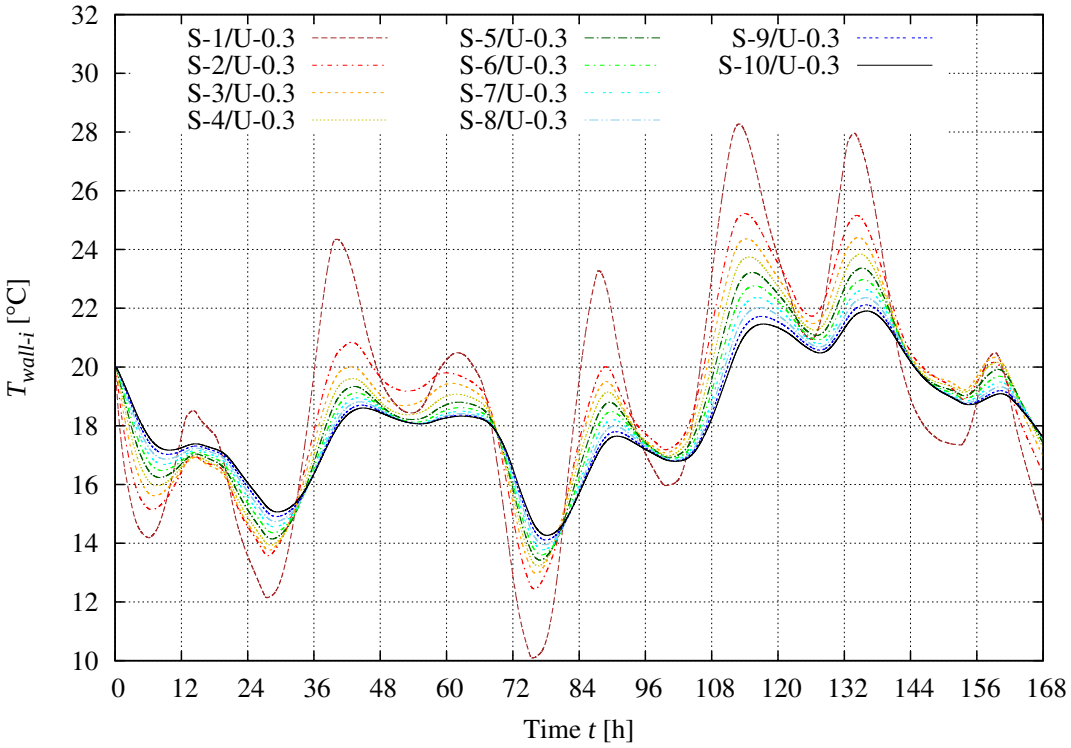

Figure 5.21: Summer week simulation (ACH = 0.3 h^{-1}, single-layer walls with U = 0.3 W/(m^2K)): average wall internal surface temperature T_{wall-i}

The results for ACH = 0.3 h^{-1} include the effect of ventilation on the indoor temperature. Fig. 5.21 depicts that the thermal capacitance has a great influence on the wall surface temperature. Surface temperature variations are greater in the case of lighter walls. The surface temperature for S-1/U-0.3 experiences weekly variations in the range of 10–28 °C, while for S-10/U-0.3 it varies approximately between 14.2 °C and 22 °C. The temperature variations dependency on the wall thermal capacitance is nonlinear. The daily amplitudes obtained by S-1/U-0.3 and S-5/U-0.3 are about 33% and 300% larger than those obtained by S-10/U-0.3, respectively.

Surface temperature variations are higher than for ACH = 0.01 h^{-1} (no ventilation). It is due to considerably higher variations of the indoor temperature (Fig. 5.22), caused by the inflow of the ventilation air.

When the ventilation rate is 0.3 h^{-1}, the wall type has considerably smaller influence on the indoor temperature, than the air exchange rate. In Fig. 5.22, the average indoor air temperature follows the inlet air temperature which is equal to the outdoor dry-bulb temperature T_{DB}. The dominant influence of the ventilation

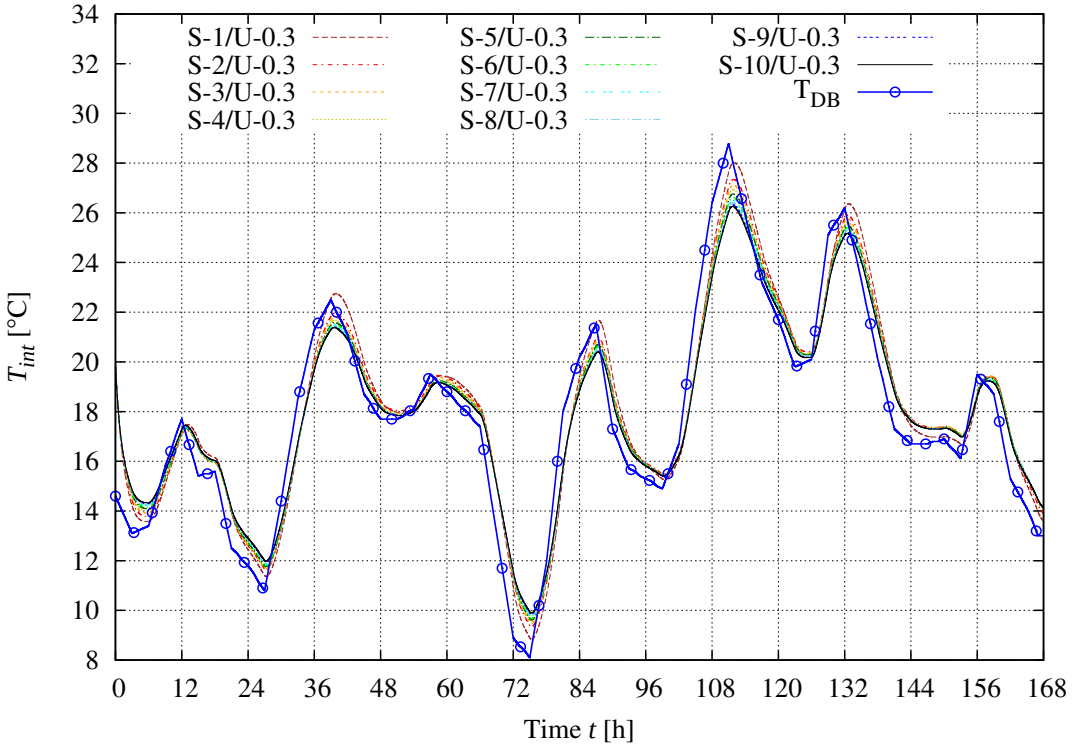

Figure 5.22: Summer week simulation (ACH $= 0.3\,\mathrm{h}^{-1}$, single-layer walls with $U = 0.3\,\mathrm{W/(m^2K)}$): average indoor air temperature T_{int} vs. ambient dry-bulb temperature T_{DB}

heat load (over the transmission heat load) is because the analyzed building is well-insulated. For ACH $= 0.3\,\mathrm{h}^{-1}$, the maximum difference in peak temperatures is only 2 °C (S-1/U-0.3 vs. S-10/U-0.3). During most of the time the average indoor temperature is similar in all cases.

As shown in Fig. 5.23, the thermal capacitance of the external wall has a negligible effect on the average air velocity. In all cases the average air velocity oscillates in the range of 0.02–0.045 m/s. The obtained velocities are 4–6 times higher as compared to ACH $= 0.01\,\mathrm{h}^{-1}$. The obtained velocity field is, however, highly nonuniform (Fig. 5.25). Maximum local velocities in the room (not including the ventilation duct) are in the range of 0.3–0.5 m/s. The obtained values are typical for indoor airflow.

According to ISO 7730 [74], the PMV model accurately predicts thermal comfort sensation for air velocities up to 1 m/s, but according to Humphreys and Nicol [70] the best accuracy is achieved for air velocities below 0.2 m/s. Under the assumed conditions, the velocity never exceeds 1 m/s (excluding the ventilation duct). In addition, in all cases, the calculated air velocity exceeds 0.2 m/s only in the window and inlet vent vicinity. Thus, the obtained air velocities are in the range of the PMV model applicability.

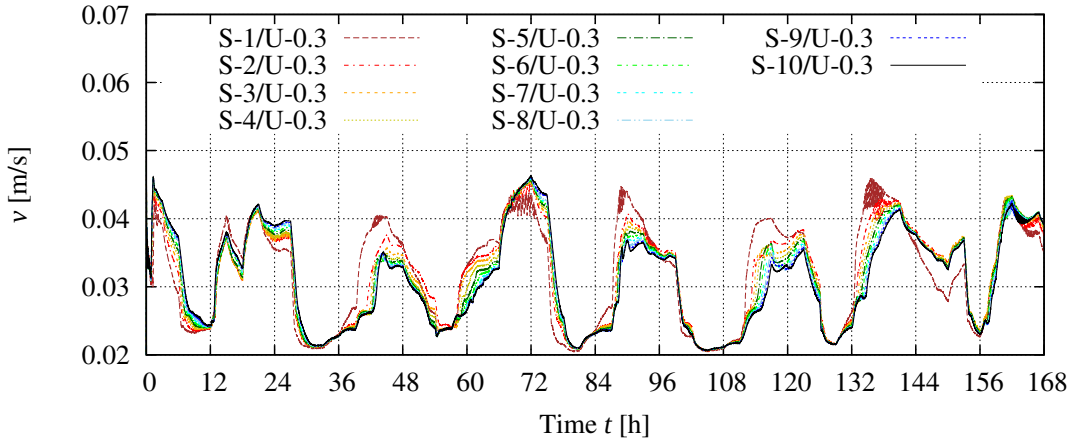

Figure 5.23: Summer week simulation (ACH = 0.3 h^{-1}, single-layer walls with U = 0.3 $W/(m^2K)$): average indoor air velocity v

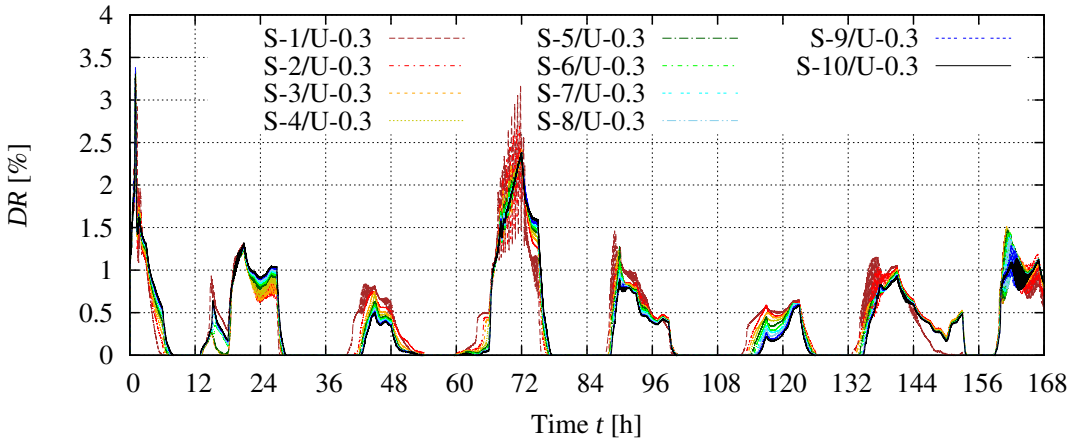

Figure 5.24: Summer week simulation (ACH = 0.3 h^{-1}, single-layer walls with U = 0.3 $W/(m^2K)$): average DR in the occupied zone

High air velocities cause the risk of the thermal discomfort due to draft (DR). The highest values of DR are observed just below the ceiling and in the occupied zone. It is because the inlet air does not drop immediately after entering the room. The inlet air has enough momentum to reach the room center, where it fully mixes with the indoor air. The maximum spatially-averaged DR in the occupied zone is about 2.5 % (Fig. 5.24), but the local maximum values reach up to 90 % near the outlet duct, and 50 % near the inlet vent (Fig. 5.26).

The thermal capacitance of the external wall has no influence on DR. By comparing Figs. 5.26 and 5.25 it can be noticed that the air velocity has a dominant influence on DR. The indoor air velocity is mainly affected by the ventilation air exchange rate and not by the natural convection (which is partially influenced by the walls' thermal capacitance).

The predicted mean vote (PMV) variations during the one week period are shown

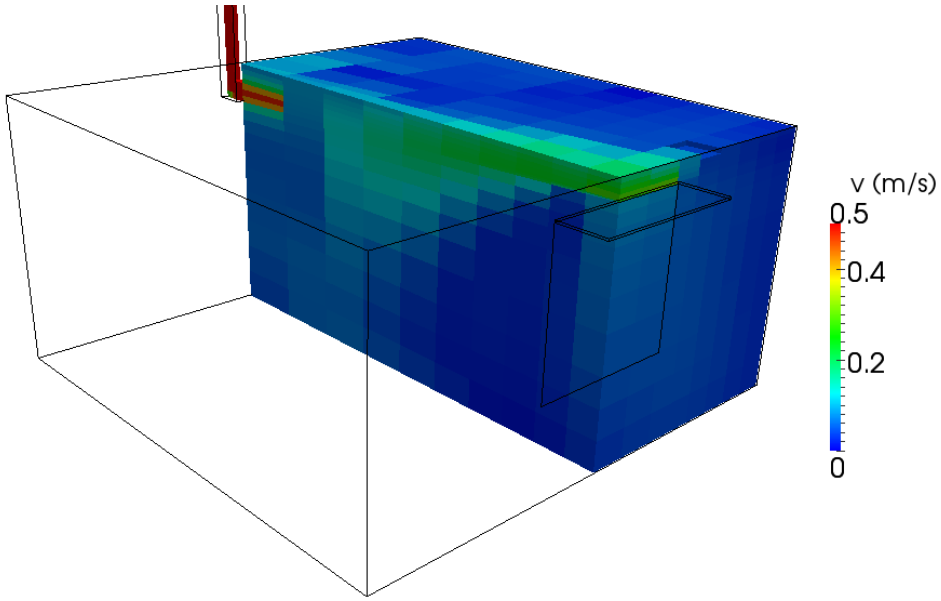

Figure 5.25: Air velocity magnitude v [m/s] distribution in room at time $t = 72\,\mathrm{h}$ (case S-1/U-0.3, ACH $= 0.3\,\mathrm{h}^{-1}$)

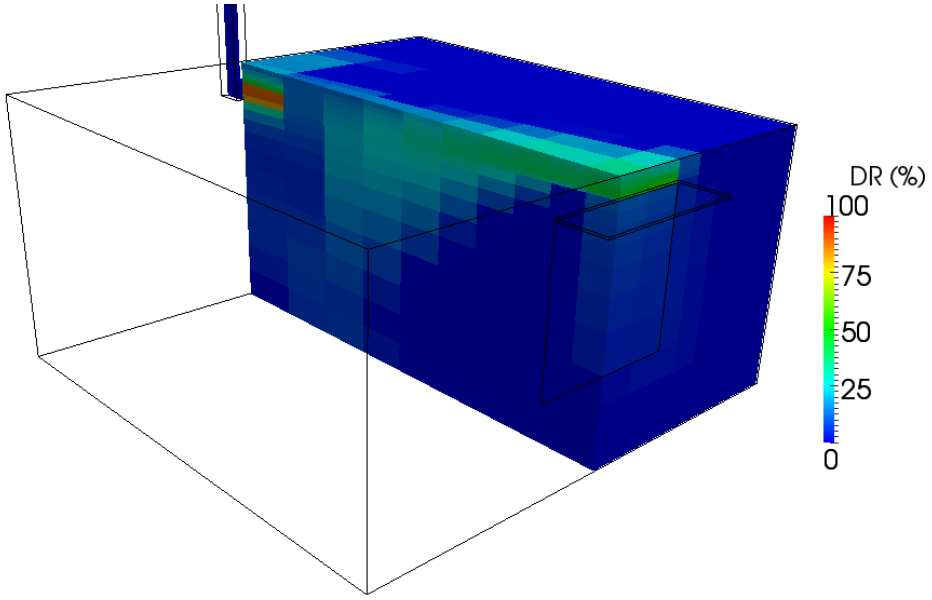

Figure 5.26: DR [%] distribution in room at time $t = 72\,\mathrm{h}$ (case S-1/U-0.3, ACH $= 0.3\,\mathrm{h}^{-1}$)

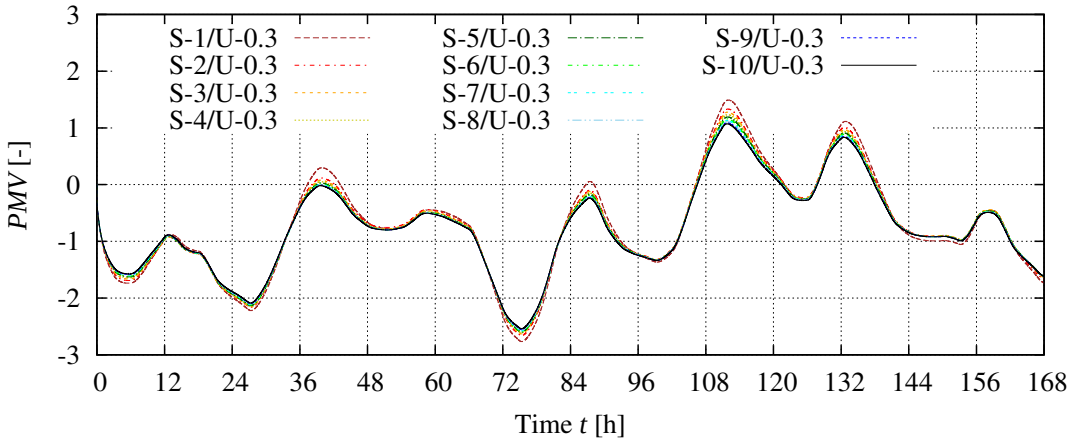

Figure 5.27: Summer week simulation (ACH $= 0.3\,\mathrm{h}^{-1}$, single-layer walls with $U = 0.3\,\mathrm{W/(m^2K)}$: average PMV in the occupied zone

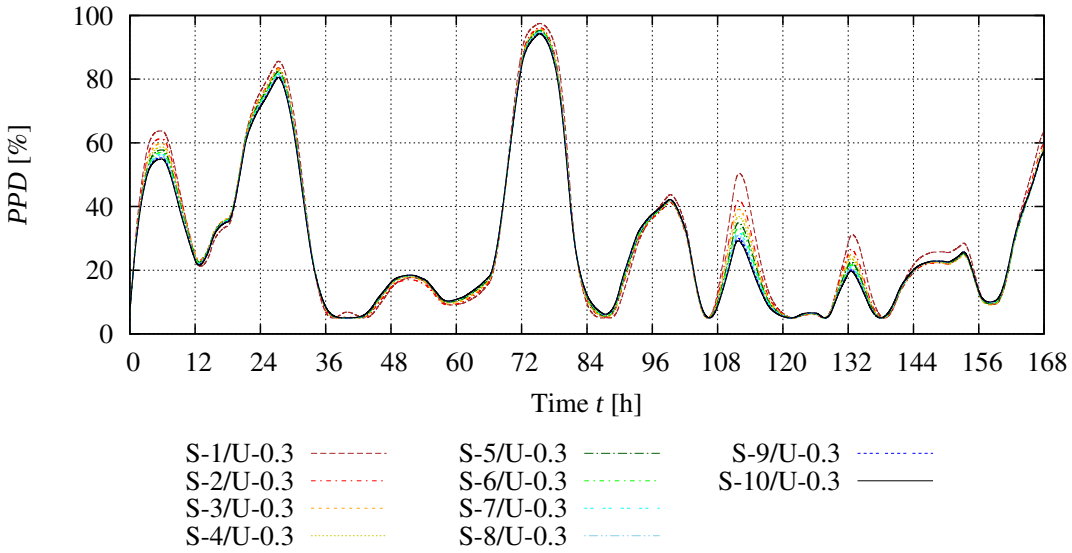

Figure 5.28: Summer week simulation (ACH $= 0.3\,\mathrm{h}^{-1}$, single-layer walls with $U = 0.3\,\mathrm{W/(m^2K)}$): average PPD in the occupied zone

in Fig. 5.27. Differences in the thermal comfort level are noticeable. The smaller thermal wall capacitance, the higher are variations in PMV. The results differ the most in the peak values. The maximum difference is observed during the fifth day and equals approximately 0.4 (S-1/U-0.3 vs. S-10/U-0.3).

The PPD results (Fig. 5.28) also show that the conditions provided by different walls are similar during most of the week, but there are significant discrepancies during peak temperatures. The highest difference in the percentage of dissatisfied people is observed during the fifth day and equals about 20 %. The differences during the rest of the time vary in the range of about 0–10 %.

5.3.2.2 Multilayer walls with $U = 0.3$ W/(m^{2}K)

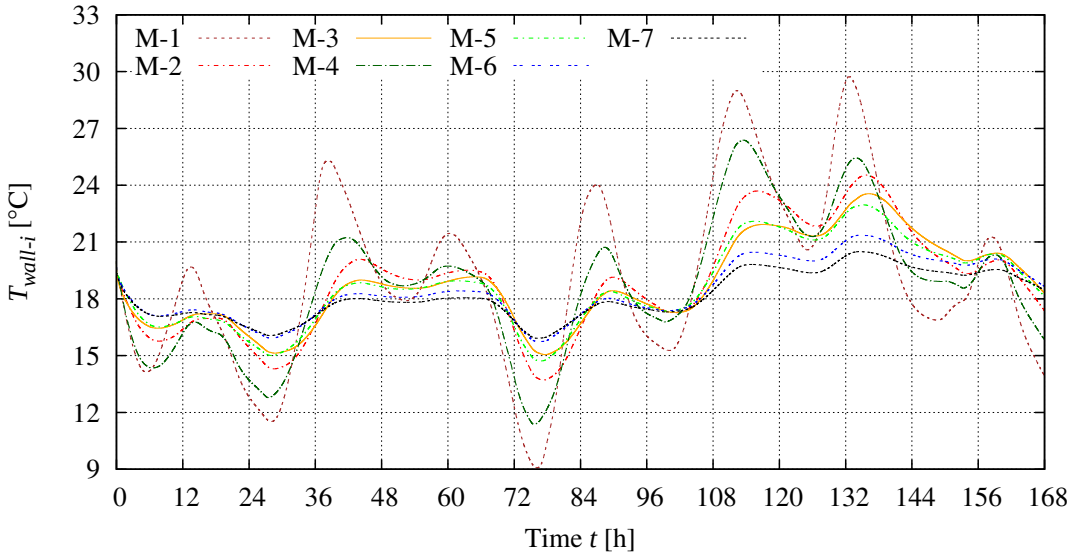

Figure 5.29: Summer week simulation (ACH = 0.3 h^{-1}, multilayer walls with U = 0.3 W/(m^{2}K)): average wall internal surface temperature T_{wall-i}

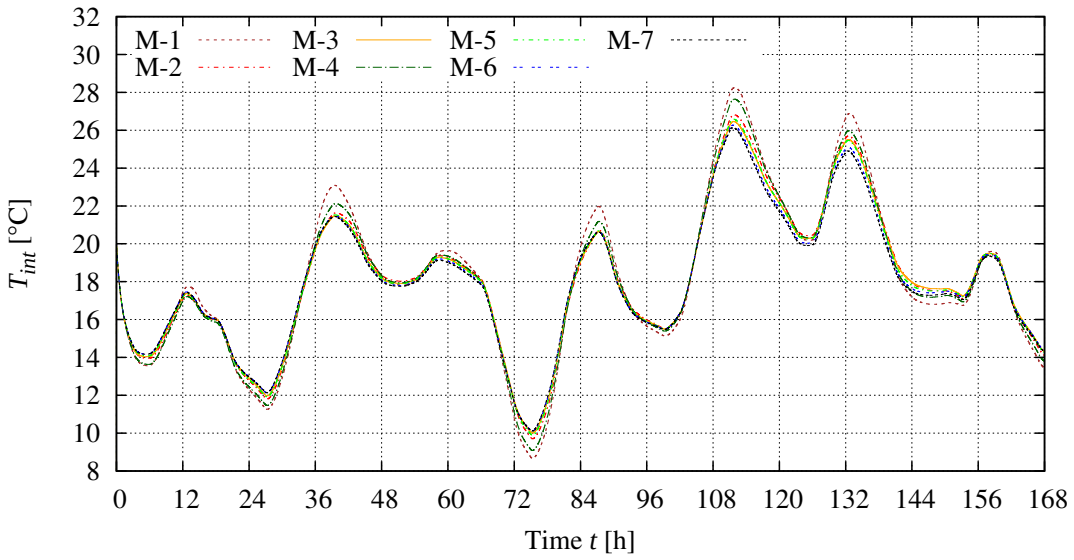

Figure 5.30: Summer week simulation (ACH = 0.3 h^{-1}, multilayer walls with U = 0.3 W/(m^{2}K)): average indoor air temperature T_{int}

As in single-layer walls, temperature variations of the wall internal surface are higher than in the case of ACH = 0.01 h^{-1} (Fig. 5.29). The effect is caused by higher indoor temperature variations which, in turn, are dominated by the air exchange rate. Surface temperature variations obtained by M-1 are in the range of 9–30 °C. Such high surface temperature amplitudes affect the indoor thermal comfort through the radiative heat transfer, but the current model cannot take this phenomena into

account directly. The radiative heat exchange between a body and the wall intensifies the negative (too cold or too hot) thermal sensation. The next wall significantly affected by the temperature swings is M-4. Although it has a greater thermal capacitance than M-2 and M-3, the unfavorable layer sequence decreases the wall's stabilizing capabilities. From the thermal stability point of view, it is not desirable to locate the high thermal capacitance layer on the external side, while the thermal insulation on the internal side of a wall. The surface temperature of the most massive wall, M-7, varies in the relatively narrow range of 16–20.5 °C. Such low variations are not considered to affect the indoor thermal comfort noticeably.

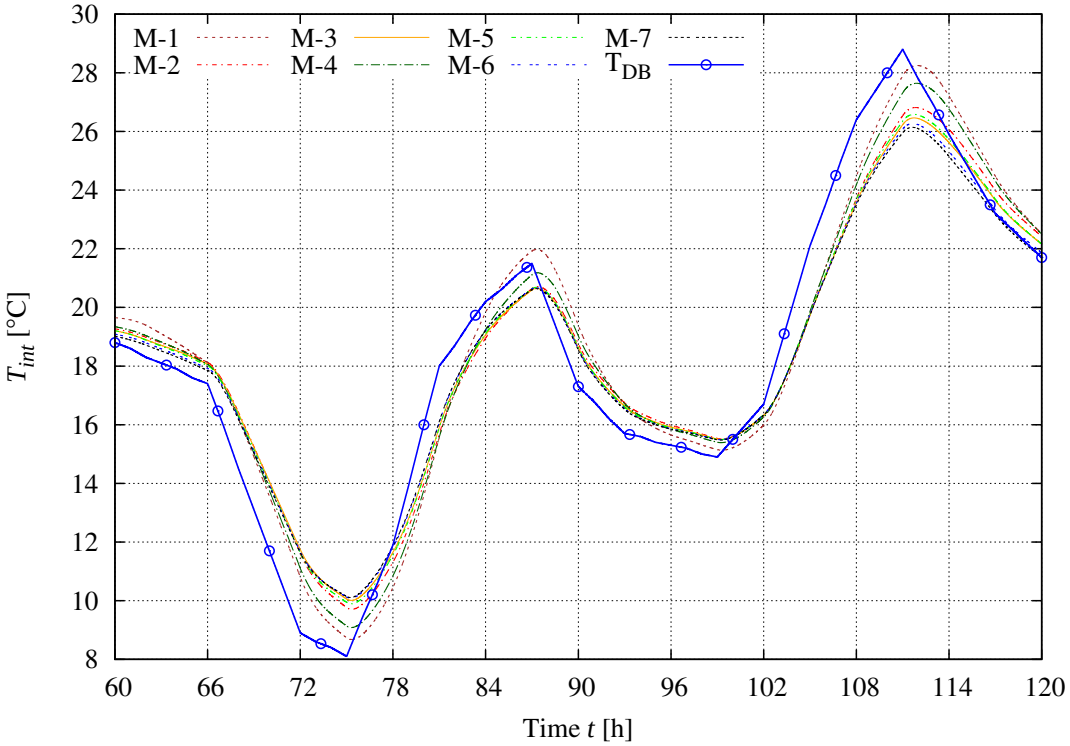

Figure 5.31: Summer week simulation (ACH = 0.3 h^{-1}, multilayer walls with U = 0.3 W/(m^2K)): average indoor air temperature T_{int} vs. dry-bulb temperature T_{DB} (results for 60–120 h)

Due to the periods when the surface temperature of some walls (especially M-1 and M-4) drops below 12–14 °C there is a high risk of a water vapor surface condensation. The risk also depends on the indoor conditions, particularly the air humidity. The simulations were performed with the assumption that there are no heat sources in the building. The building is not equipped with a heating system, because the analyzed period is in the summer season. There are also no internal heat gains due to the solar radiation or human activity. Nevertheless, the results indicate that the walls with low thermal capacitance are more exposed to the risk of the surface vapor condensation. These simulations were not aimed at the analysis

of this problem, but this is an interesting issue to be investigated in the future.

As in the case of single-layer walls, the considered multilayer walls are not able to keep indoor temperature stable when the air exchange rate is $0.3\,\mathrm{h}^{-1}$. Massive walls, like M-7, keep the indoor temperature more stabilized than light walls, but the effect is insignificant and visible mostly during the periods of highest and lowest temperatures. The maximum difference in peak temperatures is around 2 °C. The indoor temperature is mainly affected by the inlet air, what can be seen in Fig. 5.31, presenting a zoomed function of the average indoor temperature in time during the period of 60–120 h.

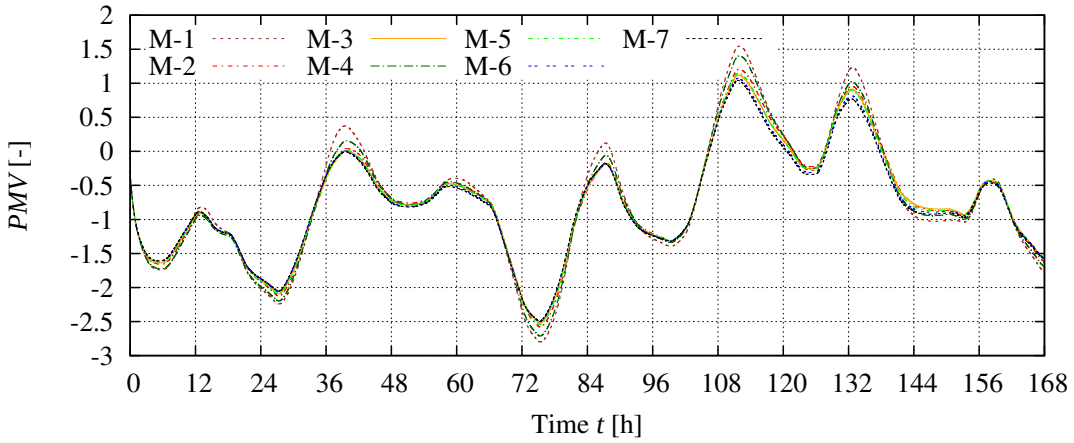

Figure 5.32: Summer week simulation (ACH $= 0.3\,\mathrm{h}^{-1}$, multilayer walls with $U = 0.3\,\mathrm{W/(m^2K)}$): average PMV in the occupied zone

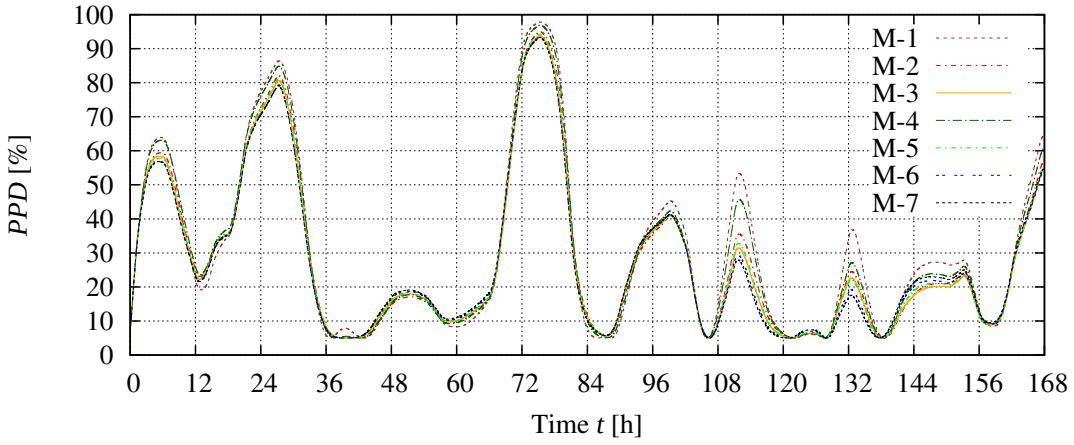

Figure 5.33: Summer week simulation (ACH $= 0.3\,\mathrm{h}^{-1}$, multilayer walls with $U = 0.3\,\mathrm{W/(m^2K)}$): average PPD in the occupied zone

The considered walls are not able to keep the indoor environment comfortable during the entire week. As shown in Fig. 5.32, PMV varies similarly to indoor temperature variations. Other cases alike, the high thermal capacitance of walls is capable to reduce indoor thermal comfort variations to some extent, at least until the

thermal capacitance is not exposed directly to the outdoor temperature, as in M-4. The PPD results (5.33) confirm that the massive walls are advantageous, especially from the point of view of the summer overheating problem. During the periods of the highest temperatures (as during the 5th and the 6th day) the percentage of dissatisfied people can be considerably reduced. The positive effect of the thermal capacitance is slightly lower during the cold nights.

5.4 Indoor environment stability test results

The purpose of the indoor environment stability test is to assess the wall capabilities to keep indoor environment stable. Outdoor temperature peaks can result in uncomfortable indoor conditions, what is shown in the results of the summer week simulation (Section 5.3). However, the results also show that the heat loads coming from the ventilation have a profound effect on the indoor temperature. When the air exchange rate is $0.3\,\mathrm{h}^{-1}$, the external wall alone is not able to prevent indoor overheating, although indoor peak temperatures are limited by a few degrees thanks to massive external walls.

The presented test enables to quantify the effect of the wall thermal capacitance on the indoor environment in various conditions. The test procedure is presented in Section 5.2. The walls taken into account in the test are presented in Section 5.1.

The results of the summer one week simulations showed that the indoor air velocity is affected almost exclusively by the ventilation rate. Thus, the air velocity and thermal comfort indices (which are calculated using air velocity results) are not considered in this test.

The effect of the outdoor temperature drop on the indoor temperature is investigated. The results confirmed that the thermal capacitance of the external walls has a significant effect on the indoor air temperature if the ventilation is not taken into account.

In all cases (Figs. 5.34 and 5.35), indoor temperature changes during the first six hours are similar. However, significant differences are found in the subsequent period. Indoor temperatures in rooms with the low thermal capacitance wall have considerably higher drop rates. In the case of high thermal capacitance walls (from S-5 to S-10), after the initial 36–60 hours, the indoor temperature drop rate stabilizes at a low level. From this point, the indoor temperature variations are close to linear in these rooms.

The analysis of both cases, $U = 0.3\,\mathrm{W/(m^2K)}$ and $U = 0.15\,\mathrm{W/(m^2K)}$, enables to compare the influence of thermal capacitance and U-value on the indoor tem-

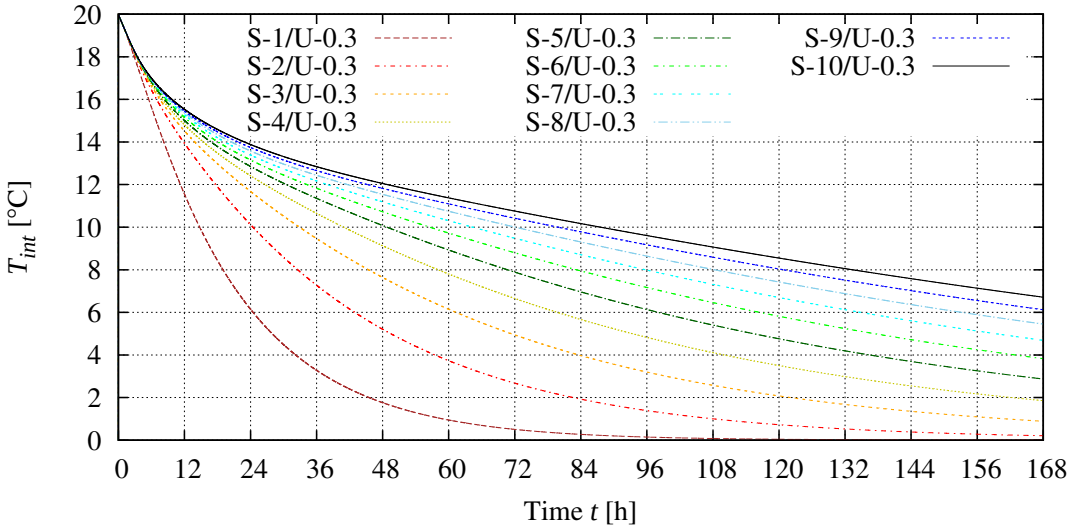

Figure 5.34: Average indoor temperature T_{int} during indoor environment stability test for ACH $= 0.01\,\mathrm{h}^{-1}$ and single-layer walls with $U = 0.3\,\mathrm{W/(m^2K)}$

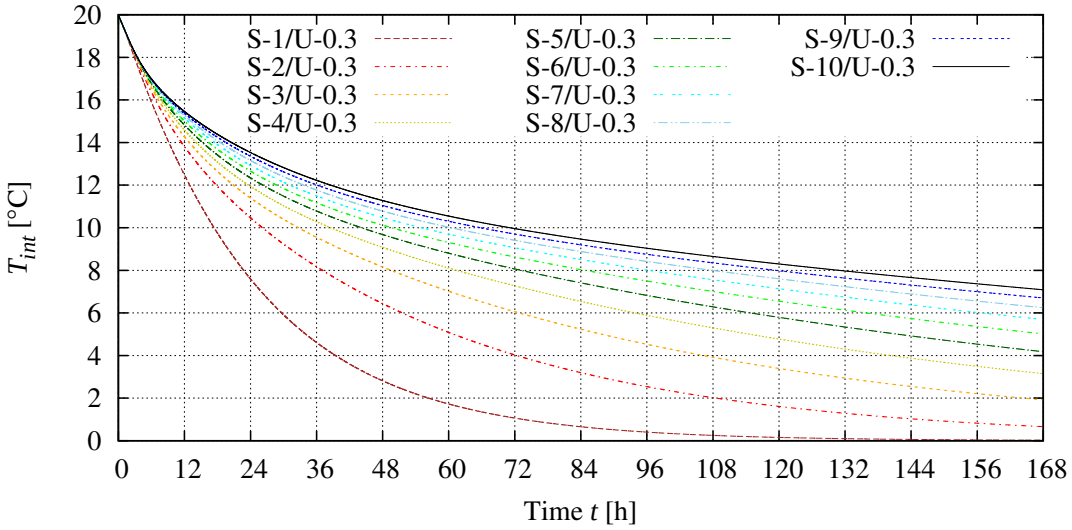

Figure 5.35: Average indoor temperature T_{int} during indoor environment stability test for ACH $= 0.01\,\mathrm{h}^{-1}$ and single-layer walls with $U = 0.15\,\mathrm{W/(m^2K)}$

perature. The differences in temperatures between walls with the same thermal capacitance but different U-values are generally not higher than 2 °C at any instant of time. From the point of view of the indoor environment stability, the wall thermal capacitance is a more important factor than the U-value, at least in the U-value range of 0.15–0.30 W/(m^{2}K).

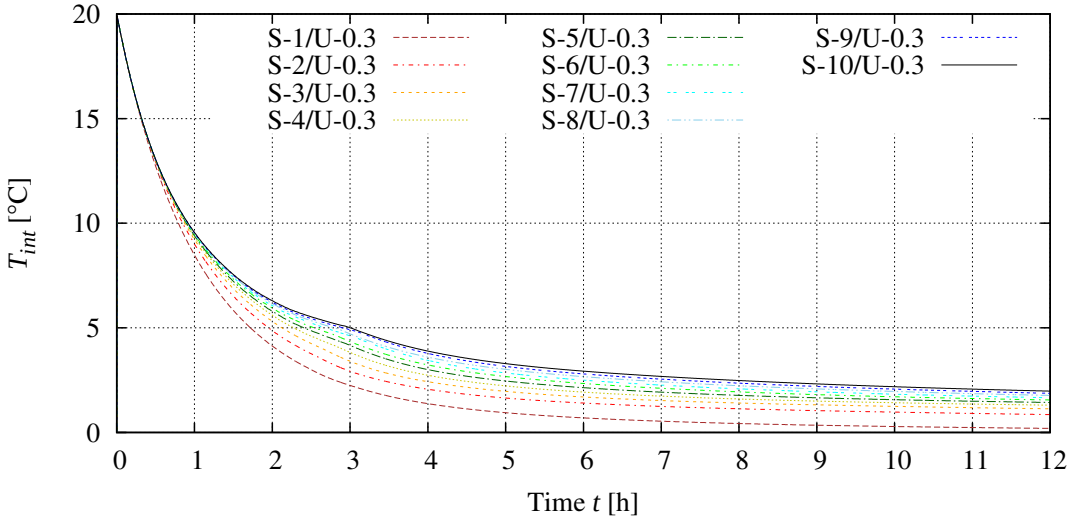

Figure 5.36: Average indoor temperature T_{int} during indoor environment stability test for ACH = 0.3 h^{-1} and single-layer walls with U = 0.3 W/(m^{2}K)

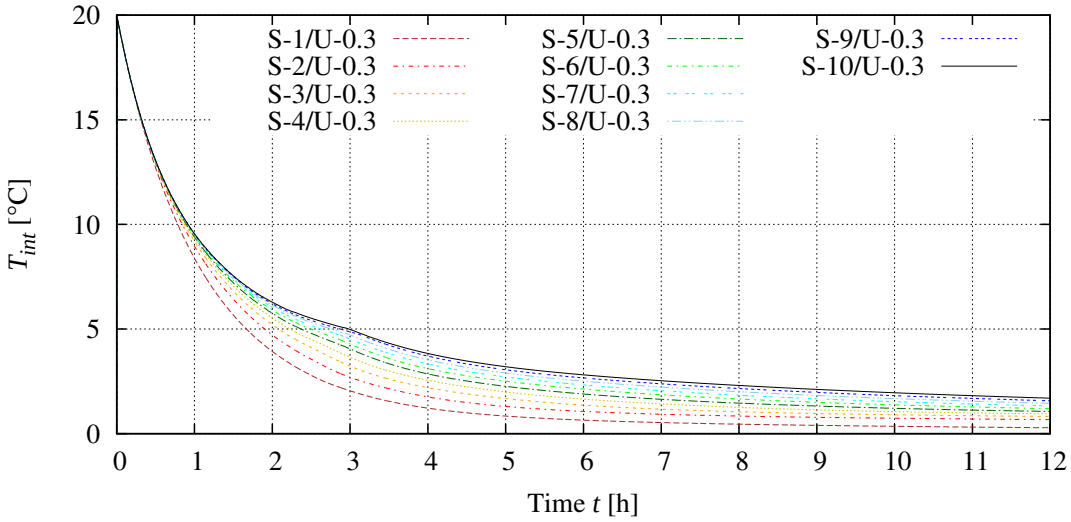

Figure 5.37: Average indoor temperature T_{int} during indoor environment stability test for ACH = 0.3 h^{-1} and single-layer walls with U = 0.15 W/(m^{2}K)

As shown in Figs. 5.36 and 5.37 the ventilation attenuates the effect of thermal capacitance. Due to the air exchange rate of 0.3 h^{-1}, it takes only 1.6–3 h for the indoor temperature to drop below 5 °C. During the first hour of simulations indoor temperature profiles are very similar in all cases with ACH = 0.3 h^{-1}. Performance

differences between different walls are found especially for time $t > 1\,\mathrm{h}$. Again, the results indicate that the U-value has a limited influence on the transient indoor temperature.

In order to quantify stabilizing capabilities of each wall, time (t_{drop}) it takes to cool down the indoor space to the temperature levels (T_{drop}) of 15 °C, 10 °C and 5 °C are measured. The level of $T_{drop} = 15\,°\mathrm{C}$ is reached first, while the level of $T_{drop} = 5\,°\mathrm{C}$ is reached as the last one. These three temperature levels are taken into account due to the nonlinear character of the indoor temperature function. The temperature comparison at three different temperature levels gives a more detailed view. The thermal inertia effects are more visible when large time periods and temperature drops are considered.

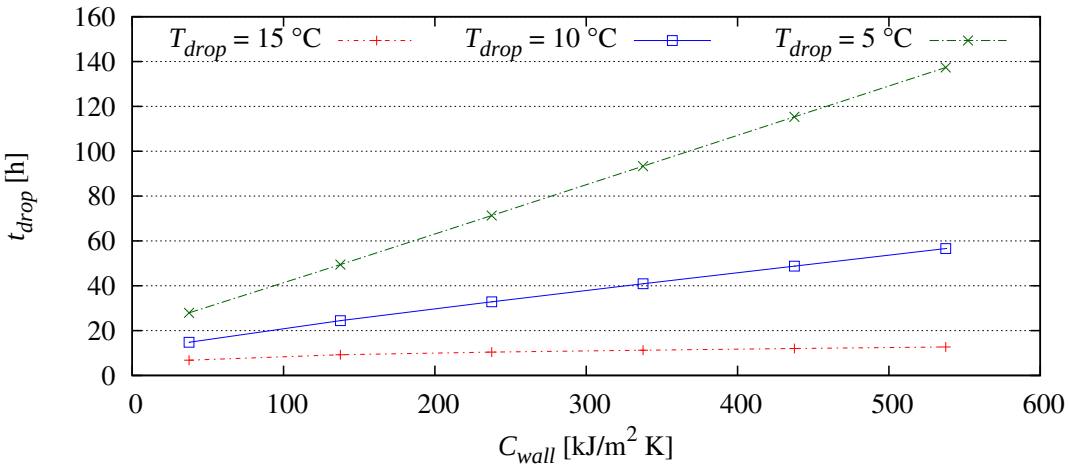

Figure 5.38: Time t [h] after which indoor temperature drops from initial 20 °C to T_{drop} (ACH = 0.01 h^{-1}, $U = 0.3\,\mathrm{W/(m^2\,K)}$)

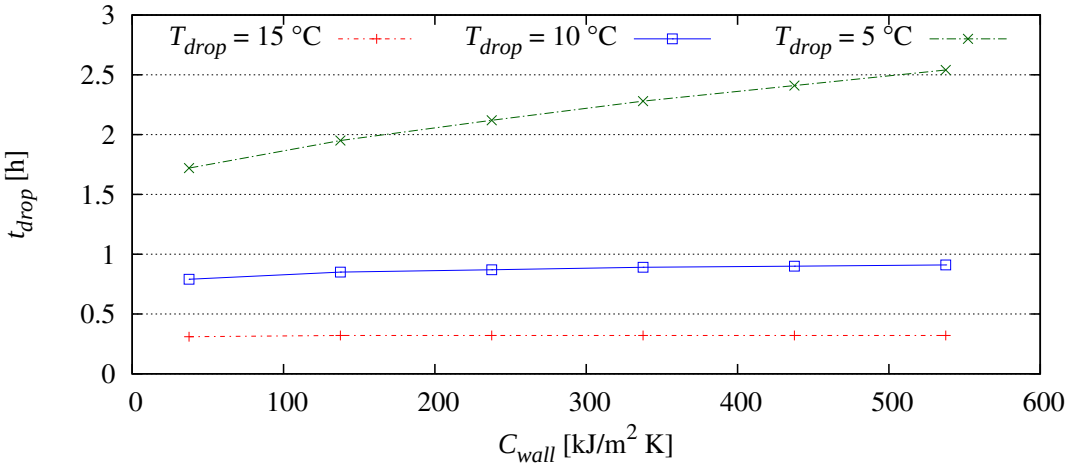

Figure 5.39: Time t [h] after which indoor temperature drops from initial 20 °C to T_{drop} (ACH = 0.3 h^{-1}, $U = 0.3\,\mathrm{W/(m^2\,K)}$)

The t_{drop} results for walls with $U = 0.3\,\mathrm{W/(m^2\,K)}$ are presented in Figs. 5.38 and 5.39 (for ACH $= 0.01\,\mathrm{h^{-1}}$ and ACH $= 0.3\,\mathrm{h^{-1}}$, respectively). As shown, there is a positive close-to-linear correlation between the time t_{drop} and wall thermal capacitance C_{wall}. The higher wall thermal capacitance, the longer it takes to cool down the indoor space. When a small temperature drop is considered (e.g. $T_{drop} = 15\,^{\circ}\mathrm{C}$) the time t_{drop} is almost similar for all the thermal capacitances and regardless of the air exchange rate.

The influence of the wall thermal capacitance is more visible if the temperature $T_{drop} = 5\,^{\circ}\mathrm{C}$ is considered, i.e. when a longer time period is analyzed. In this case, the time t_{drop} ranges between 1.7 h and 2.5 h, if ACH $= 0.3\,\mathrm{h^{-1}}$(Fig. 5.39). In contrast, if ACH $= 0.01\,\mathrm{h^{-1}}$, the indoor air cools down to 5 °C in 24–139 h, depending on the wall thermal capacitance C_{wall}. It means that the presence of the ventilation decreases the time needed for the indoor temperature to drop below 5 °C by a factor of about 14 (low thermal capacitance walls) up to 56 (high thermal capacitance walls). Thus, the thermal capacitance effect is significantly limited by the ventilation heat load.

The wall thermal capacitance is an important factor contributing to the indoor temperature stabilization (or more precisely: temperature inertia). However, still the ventilation intensity has a dominating influence on the indoor temperature.

Chapter 6

Conclusions and future work

The following conclusions can be derived from numerical results presented in this work:

- The biggest differences in the performance of walls with different thermal capacitances were observed for peak temperatures, especially maximum temperatures. The massive walls are more advantageous. Even though they cannot fully protect the indoor space from overheating, they still limit the indoor peak temperatures by few degrees. The very low thermal capacitance walls are disadvantageous from this point of view.

- The stabilizing effects of the thermal capacitance are significantly limited by the ventilation. Even under the conditions of a relatively low ventilation intensity (air exchange rate $0.3\,\mathrm{h}^{-1}$), walls with considerably different thermal capacitances provide very similar indoor temperature variations. In the considered cases with $\mathrm{ACH} = 0.3\,\mathrm{h}^{-1}$, the maximum difference in the indoor temperature provided by the different walls was only $2\,^{\circ}\mathrm{C}$. However, with ACH limited to $0.01\,\mathrm{h}^{-1}$, the differences in the indoor peak temperatures were as high as $7.5\,^{\circ}\mathrm{C}$.

- Although the differences in indoor temperatures caused by walls with different thermal capacitances were not significant during most of time (if the ventilation is taken into account), there are still pronounced discrepancies in surface temperatures. Depending on the day of the analyzed summer week, the high thermal capacitance walls have 1–7 °C lower peak temperatures of the wall internal surface than the low thermal capacitance walls. At the same time, when $\mathrm{ACH} = 0.3\,\mathrm{h}^{-1}$, the differences in peak temperatures of the indoor air in rooms with different walls were kept in a narrow range of 0–2 °C. The surface temperature of high thermal capacitance walls can be several degrees lower / higher

than the indoor air temperature. Since the temperature of the wall internal surface affects the radiative heat exchange with a human body, it influences the thermal sensation. In this regard, high thermal capacitance walls are even more favorable than the calculated PMV results suggest. This effect is hard to quantify, since in the developed model the mean radiant temperature is assumed to be equal to the spatially averaged indoor temperature. One of the next tasks of the author is to extend the capabilities of the current model in order to evaluate the efficiency of the thermal capacitance by taking into account a realistic radiative heat exchange between a body and building internal surfaces.

- The overheating risk is not linearly dependent on the thermal capacitance. The thermal capacitance level characteristic for (composite) structural insulated panels (SIPs or CSIPs), $C_{wall} < 50\,\mathrm{kJ/(m^2\ K)}$, introduces a significant overheating risk, as compared to other wall structures. The risk is significantly limited when the thermal capacitance is increased even by a small amount ($C_{wall} > 150\,\mathrm{kJ/m^2\ K}$). It can be achieved by adding a single, several centimeters wide layer of a high heat capacity material, e.g. light concrete. On the other hand, there are small performance differences between walls with moderate and high thermal capacitances. If the external wall already has at least one layer composed of a high heat capacity material, any further increase of the thermal capacitance brings little effect.

- The stabilizing effects of the high wall thermal capacitance can be lost due to an improper layer sequence. A typical example of an unfavorable layer sequence is a high thermal capacitance layer located at the exterior side of a thermal insulation. The results show that the performance of the wall (M-4) with $C_{wall} \approx 300\,\mathrm{kJ/(m^2\,K)}$ but with the thermal insulation located at the interior side was worse than the wall (M-2) with $C_{wall} \approx 125\,\mathrm{kJ/(m^2\,K)}$ but with a proper layer sequence.

- The results do not indicate strong differences in the performance between walls with U-value of 0.15 and $0.30\,\mathrm{W/(m^2K)}$, at least from the thermal comfort point of view. If two walls have the same thermal capacitance, the wall with $U = 0.15\,\mathrm{W/(m^2K)}$ undergoes only slightly lower indoor temperature variations than the wall with $U = 0.3\,\mathrm{W/(m^2K)}$. When the ventilation is taken into account, this effect is almost unnoticeable. The influence of the U-value on the indoor temperature is higher for low thermal capacitance walls, and lower for high thermal capacitance walls. The thermal capacitance has a stronger

effect on the transient indoor temperature in the considered range of U-values.

- The thermal capacitance of external walls has no influence on the draft occurrence. The drafts were influenced mainly by the inlet air, and not by the natural convection near the wall surface. The DR results (amount of people dissatisfied due to the draft) show that the indoor air velocity can be accelerated by the natural convection up to the uncomfortable magnitude only in the window vicinity, which has the several times higher U-value than the external wall ($U = 1.5\,\mathrm{W/m^2K}$). The maximum local DR generated by the natural convection near the window is about 8.5 % (measured in the case of $\mathrm{ACH} = 0.01\,\mathrm{h^{-1}}$).

- The thermal stratification effect is not significant in such low volumes and under the considered range of conditions. The difference between the temperatures near the floor and ceiling is usually within 1 °C. However, the results are obtained using the Finite Volume Method with a coarse computational grid, that contributes to the solution spatial averaging. The real temperature difference in the vertical direction is expected to be slightly higher.

- The conclusions are valid for buildings with a similar geometry and running under similar conditions, like those modeled within this work. The extrapolation of these conclusions to other cases is possible, but should be conducted with a special care. The presented conclusions particularly do not refer to high indoor spaces like atriums, where a thermal stratification is an important issue.

- The analyzed period of time is still too short to fully evaluate the performance of different walls from the thermal comfort point of view.

- The developed model is capable of providing the detailed information on indoor environments. The structure of the numerical model is suitable for thermal simulations of real buildings. There are, however, two major limitations that hinder its use: (1) the grid generation for complex domains is extremely difficult, and (2) the computing demand of the model is significant for CFD. Nevertheless, the author intends to continue his work in the field of building thermal simulations. The model will be extended by additional features. One of the goals is to take into account the effect of the solar radiation by distributing solar heat gains over building internal surfaces. Also, the long-wave radiation between internal surfaces will be implemented. The author hopes

that the ongoing efforts (of many researchers) to couple building energy simulations with CFD will eventually result in a consistent and reliable building thermal modeling tool, that will be also available for engineers.

References

[1] 2011 Buildings Energy Data Book, U.S. Department of Energy, http://buildingsdatabook.eere.energy.gov, March 2012.

[2] R. Absi, A simple eddy viscosity formulation for turbulent boundary layers near smooth walls, *C. R. Mecanique* 337 (2009), pp. 158–165.

[3] A. Alahmer, A. Mayyas, Abed A. Mayyas, M.A. Omar, D. Shan, Vehicular thermal comfort models; a comprehensive review, *Applied Thermal Engineering* 31 (2011), pp. 995–1002.

[4] ANSI/ASHRAE Standard 55-2004, Thermal Environmental Conditions for Human Occupancy, American Society of Heating, Refrigerating and Air-Conditioning Engineers, Inc., 2004.

[5] ANSI/ASHRAE Standard 62.1-2004, Ventilation for Acceptable Indoor Air Quality in Commercial, Institutional, Industrial and High Rise Residential Buildings, American Society of Heating, Refrigeration and Air-Conditioning Engineers, Inc., 2005.

[6] K. Arendt, M. Krzaczek, J. Florczuk, Numerical analysis by FEM and analytical study of the dynamic behavior of hollow bricks with different cavity concentration, *International Journal of Thermal Sciences* 50 (2011), pp. 1543–1553.

[7] H. Asan, Y.S. Sancaktar, Effects of Wall's thermophysical properties on time lag and decrement factor, *Energy and Building* 28 (1998), pp. 159–166.

[8] H. Asan, Investigation of wall's optimum insulation position from maximum time lag and minimum decrement factor point of view, *Energy and Buildings* 32 (2000), pp. 197–203.

[9] H. Asan, Numerical computation of time lags and decrement factors for different building materials, *Building and Environment* 41 (2006), pp. 615–620.

[10] ASHVE, *Guide*, American Society Of Heating And Ventilating Engineers, 1932.

[11] A. Auliciems, S.V. Szokolay, *Thermal Comfort, Design Tools and Techniques*, note 3, Passive and Low Energy Architecture International, Brisbane, 2007.

[12] H.B. Awbi, Calculation of convective heat transfer coefficients of room surfaces for natural convection, *Energy and Buildings* 28 (1998), pp. 219–227.

[13] C.A. Balaras, The role of thermal mass on the cooling load of buildings, An overview of computational methods, *Energy and Buildings* 24 (1996), pp. 1–10.

[14] C.A. Balaras, K. Droutsa, E. Dascalaki, S. Kontoyiannidis, Heating energy consumption and resulting environmental impact of European apartment buildings, *Energy and Buildings* 37 (2005), pp. 429–442.

[15] M. Bartak, I. Beausoleil-Morrison, J.A. Clarke, J. Denev, F. Drkal, M. Lain, I.A. Macdonald, A. Melikov, Z. Popiolek, P. Stankov, Integrating CFD and building simulation, *Building and Environment* 37 (2002), pp. 865–871.

[16] K.J. Bathe, *Finite Element Procedures in Engineering Analysis*, Prentice-Hall, Englewood, New Jersey, USA, 1982.

[17] K.J. Bathe, *Finite Element Procedures*, Prentice Hall, Upper Saddle River, New Jersey, USA, 1996.

[18] Bill Dunster Architects, *UK Housing and Climate Change: Heavyweight vs. lightweight construction*, ArupResearch+Development, London, 2005.

[19] J. Blazek, *Computational Fluid Dynamics: Principles and Applications*, Elsevier Science Ltd., Kidlington, 2001.

[20] J. Boussinesq, *Essai sur la théorie des eaux courantes*, Mémoires présentés par divers savants à l'Académie des Sciences XXIII, 1, 1877.

[21] P. Bradshaw, T. Cebeci, J.H. Whitelaw, *Engineering Calculation Methods for Turbulent Flow*, Academic Press, London, 1981.

[22] G.S. Brager, R.J. de Dear, Thermal adaptation in the built environment: a literature review, *Energy and Buildings* 27 (1998), pp. 83–96.

[23] G. Buonanno, A. Frattotillo, L. Vanoli, Direct and indirect measurement of WBGT index in transversal flow, *Measurement* 29 (2001), pp. 127–135.

[24] D.M. Causon, C.G. Mingham, L. Qian, *Introductory Finite Volume Methods for PDEs,* Ventus Publishing ApS, Bookboon.com, 2011.

[25] K.E. Charles, *Fanger's Thermal Comfort and Draught Models*, IRC Research Report RR-162, National Research Council of Canada, Ottawa, 2003.

[26] Q. Chen, Ventilation performance prediction for buildings: A method overview and recent applications, *Building and Environment* 44 (2009), pp. 848–858.

[27] Q. Chen, K. Lee, S. Mazumdar, S. Poussou, L. Wang, M. Wang, Z. Zhang, Ventilation performance prediction for buildings: Model assessment, *Building and Environment* 45 (2010), pp. 295–303.

[28] Y. Cheng, J. Niu, N. Gao, Thermal comfort models: A review and numerical investigation, *Building and Environment* 47 (2012), pp. 13–22.

[29] The Climate Database of Typical Meteorological Year, Polish Ministry of Infras- tructure, Warsaw, 2009.

[30] S. Dartevelle, *Comprehensive Approaches to Multiphase Flows in Geophysics — Application to nonisothermal, nonhomogenous, unsteady, large-scale, turbulent dusty clouds, I. Hydrodynamic and Thermodynamic RANS and LES Models*, LA-14228, Los Alamos National Laboratory, 2005.

[31] Dassault Systèmes Simulia Corp., ABAQUS Version 6.8 Documentation, Providence, RI, USA, 2008.

[32] R. de Dear, G. Brager, D. Cooper, *Developing an Adaptive Model of Thermal Comfort and Preference*, Final Report, ASHRAE RP - 884, 1997.

[33] R.J. de Dear, A global database of thermal comfort field experiments, Field Studies of thermal comfort and adaptation, *ASHRAE Technical Data Bulletin* 14 (1) (1998) 15–26; *ASHRAE Transactions* 104 (1) (1998), ASHRAE, Atlanta, USA.

[34] R.J. de Dear, G.S. Brager, Developing an adaptive model of thermal comfort and preference, Field studies of thermal comfort and adaptation, *ASHRAE*

Technical Data Bulletin 14 (1) (1998) 27–49; *ASHRAE Transactions* 104 (1) (1998), ASHRAE, Atlanta, USA.

[35] R.J. de Dear, G.S. Brager, Thermal comfort in naturally ventilated buildings: revisions to ASHRAE Standard 55, *Energy and Building* 34 (2002), pp. 549–561.

[36] N. Djongyang, R. Tchinda, D. Njomo, Thermal comfort: A review paper, *Renewable and Sustainable Energy Reviews* 14 (2010), pp. 2626–2640.

[37] D. DuBois, E.F. DuBois, A formula to estimate approximate (body) surface area if weight and height are known, *Archives of Internal Medicine* 17 (1916), pp. 863–871.

[38] EN 15251:2007, Indoor environmental input parameters for design and assessment of energy performance of buildings addressing indoor air quality, thermal environment, lighting and acoustics, European Committee for Standarization, Brussels, 2007.

[39] EN ISO 14683:2007, Thermal bridges in building construction - Linear transmittance - Simplified methods and default values, European Committe for Standarization, Brussels, 2007.

[40] P.O. Fanger, *Thermal Comfort*, Danish Technical Press, 1970 (republished by McGraw-Hill, New York, 1973).

[41] P.O. Fanger, O. Östberg, A.G. McK. Nicholl, N.O. Breum, E. Jerking, Thermal Comfort Conditions during Day and Night, *European Journal of Applied Physiology* 33 (1974), pp. 255–263.

[42] P.O. Fanger, H. Melikov, H. Hanzawa, J. Ring, Air turbulence and sensation of draught, *Energy and Buildings* 12 (1988), pp. 21–39.

[43] P.O. Fanger, J. Toftum, Extension of the PMV model to non-air-conditioned buildings in warm climates, *Energy and Buildings* 34 (2002), pp. 533–536.

[44] D. Fiala, K. Lomas, M. Stohrer, A computer model of human thermoregulation for a wide range of environmental conditions: the passive system, *Journal of Applied Physiology* 87 (1999), pp. 1957–1972.

[45] D. Fiala, K. Lomas, M. Stohrer, Computer prediction of human thermoregulatory and temperature responses to a wide range of environmental conditions, *International Journal of Biometeorology* 45 (2001), pp. 143–159.

[46] Fluent, Inc., Fluent Version 6.1 Manual, Lebanon, New Hampshire, USA, 2003.

[47] E. Foda, I. Almesri, H.B. Awbi, K, Sirén, Models of human thermoregulation and the prediction of local and overall thermal sensations, *Building and Environment* 46 (2011), pp. 2023–2032.

[48] S. Fohanno, G. Polidori, Modelling of natural convective heat transfer at an internal surface, *Energy and Buildings* 38 (2006), pp. 548–553.

[49] M.E. Fountain, C. Huizenga, *A thermal sensation model for use by the engineering profession*, *Results of Cooperative Research Between ASHRAE and Environmental Analytics*, ASHRAE RP-781 Final Report, Piedmont, 1995.

[50] M. Fountain, G. Brager, R. de Dear, Expectations of indoor climate control, *Energy and Buildings* 24 (1996), pp. 179–182.

[51] G. Fu, A transient, 3-D mathematical thermal model for the clothed human, *Ph.D. dissertation*, Kansas State University, Manhattan, Kansas, 1995.

[52] A.P. Gagge, J.A.J. Stolwijk, Y. Nishi, An effective temperature scale based on a simple model of human physiological regulatory response, *ASHRAE Transactions* 77 (1971), Part 1: pp. 247–262.

[53] A.P. Gagge, A.P. Fobelets, L.G. Berglund, A standard predictive index of human response to the thermal environment, *ASHRAE Transactions* 92 (1986), pp. 709–31.

[54] A. Gagliano, F. Patania, F. Nocera, A. Ferlito, A. Galesi, Thermal performance of ventilated roofs during summer period, *Energy and Buildings* (2012), article in press, doi: 10.1016/j.enbuild.2012.03.2007.

[55] K. Ghali, N. Ghaddar, M. Salloum, Effect of stove asymmetric radiation field on thermal comfort using a multisegmented bioheat model, *Building and Environment* 43 (2008), pp. 1241–1249.

[56] Z. Ghiabaklou, Thermal comfort prediction for a new passive cooling system, *Building and Environment* 38 (2003), pp. 883–891.

[57] gnuplot, official website, http://www.gnuplot.info/, retrieved July 4, 2012.

[58] M. Gorgolewski, Thermal Mass in Buildings, *Advantage Steel* No. 20, Canadian Institute of Steel Construction, 2004.

[59] M. Gorgolewski, Framing Systems and Thermal Mass, *Advantage Steel* No. 26, Canadian Institute of Steel Construction, 2006.

[60] L. Gu, Airflow network modeling in EnergyPlus, *Proceedings: Building Simulation 2007*, IBPSA, Pekin, 2007.

[61] A. Guntermann, A Simplified Degree-day Method for Commercial and Industrial Buildings, *ASHRAE Journal*, March 1982.

[62] F. Haghighat, Y. Li, A.C. Megri, Development and validation of a zonal model — POMA, *Building and Environment* 36 (2001), pp. 1039–1047.

[63] J.W. Hand, *The ESP-r Cookbook*, *Strategies for Deploying Virtual Representations of the Build Environment*, ESRU, University of Strathclyde, Strathclyde, 2010.

[64] J.L.M. Hensen, On the thermal interaction of building structure and heating and ventilating system, *Ph.D. dissertation*, Eindhoven University of Technology (FAGO), Eindhoven, 1991.

[65] J.L. Hensen, *Integrated building airflow simulation*, in Advanced Building Simulation, A. Malkawi and G. Augenbroe (eds.), Spon Press, New York, 2004, pp. 87–118.

[66] F.C. Houghten, C.P. Yagloglou, Determination of comfort zone, *Trans. Am. Soc. Heat. & Vent. Engrs.* 29 (1923), p. 361.

[67] F.C. Houghten, C.P. Yagloglou, Determining equal comfort lines, *J. Am. Soc. Heat. & Vent. Engrs.* 29 (1923), p. 165.

[68] C. Huizenga, H. Zhang, E. Arens, A model of human physiology and comfort for assessing complex thermal environments, *Building and Environment* 36 (2001), pp. 691–699.

[69] M.A. Humphreys, Field studies of thermal comfort compared and applied, *Building Services Engineering*, Vol. 44 (1976), pp. 6–23.

[70] M.A. Humphreys, J.F. Nicol, The validity of ISO-PMV for predicting comfort votes in every-day thermal environments, *Energy and Buildings* 34 (2002), pp. 667–684.

[71] M.A. Humphreys, J.F. Nicol, I.A. Raja, Field studies of indoor thermal comfort and the progress of the adaptive approach, *Journal of Advances on Building Energy Research* 2007, 1:55–88.

[72] ISO 7243, Hot environments — estimation of the heat stress on working man, based on the WBGT-indes (wet bulb globe temperature), International Organization for Standardization, Geneva, 2003.

[73] ISO 13790:2004, Thermal performance of buildings — Calculation of energy use for space heating, International Organization for Standarization, Geneva, 2004.

[74] ISO 7730:2005, Ergonomics of the thermal environment - Analytical determination and interpretation of thermal comfort using calculation of the PMV and PPD indices and local thermal comfort criteria, International Organization for Standarization, Geneva, 2005.

[75] ISO 6946:2007, Building components and building elements – Thermal resistance and thermal transmitance – Calculation method, International Organization for Standardization, Geneva, 2007.

[76] R.I. Issa, Solution of the implicitly discretized fluid flow equations by operator-splitting, *Journal of Computational Physics* 62 (1986), pp. 40–65.

[77] H. Jasak, Error analysis and estimation for the finite volume method with applications to fluid flow, *Ph.D. thesis*, Imperial College, University of London, 1996.

[78] S.E.G Jayamaha, N.E. Wijeysundera, S.K. Chou, Measurement of the Heat Transfer Coefficient for Walls, *Building and Environment* 31 (1996), pp. 399–407.

[79] Y. Jiang, Q. Chen, Study of natural ventilation in buildings by large eddy simulation, *Journal of Wind Engineering and Industrial Aerodynamics* 89 (2001), pp. 1155–1178.

[80] The John B. Pierce Laboratory, official website, http://www.jbpierce.org/, retrieved August 26, 2012.

[81] B.W. Jones, Capabilities and limitations of thermal models for use in thermal comfort standards, *Energy and Buildings* 34 (2002), 653–659.

[82] G. Kalitzin , G. Medic, G. Iaccarino, P. Durbin, Near-wall behavior of RANS turbulence models and implications for wall functions, *Journal of Computational Physics* 204 (2005), pp. 265–291.

[83] C. Kendrick, R. Ogden, X. Wang, B. Baiche, Thermal mass in new build UK housing: A comparison of structural systems in a future weather scenario, *Energy and Buildings* 48 (2012), pp. 40–49.

[84] A. Kurz, Physiology of Thermoregulation, *Best Practise & Research Clinical Anaesthesiology* 22 (2008), No. 4, pp. 627–644.

[85] B.E. Launder, D.B. Spalding, The Numerical Computation of Turbulent Flows, *Computer Methods in Applied Mechanics and Engineering* 3 (1974), pp. 269–289.

[86] R.W. Lewis, P. Nithiarasu, K.N. Seetharamu, *Fundamentals of the Finite Element Method for Heat and Fluid Flow*, John Wiley & Sons, Ltd, Chichester, 2004.

[87] Z. Lin, T.T. Chow, C.F. Tsang, K.F. Fong, L.S. Chan, CFD study on effect of the air supply location on the performance of the displacement ventilation system, *Building and Environment* 40 (2005), pp. 1051–1067.

[88] K. Martín, I. Flores, C. Escudero, A. Apaolaza, J.M. Sala, Methodology for the calculation of response factors through experimental tests and validation with simulation, *Energy and Buildings* 42 (2010), pp. 461–467.

[89] O.A. Marzouk, E.D. Huckaby, Simulation of a Swirling Gas-Particle Flow Using Different k-epsilon Models and Particle-Parcel Relationships, *Engineering Letters*, 18:1, EL_18_1_07, International Association of Engineers, 2010.

[90] D.A. McQuarrie, *Mathematical Methods for Scientists and Engineers*, University Science Books, Sausalito, CA, USA, 2003.

[91] G.P. Mitalas, D.G. Stephenson, Room thermal response factors, *ASHRAE Transactions*, Vol. 73, Part 1, 1967.

[92] T. Mochida, T. Sakoi, ET* and SET*: Its Originality and Characteristics, *Journal of the Human-Environmental System*, Vol. 6; No. 2: 51–59, 2003.

[93] B. Mohammadi, G. Puigt, Wall functions in computational fluid mechanics, *Computers & Fluids* 35 (2006), pp. 1108–1115.

[94] L. Mora, A.J. Gadgil, E. Wurtz, Comparing zonal and CFD model predictions of isothermal indoor airflows to experimental data, *Indoor Air* 13, 2003, pp. 77–85.

[95] M.V. Morkovin, *Effects of Compressibility on Turbulent Flow, The Mechanics of Turbulence*, A. Favre (ed.), Gordon and Breach, New York, 1964.

[96] M.A. Mousa, N. Uddin, Structural behavior and modeling of full-scale composite structural insulated wall panels, *Engineering Structures* 41 (2012), pp. 320–334.

[97] A. Munir, S. Takada, T. Matsuchita, Re-evaluation of Stolwijk's 25-node human thermal model under thermal-transient conditions: Prediction of skin temperature in low-activity conditions, *Building and Environment* 44 (2009), pp. 1777–1787.

[98] M. Musy, F. Winkelmann, E. Wurtz, A. Sergent, Automatically generated zonal models for building air flow simulation: principles and applications, *Building and Environment* 37 (2002), pp. 873–881.

[99] F. Nicol, M. Humphreys, Derivation of the adaptive equations for thermal comfort in free-running buildings in European standard EN 15251, *Building and Environment* 45 (2010), pp. 11–17.

[100] OpenFOAM: *Programmer's Guide*, Version 2.0.0, 16th June 2011.

[101] Unofficial OpenFOAM wiki, http://openfoamwiki.net/, retrieved July 2, 2012.

[102] OpenFOAM Foundation, OpenFOAM: *User Guide*, http://www.openfoam.org/docs/user/, retrieved July 2, 2012.

[103] OpenFOAM Foundation, OpenFOAM C++ documentation, http://foam.sourceforge.net/docs/cpp/, retrieved July 4, 2012.

[104] M. Ozel, K. Pihtili, Optimum location and distribution of insulation layers on building walls with various orientations, *Building and Environment* 42 (2007), pp. 3051–3059.

[105] K. Parsons, Heat stress standard ISO 7243 and its global application, *Industrial Health* 44 (2006), pp. 368–379.

[106] S.V. Patankar, *Numerical Heat Transfer and Fluid Flow*, W.J. Minkowycz and E.M. Sparrow (eds.), Hemisphere Publishing Corporation, New York, 1980.

[107] J. Peltola, T. Pättikangas, Validation and Adaptation of OpenFOAM® Solvers for Heat Transfer and Bubbly Two-phase Flows, OpenFOAM User's Day, 17.5.2011, CSC, Espoo, 2011.

[108] J. Pogorzelski, *Budownictwo Ogólne*, Vol. 2: Fizyka budowli, Chapter 4, P. Klemm (editor), Arkady, Warszawa, 2009 (in Polish).

[109] W.H. Press, S.A. Teukolsky, W.T. Vetterling, B.P. Flannery, *Numerical Recipes: The Art of Scientific Computing* (3rd ed.), New York: Cambridge University Press, 2007.

[110] P. Ravikumar, D. Prakash, Analysis of thermal comfort in a residential room with insect proof screen: A case study by numerical simulation methods, *Building Simulation* 4 (2011), pp. 217–225.

[111] W. Rodi, DNS and LES of some engineering flows, *Fluid Dynamics Research* 38 (2006), pp. 145–173.

[112] L.T. Rodrigues, An investigation into the use of thermal mass to improve comfort in British housing, *Ph.D. dissertation*, University of Nottingham, Nottingham, 2009.

[113] Rozporządzenie Ministra Infrastruktury w sprawie warunków technicznych, jakim powinny odpowiadać budynki i ich usytuowanie z dnia 12 kwietnia 2002 r., Dz.U. Nr 75, poz. 690, (Technical requirements for buildings and their locations, Ordinance of The Polish Minister of Infrastructure of 12 April 2002).

[114] Salim .M. Salim, S.C. Cheah, Wall y^+ Strategy for Dealing with Wall-bounded Turbulent Flows, *Proceedings of the International MultiConference of Engineers and Computer Scientists* (IMECS) 2009, Vol. II, March 18–20, Honk Kong, 2009.

[115] F.G. Schmitt, About Boussinesq's turbulent viscosity hypothesis: historical remarks and a direct evaluation of its validity, *Comptes Rendus Mecanique* 335, 9-10 (2007), pp. 617–627.

[116] Silicon Graphics International Corp., *Features of OpenFOAM*, http://www.openfoam.com/features/, retrieved June 14, 2012.

[117] C.E. Smith, A transient, three-dimensional model of human thermal system, *Ph.D. dissertation*, Kansas State University, Manhattan, Kansas, 1991.

[118] P. Sobotka, H. Yoshino, S. Matsumoto, Thermal Comfort in Passive Solar Earth Integrated Rooms, *Building and Environment* 31 (1996), pp. 155–166.

[119] B. Staniszewski, Wymiana ciepła, Podstawy teoretyczne, PWN, Warszawa, 1980.

[120] G.M. Stavrakakis, M.K. Koukou, M.Gr. Vrachopoulos, N.C. Markatos, Natural cross-ventilation in buildings: Building-scale experiments, numerical simulation and thermal comfort evaluation, *Energy and Buildings* 40 (2008), pp. 1666–1681.

[121] G.M. Stavrakakis, D.P. Karadimou, P.L. Zervas, H. Sarimveis, N.C. Markatos, Selection of window sizes for optimizing occupational comfort and hygiene based on computational fluid dynamics and neural networks, *Building and Environment* 46 (2011), pp. 298–314.

[122] D.G. Stephenson, G.P. Mitalas, Cooling Load Calculations by Thermal Response Factor Method, *ASHRAE Transactions*, Vol. 73, Part 1, 1967.

[123] J.A.J. Stolwijk, *A mathematical model of physiological temperature regulation in man,* NASA-Langley, CR-1855, 1971.

[124] L. Śliwowski, *Budownictwo Ogólne*, Vol. 2: Fizyka budowli, Chapter 3, P. Klemm (editor), Arkady, Warszawa, 2009 (in Polish).

[125] S. Takada, H. Kobayashi, T. Matsuchita, Thermal model of human body fitted with individual characteristics of body temperature regulation, *Building and Environment* 44 (2009), pp. 463–470.

[126] S. Takada, T. Sakiyama, T. Matsuchita, Validity of the two-node model for predicting steady-state skin temperature, *Building and Environment* 46 (2011), pp. 597–604.

[127] S. Tanabe, K. Kobayashi, J. Nakano, Y. Ozeki, M. Konishi, Evaluation of thermal comfort using combined multi-node thermoregulation (65 MN) and radiation models and computational fluid dynamics (CFD), *Energy and Buildings* 34 (2002), pp. 637–646.

[128] K. Tesch, *Mechanika Płynów*, Wydawnictwo Politechniki Gdańskiej, Gdańsk, 2008 (in Polish).

[129] P.T. Tsilingiris, On the thermal time constant of structural walls, *Applied Thermal Engineering* 24 (2004), pp. 743–757.

[130] P.T. Tsilingiris, Wall heat loss from intermittently conditioned spaces — The dynamic influence of structural and operational parameters, *Energy and Buildings* 38 (2006), pp. 1022–1031.

[131] K. Ulgen, Experimental and theoretical investigation of effects of wall's thermophysical properties on time lag and decrement factor, *Energy and Buildings* 34 (2002), pp. 273–278.

[132] H.K. Versteeg, W. Malalasekera, *An introduction to Computational Fluid Dynamics, The Finite Volume Method*, Longman Group Ltd., Harlow, 1995.

[133] G. Villi, W. Pasut, M. De Carli, CFD modelling and thermal performance analysis of a wooden ventilated roof structure, *Building Simulation* 2 (2009), pp. 215–228.

[134] L. Wang, N.H. Wong, Coupled simulations for naturally ventilated residential buildings, *Automation in Construction* 17 (2008), pp. 386-398.

[135] L. Wang, N.H. Wong, Coupled simulations for naturally ventilated rooms between building simulation (BS) and computational fluid dynamics (CFD) for better prediction of indoor thermal environment, *Building and Environment* 44 (2009), pp. 95–112.

[136] Wei-Hwa Chiang, Chia-Ying Wang, Jian-Sheng Huang, Evaluation of cooling ceiling and mechanical ventilation systems on thermal comfort using CFD study in an office for subtropical region, *Building and Environment* 48 (2012), pp. 113–127.

[137] C.E.A. Winslow, L.P. Herrington, A.P. Gagge, Physiological reactions to environmental temperature, *American Journal of Physiology* 120 (1937), pp. 1–22.

[138] E.H. Wissler, *Mathematical simulation of human thermal behavior using whole body models*, in: A. Shitzer and R. Eberhart (Eds.), Heat transfer in medicine and biology, Vol. 1, Plenum Press, New York, USA, 1985, pp. 325–373.

[139] E. Wurtz, J.M. Nataf, F. Winkelmann, Two- and three-dimensional natural and mixed convection simulation using modular zonal models in buildings, *International Journal of Heat and Mass Transfer* 42 (1999), pp. 923–940.

[140] E. Wurtz, L. Mora, C. Inard, An equation-based simulation environment to investigate fast building simulation, *Building and Environment* 41 (2006), pp. 1571-1583.

[141] C.P. Yaglou, D. Minard, Control of heat casualties at military centers, *AMA Archives of Industrial Health* 16 (1957), p. 302.

[142] J. Yam, Y. Li, Z. Zheng, Nonlinear coupling between thermal mass and natural ventilation in buildings, *International Journal of Heat and Mass Transfer* 46 (2003), pp. 1251–1264.

[143] L. Yang, Y. Li, Cooling load reduction by using thermal mass and night ventilation, *Energy and Buildings* 40 (2008), pp. 2052–2058.

[144] Z. Zhai, Q. Chen, P. Haves, J.H. Klems, On approaches to couple energy simulation and computational fluid dynamics programs, *Building and Environment* 37 (2002), pp. 857–864.

[145] Z. Zhai, Q. Chen, Numerical determination and treatment of convective heat transfer coeffcient in the coupled building energy and CFD simulation, *Building and Environment* 39 (2004), pp. 1001–1009.

[146] Y. Zhang, K. Lin, Q. Zhang, H. Di, Ideal thermophysical properties for free-cooling (or heating) buildings with constant thermal physical property material, *Energy and Buildings* 38 (2006), pp. 1164–1170.

[147] Y. Zhang, R. Zhao, Overall thermal sensation, acceptability and comfort, *Building and Environment* 43 (2008), pp. 44–50.

[148] J. Zhou, G. Zhang, Y. Lin, Y. Li, Coupling of thermal mass and natural ventilation in buildings, *Energy and Buildings* 40 (2008), pp. 979–986.

[149] J. Zhou, G. Zhang, Y. Lin, H. Wang, A new virtual sphere method for estimating the role of thermal mass in natural ventilated buildings, *Energy and Buildings* 43 (2011), pp. 75–81.

[150] O.C. Zienkiewicz, K. Morgan, *Finite elements and approximation*, John Wiley & Sons, New York, USA, 1983.

Streszczenie

Praca doktorska przedstawia wyniki analizy numerycznej wpływu akumulacyjności cieplnej ścian na komfort cieplny w budynku. Odpowiedni dobór parametrów cieplnych przegród budynku, w tym akumulacyjności cieplnej, może znacząco obniżyć zapotrzebowanie budynku na energię do ogrzewania i chłodzenia oraz poprawić warunki komfortu cieplnego w pomieszczeniach. Jednak wpływ akumulacyjności cieplnej przegród na warunki wewnętrzne jest złożony i nie zawsze korzystny. Spośród znacznej liczby czynników mających wpływ na wydajność przegród o dużej akumulacyjności można wymienić m.in. warunki klimatyczne, kształt bryły budynku, typ systemu wentylacji, czy sposób użytkowania budynku. Celem niniejszej pracy jest analiza wpływu akumulacyjności cieplnej ścian zewnętrznych budynku na parametry komfortu cieplnego w pomieszczeniach budynków w warunkach klimatu Polski.

Analiza przeprowadzona jest w oparciu o serię symulacji wykonanych na modelu numerycznym reprezentatywnej części budynku. Opracowany model numeryczny zawiera dwa modele składowe: model powietrza wewnętrznego i model przegród zewnętrznych. Modele składowe uruchamiane są w ko-symulacji, wymieniając między sobą dane opisujące przebieg zjawisk fizycznych na wspólnym brzegu obszarów (powierzchni wewnętrznej przegród zewnętrznych). Model uwzględnia niejednorodność środowiska wewnętrznego w budynku oraz dostarcza lokalne wskaźniki komfortu obliczone na podstawie pola rozkładu temperatury oraz pola prędkości powietrza. Znacząca część kodu w języku programowania C++ została opracowana przez autora.

Symulacje numeryczne przeprowadzono dla kilkunastu typów przegród zewnętrznych, dwóch poziomów wymian powietrza wentylacyjnego oraz dwóch profili temperaturowych powietrza zewnętrznego.

Wyniki pokazały, że komfort cieplny w budynkach może zostać poprawiony w sposób pasywny za pomocą odpowiedniego doboru akumulacyjności cieplnej przegród zewnętrznych. Równocześnie jednak wykazano, że intensywność wymian powietrza wentylacyjnego ma dominujący wpływ na warunki klimatu wewnętrznego, co znacznie obniża pozytywny wpływ przegród o dużej akumulacyjności cieplnej na stabilizację parametrów komfortu cieplnego w pomieszczeniach.

List of publications

Publications in journals from ISI Master Journal List (1)

1. K. Arendt, M. Krzaczek, J. Florczuk, Numerical analysis by FEM and analytical study of the dynamic thermal behavior of hollow bricks with different cavity concentration, *International Journal of Thermal Sciences* 50 (2011), 1543–1553. (*32 punkty na liście Ministerstwa Nauki i Szkolnictwa Wyższego*)

Publications in reviewed journals (1)

1. J. Florczuk, K. Arendt, Analiza wydajności kolektora słonecznego przeznaczonego dla systemu ogrzewania budynku o niskim zapotrzebowaniu na ciepło, *Aparatura Badawcza i Dydaktyczna*, T. XV, nr 2 (2010), 23-29. (*6 punktów na liście Ministerstwa Nauki i Szkolnictwa Wyższego*)

Project reports (4)

1. Longlife Report 2, *Development of standards, criteria, specifications*, Ed. K. Rückert, TU Berlin Publications, Berlin, 2010. (ISBN 978-3-7983-2213-4)

2. Longlife Report 3.1, *Sustainable, energy efficient and resource saving residential design*, Ed. K. Rückert, TU Berlin Publications, Berlin, 2011. (ISBN 978-3-7983-2390-2)

3. Longlife Report 3.2, *Prototype Catalogue*, Ed. K. Rückert, TU Berlin Publications, Berlin, 2011. (ISBN 978-3-7983-2391-9)

4. Longlife Report 3.3, *Pilot Projects*, Ed. K. Rückert, TU Berlin Publications, Berlin, 2011. (ISBN 978-3-7983-2392-6)